André Filipe Chaínho Rebelo

Master of Engineering Physics

Investigating conformation-dependence in radiation-induced reactions in isolated biomolecules and clusters

Thesis submitted in partial fulfillment
of the requirements for the degree of

Doctor of Philosophy in
Radiation Biology and Biophysics Applied Atomic and Molecular Physics

Adviser:	Samuel Peter Eden, Senior Lecturer, The Open University
Co-advisers:	Jimena Gorfinkiel, Senior Lecturer, The Open University
	Paulo Limão-Vieira, Full Professor, Universidade Nova de Lisboa

Examination Committee

Chair:	Prof. Doutor Ricardo Luis Rosa Jardim Gonçalves
Rapporteurs:	Prof. Doutor Gustavo García Gómez-Tejedor
	Prof. Doutora Sylwia Ptasinska
Members:	Prof. Doutor Samuel Peter Eden
	Prof. Doutor Jean-Christophe Poully
	Prof. Doutora Kate Nixon
	Prof. Doutor Pedro António de Brito Tavares

FACULDADE DE CIÊNCIAS E TECNOLOGIA
UNIVERSIDADE NOVA DE LISBOA

December, 2020

Investigating conformation-dependence in radiation-induced reactions in isolated biomolecules and clusters

Copyright © André Filipe Chaínho Rebelo, Faculty of Sciences and Technology, NOVA University Lisbon.

The Faculty of Sciences and Technology and the NOVA University Lisbon have the right, perpetual and without geographical boundaries, to file and publish this dissertation through printed copies reproduced on paper or on digital form, or by any other means known or that may be invented, and to disseminate through scientific repositories and admit its copying and distribution for non-commercial, educational or research purposes, as long as credit is given to the author and editor.

This document was created using the (pdf)LaTeX processor, based on the "novathesis" template[1], developed at the Dep. Informática of FCT-NOVA [2].
[1] https://github.com/joaomlourenco/novathesis [2] http://www.di.fct.unl.pt

“Be formless, shapeless, like water. When you pour water in a cup, it becomes the cup. When you pour water in a bottle, it becomes the bottle. When you pour water in a teapot, it becomes the teapot. Water can flow or it can crash. Be like water my friend” - Bruce Lee

Acknowledgements

During a Ph.D. you are brought away from your comfort zone: you are expected to work autonomously and in some cases, away from your home country. Sometimes you leave the laboratory feeling that you have made progress; however, there are other days where things do not go as well as expected and you start to get frustrated and demotivated...and that will definitely happen at some point of your Ph.D., whatever it is, wherever you are! At those specific moments it is crucial to feel a supportive environment, which helps you to understand how to deal with frustration, demotivation, and other factors that stop you from keeping going. You will need to learn how to adapt. I consider that the biggest achievement in my Ph.D. was not professional, but rather personal. I learned how to leave my comfort zone and how to surpass the inherent difficulties. I would like to thank to all the people that made it possible. In particular, I would like to thank to my supervisor, Dr. Samuel Eden, who always trusted me, even when I started to doubt in myself and gave me all the conditions to perform the work here presented. I would also like to thank him for the insightful discussions about Science and the opportunities that he gave me to attend several conferences and meetings where I met fellows from the research community. I want to acknowledge the support of Dr. Jimena Gorfinkiel, one of my co-supervisors, not only for the corrections, suggestions and discussions regarding my thesis but also for the knowledge conveyed during her presentations at conferences or group meetings. I also acknowledge Professor Paulo Limão-Vieira, my second supervisor, for the thesis corrections, the contributions for the manuscripts and by establishing the link between Faculdade de Ciências e Tecnologias and the Open University. I am grateful to Professor Nigel Manson who always supported and entrusted our work and for having funded my stay at BESSY II synchrotron in Berlin, Germany. I want to thank Dr. Jean-Christophe Poully and Dr. Thomas Schlatholtër for having supervised my theoretical work, for having introduced to synchrotron journeys and for the work developed together through time. I want to thank Dr. Kate Nixon and Dr. Violaine Vizcaino for their know how and help provided in the improvement of the experiments and data acquisition. Another researcher which I would like to acknowledge and for whom I have a great respect and admiration is professor Nick Braithwaite. He was always willing to help us with anything, from teaching us how to spot weld to lending us power supplies.

After the 'high ranking' members, I would like to thank my colleagues and friends. Here a special thanks goes for my friends Janka Bocková and Telma Marques, with whom I spent most of my laboratory time. Janka was my research colleague and her help for the work presented was valuable. My gratitude goes to Marcin Dampc, Bartec Barc, Mychal Ryska, Rahul Pandey, Tiago Cunha, Dusan Mezsáros, Rebecca Ward, Tony Hajj and Daniel Debes who worked in the Molecular

Clusters Laboratory during or prior to my Ph.D. To my friends at The Open University, namely, Alexandra Loupas, Rachel James, Yadu Krishnan, Mark Parker, Matthew Sylvest, Gonçalo Ferreira, Vicent Deguin, Pierre, Thomas Webley, Lis Moro, Katarzyna Kryzanowska and Ayo Odufowora, I just want you to say that I am really thankful for all the support and of course, the joyful coffee breaks that we shared together. Also related to my period in the UK, a special thanks goes for my JKD/Kali pals and to my instructor Damien Mills. You had such a massive influence in my well-being, either in the classes where we could interact and release stress or in our dinners and movie sessions.

Now, back to my home country, Portugal, I want to thank my friend and colleagues at Faculdade de Ciências e Tecnologia who were always willing to meet me after the long periods abroad. I want to leave a special thank to my closest friends, Pedro Santos and David Fernandes: your unconditional friendship is worth more than anything else. I will always remember your great advices and the effort in my upbringing! Last but not the least, I need to thank my family for the support given during these four years. I am aware that all of you struggled during the time I was away, but you knew that this experience was an added value for my personal and professional life.

Finally, I would like to acknowledge the Portuguese National Funding Agency FCT-MCTES for the grant that was awarded to me (PD/BD/114449/2016) and enabled me to perform the work of my Ph.D. This work was also supported by the Radiation Biology and Biophysics training programme (RaBBiT, PD/00193/2012), and CEFITEC (UID/FIS/00068/2020) and UCIBIO (UID/-Multi/04378/2020) units.

Abstract

Understanding the radiation response of biological material on the nano-scale is a major goal in Chemical Physics. A valuable tool for identifying critical excitation processes and reactions is to compare studies of sequentially more complex molecular systems. However, as the system's complexity increases, so does the number of different conformations within an experimental target – notably different tautomers or cluster arrangements. This complicates experimental interpretations and analogies with biology. This thesis responds to this problem by investigating conformation-specific radiation-induced reactivity in gas-phase biomolecules and clusters.

Firstly, we probe the dissociative ionisation of guanine – the only DNA base with significant populations of multiple tautomers in the gas phase and one of the bases with lowest volatility. We used a desorption method (indirect laser-induced thermal desorption, ILTD) that has recently been shown to be effective at producing intact targets of non-volatile molecules and carried out experiments to confirm the absence of thermal decomposition in our targets. The comparison of metastable dissociation experiments with DFT calculations reveals new evidence for tautomer-dependent fragmentation pathways. We have also extended this work to guanosine targets and investigated the contribution of its tautomers and conformers to the radiation response through DFT and TDDFT calculations.

Secondly, this thesis demonstrates a new approach to trace radiation-induced reaction products to the respective neutral clusters precursors in Stark-deflected supersonic beams. Molecular and cluster ion signals produced by an electron beam crossing the central axis of a nitromethane-argon beam are recorded as a function of deflection voltage. Comparing the resultant Stark removal curves with simulations shows that the detected protonated nitromethane and nitromethane-CH_3^+ ions are reaction products from one specific dimer configuration. This success highlights the method's great potential for elucidating precise intermolecular bonding effects in radiochemistry.

Furthermore, we report on the development of a new experiment to study low-energy electron interactions with Stark-deflected molecules and clusters, as well as with ILT-desorbed molecules.

Keywords: Biomolecules, clusters, radiation, ILTD, Stark deflection

Resumo

Compreender a resposta radiativa do material biológico à nano-escala é um dos maiores objectivos da Química-Física. Uma ferramenta valiosa para identificar processos críticos de excitação e reações é comparar estudos de sistemas moleculares sequencialmente mais complexos. Contudo, à medida que a complexidade do sistema aumenta, também aumenta o número de diferentes conformações do alvo experimental – notavelmente, diferentes tautomeros ou arranjos de agragados. Isto complica a interpretação experimental e analogias com a biologia. Esta tese responde a este problema investigando reatividade induzida por radiação em conformações específicas de biomoléculas e agregados na fase gasosa.

Primeiro, investigamos a ionização dissociativa da guanina – a única base de ADN com populações significantes de múltiplos tautomeros na fase gasosa e uma das bases com menor volatibilidade. Utilizámos um método de desorção (desorção térmica por laser indirecta) que tem mostrado recentemente ser eficaz em produzir alvos intactos de moléculas não-volateis e realizámos estudos para confirmar a ausência de decomposição térmica dos nossos alvos. A comparação da dissociação metaestável com cálculos *DFT* revela novas evidências para caminhos fragmentação dependente dos tautomeros. Extendemos também este trabalho a alvos de guanosina e invetigámos a contribuição dos seus tautomeros e conformeros para a resposta radiativa através de cálculos *DFT* (dependente e independente do tempo).

Em seguida, esta tese demostra uma nova aproximação para atribuir a origem de produtos de reação induzidos por radiação aos respectivos precursores de agregados neutros em feixes supersónicos defletidos por efeito de Stark. Sinais de iões moleculares e de agregados produzidos por um feixe de eletrões cruzando o eixo central de um feixe de nitromethano-argon são registados em função da tensão de deflexão. Comparando as curvas de remoção de Stark resultantes com simulações mostra que os iões de nitrometano protonado e metilado são produtos de reação de um dimero específico. O sucesso deste estudo destaca o grande potencial do método em elucidar efeitos precisos de ligações intermoleculares em radioquímica.

Além do mais, mencionamos o desenvolvimento de um novo aparelho para estudar interações de eletrões de baixas energias com moléculas e agregados defletidos por efeito de Stark, tal como de moléculas desorvidas por laser térmico indirecto.

Palavras-chave: Biomoléculas, agregados, radiação, desorção térmica por laser indirecta, deflexão de Stark

Contents

1 Introduction **1**

1.1 The role of nucleic acids (DNA and RNA) and proteins in living organisms . . . 2

1.2 DNA damage agents and repair mechanisms . . . 3

1.2.1 Direct radiation-induced damage to DNA and RNA . . . 5

1.2.2 Indirect radiation-induced damage to DNA and RNA . . . 8

1.2.3 Timescales for radiation-induced damage . . . 8

1.3 Establishing the bridge between gas phase and biological media . . . 10

1.3.1 Environment effects in radiation induced damage to biomolecules and respective analogues . . . 10

1.3.2 Tackling the key challenges within the bottom-up approach for experiments on neutral biomolecular systems . . . 10

1.4 Layout of the thesis . . . 13

2 Physical chemistry and computational chemistry methods **15**

2.1 Excitation and de-excitation of molecules . . . 15

2.1.1 Rotational, vibrational and electronic states . . . 15

2.1.2 Spin multiplicity of neutral molecules and molecular ions . . . 16

2.1.3 Adiabatic potential energy surfaces (PES) and the Born-Oppenheimer approximation (BOA) . . . 18

2.1.4 Non-adiabatic processes: Avoided crossings and Conical Intersections (CI) 19

2.1.5 Franck-Condon principle . . . 21

2.1.6 General picture of molecular (de)excitation mechanisms . . . 23

2.2 Molecular excitation and ionisation processes induced by photons and electrons . 24

2.2.1 Multi-photon ionisation (MPI) . . . 24

2.2.2 Electron impact ionisation (EII) . . . 26

2.2.3 Dissociative electron attachment (DEA) . . . 27

2.3 Unimolecular reactions . . . 28

2.3.1 Quasi-equilibrium theory (QET) . . . 29

2.3.2 Fragmentation with and without rearrangement . . . 30

2.3.3 Prompt and metastable fragmentation . . . 31

2.3.4 Kinetic energy release . . . 33

2.4 Approximate methods for electronic description and computational quantum chemistry . . . 34
2.4.1 *Ab initio*: Hatree-Fock theory . . . 34
2.4.1.1 Linear combination of atomic orbitals (LCAO) and the Self-Consistent Field (SCF) procedure . . . 35
2.4.2 Density functional theory (DFT) . . . 36
2.4.3 The choice of atomic orbitals basis set . . . 39
2.4.3.1 Pople's basis sets: Split valence basis set . . . 39
2.4.3.2 Polarisation and diffuse functions . . . 40
2.4.3.3 Dunning's basis sets: Correlated consistent basis sets . . . 40
2.4.4 Calculation of transition states and dissociation pathways with computational methods . . . 41
2.5 Intermolecular forces and their description . . . 42
2.5.1 Van der Waals interactions . . . 42
2.5.2 Other electronic multipole interactions . . . 44
2.5.3 Hydrogen bonding . . . 44
2.6 Summary . . . 45

3 Dissociative ionisation of guanine and guanosine tautomers: experiments exploiting ILTD and DFT calculations 47
3.1 Introduction . . . 47
3.2 Experiment . . . 48
3.2.1 The compact MPI-TOF mass spectrometry experiment . . . 48
3.2.2 Indirect laser-induced thermal desorption (ILTD) . . . 51
3.2.2.1 Background of ILTD and comparison with other types of desorption sources . . . 51
3.2.2.2 Description of the ILTD system . . . 54
3.2.2.3 Experimental determination of foil surface temperatures in the OU ILTD system . . . 56
3.3 Guanine: MPI experiments and DFT calculations . . . 61
3.3.1 General introduction . . . 61
3.3.2 Thermal decomposition assessment of guanine targets vaporised in in a resistively-heated nozzle and in an ILTD source . . . 62
3.3.3 Gas-phase tautomers/conformers of guanine and tautomeric effects on prompt fragment ion production . . . 70
3.3.4 Metastable fragmentation of guanine . . . 74
3.3.4.1 Identifying fragmentation pathways using a reflectron-TOF mass spectrometer . . . 74
3.3.4.2 Determining KER of ions produced by metastable dissociation in a reflectron-TOF mass spectrometer . . . 76
3.3.4.3 Results and discussion . . . 77

3.4 Guanosine: MPI experiments and DFT calculations . . . 83
3.4.1 General introduction . . . 83
3.4.2 Investigating thermally-driven effects on ion production from multi-photon ionised guanosine . . . 84
3.4.2.1 Thermal decomposition assessment . . . 84
3.4.2.2 Investigating mechanisms that could be responsible for reduced fragment ion production by guanosine MPI as a function of the desportion laser power: tautomer and conformer populations . 90
3.4.2.3 Investigating mechanisms that could be responsible for reduced fragment ion production by guanosine MPI as a function of the desportion laser power: thermally-enhanced reactivity in neutral excited states . . . 93
3.4.3 Investigating exceptionally strong guanine ion production by guanosine ionisation . . . 96
3.5 Summary . . . 100
3.6 Acknowledgments . . . 101

4 Manipulation of neutral CW molecular beams using Stark deflection 103
4.1 Manipulation of neutral atoms and molecules: an overview . . . 103
4.2 Fundamental physics behind Stark deflection . . . 105
4.3 The Stark deflection apparatus at the OU . . . 107
4.4 Stark deflector electric field . . . 110
4.5 Stark energy shifts . . . 110
4.6 Supersonic molecular beams . . . 111
4.6.1 Supersonic expansion . . . 112
4.6.2 Translational cooling of an expanding gas . . . 114
4.6.3 Seeded beams . . . 116
4.6.4 Rotational and vibrational cooling . . . 116
4.6.5 Clustering . . . 116
4.7 Simulation of deflection profiles . . . 117
4.8 Results . . . 118
4.8.1 Manipulation of neutral nitromethane molecules seeded in helium . . . 118
4.8.2 Tracing reaction products to specific neutral clusters of nitromethane in Stark deflected beams . . . 121
4.8.2.1 CD→SSD neutral conformational dynamics . . . 128
4.8.2.2 BOMD in the electronic ground state of side-by-side dimer cation 130
4.9 Summary and future work . . . 133
4.10 Acknowledgments . . . 134

5 Development of a new DEA / EII / MPI experiment on ILT-desorbed molecules and molecules / clusters in Stark deflected beams 135

5.1 General introduction . . . 135
5.2 Movable skimmer chamber, crossed-beam chamber and reflectron time-of-flight mass spectrometer . . . 137
5.3 The custom *indirect laser-induced thermal desorption* source . . . 141
5.4 Electron gun and Faraday cup . . . 144
5.4.1 Electron gun and time-of-flight mass spectrometer optimisation in preparation for electron impact ionisation experiments . . . 147
5.4.2 Testing the electron gun performance in preparation for dissociative electron attachment experiments . . . 151
5.4.2.1 Pulsing of the electron gun . . . 152
5.4.2.2 The calibration gas inlet system . . . 152
5.5 Summary and future work . . . 154
5.6 Ackowledgments . . . 155

6 Conclusions and outlook **157**
6.1 Highlights . . . 157
6.2 Summary and conclusions . . . 159
6.2.1 Chapter 3 – Dissociative ionisation of guanine and guanosine tautomers: experiments exploiting ILTD and DFT calculations . . . 159
6.2.2 Chapter 4 – Manipulation of neutral CW molecular beams using Stark deflection . . . 160
6.2.3 Chapter 5 – Development of a new DEA / EII / MPI experiment on ILT-desorbed molecules and molecules / clusters in Stark deflected beams . . . 161
6.3 Future work . . . 161

Bibliography **163**

Apêndices **185**

A Unimolecular rate constants for guanine cation tautomers **185**
A.0.1 Simulation of unimolecular rate constants within QET . . . 185
A.0.2 Calculation of mean kinetic energy release and unimolecular rate constants from mass spectra information . . . 196

B Vertical and adiabatic excitations of guanosine tautomers **201**

C C++ code for simulation of Stark deflection profiles **203**

D Extended tests on Stark deflection profiles and Stark removal curves **217**

E CAD of the new DEA / EII / MPI experiment **219**

F Publications **221**

List of Figures

1.1 DNA model. The nucleotide pairing scheme is shown on the right. Original file from [8] 4

1.2 Examples of direct and indirect radiation-induced damage to DNA. Single strand breaks (SSB), double strand breaks (DSB), base change and cross-links alters the genomic code. Depending on the severity of the damage, different cell mechanisms are activated to repair or avoid replication of the faulty codification. Adapted from [12] 6

1.3 Absorption spectrum of RNA and DNA nucleobases: a) adenine, b) guanine, c) thymine, d) uracil, and e) cytosine. Circles represent simulated photo-excitation energies and cross sections. Light and dark purple corresponds to UV-B and UV-C wavelength window of the electromagnetic spectrum, respectively. Adapted from [14]. 7

1.4 Times scales for radiation induced damage and respective stages. Adapted from [18]. 9

2.1 Schematic of the rotational (blue lines, J quantum number), vibrational (red lines, ν quantum number) and electronic (black line, Ground state) energy levels. 16

2.2 Possible spin configurations for singlet and triplet states. Due to indistinguishability of electrons, anti-parallel configurations are expressed as a superposition of states. Note that the singlet state is represented by an antisymmetric configuration, whereas triplet state is represented by symmetric configurations. 17

2.3 Schematic of two potential energy curves, representing the potential energy along a nuclear coordinate, for the electronic ground state and an electronic excited state [43]. The distinct zones of the PECs will be addressed in this chapter. 18

2.4 Two potential energy surfaces, S_0 (electronic GS) and S_1 (first electronic state), representing the photoisomerization process of azobenzene. CoIn refers to the conical intersection point, where S_1 and S_0 are degenerate. 20

2.5 Franck-Condon (vertical) transitions from the vibronic GS to different vibronic levels. Three distinct situations are presented according to the topology of the PEC of the electronic excited state. Adapted from [52]. 22

2.6 Jablonski diagram concerning several excitation and de-excitation processes in molecules. S refers to electronic singlet states and T refers to electronic triplet states. Dark blue arrows represent excitation processes, for example, photon absorption; green and red arrows represent the radiative de-excitation processes, fluorescence and phosphorescence, respectively; radiationless de-excitation processes, IC and ISC are represented by light blue wavy arrows; Vibrational relaxation is represented by black wavy arrows. Adapted from [55] 24

2.7 Comparison between a) EII and b)−e) MPI schemes. In EII, the ionic states of the ion are directly accessed from the electronic GS of the neutral. MPI may involve b) a resonant vibronic excitation with one photon and ionisation with another photon, both with the same energy (resonant enhanced one-color multiphoton ionisation) c) a resonant vibronic excitation with one photon and ionisation with another photon, with different energies (resonant enhanced two-color multiphoton ionisation) d) A resonant vibronic excitation via an off-resonant state, proceeded by ionisation, with photons of different energy (two-color multiphoton ionisation) e) an off-resonant excitation and ionisation, with photons of different energy (two-color multiphoton ionisation) 26

2.8 Left: Schematic showing the possible processes resultant from interaction of low-energy electron with a molecule AB; Right: potential energy curves of the neutral parent and transient negative anion [59]. 27

2.9 Competitive fragmentation pathways of an ABC^+ ion into $AB^+ + C^{\cdot}$, $A^{\cdot} + BC^+$ and $A^+ + BC^{\cdot}$, having energy barriers of E_{01}, E_{02} and E_{03}, respectively [58]. 29

2.10 A schematic PEC associated to a fragmentation with rearrangement. The parent ion $M^{+\cdot}$ is vibrationally excited with an energy E_{int} which is sufficient to surmount the activation energy of the forward reaction E_0, with an excess of E_{exc}. The energy of the products is much lower than that of the TS energy and therefore the activation energy associated with the reverse reaction E_{0r} is not null. The total excess energy is then converted in vibrational E_{vib} and translation energy, KER, of the products [58]. . . . 31

2.11 Schemtatic of a prompt fragmentation (red reaction) and metastable fragmentation (blue reaction) taking place in the interaction and free field regions of a reflectron time-of-flight mass spectrometer, respectively. Adapted from [63]. 32

2.12 Dependence of the metastable ion peak shapes on the activation energies of reverse reactions. Adapted from [58]. 33

2.13 Pictorial example of LCAO procedure to produce two MO of H_2 from two H1s atomic orbitals. When the two atoms approach each other, the intereference can be a) constructive, with both coefficients positive or c) destructive, with one coefficient positive and the other negative. We obtain repectively, a b) σ_{1s} bonding orbital, where there is a significant probability of finding the electrons in between atoms and a d) σ^*_{1s} anti-bonding orbital, where the probability of finding electrons in between atoms is null, represented by a node 36

2.14 Schematic of the Jacob's ladder for DFT. The accuracy increases from the bottom to the top of the ladder. Each exchange-correlation functional is inserted in a rung depending on the of terms used to express it [69]. 38
2.15 Intermolecular geometries/configurations arising from interactions involving the quadrupole moments of the molecules involved [81]. 44
2.16 Representation of a hydrogen bond between a water molecule and an ammonia molecule. The water molecule is referred as the hydrogen bond donor, whereas ammonia is the hydrogen bond acceptor [81]. 45

3.1 Schemes for the two different operation modes of the Compact MPI-TOF experiment: a) Supersonic beam mode and b) ILTD mode. The detailed top view in diagram (b) shows the ILTD source and the extraction grid of the TOF-MS. These are situated in the centre of the diagnostic chamber. 49
3.2 Image of the Compact setup at the OU for MPI–TOF experiments on molecules seeded in supersonic jets or desorbed from a foil with ILTD. A: Expansion chamber for establishing a supersonic jet. B: Diagnostic chamber. C: Gas line supplying He or Ar to the supersonic expansion nozzle. D: DN40CF window for the UV pulses that multi-photon ionise molecules in the supersonic jet or the ILTD target. E: DN16CF viewport for the CW desorption laser fot ILTD. F: CW desorption laser. G: reflectron TOF–MS. H: Pyroelectric joulemeter. 51
3.3 Kinetic diagram for decomposition and melting of a hypothetical thermally-labile solid sample. See the explanation in the text. Taken from [25]. 53
3.4 ILTD system. Top: disassembled 'TOF source' electrodes. A sample is visible on the stainless steel foil gripped by the backplate system. Bottom: the reassembled TOF source with the adhered sample layer on the foil, ready for installation in the Compact MPI-TOF experiment (ILTD mode). 55
3.5 Setup used to measure the temperature of the foil in response to different *laser current* values, mirror angles, and chamber pressures. 57
3.6 Foil temperature vs. *laser current* for two different pressure values. The foil temperatures correspond to the maximum that can be observed after a fine optimisation of the alignment mirror. A polynomial fit is shown for the low-pressure results. The uncertainties on the temperature values are estimated ±2 K, based on the maximum temperatures obtained for separate fine optimisations of the mirror angle. Error bars are not shown for ease of recognizing both data series in the figure. 59
3.7 Laser power impinging on the foil as a function of laser current. The grey data set represents measurements without window or lens. The orange data set represents the mirror + window arrangement in the current measurements. The blue relation applies to power loss due to window only in the MPI-TOF / ILTD experiments. 60
3.8 Maximum temperature on the foil vs. 445 nm laser power hitting the reverse side of the foil. The uncertainties on the temperature values are estimated ±2 K, based on the maximum temperatures obtained for separate fine optimisations of the mirror angle. . 61

3.9 Comparison of two 225 nm MPI-TOF mass spectra of guanine produced by a) heating the sample in a nozzle and seeding the vaporised molecules in helium to produce a molecular beam (MPI with UV average laser pulses of 5×10^7 W/cm^2) b) indirect laser-induced thermal desorption (ILTD) using 0.36 W (foil temperature 404 K) of a 445 nm CW laser (MPI with UV average laser pulses of 7×10^6 W/cm^2). Red dash-dotted lines indicate the presence of thermal reactivity products in the molecular beam and their absence in the ILTD experiments. Figure adapted from [84]. 67

3.10 Two guanine MPI mass spectra acquired at different desorption powers: blue solid line, 0.36 W (foil temperature 404 K); red solid line, 0.81 W (foil temperature 506K). The gas phase molecules were ionised by 225 nm photons with a fluence of 7×10^6 W/cm^2. The guanine+ peak is partially saturated in both mass spectra, as are the strongest fragment ion peaks (notably m/z 43 and 54) in the 0.81 W result. 69

3.11 Ratio of fragment ion signals relative to the $H_3CN_2^+$ / $HCNO^+$ (m/z = 43) fragment ion signal. Open symbols represent the measurement performed after using the highest desorption power 0.81 W. 70

3.12 Structures and atom labelling of the guanine tautomers / conformers reported in the literature [115]. 72

3.13 Time-of-flight mass spectra of guanine fragment ions against reflection voltage. Experimental signal is represented by yellow bands, whereas simulated bands are given by red dotted lines. Guanine was ionised by MPI at 225 nm with a fluence of 7×10^6 W/cm^2. A letter is assigned to each band (see table A.1 for more details). 79

3.14 Sum of MPI mass spectra of guanine at 225 nm and 7×10^6 W/cm^2 for a reflection voltage of -340 V. The inset plot shows the weak bands M, N, O, P in more details. . 80

3.15 Reaction pathways for HCN neutral loss from various guanine tautomer ions: a) keto-N9H-amino; b) enol(*trans*)-N9H-amino; c) keto-N7H-imino; d) keto-N7H-amino; e) enol(*cis*)-N7H-amino. Calculated at DFT level, with the M06-2X functional and 6-311G(d,p) basis set, employing the methodology described in section 2.4.4. 81

3.16 Reaction pathways for HNCO neutral loss from various guanine tautomer ions: a) keto-N9H-amino and enol(*trans*)-N9H-amino; b) keto-N7H-imino and keto-N7H-amino; c) enol(*cis*)-N7H-amino. Calculated at DFT level, with the M06-2X functional and 6-311G(d,p) basis set, employing the methodology described in. Energies are given in eV and include zero-point corrections. 82

3.17 Atom labelling of guanosine and respective ball and stick representation [156]. The atomic labelling in the nucleobase is the same as the atomic labelling of guanine given in the previous section. 84

3.18 Mass spectra of guanosine. Top: our one-colour MPI experiment with 270 nm pulses and fluence of 3.0×10^7 W/cm^2. The desorption laser power of 0.30 W corresponds to 388 K at the hottest part of the foil in contact with the sample. Bottom: De Camillis *et al's* two-colour MPI experiment using simultaneous 267+800 nm pulses from a fs laser. Desorption laser power is not specified, but the authors note foil temperatures of approximately 423−523 K in their paper about all four DNA nucleosides [31]. The letter b stands for base fragment ions. 87

3.19 Ratios of fragment ion yield over guanosine$^+$ yield plotted against desorption laser power for the major (left) and minor (right) ion peaks in the present MPI-TOF mass spectra. Relative yields for the [B+H]$^+$ fragment ion are not given for desorption powers ≥ 0.36 W due to saturation of the signal. Dashed-dotted lines are exponential fits to data points. The error bars are given by the standard deviation of the ratios. . . 88

3.20 Structures and relative zero-point energies of keto and enol tautomers of guanosine. For the keto and enol tautomers, the two distinct *syn* (with a 5'OH···N3 hydrogen bond) and *anti* (with a 2'OH···N3 hydrogen bond) conformers are also presented. Various conformers of the enol tautomer have been described by Nir *et al* but here we only present the lowest energy structure reported in their work [157]. This conformer is more stable than the *anti* conformer, the next lowest-energy structure, by 0.09 eV, calculated at the HF/6-31G(d,p) level. The *syn* conformer of the keto tautomer of 3'OH-deoxyguanosine was predicted by Nir *et al* to be more stable than the *anti* conformer by 0.07 eV at HF/6-31G(d,p) level [97]. 91

3.21 Boltzmann distribution for the different tautomers/conformers of guanosine, calculated based on the relative thermal energies in the 250−450 K range. The population of keto-*anti*+enol-*anti* is negligible compared with populations of the remaining two tautomers (<1% at 450 K). Note that the foil temperatures in the present experiments on guanosine ranged from 388 to 426 K (see Fig. 3.18). 92

3.22 Potential energy curves along 5'O−H bond distance of keto and enol tautomers of guanosine with a *syn* conformation. In a) and b), a linear coordinate interpolation was performed between the S_0 optimized geometry (crossed red open square) and the first point of the S_1 state with CT character (crossed blue open circle). Red open squares represent the energy of the S_0 state at the optimised S_1 geometry. In panels c) and d), the red open squares represent the energy of the optimised S_0 state. S_1 depicts the adiabatic PEC for the first neutral excited state and the red full squares the energy of the S_0 state at those geometries. The fundamental (v" = 0) and first excited (v" = 1) vibrational levels of the 5'O−H stretching motion are represented by solid black lines. 95

3.23 Reaction pathways of keto-*syn*-guanosine. The pathways shown in green and red produce a guanine fragment ion and a dehydrogenated neutral sugar. The pathway shown in blue produces a double hydrogenated guanine ion and a doubly dehydrogenated neutral sugar. 99

4.1 Schematic of the Stark experiment. 107

4.2 Schematic of the gas line mounted in the first chamber of Stark apparatus. The insert shows a cut of the nozzle where the cartridge for solid samples is mounted (not used in the present chapter). 108

4.3 Top view of the electron chamber. The electron beam produced by the Kimball electron gun (red dashed line) crosses the supersonic beam (green solid line) in the extraction region of the TOF mass spectrometer. The movable skimmer can be moved in a direction perpendicular to the cross section of the figure. Adapted from [106]. 109

4.4 Stark deflector CAD on the left and pictorial representation of the electric field in the gap between rod and trough. Electric field values are given in kV/mm. 110

4.5 Electric field strength inside the Stark deflector, along the vertical direction (Y) for an applied voltage of 4 kV on the rod. Calculated using Quickfield 6.3 student version. . 111

4.6 Stark energy curves for some of the nitromethane rotational states. Right: calculated by Schwettmann *et al* [195] using the nomenclature |J, τ, M⟩, where τ is a pseudo-quantum number with integer values between -J and +J for fixed J and M. Left: Calculated by our group using the CMIStark programme and using the rotational constants and the electric dipole moment given in Schwettemann work. 112

4.7 Scheme of the different zones comprising the expanded beam. M denotes the Mach number. Reproduced from [200]. 113

4.8 M=0 represents a Maxwell-Boltzmann velocity distribution, while M=10 and M=25 represent two velocity distributions of supersonic jets. Widths of supersonic distributions reflect the translational temperature of the beam: the narrower the width, the lower the translational temperature and larger the Mach number. Reproduced from [202]. 115

4.9 Deflection profiles of nitromethane ion signal seeded in helium at 4 kV and 8 kV. Blue crosses correspond to the intensity of the undeflected beam. The solid blue curve was obtained from a fit to the points. Red open circles correspond to the measured intensity of the deflected beam and the solid red lines represent the simulated deflected profiles. The recovered percentage of the nitromethane ion signal is given for both cases. The vertical dashed green line represents the movable skimmer position at which our simulations begin to disagree with the experimental points. 120

4.10 Electron impact ionisation mass spectra of nitromethane seeded in argon at 0 kV (red) and 12 kV (blue) deflection voltages. The upper panel shows an extended m/z range, where cluster ions up to the pentamers can be observed. Prominent signals for fragment ions from clusters are visible at m/z=62 (protonated nitromethane, $(NM)H^+$) and m/z=76 (methylated nitromethane, $(NM)CH_3^+$). The bottom panel shows that the NM^+ ion signal exhibits a larger degree of removal than cluster fragment ions and the dimer ion ($(NM)_2^+$), and this is attributed due to the distinct Stark effects of the respective neutral precursors. 123

4.11 Geometries of the optimised monomer, dimer and trimer structures at M06−2X/aug−cc−pVDZ level. 124

4.12 Upper panel: simulated removal curves of nitromethane monomers (dashed) and combinations of monomers and side-by-side dimers (full) at different rotational temperatures. Experimental points of NM^+ ion signal are given by open circles; Bottom panel: removal curves of side-by-side dimers (dashed) and collinear dimers (full). Experimental points of $(NM)H^+$ and $(NM)CH_3^+$ ion signals are given by open triangles and crosses, respectively. Removal curves for the dimer ion itself and for the protonated dimer ion are not presented due to large fluctuations linked to relatively low signal-to-noise ratios. 126

4.13 Simulated removal curves of mixed nitromethane monomers and side-by-side dimers with the same rotational temperature of 10 K (blue) and a rotational temperature of 10 K for the monomer and 50 K for the SSD (red). The experimental points of nitromethane ion signal are shown as open black circles. 127

4.14 N-C-N bend and N-C-N-C dihedral angles established between molecules in nitromethane dimers as function of MD simulation time, at an initial temperature of 300 K (left panels) and 10 K (right panels). The starting point of the simulation is the collinear dimer (CD) with optimised bend and dihedral angles of the 19º and -110º, respectively. The bend and dihedral angles of the side-by-side dimer are approximately 140º and 0º, respectively. Hence the simulation indicates rapid relaxation from the CD to the SD. 129

4.15 Optimised structures of $(NM)CH_3^+$, $(NM)H^+$ and NM^+ products and respective intermediates after ionisation of the SSD. Energies are given relative to the vertical ionised SSD energy, $(NM)_2^+$. Note that the optimisation of the vertical ionised SSD converges to the $(NM)_{2,adiab}^+$ structure; therefore, it is a local minimum. Lower energy structures, namely $(NM)H^+\cdots(NM{-}H)$ and $(NM)CH_3^+\cdots NO_2$ may connect to the vertically ionised SSD through transition states (TS) in the multidimensional potential energy surface (PES). 131

5.1 Components featuring the crossed beam chamber of the new DEA / EII / MPI experiment. Briefly the main parts of the experiment that are not shown in the interest of simplicity: (i) the inlet system for effusive calibration gas and (ii) the supersonic beam that can cross the electron beam or the UV laser beam as an alternative target to the ILTD system. Figure taken from [84]. 137

5.2 CAD drawing of the new SS316L chamber. Dimension are given in mm. The top image is a view from above and the bottom image is a view from the slide. Key flange purposes include: G: Stark-manipulated molecular beam entrance, E: electron gun insertion, H: UV laser pulse entrance, I: mass spectrometer mount, and J: ILTD source insertion. 138

5.3 Photographs of the new DEA / EII / MPI experiment. a) Side view of the experiment. The supersonic beam generated in the expansion chamber propagates from the left to the right. b) The support system for the turbobomolecular pump of the movable skimmer chamber. Adapted from [84]. 140

5.4 CAD drawing of the *indirect laser-induced thermal desorption* source assembled in the new apparatus. The ILTD source is composed by a titanium disk and ring, which lock the SS304 foil. The larger surface of the foil permits longer acquisition times compared with the ILTD source existent in the compact experiment. 142
5.5 Left: View of ILTD source and ion optics from a DN100CF flange. A: Sample plate; B: Holder with fibre optic; C: Calibration gas inlet; D: Backplate of ion optics; E: Faraday cup. Right: Bottom flange partially-disassembled (note that the fibre optic holder and the calibration gas inlet are not present). The black knob allows the rotation of the ILTD source. 142
5.6 Electron gun scheme. The diameter of cathode aperture is 1.6 mm, whereas the diameter of grid and anode apertures is 1 mm. The red line indicates the trajectory of the electrons. 145
5.7 Electronic scheme of the electron gun and Faraday cup. Adapted from [240] 145
5.8 Electron gun and Faraday cup extension (red and blue dots, respectively) to shield the electron beam from field leaks from the TOF source electrodes above the pulser grid. 147
5.9 Optimisation of EG parameters at 70 eV. Red triangles and blue diamonds refer to currents measured on the grid and FC, respectively, as a function of: a) Current passing through the filament (cathode voltage 29 V and grid voltage 31.8 V, Helmholtz coils current 4.5 A); b) Voltage applied to the grid (EG current 2.25 A, cathode voltage 29 V, and Helmholtz coils current 4.5 A); c) Voltage applied to the cathode with respect to −70 V (EG current 2.25 A, grid voltage 31.8 V, and Helmholtz coils current 4.5 A); d) Current applied to the Helmholtz coils (EG current 2.25 A, cathode voltage 29 V, and grid voltage 31.8 V). All voltages given are with respect to the beam voltage that the electron gun is floated at (-70 V). 149
5.10 a) TOF source of the new DEA / EII / MPI appartus. b) Front view of the crossed-beam chamber with the TOF source assembled on the top. 150
5.11 EII-TOF mass spectra of methanol seeded in helium at 70 eV. A supersonic beam was generated in a 50 μm nozzle by seeding 120 mbar of methanol in 1.1 bar of helium. The nozzle and the sample's reservoir were kept at room temperature. The expansion chamber was evacuated with a speed of 3300 l/s. The black solid line represents a mass spectrum where the Stark deflector was off (0 kV) and the dashed red curve represents a mass spectrum with 10 kV difference between rod and trough of the Stark deflector. Experimental Stark removal points are shown as inset. 151
5.12 Top: Pulsing scheme for the grid of the EG and the extraction grid of the ion optics. Bottom: Optimisation of 33^+ ion signal resultant from fragmentation of methanol clusters seeded in He, upon collision with 70 eV electrons. 153

A.1 Unimolecular rate constants calculated with the quasi-equilibrium theory for the five lowest guanine tautomers concerning the $G^+ \rightarrow [G\text{-}HCN]^+ + HCN$ reaction. 195
A.2 Unimolecular rate constants calculated with the quasi-equilibrium theory for the five lowest guanine tautomers concerning the $G^+ \rightarrow [G\text{-}HCNO]^+ + HCNO$ reaction. 195

A.3 Time of flight broadening of the $[G-HCN]^+$ fragment ion signal due to kinetic energy released in the dissociation. Owing to the low intensity of the fragment ion signal, four different mass spectra were summed. 198

A.4 Time of flight broadening of the $[G-HCNO]^+$ fragment ion signal due to kinetic energy released in the dissociation. This is one of the four ion signals used to calculate the mean KER. 199

B.1 Vertical excited states of a) guanosine-keto-*syn* and b) guanosine-enol-*syn*. Optimised S_1 geometry of c) guanosine-keto-*syn* for 5'O-H bond distance of 0.98 Å , d) guanosine-enol-*syn* for 5'O-H bond distance of 0.98 Å and e) guanosine-enol-*syn* after hydrogen transfer from the 5'O position to the N3 site. The optimised geometry of guanosine-keto-*syn* after hydrogen transfer could not be found due to a degenerancy of S_1 and S_2 electronic states. The calculations were performed at TDDFT level with the M06-2X functional and 6-31+G(d) basis set. 201

D.1 Simulated removal curves of side-by-side monomers with a rotational temperature of 10 K (dashed blue) and 50 K (dashed purple). Removal curves for SSD-argon complexes are represented by dashed-dotted, dashed-dotted-dotted, solid and dotted lines. These curves were obtained by scaling the pure SSD curves. The experimental protonated nitromethane and methylated nitromethane ion signals are represented by open black triangles and black crosses, respectively. 217

E.1 CAD of the new DEA / EII / MPI apparatus. The expansion chamber is not depicted. The bottom figure shows a cut plane of the experiment where components in the vacuum side are visible. The supersonic beam, the electron beam and the ILT-desorbed plume are represented by blue, red and green colours, respectively. 220

List of Tables

2.1 Mean unsigned errors (MUE) of functionals and *ab initio* methods discussed in the present chapter. TC: Thermochemistry; DBH: Diverse barrier heights; TK: Thermochemical kinetics; NCIE: Non-covalent interaction energies; TKNC: Thermochemical of non-covalent. All values are given in kcal/mol. Adapted from [70] 39

3.1 Literature review on volatilisation techniques and tests of target decomposition or reactivity in experiments on guanine. Adapted from [84]. 66

3.2 Relative energies of different guanine tautomers. [a]:Obtained at (DFT/MRCI)//B3LYP/TZVP level; [b]: Obtained at B3LYP/6-311++G(d,p) level; [c]: Obtained at MP2/6−311G(d,p) level. . 71

3.3 Percentage of fragment ion signal relative to fragment ion m/z=43 obtained from EII mass spectrometry studies employing different vaporization methodologies: **Minaev** [126]: Effusive thermal source at 410 K; **Rice** [115]: Thermal heating (the temperature is not specified); **Zavilopulo** [127]: Effusive thermal source at 610 K; **This work**: ILTD source at different laser powers (temperatures of the foil). The assignment of fragment ions follows previous assignments in the literature [124, 126, 137]. 73

3.4 Summary of the metastable assignments to the bands observed in the present experiments (figures 3.13 and 3.14) and in Rice's EII experiments [115]. Bands G and M-P are very weak. There is a ±1 m/z uncertainty on the identity of the precursor and daughter ions for these bands. The dissociation channels highlighted in red or blue could plausibly be activated sequentially following an ionisation event. 78

3.5 Adiabatic ionisation energies of different guanine tautomers (including zero-point corrections). Dissociation and appearance energies for reaction pathways leading to bands A and D are also given. The uncertainty for ionisation energies is ±0.11 eV, for dissociation energies ±0.05 eV, and for the appearance energies ±0.16 eV. 83

3.6 Literature summary of volatilisation techniques and information relevant to target decomposition in experiments on neutral guanosine. See the list of acronyms at the beginning of the thesis for full names of experimental methods. 86

3.7 Fragment ions observed in the MPI mass spectrum of guanosine and guanosine. The guanosine sample was desorbed at 0.30 W (foil temperature 388 K) and ionised with 270 nm photons at a fluence of 3×10^7 W/cm^2. The guanine sample was desorbed at 0.36 W (foil temperature 404 K) of and ionised with 225 nm photons at a fluence of 5×10^7 W/cm^2. *: Weak channels with an intensity larger than 0.5% and smaller than 5%, relative to the most intense feature in the mass spectrum. [a]: This signal is too strong to be attributable solely to isotopes of $[B+H]^+$. 97

4.1 Terminal velocities for He, Ar and Kr at 300 and 393 K. Values calculated using equation 4.6 114

4.2 Electric dipole moment, rotational constants and relative energies of the optimized nitromethane monomer, dimers and trimers. Relative energies include zero-point corrections.[a]: The electric dipole moment value was taken from [195] and the rotational constants from [211]. 125

4.3 Ions' branching ratios resultant from the BOMD in the electronic ground state of the SSD ion. 133

5.1 Relative magnetic permeabilities of materials used in the new apparatus. 139

A.1 Reflectron time of flight parameters and deduced parameters for the estimation of metastable kinetics for a reflection voltage of V_r=−580 V. Under these conditions, the fragment ion originated from HCNO loss from guanine cation has the same ToF as the parent ion at V_r=−100 V. 197

A.2 Reflectron time of flight parameters and deduced parameters for the estimation of metastable kinetics for a reflection voltage of V_r=−400 V. Under these conditions, the fragment ion originated from HCN loss from guanine cation has the same ToF as the parent ion at V_r=−100 V. 197

Acronyms

AIE	Adiabatic ionisation energy
AO	Atomic orbitals
BOA	Born-Oppenheimer approximation
BOMD	Born-Oppenheimer molecular dynamics
cGTO	Contracted gaussian type orbital
CI	Conical intersection
CT	Charge transfer
CW	Continuous wave
DE	Dissociation energy
DEA	Dissociative electron attachment
DFT	Density functional theory
DFTB	Density functional tight binding
DNA	Deoxyribonucleic acid
EG	Electron gun
EII	Electron impact ionisation
ESI	Electrospray ionisation
FC	Faraday cup
FEA	Finite element analysis
FFR	Free field region
GS	Ground state
GTO	Gaussian type orbitals
HEE	High energy electrons
HF	Hartree-Fock

HOMO	Highest occupied molecular orbital
IC	Internal conversion
IE	Ionization energy
ILTD	Indirect laser-induced thermal desorption
IRC	Intrinsic reaction coordinate
ISC	Intersystem crossing
KER	Kinetic energy release
KS	Kohn-Sham
LCAO	Linear combination of atomic orbitals
LEE	Low energy electrons
LIAD	Laser induced acoustic desorption
LUMO	Lowest unoccupied molecular orbital
m/z	Mass/charge
MALDI	Matrix-assisted laser desorption ionisation
MCP	Microchannel plate
MO	Molecular orbital
MPI	Multi-photon ionisation
NAC	Non-adiabatic coupling
NIST	National Institute of Standards and Technology
OU	Open University
PEC	Potential energy curve
PeS	Photoelectron spectroscopy
PES	Potential energy surface
PFD	Peterssen-Frisch dispersion
PIPECO	Photo-ion photo-electron in coincidence
QET	Quasi-equilibrium theory
QST	Quadratic synchronous transit
R2PI	Resonant 2 photon ionisation
REMPI	Resonance enhanced multi-photon ionization
RFT	Relative flow technique

RNA	Ribonucleic acid
SCF	Self-consistent field
SHB	Spectral hole-burning
SPI	Single-photon ionisation
TDDFT	Time-dependent density functional theory
TDSE	Time-dependent Schrodinger equation
TNI	Transient negative ions
TOF	Time-of-flight
TS	Transition state
UV	Ultraviolet
VdW	Van der Waals
VIE	Vertical ionisation energy
WF	Wavefunction
XC	Exchange-correlation

*

Chapter 1

Introduction

Ionising radiation has the ability to induce structural and chemical alterations to biological macromolecules, for example DNA, leading to undesirable effects: cell death and mutations [1] that can lead to cancer if left unrepaired. Macroscopic parameters such as the effective dose and the irradiated volume can be monitored to quantify radiation effects of individuals exposed to high fluxes of ionising radiation, for example in radiotherapy and diagnosis. However, the exposure to low doses of radiation do not lead to deterministic effects, but rather to stochastic effects: the primary radiation has a certain probability of forming ionisation clusters along the radiation track; at these sites, secondary species such as low energy electrons and radicals are generated and these also have a certain probability for inducing further biomolecular damage in a nanoscopic volume [2]; therefore, an extensive number of studies on radiation induced molecular damage have been conducted in the last decades for establishing a correlation between nanodosimetric parameters and biological effects of radiation [3]. Investigating how DNA, RNA, and other organic molecules react to radiation may also answer some questions related with the molecular origin and evolution of life on Earth [4]. Despite all the efforts made, the fundamental mechanisms involved in biomolecular damage induced by radiation and the respective secondary effects are only partially understood.

The bottom-up approach enables researchers to evaluate critical processes taking place in large molecular systems after its irradiation. The bottom-up approach initially studies the radiation responses of building blocks of larger molecular systems, free from any environment effect, that is, in the gas phase. The molecular complexity is then progressively increased, which permits the evaluation of environment effects by monitoring changes in the dynamics [5], manifested, for example, as new products being formed after irradiation. Studying a relatively small biomolecule in the gas phase enables us to draw comparisons between experiments (with precise knowledge of the exact configuration of the target) and high-level calculations. Such comparisons give us the best chance for characterising precisely radiation induced processes in a molecule. As we start moving towards more *realistic* targets (bigger biomolecules which have more in common with key macromolecules and clusters) we generally have less precise knowledge about the target (e.g. the target will comprise many different structures) and calculations depend on more approximations to remain computationally affordable. The idea behind the bottom-up approach is that the studies of radiation interactions with sequentially more complex targets will contain signatures of certain

processes that we were able to characterise precisely in the less complex targets. This approach has delivered many sucesses, one example being Leon Sanche's experiments back in 2000, where they observed that strand breaks of DNA bound to a surface showed a similar dependence on the incident electron energy compared with dissociative electron attachment (DEA) to the individual building blocks of DNA (bases, sugar ring, and water) [6]. The authors also showed that electrons with energy below the ionisation threshold can induce more damage to DNA than photons with energies above the ionisation threshold. Such experiments provided the breakthrough evidence supporting that DEA plays a significant role in radiation damage to DNA. Understanding radiation processes at the most fundamental level can offer insights into how to modify radiation response on the nanoscale, e.g. by tuning the energy and type of radiation or the chemical environment of the molecules. in such a way that they suffer more or less damage. This must be a promising route for enhancing radiotherapies since understanding how these factors affect the different molecules may enable medical physicists to spare the genetic material of healthy cells while increasing the lethality to that of cancer cells. However, the bottom-up approach has some challenges that need to be overcome before it can be used in its entirety. The first is related with the non-volatility of solid samples of complex molecules. The second relates with the difficulty of gradually probing more complex clusters of biomolecules due to the mixture of sizes and arrangements in cluster beams. The main goal of the present thesis is to test some of the approaches existent in the literature for overcoming the problems of the bottom-up approach.

In the first part of this chapter we describe the radiation processes responsible for inducing damage to biomolecules and the physiological implications. Then we provide a brief overview on how the environment affect the radiation responses of biomolecules. Finally, we discuss the main problems of the bottom-up approach and explain how the present work may contribute towards overcoming them.

1.1 The role of nucleic acids (DNA and RNA) and proteins in living organisms

Deoxyribonucleic acid (DNA) is a nucleic acid that carries information about the development, functioning, growth and reproduction of organisms. It is responsible, for example, for protein synthesis and can be mainly found in cells' nucleus. Nucleic acids comprise one of the four types of macromolecules present in human bodies alongside with lipids, proteins and carbohydrates. DNA is formed by two coiled chains that originate a double helix structure. Each coil is composed of a series of units called nucleotides, which contain a phosphate group, a deoxyribose sugar and a nucleobase. The phosphate group of one nucleotide establishes a covalent bond with the deoxyribose sugar of the next nucleotide and this occurs in a long sequence to form the backbone of DNA. The four nucleobases in DNA — thymine (T), cytosine (C), adenine (A) and guanine (G) — provide the binding structure that join the two coiled sugar-phosphate chains together. It is the sequence of nucleobases along the molecule that dictates the genetic information contained in DNA. The nucleobases of one chain arrange in a specific way with the nucleobases of the opposing

chain: adenine pairs with thymine (A-T) and cytosine pairs with guanine (C-G) through hydrogen bonds. Nucleobases also interact with other nucleobases of the same chain (through stacking) but such interactions are weaker than hydrogen bonding. A model of a portion of DNA and respective pairing scheme of the nucleotides is shown in Fig 1.1.

In cellular medium, DNA is surrounded by water and proteins, e.g. histones, around which DNA winds and acquires a compact structure. These proteins also regulate the transcription regions of DNA [7]. Another nucleic acid existent in human organisms is the ribonucleic acid (RNA). RNA has as primary role the regulation of protein synthesis. Unlike DNA, RNA molecules are single strands folded onto themselves. Moreover, thymine nucleobases are replaced by uracil in RNA. RNA can be subdivided into three categories according to its task in the synthesis process: messenger RNA (mRNA), transfer RNA (tRNA) and ribossomal RNA (rRNA). The mRNA carries information of DNA regarding protein encoding and it is transcripted by an enzyme called RNA polymerase in the cell's nucleus. Then, this mRNA migrates to ribossomes found in the cell cytoplasm, where proteins are synthesized. The tRNA is responsible to transfer the required amino acids — defined by the codon (set of three successive nucleotides) of the mRNA — to the ribossome. The rRNA constitute most part of the ribossome organelle, which is also composed of stabilising proteins. The molecules studied in chapter 3 — guanine and guanosine — are building blocks of both DNA and RNA and hence, their radiation responses are particularly important to elucidate.

While this thesis is most relevant to DNA and RNA damage, it is important to keep in mind that these are not the only macromolecules that cells rely on for survival and healthy replication. Proteins are important in several biological mechanisms, notably in enzymatic routes where they facilitate chemical reactions. Enzymes are involved, among other processes, in cell cycle regulation. The tumour suppressor p53 protein is activated once cell injuries, for example DNA damage, have been identified and is responsible for triggering responses for cell repair or programmed cell death [9]; however, if the TP53 gene becomes permanently damaged, the production of p53 proteins is compromised as well as the ability to spot cellular injuries and repair DNA. Cell division proceeds with damaged genome and the accumulation of faults can lead to suppression of key biological mechanisms and ultimately, cancer. Cancer is an abnormal cell replication induced by alterations of the cell cycle, which may give origin to solid tumours.

1.2 DNA damage agents and repair mechanisms

DNA damage can occur by endogenous or exogenous agents, the former being responsible for tens of thousands (to the nearest order of magnitude) of DNA changes everyday in a human cell [7]. Endogenous damage results from reaction with metabolic byproducts such as reactive oxygen species (ROS) or alkyl groups. *Spontaneous hydrolysis* of nucleotides, a type of endogenous damage, can lead to base change (cytosine→uracil) and depurination of DNA (cleavage of the N-glycosidic bond established between the sugar ring and purine nucleobases, guanine and adenine). Alternatively, these same damage processes (and many others) can be triggered by an external agent

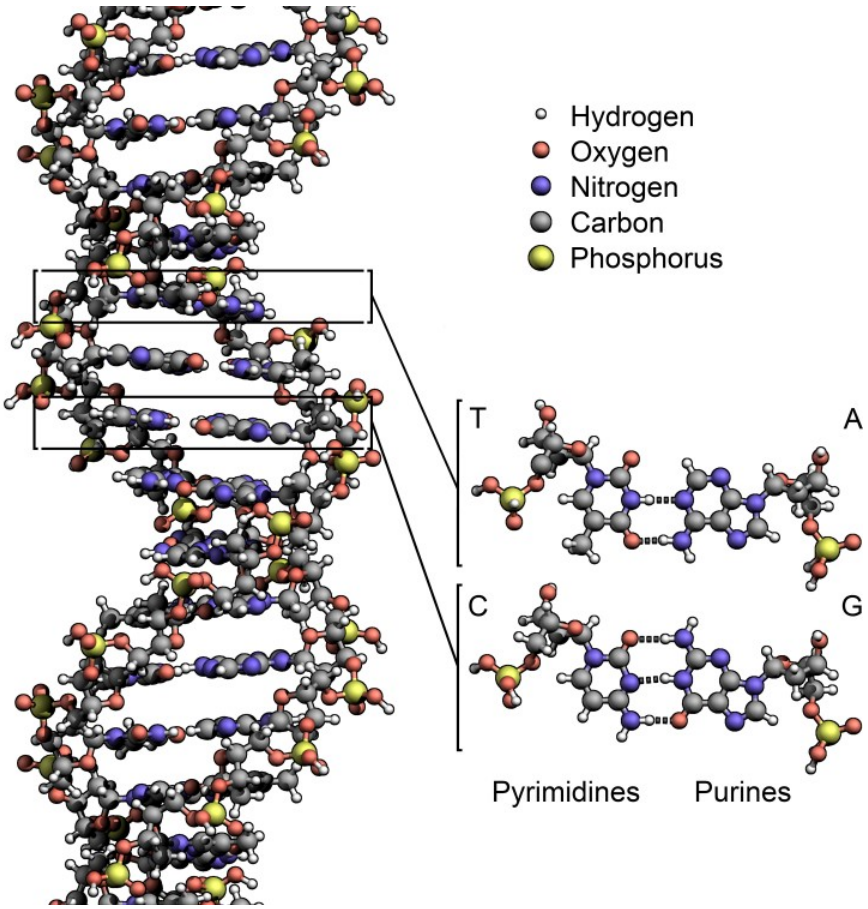

Figure 1.1: DNA model. The nucleotide pairing scheme is shown on the right. Original file from [8]

instead of being endogenous. The experiments and calculations in this thesis are only relevant to exogenous damage. Processes by which exogenous agents can cause DNA damage include:

- Ultraviolet (UV) radiation, inducing water hydrolysis and generation of free radicals that subsequently attack the DNA chain. It can also promote cross-linking (covalent bonding) of adjacent cytosine and thymine nucleobases.

- Ionising radiation, generating a cascade of free radicals. A high density of reactions between these radicals and a localised part of DNA can cause a strand break.

- Chemical mutagens, for example polycyclic aromatic hydrocarbons (PAH) resultant from combustion of fossil fuels [10] reacting with a localised part of DNA.

Radiation can induce DNA damage in a direct or indirect way, and this distinction is discussed in sections 1.2.1 and 1.2.2. Direct damage results from the direct interaction of genotoxic agents with a localised portion of DNA, promoting its disruption. Indirect damage results from interaction of secondary species originated in the track of primary radiation (ROS, free radicals, low energy electrons...) with a localised part of DNA. Fig. 1.2 shows examples of direct and indirect

damage induced to a portion of DNA and some of the lesions that can result. Cells have intrinsic mechanisms to deal and repair DNA damage during cell cycle, for example [7]:

- *Base exchange repair* addresses the conversion of one nucleobase into another, for example deamination of cytosine into uracil. It reinserts the appropriate nucleobase.
- *Nucleotide excision repair* allows to repair large changes in the DNA structure such as the formation of new covalent bonds within the helix or with other molecules.
- *Chemical reversal* of DNA damage permits the removal of alkylated nucleobases.
- *Nonhomologous end joining* and *homologous recombination* are mechanisms used to repair double strand breaks (DSBs). The first mechanism has a higher risk of linking DNA portions of different chromosomes. Homologous recombination is much more efficient but requires an undamaged template, which is only available during specific phases of the cell cycle.

Repair mechanisms, although efficient under most circumstances, are not flawless. DSBs represent the most dangerous type of damage induced to DNA, especially when a template for homologous recombination repair is unavailable. When DNA suffers heavy damage, emergency repair mechanisms may be activated to cope with it. However, such mechanisms exhibit low fidelity in DNA repair, and therefore they should only be activated when they are really necessary. The survival of cells with this type of mechanism is often associated with risk of mutagenesis and carcinogenesis [11]. In the context of this thesis, the fact that repair processes are imperfect and can themselves lead to new problems highlights the importance of understanding radiation interactions with local parts of DNA in as much detail as possible. Furthermore, it reminds us that understanding radiation damage to biological material is a cross-disciplinary challenge and Chemical Physics only addresses the earliest stage in the progression from radiation exposure to cellular death, mutation, or cancer. This is discussed further in section 1.2.3.

1.2.1 Direct radiation-induced damage to DNA and RNA

Direct damage is triggered when incident photons, ions, neutral particles, electrons or protons interact with RNA or DNA molecules causing excitation and ionisation. When ionisation takes place, the hole created in DNA structure weakens the backbone and compromises the molecular integrity. Lewis *et al.* studied the dynamics of holes and showed that they can travel long distances between trapping sites in the DNA strand [13]. This shows that the DNA damage site is not restricted to the interaction site of DNA with radiation. Whether hole dynamics is dominated by inter-strand or intra-strand conduction is still a matter of debate but there is a consensus that guanine is the preferential hole trapping site in DNA since it is the nucleobase with with lowest ionisation energy. This gives extra importance for elucidating the fragmentation pathways of guanine and guanosine ions (chapter 3).

UV radiation is one exogenous agent that causes direct damage to DNA. UV radiation itself covers a wide range of wavelengths and can be subdivided into UV-A (400 – 315 nm, 3.1–3.9 eV), UV-B (315 – 280 nm, 3.9–4.4 eV), UV-C (280 – 100 nm, 4.4–12.4 eV) [15]. More energetic

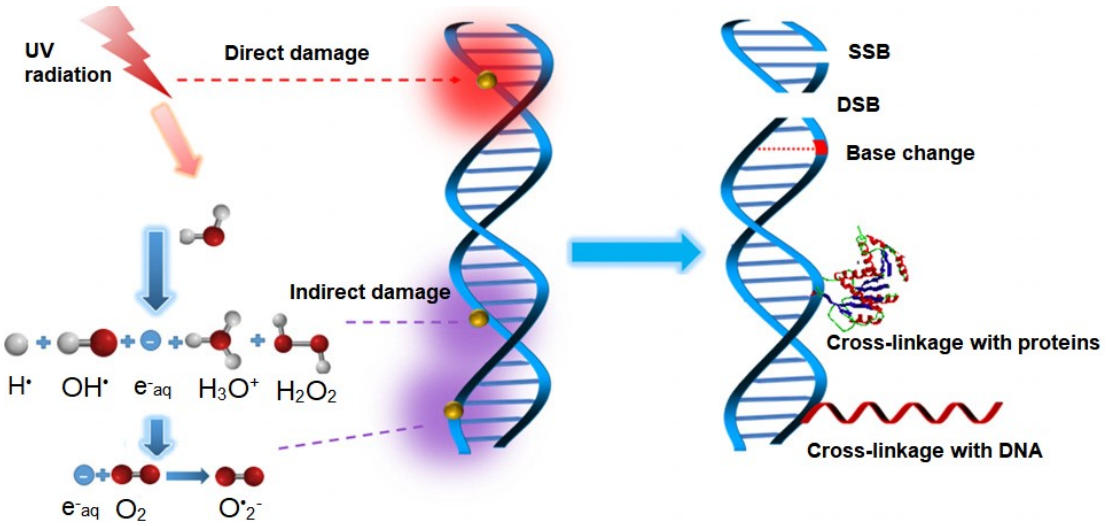

Figure 1.2: Examples of direct and indirect radiation-induced damage to DNA. Single strand breaks (SSB), double strand breaks (DSB), base change and cross-links alters the genomic code. Depending on the severity of the damage, different cell mechanisms are activated to repair or avoid replication of the faulty codification. Adapted from [12]

UV radiation is not discussed here. UV-A radiation represents most of the UV radiation reaching Earth's surface (95%); however, it is very inefficient in causing DNA damage. UV-B and UV-C radiation are greatly absorbed by stratospheric ozone, reaching the Earth's surface only in small doses. However, studying radiation response of molecules in the UVC region is still relevant in the radiobiological point of view: UV-C photon absorption provides are a great way to achieve controlled access to electronic excited states and ionic states in experiments. There are many ways that these states can be accessed in natural or clinical environments (e.g. in interactions with the energetic secondary electrons produced in radiotherapy treatments) so we need to understand the dynamics, relaxation pathways (particularly fragmentation), and reactivities of biomolecules in these states. So this is the main reason we use UV photons in our experiments – as a tool to study molecules and ions in excited states that can be accessed by exposure to diverse types of radiation.

As can be observed in Fig. 1.3, the DNA nucleobases present one broad absorption band with a maximum approximately at 250 – 270 nm (within the UV-C) and another broad band with its maximum one in the VUV (< 200 nm) region of the electromagnetic spectrum. The absorption spectrum of nucleobases overlaps slightly with the UV-B region. Both UV-C and UV-B radiation are responsible for direct excitation and subsequent damage of DNA. In contrast to nucleobases, the DNA backbone absorbs radiation mainly below 220 nm (VUV). The Molecular Clusters Laboratory at the Open University (OU) hosts a tunable pulsed UV laser (270 – 220 nm) giving the chance to access the UV-C absorption bands of nucleobases. More specifically, the experiments on guanine and guanosine in chapter 3 were carried out at 225 and 270 nm, respectively (within the UV-C).

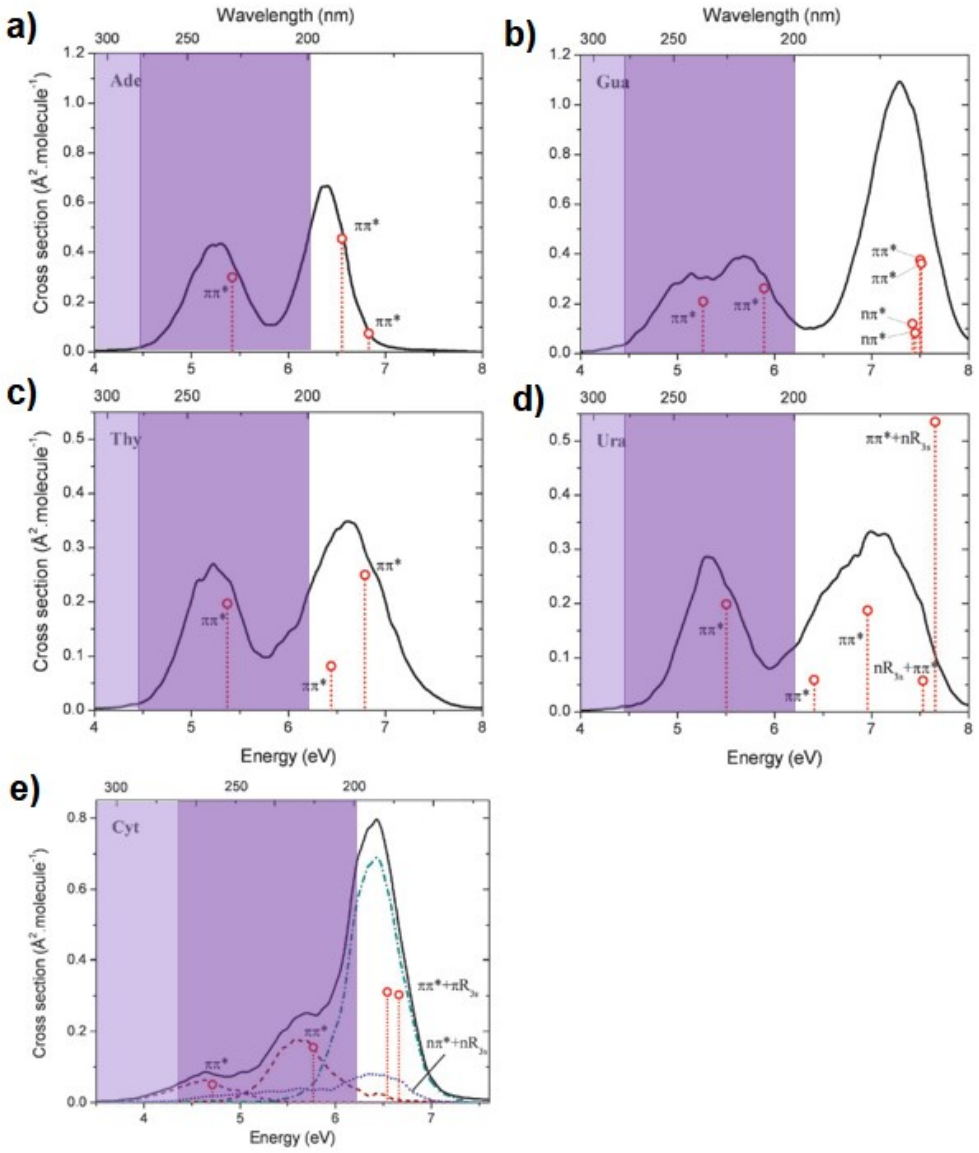

Figure 1.3: Absorption spectrum of RNA and DNA nucleobases: a) adenine, b) guanine, c) thymine, d) uracil, and e) cytosine. Circles represent simulated photo-excitation energies and cross sections. Light and dark purple corresponds to UV-B and UV-C wavelength window of the electromagnetic spectrum, respectively. Adapted from [14].

1.2.2 Indirect radiation-induced damage to DNA and RNA

When high energy radiation interacts and ionises biomolecules surrounding DNA, for example water or proteins, *secondary species* as reactive oxygen species (ROS) or secondary electrons are generated. High energy electrons (HEE) propagate through the medium and are scattered by other molecules. The scattering can be elastic, when no kinetic energy is transferred, or inelastic. Depending on the amount of kinetic energy transferred, inelastic scattering can promote rotational, vibrational and/or electronic excitation or ionisation. Electron impact ionisation (EII) releases additional electrons, triggering a subsequent cascade of collision events [16]. Energy transfer ceases when secondary electrons have nearly no kinetic energy left and become thermalised. Low energy electrons (LEE), with energies < 20 eV, can also temporarily attach to biomolecules, forming a transient negative ion (TNI) which may fragment. The latter process, capable of inducing efficient damage, even at energies below the ionisation energy, is known as dissociative electron attachment (DEA). For each MeV of deposited energy in an aqueous medium, approximately 5×10^4 secondary electrons and roughly the same amount of radicals are generated [17]. Therefore, exposure to energetic radiation not only produces direct damage, but also indirect damage to DNA and RNA. In order to better understand the interactions of secondary electrons with key biomolecules in the gas phase and in clusters, we designed and built a new DEA / EII experiment in the Molecular Clusters Laboratory. The development of this system is described in chapter 5.

1.2.3 Timescales for radiation-induced damage

Radiation damage at the molecular level is triggered by the ionisation and excitation of molecules, generally referred to as *physical stage* of radiation damage, these processes occur very quickly after the interaction between the radiative particle and the molecule (<ps). In the picosecond to second range, molecules can fragment or change their structure (the chemical stage). The experiments and calculations in this thesis relate to the physical and chemical stages, whereas biological effects manifest themselves on much longer timescales. This broad description of radiation damage phases and timescales is summarised in Fig. 1.4.

The large time window for chemical processes arises from their dependency on the energy absorbed by the target. If the energy absorbed is much larger than the energy required to break a bond or change the structure of the molecule then the chemical process occurs fast; if not then the process is rather slow. The timescales for radiation-induced damage to gas-phase molecular targets that can be evaluated in laboratories depend on the type of mass spectrometer used, its geometry and voltages. In the Molecular Clusters Laboratory at the OU, we use reflectron time-of-flight mass spectrometers to evaluate damage induced to the targets by ionisation/excitation through UV radiation or electron impact. With the typical voltages used in this instrument, we can probe damage as soon as the molecule is ionised or excited to approximately 1 μs afterwards. This time window is not sufficient to identify all the chemical types mentioned in Fig. 1.4. However, we can extend this time window up to several tens of μs to identify delayed (often referred as *metastable*) fragmentations by varying the voltages of the mass spectrometer. Such metastable routes are not necessarily the same as the *prompt* (which in the context of our experiments means within several

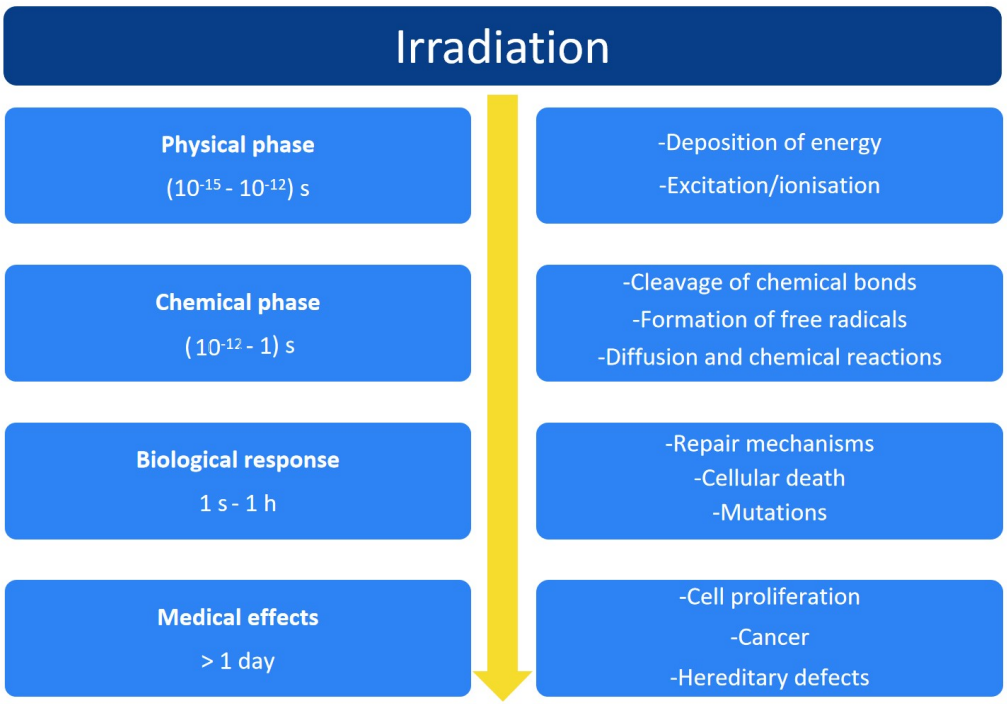

Figure 1.4: Times scales for radiation induced damage and respective stages. Adapted from [18].

tens of ns of ionisation) fragmentations, as will be demonstrated in chapter 3. However, many other fragmentations in our experiments are also visible as metastable fragmentations and we can better understand them by analysing both ions. For example, it is possible to assign *precursor* and *daughter* ions to a specific prompt fragmentation and to identify sequential fragmentations using information obtained in metastable analysis, something that is not possible to achieve solely based on prompt fragmentation studies. Bocková *et al* observed a strong prompt fragmentation of 3-aminophenol into $C_5H_6N^+$, but after analysing the delayed dissociation, they concluded that $C_5H_6N^+$ further decomposes into $C_4H_5^+$ and then into $C_2H_3^+$ [19]. This chain mechanism could not be detected in prompt mass spectra alone, since it requires longer fragmentation timescales. On the other hand, the absence of precursor or daughter ions in the metastable mass spectrum that are observed in the prompt mass spectrum, indicates that these do not dissociate further in timescales up to tens of μs. Metastable studies are very laborious since they require the acquisition of several mass spectra with different voltages applied on the mass spectrometer. However, the additional information that is extracted compared with mass spectrometry studies regarding prompt fragmentation is sometimes justified and necessary. The procedure is discussed in detail in chapter 3.

1.3 Establishing the bridge between gas phase and biological media

1.3.1 Environment effects in radiation induced damage to biomolecules and respective analogues

Studying radiation-induced processes with gas phase molecules as the step of bottom-up approach generally yields the clearest fundamental interpretations thanks to absence of environment effects. However, a molecule's environment can affect dramatically its response to radiation. For example, microhydrated nucleobases and isolated nucleosides capture LEE more readily (i.e. with greater probabilities or *cross-sections*) than isolated nucleobases [20]. Conversely, hydration suppresses high lying resonances responsible for the formation of pyrimidine dimer anions [21]. Such environmental radio-sensitising or radio-protecting effects are not limited to electron attachment induced processes. For example, Kim *et al* observed large differences in the ratios of hydrated and unhydrated adenine ion signals upon ionisation of adenine-water clusters with multiple UV photons and high energy electrons [22]. Below the ionisation limit, the evaporation of solvent molecules is selective, only occurring for hydrated adenine monomers and hydrogen acceptor solvents. Eden and co-workers observed a protective effect of water in UV laser irradiated hydrated adenine: the degree of fragmentation substantially decreased with the increased number of water molecules [23]. The authors concluded that the evaporation of water molecules provides a rapid mechanism to dissipate the energy internally deposited in adenine, and hence a protective effect of this DNA building block. In view of these results, we can conclude that a small biomolecular environment or intermolecular interactions may reduce or enhance the radiation damage. Research of this kind can be extended to larger biomolecular systems, using the bottom-up approach, to better understand how the biological medium responds to radiation.

1.3.2 Tackling the key challenges within the bottom-up approach for experiments on neutral biomolecular systems

The study of progressively more complex molecular systems in the gas phase and in the form of clusters is unquestionably useful to understand biomolecular damage in the cellular environment. However, it also presents some problems, particularly from the the experimental standpoint. The three key challenges that are tackled in this thesis are listed below:

- **Bringing neutral biomolecules into the gas phase without thermal damage**. The low vapour pressure of some molecules can make it difficult to acquire experimental results with good signal-to-noise ratio, particularly when focusing on procedures with low cross sections. In some cases, the temperatures at which the sample is subjected can be increased to solve this problem, but in many biomolecules this can lead to significant thermal decomposition. Cytosine and guanine are the nucleobases with the lowest vapour pressures [24, 25] and accordingly many experimentalists have had difficulties producing high-density targets of these molecules without thermal decomposition. For example, previous members of the Molecular Clusters Group managed to produce a cytosine target without evidence for thermal

decomposition using our heated supersonic beam nozzle but the signals were too weak to allow an in-depth study of the molecule's MPI pathways [26]. For guanine, it proved impossible for us to produce a viable target using this system and, while various studies of guanine using conventional heated sources have been reported (listed in chapter 3), none have presented their evidence for the absence of thermal decomposition. Molecular targets become less volatile as the number of polar groups in its constitution increases. Previous studies on cytidine and guanosine nucleosides reported thermal decomposition of these species when vaporised in conventional sources [27]. Nucleotides represent an even more difficult case. For example, Fang and co-workers analysed triphosphate nucleotide samples (adenosine triphosphate – ATP, uridine triphosphate – UTP, and guanosine triphosphate – GTP) through high-performance liquid chromatography (HPLC) after heating them at 250 ºC. After just 300 s had elapsed, all of the samples had decomposed into the mono-phosphate nucleotide forms [28]. Derivatisation is a common process to increase the volatility of molecules. In such process, polar groups are replaced by non-polar ones such as trimethylsilyl. The drawbacks of this chemical change are the change of response of molecules to radiation and the efficiency of the process which can vary greatly between small molecules [28, 29].

In chapter 3 we investigate the potential of *indirect laser thermal desorption* (*ILTD*) sources in generating dense plumes of intact vaporised molecules of small and medium sizes with small vapour pressures (guanine and guanosine). This kind of source was first developed by Greenwood and co-workers. The group used the source to vaporise the four DNA nucleosides for studying the respective fragmentation when irradiated with 5 keV protons and with UV photons [30, 31]. The only molecules that have been tested thoroughly for the absence of thermal decomposition using ILTD prior to the present work are uracil [32], and four pyrimidine-based nucleosides and the method successfully produced intense pure targets [33]. Uracil is one of the most thermally stable nucleobases and the pyrimidine nucleosides are widely recognised as the most stable nucleosides. The molecules studied in the present thesis – guanine and guanosine – represent a greater challenge for this recently-developed method. Although the method was developed several years ago, the number of applications where a ILTD source has been used is limited to the mentioned works.

- **Combinations of different biomolecular structures and/or clusters in neutral gas-phase targets**. Molecules can adopt several conformers, tautomers or isomers in the gas phase and clusters can have distinct geometries and sizes. Selecting the desired specie(s) in a molecular beam is crucial to draw effective comparisons with calculations and hence obtain a clear interpretation of the experimental results. It has been proposed that different structures with the same chemical formula can give rise to specific mass spectral features. Mass spectrometry studies of molecules with keto-enol tautomers, e.g. aldehydes and thioaldehydes [34] or acetylacetone, 3-methyl acetylacetone and 3-allyl acetylacetone are a few examples where evidence for tautomer-dependent dissociative ionisation pathways have been reported. [35]. Molecular simulations performed by Grimme and Bauer also point to a keto-enol tautomer dependent fragmentation of excited guanine ions [36]. Characteristic fragment ions from

different isomers have been identified in pyrimidine and pyridazine mass spectra too [37].

The electronic and vibrational levels of tautomers, isomers and conformers are often distinct, enabling their selective excitation and identification of individual contributions to the production of specific fragment ions through resonance enhanced multi-photon ionisation (REMPI) spectroscopy and ion-dip or hole-burning spectroscopy [38]. To perform REMPI spectroscopy, molecules need to possess a chromophore that is accessible with the available laser systems, generally ruling out its application to aliphatic compounds, and multiple lasers are required to perform double resonance IR-UV (infrared-ultraviolet) ion-dip and hole-burning spectroscopies. Both of these factors are major issues in studies addressing isomer, tautomer or conformer dependent fragmentation upon REMPI. Hu and co-workers reviewed and discussed double IR-VUV (infrared-vacuum ultraviolet) spectroscopy for exploiting the structure of molecules and clusters and the respective contributions in the VUV mass spectrum [39]. Although removing the requirement of chromophore molecules, generating VUV photons for single photon ionisation (SPI) is not a straightforward task. In laboratories, VUV photons can be produced via third harmonic generation (THG) of intense Nd:YAG laser pulses (355 nm) that transverse a non-linear medium, notably a noble gas cell [39]. VUV radiation can also be accessed in large facilities like synchrotrons. Tracing fragment ions to specific structures via double resonance spectroscopy is therefore not applicable to all molecules and may involve expensive or complex apparatus. Simpler approaches that can probe any molecule or cluster and, more importantly, that are applicable to any kind of ionisation/excitation/spectroscopic or imaging (MPI, SPI, EII, DEA and many more) are required.

Stark deflection of neutral species has shown applicability in spatial separation of isomers and conformers of molecules. Küpper *et al* successfully separated *cis* and *trans* conformers of 3-aminophenol cold molecules with non-homogeneous electric fields and probe them via REMPI. The spectrum showed spectral features that corresponded exclusively to one of the each conformer when laser pulses were redirected to appropriate positions along the deflection plane [40]. Additionally, the same group was able to achieve highly pure molecular beams of water dimers from an initially cold molecular beam of water clusters [41]. So far *Stark deflection* has only been applied to small biomolecules and clusters in pulsed supersonic beams. In some type of experiments, notably those investigating low cross section processes such as DEA, it can be highly advantageous to work with CW beams to achieve good signal-to-noise ratios in reasonable measurement times.

- **Variation between gas phase targets of biomolecules and clusters depending on source conditions**. Building on the points made above, gas-phase targets of biomolecules can be highly sensitive to the specific vaporisation method that was employed. Hence, experiments using different apparatus to probe a biomolecule such as guanosine can include different populations of thermal decomposition products and different populations of tautomers in the targets. Experiments on clusters are likely to have even greater differences between the targets probed from different sources. In almost any investigation, it is valuable to compare

results from different types of experiments on the same target. For example, comparing fragment ion production by MPI with fragment ion production by SPI or EII can yield evidence for fragmentation or isomeric transitions in neutral electronic excited states [42]. Therefore the variation between molecular and cluster targets probed using different experimental systems poses a particular problem to studying radiation-induced process in progressively more complex biomolecular systems. One solution to this problem is to build a single multi-functional apparatus that allows several different types of radiation experiments to be carried out on the same preparation of the gaseous / cluster target. In chapter 5 we describe a new apparatus that was assembled at the Molecular Clusters Laboratory with the purpose of performing different type of ionisation/excitation experiments (MPI, EII, DEA) under the same target conditions. This not only removes the uncertainties concerning the experimental conditions, but also improves the number of radiation induced damage processes that can be explored in the Molecular Clusters Laboratory since the new apparatus features an electron gun that can operate at high and low energy modes (to perform EII and DEA experiments, respectively).

It is worth noting that the previous first two problems are not encountered in experiments on ions: complex molecular ions can be brought into the gas-phase without thermal decomposition by electrospray ionisation (ESI) sources; and mass selection prior to irradiation experiments can be achieved by using conventional mass spectrometry methods, e.g. quadrupole filters, deflection in sector fields or ion drift tubes. A set of equivalent solutions for neutrals are necessary.

1.4 Layout of the thesis

To gain insights about the fundamental radiation-induced processes that can trigger macromolecular alterations in cellular environments, studying gas-phase systems of increased complexity is extremely valuable. The *bottom-up approach* can provide a basis to a comprehensive understanding of the radiation response of large scale biomolecular systems. However, some experimental challenges must be studied and addressed in order to exploit this approach to its maximum potential. One of these problems is mixtures of different molecular and cluster structures in neutral gas-phase targets can limit precise comparisons between experiments and theoretical calculations. This thesis focuses on developing and applying methods to assess the radiation response of different biomolecular tautomers or conformers and of different arrangements of molecular clusters. It is organised as follows:

- In chapter 2 we describe in more detail some of the chemical and physical processes introduced in this section and that will be relevant for discussing the results presented in subsequent sections. Computational methods are also included in this chapter since most of the experimental results are complemented with theoretical calculations for a more clear interpretation.

- In chapter 3 we discuss the working principle of laser vaporisation sources with major applications in mass spectrometry, including ILTD, and highlight the known differences relative to conventional heating sources. Characterisation of the ILTD source installed in the *compact experiment* at the Molecular Clusters Laboratory is performed by experiments involving thermocouple measurements. We evaluate the degree of thermal decomposition of guanine and guanosine molecules and study the respective fragmentation induced by UV multi-photon ionisation (MPI) through mass spectrometry. We try to pinpoint signs of tautomer dependent fragmentation of guanine based on its prompt and metastable mass spectra, and in theoretical calculations for some key unimolecular reactions.

- In chapter 4 we describe beam manipulation techniques, including Stark deflection, and justify why this is a suitable choice for our intention of studying radiation induced processes in specific cluster configurations. We then evaluate the performance of the Stark deflector assembled at the Molecular Clusters Laboratory in manipulating neutral CW beams of molecules and clusters. The degree of manipulation is compared with experiments encompassing pulsed beams executed by other groups. We demonstrate a new methodology to assign fragment ions to specific molecular and cluster structures.

- In chapter 5 we describe the development of a new multi-purpose apparatus that will enable us to investigate radiation induced processes with both direct and indirect damaging agents (UV photons, high and low energy electrons) in gas phase targets with low volatility produced by a ILTD source or clusters produced by a supersonic expansion source, under the same experimental conditions.

Chapter 2

Physical chemistry and computational chemistry methods

In this chapter we describe the basic concepts of molecular physics/chemistry and quantum chemistry methodologies, which will be important for the analysis and discussions presented in the following sections of this thesis. We make a brief description regarding molecular excitation processes induced by photons and electrons, namely, multi-photon ionisation (MPI), electron impact ionisation (EII) and dissociative electron attachment (DEA). The relevant de-excitation are also discussed. Throughout this work, we utilize computational chemistry methods, mainly based on density functional theory (DFT), to aid the interpretation of experimental results. Such computational methods and theories will also be reviewed in the current chapter.

2.1 Excitation and de-excitation of molecules

Isolated molecules and nanoscale structures have dimensions much smaller than objects we contact with in our daily life. The laws that describe their behaviour are therefore distinct. While large sized objects obey Newton's mechanics, small sized systems like molecules obey quantum mechanics laws. In quantum mechanics, the properties of the system are mere probabilities until we measure them. Those probabilities are 'encoded' in its wavefunction, Ψ, which evidently is of major importance. Throughout this chapter we will refer to the molecular wavefunction as $\Psi(\vec{r},\vec{R},t)$, where $\vec{r}$ are the electronic coordinates, $\vec{R}$ are the nuclear coordinates and t is the time.

2.1.1 Rotational, vibrational and electronic states

Opposed to atoms, molecules have nuclear degrees of freedom other than the ones reflecting the translational motion. A diatomic molecule has 2 rotational degrees of freedom and 1 vibrational degree of freedom. Additionally, it has three translational degrees of freedom because it can move along three dimensions. Polyatomic molecules posses 3 rotational degrees of freedom, $3N-6$ vibrational degrees of freedom where N is the number of atoms composing the molecule and 3 translational degrees of freedom. In general, the total degrees of a molecule are $3N$, being $3N-5$

and $3N-6$ the number of vibrational degrees for diatomic and polyatomic molecules, respectively. The translational degrees can have any value of energy. On the contrary, rotational and vibrational degrees can have only specific (quantised) values of energy. The energy separating successive rotational levels are of the order of some meV, while consecutive vibrational levels are separated by some hundreds of meV. A further discussion about rotational levels of molecules is presented in chapter 4.

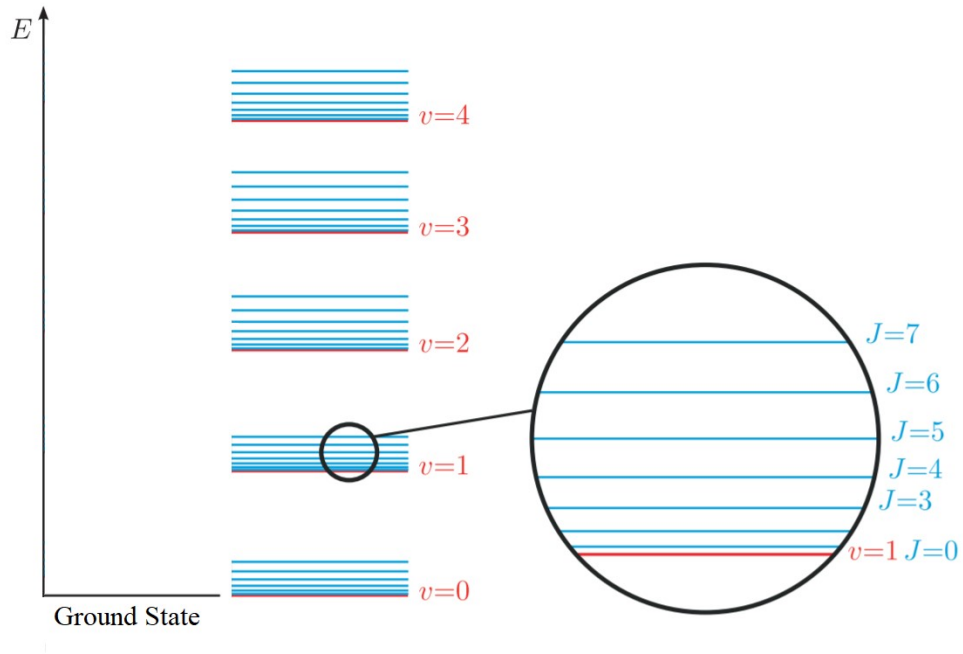

Figure 2.1: Schematic of the rotational (blue lines, J quantum number), vibrational (red lines, v quantum number) and electronic (black line, Ground state) energy levels.

Electrons occupy a certain spatial region around the molecule. The probability of finding the electron in such spatial positions is given by the square of the single particle electronic wave-function, which is normally referred to as molecular orbitals (MOs). Methodologies to find the electronic properties of molecules are presented in section 2.4. The energy separating different electronic levels is normally of the order of some eVs. At room temperature (298 K), the available thermal energy is 25 meV, enough to excite rotational levels of the molecules (J > 0). At the same temperature, most of the molecules are found in the fundamental vibrational level ($v = 0$), and are definitely in the lowest electronic energy level (herein referred as electronic ground state, GS). Within each electronic level, several vibrational levels exist, and within each vibrational level, there are several rotational energy levels (see Fig. 2.1). The levels described above may be excited if enough energy is absorbed by the molecule.

2.1.2 Spin multiplicity of neutral molecules and molecular ions

Electrons posses an intrinsic angular momentum called spin, which assume a value of $s = \frac{1}{2}$. In neutral molecules with an even number of electrons, a pair of electrons can occupy the same

MO with the spins arranged in an anti-parallel configuration, resulting in a null total spin, $S = 0$. However, it is also possible that two electrons occupy different MOs with the spins arranged in a parallel configuration, being the total spin one, $S = 1$. For most of the molecules, the lowest electronic energy level corresponds to an anti-parallel configuration of the spins ($S = 0$), but exceptions exist, for example, the O_2 molecule, where the electronic state with lowest energy has $S = 1$. Further details about MOs and electronic spin are presented in section 2.4.1. The spin multiplicity of an electronic state is given by:

$$2S + 1 \tag{2.1}$$

The spin multiplicity reflects the number of possible spin configurations that lead to a certain total spin quantum number S. When $S = 0$, the spin multiplicity is 1, meaning that the electronic spins can be arranged only in one manner. This is called a singlet electronic state. When $S = 1$, the spin multiplicity is 3, meaning that the electronic spins can be arranged in 3 different manners. This is called a triplet electronic state. The different spin configurations for singlet and triplet states are depicted in Fig. 2.2. Throughout this thesis, electronic states corresponding to singlet states will be denoted by S, whereas triplet states will be denoted by T.

When one electron is removed from the molecule, a molecular ion is formed with an unpaired electron and the total spin quantum number is $S = \frac{1}{2}$. In that case, the spin multiplicity is two (the spin can be arranged in two ways), and the electronic state is called a doublet. Doublets are denoted by letter D.

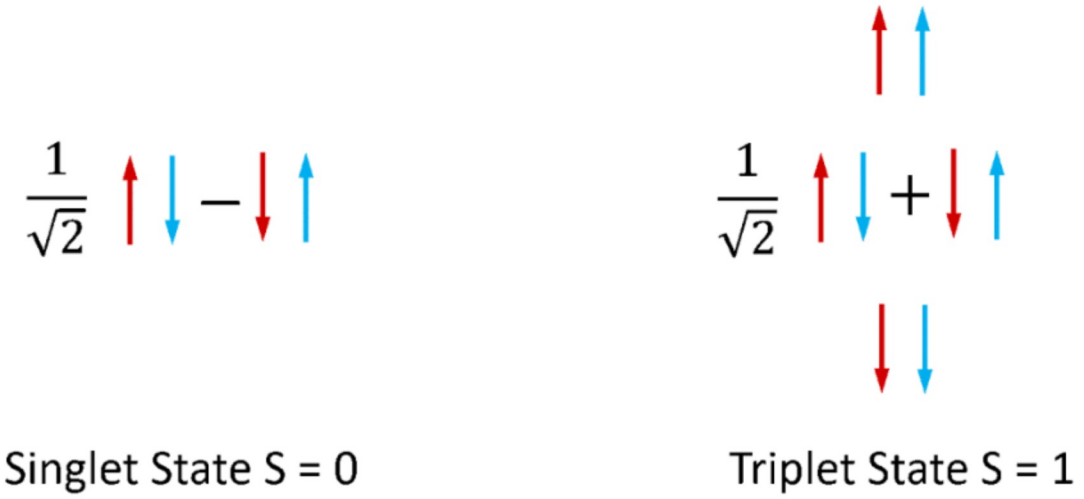

Figure 2.2: Possible spin configurations for singlet and triplet states. Due to indistinguishability of electrons, anti-parallel configurations are expressed as a superposition of states. Note that the singlet state is represented by an antisymmetric configuration, whereas triplet state is represented by symmetric configurations.

2.1.3 Adiabatic potential energy surfaces (PES) and the Born-Oppenheimer approximation (BOA)

Adiabatic potential energy surfaces (PES) evaluate the potential energy of an electronic state of a molecule at different nuclear geometries. Often, displacements of specific vibrational degrees of freedom (for example, stretching of a bond or bending) are chosen to evaluate the variations in potential energy. When only one nuclear degree of freedom is varied, a potential energy curve (PEC) is obtained. These PECs and PESs can be constructed based on the Born-Oppenheimer

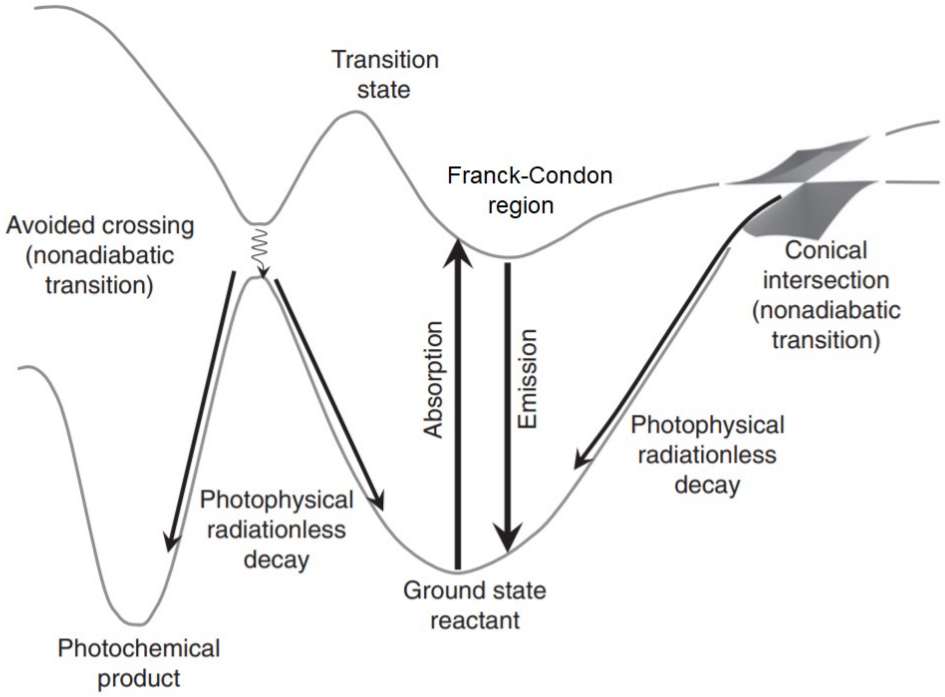

Figure 2.3: Schematic of two potential energy curves, representing the potential energy along a nuclear coordinate, for the electronic ground state and an electronic excited state [43]. The distinct zones of the PECs will be addressed in this chapter.

approximation (BOA). The BOA assumes the separation of electronic and nuclear motions since electrons have much lighter masses and can readjust instantaneously to displacements of the nuclei [44]. That is equivalent to say that the kinetic energy of electrons is much larger than the kinetic energy of the nuclei, which can be neglected in a first instance. The PESs/PECs are then constructed by evaluating the potential energy of the molecule at various fixed-nuclei positions by solving the time-independent electronic Schrödinger equation:

$$\hat{H}_e(\vec{r};\vec{R})\phi_i(\vec{r};\vec{R}) = E_{e,i}(\vec{R})\phi_i(\vec{r};\vec{R}) \tag{2.2}$$

where $\hat{H}_e(\vec{r};\vec{R}) = \hat{K}_e(\vec{r}) + \hat{V}_{eN}(\vec{r};\vec{R}) + \hat{V}_{ee}(\vec{r})$ is the electronic Hamiltonian represented by the sum of the electronic kinetic energies, $\hat{K}_e(\vec{r})$, the electron-nuclei potential energies, $\hat{V}_{eN}(\vec{r},\vec{R})$, and the electron-electron potential energies $\hat{V}_{ee}(\vec{r})$. $\phi_i(\vec{r};\vec{R})$ are the electronic wavefunctions associated with the electronic state i which, for any nuclear geometry, are eigenstates of the electronic

Hamiltonian with eigenvalues $E_{e,i}(\vec{R})$ (electronic potential energy). Therefore, by solving the eigenvalue problem for several nuclear geometries, one obtains adiabatic potential energy surfaces or curves [45]. The BOA assumes that the nuclear dynamic evolves along a single electronic state, dictated by the topology of the correspondent PEC/PES. This is a fair description for nuclear dynamics processing in the ground electronic states, but the BOA often breaks down when nuclear dynamics processes in electronic excited states, as we will see in the next section.

2.1.4 Non-adiabatic processes: Avoided crossings and Conical Intersections (CI)

In the previous section, we introduced the BOA which permits the separation of nuclear and electronic degrees, justified by fact that electrons 'easily follow' the dynamics of the nuclei due to their much lighter masses. However, as mentioned in the end of the last section, this is not always valid. To address under which conditions the BOA breaks down, the dynamical evolution of the system needs to treated with the time-dependent Schrödinger equation (TDSE):

$$\hat{H}(\vec{R},\vec{r})\Psi(\vec{r},\vec{R},t) = i\hbar\frac{\partial}{\partial t}\Psi(\vec{r},\vec{R},t) \tag{2.3}$$

using the complete Hamiltonian (nuclear + electronic terms)

$$\hat{H}(\vec{R},\vec{r}) = \hat{K}_e(\vec{r}) + \hat{K}_N(\vec{R}) + \hat{V}(\vec{r},\vec{R}) = -\frac{\hbar^2}{2m_e}\sum_n \hat{\nabla}^2_{r_n} - \frac{\hbar^2}{2M_l}\sum_l \hat{\nabla}^2_{R_l} + \hat{V}(\vec{r},\vec{R}) \tag{2.4}$$

Note that this Hamiltonian *does not neglect the nuclear kinetic energy operator* and the potential energy operator now includes a potential energy repulsion term between nuclei, $\hat{V}(\vec{r},\vec{R}) = \hat{V}_{NN}(\vec{R}) + \hat{V}_{eN}(\vec{r},\vec{R}) + \hat{V}_{ee}(\vec{r})$. The TDSE 2.3 accepts a superposition of products of electronic and nuclear wavefunctions as solution [46, 47], the so called Born-Oppenheimer expansion:

$$\Psi(\vec{r},\vec{R},t) = \sum_i \phi_i(\vec{r},\vec{R})\chi_i(\vec{R},t) \tag{2.5}$$

$\chi_i(\vec{R},t)$ provides information about nuclear positions, and its magnitude $\left(|\chi_i(\vec{R},t)|^2\right)$ represents the probability of finding the system in the electronic state $\phi_i(\vec{r},\vec{R})$. Integrating over nuclear coordinates the projection of the TDSE 2.3 into an electronic state $\phi_m(\vec{r},\vec{R})$ results in a complex expression which reflects the nuclear dynamic (the reader is referred to ref. [47] to a full demonstration):

$$i\hbar\frac{\partial}{\partial t}\chi_i(\vec{R},t) = -\sum_{l,j}\frac{\hbar^2}{2M_l}\left(\langle\phi_i|\hat{\nabla}^2_{R_l}|\phi_j\rangle + 2\langle\phi_i|\hat{\nabla}_{R_l}|\phi_j\rangle.\hat{\nabla}_{R_l}\right)\chi_j(\vec{R},t) + \left(\sum_l -\frac{\hbar^2}{2M_l}\hat{\nabla}^2_{R_l} + E_i(\vec{R})\right)\chi_i(\vec{R},t) \tag{2.6}$$

We can see that the nuclear dynamic is not only associated with the respective electronic state (second term on the right hand-side) as described by the BOA, but also with the remaining electronic states (first term on the right hand-side). The second term describes the molecular dynamics taking place in a single PEC or PES and is denominated by Born-Oppenheimer Molecular Dynamics (BOMD). The off-diagonal matrix elements of the nuclear kinetic energy operator contained in first term on the right hand side are denominated by kinetic $\left(\langle\phi_i|\hat{\nabla}^2_{R_l}|\phi_j\rangle\right)$ and derivative $\left(\langle\phi_i|\hat{\nabla}_{R_l}|\phi_j\rangle\right)$

non-adiabatic couplings (NAC). Kinetic couplings can be expressed in terms of derivative couplings (equation 15 in ref. [47]). In turn, resorting to the Hellman-Feynman theorem, we can find a relation for derivative couplings [47, 48]:

$$\langle \phi_i | \hat{\nabla}_{R_l} | \phi_j \rangle = \frac{\langle \phi_i | \hat{\nabla}_{R_l} \hat{H}_e | \phi_j \rangle}{(E_j - E_i)} \tag{2.7}$$

The energy derivative in the numerator is a force like term. Hence, non-adiabatic coupling terms become relevant when forces acting on nuclei are intense (fast nuclear motion) or when electronic states become quasi-degenerate. In such cases, the nuclear wavefunctions evolves along PES of different electronic states coupled by non-adiabatic couplings and the BOA breaks down. In practical terms, the BOMD is a satisfactory description of nuclear dynamics in ground electronic states because ground and excited electronic state are usually separated by large values of energies. Whenever a molecule is electronically excited, several PEC/PES may come very close (avoided

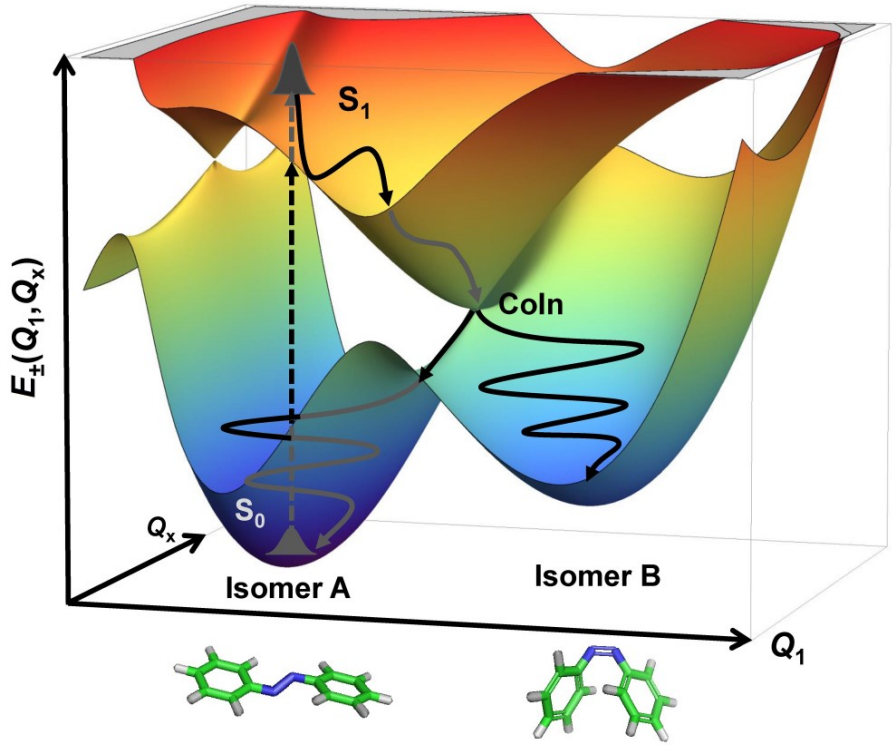

Figure 2.4: Two potential energy surfaces, S_0 (electronic GS) and S_1 (first electronic state), representing the photoisomerization process of azobenzene. CoIn refers to the conical intersection point, where S_1 and S_0 are degenerate.

crossings) or even cross with others (conical intersections) and the BOA no longer provides a fair description of the system. Avoided crossings and conical intersections (CI) of PESs/PECs provide raditionless relaxation mechanism for electronically photoexcited molecules. CIs act as very efficient deactivation funnels to electronic states of lower energy. The denomination of conical intersection derives from the conical shape resultant from the intersection of the two PESs in a single point of the nuclear coordinate space. CIs are solely allowed in a subspace of two nuclear

degrees of freedom, called the branching space [49]. The energy of the electronic states varies along those coordinates but remains constant along the others. For systems with only one nuclear degree of freedom, for example, diatomic molecules, CIs can not occur. Instead, non-adiabatic transitions between electronic states are mediated by avoided crossings. An example of a CI is shown in Fig. 2.4, involving the photoisomerization of azobenzene. CoIn denotes the conical intersection region. An avoided crossing can be observed in Fig. 2.3.

2.1.5 Franck-Condon principle

In 1925–1926, Franck and Condon developed a theory to determine the relative intensities of vibronic (simultaneous electronic and vibrational) bands [50, 51] produced in a vibronic excitation. Franck proposed that after absorption of light, the electron transits to another electronic state and that no other changes occur in the molecule. In other words, at the time of excitation, the nuclear geometry is not altered. This is what is referred as a *vertical excitation* between electronic states and corresponds to drawing a vertical arrow between the two PECs or PES inolved in the transition as shown in Fig. 2.5. This is reasoned by the much faster dynamics of electrons compared with the nuclei, just like in the case of BOA. Franck also interpreted the photofragmentation of diatomic molecules as having origin in the access of purely repulsive PEC after electronic excitation. Condon extended Franck's ideas by stating that the various vibrational levels could be accessed in the electronic excited state depending on the nuclear coordinates and momentum right after the transition. The intensities of each vibronic transition are determined by the overlap integral:

$$P_{\nu''\to\nu'} = |\langle\chi_{\nu'}|\chi_{\nu''}\rangle|^2 \tag{2.8}$$

where $\chi_{\nu''}$ is the vibrational wavefunction associated with the vibrational level ν'' of the initial electronic state and $\chi_{\nu'}$ is the vibrational wavefunction associated with the vibrational level ν' of the final electronic state. Depending on the equilibrium geometry and topology of the GS and electronic excited state PEC/PES, three disinct situations may result:

- When the equilibrium position of the initial and final electronic states are similar ($R'_e = R''_e$), the dominant vibronic transition involves $\nu' = 0 \leftarrow \nu'' = 0$ (e.g. O_2 transition intensities in Fig. 2.5 a)). In Fig. 2.5 b) are shown the same PECs with the vibrational wavefunctions for each vibrational state. The transition from A to B preserves the nuclear position and nuclear kinetic energy being therefore the most probable transition. From A to C or from A to D, there is a change in the initial nuclear geometry. From A to E there is a change in the nuclear kinetic energy. So, the $\nu' = 2 \leftarrow \nu'' = 0$ is much less probable than the $\nu' = 0 \leftarrow \nu'' = 0$ transition. The $\nu' = 1 \leftarrow \nu'' = 0$ corresponds to an intermediate case;

- When the equilibrium geometries of the initial and final states are slightly different ($R'_e > R''_e$), intense transitions to vibrational levels above $\nu' = 0$ take place (e.g., CO transition intensities in Fig. 2.5 a));

- When the equilibrium position of the initial and final states are very different ($R'_e \gg R''_e$), the dominant transitions occur for high lying vibrational states or states in the continuum driving molecular fragmentation (e.g., I_2. transition intensities in Fig. 2.5 a)).

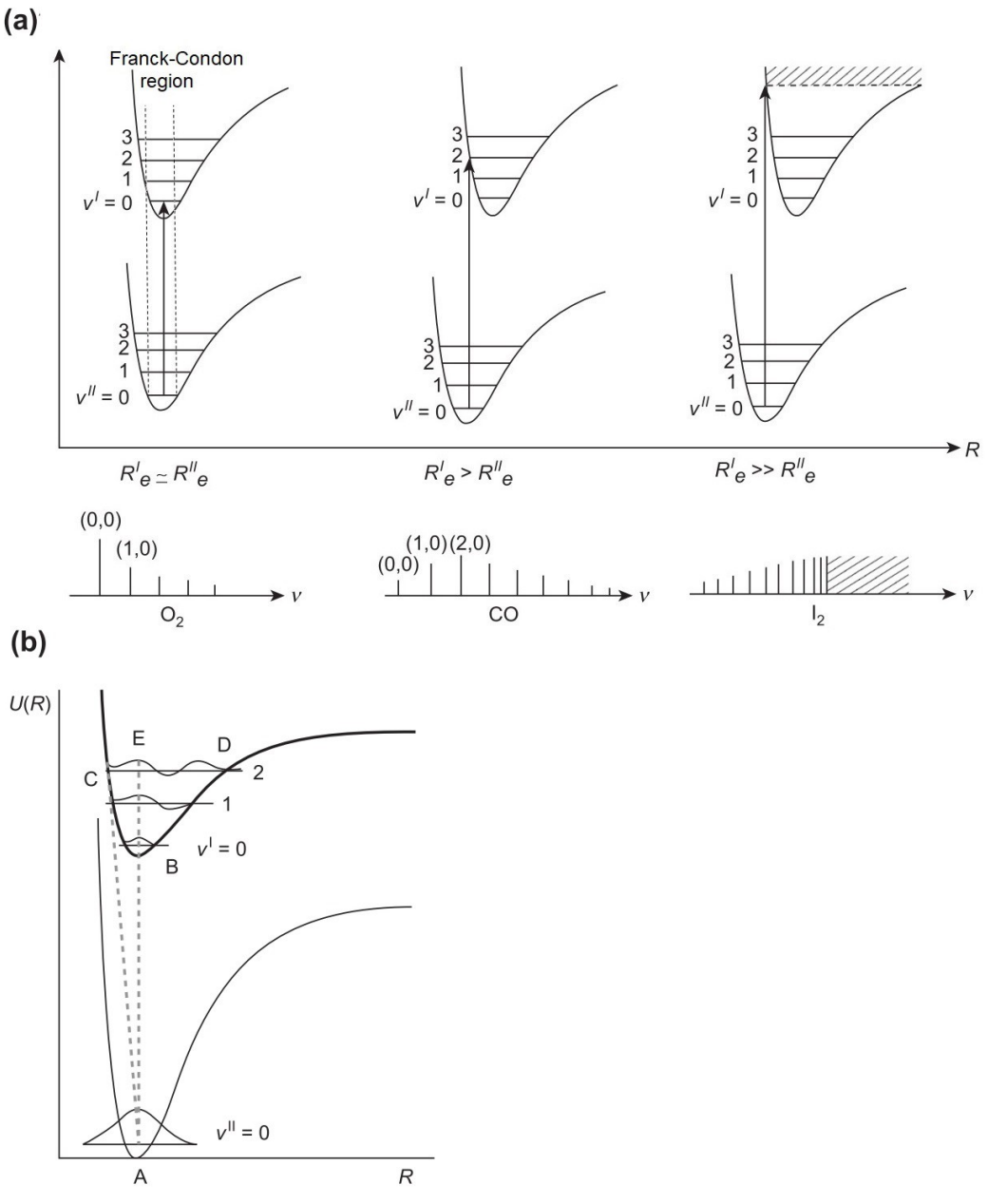

Figure 2.5: Franck-Condon (vertical) transitions from the vibronic GS to different vibronic levels. Three distinct situations are presented according to the topology of the PEC of the electronic excited state. Adapted from [52].

2.1.6 General picture of molecular (de)excitation mechanisms

The two types of the experiments performed in the Molecular Clusters Laboratory, MPI and EII, induce ionisation and excitation of the molecular targets. In MPI experiments, the energy contained in multiple photons is absorbed by the target. In EII experiments, the energy is imparted to the target by momentum transfer from high energy electrons. As the energy of one photon employed in MPI is not enough to remove an electron from the molecule, ionic states are accessed via intermediate vibronic excited states of the neutral molecule. On the other hand, during EII experiments, vibronic states of the molecular ion are directly accessed from the ground state of the neutral molecule. If a large quantity of energy is transferred to the target, both mechanisms may generate vibronic excited ions or even fragment ions. With this regard, MPI and EII are referred as ionisation/excitation processes. More details about these processes are given in sections 2.2.1 and 2.2.2. The dissipation of vibronic excess energy, either in neutral or cationic states, is accomplished by radiative and non-radiative de-excitation mechanisms. Radiative mechanisms involve transition between electronic levels through emission of radiation and may be subdivided into two categories [53, 54]:

1. *Fluorescence:* emission of radiation, normally involving a transition from the lowest electronic excited state and the electronic GS, with the same spin multiplicity. Timescales of *fluorescence* are near 10^{-8} s [54]. In Fig. 2.6, $S_1 \rightarrow S_0$ corresponds to a fluorescence transition;

2. *Phosphorescence:* emission of radiation resultant from a transition between an excited electronic state and the GS, with different spin multiplicity. It is a spin-forbidden transition whose lifetimes range from 10^{-3} s to several seconds [54].

The raditionless mechanisms are the following:

1. *Vibrational relaxation:* the molecule rapidly relaxes to the lowest vibrational level of the electronic state. Timescales of vibrational relaxation are $10^{-14} - 10^{-12}$ s, shorter than any radiative process [54]. Therefore, vibrational relaxation precedes relaxation processes that involve emission of radiation;

2. *Internal conversion (IC):* transition between electronic states with the same spin multiplicity, either through conical intersections or avoided crossings. Usually the energy difference between the GS state and the first electronic excited state is larger than between electronic excited states. This explains why fluorescence often competes with IC for transitions from the first electronic excited state to the electronic GS. In Fig. 2.6, the $S_2 \rightarrow S_1$ transition represents an IC process. IC occur in timescales of $10^{-14} - 10^{-12}$ s [54];

3. *Intersystem crossing (ISC):* transition between electronic states of different spin multiplicity. The change of spin is facilitated by spin-orbit coupling which requires the presence of heavy atoms in the molecule. Being a spin-forbidden transition, timescales for ISC are longer than for IC ($\sim 10^{-8}$ s [54]). In Fig. 2.6, the $S_1 \rightarrow T_1$ transition corresponds to an ISC process.

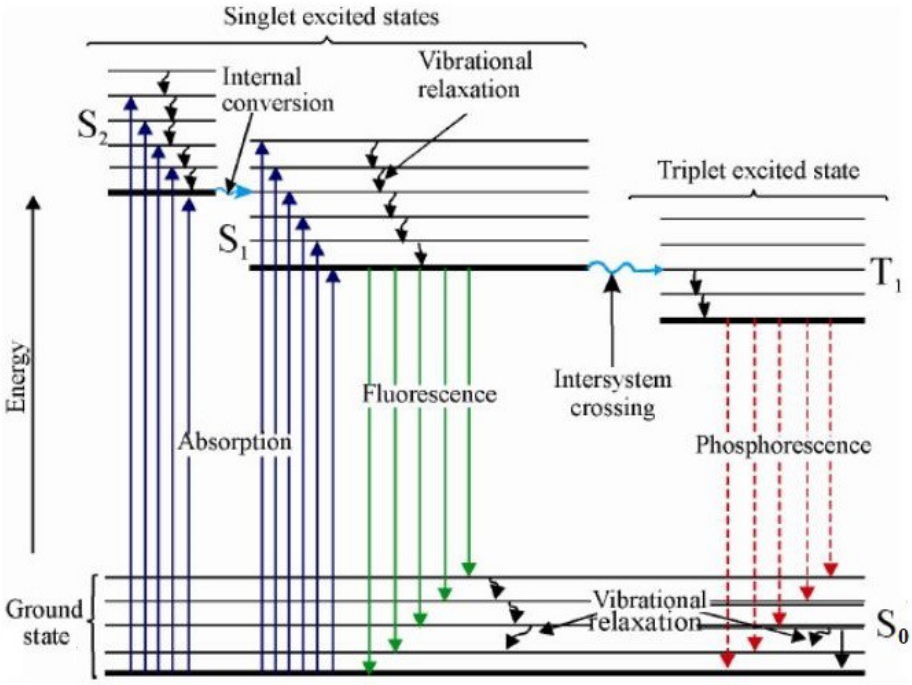

Figure 2.6: Jablonski diagram concerning several excitation and de-excitation processes in molecules. S refers to electronic singlet states and T refers to electronic triplet states. Dark blue arrows represent excitation processes, for example, photon absorption; green and red arrows represent the radiative de-excitation processes, fluorescence and phosphorescence, respectively; radiationless de-excitation processes, IC and ISC are represented by light blue wavy arrows; Vibrational relaxation is represented by black wavy arrows. Adapted from [55]

Aminoacids and nuclobases/nucleosides do not incorporate heavy atoms in their chemical structure. Therefore, spin-orbit coupling is generally weak and de-excitation processes involve mainly electronic states with the same spin multiplicity (vibrational relaxation, IC and fluorescence). We therefore focus our attention on spin-allowed transitions. We should note however that spin-forbidden processes may occur in peptides and nucleotides due to the presence of heavy atoms in their composition (dissulfide bonds in the former and phosphate group in the latter).

2.2 Molecular excitation and ionisation processes induced by photons and electrons

2.2.1 Multi-photon ionisation (MPI)

When a photon interacts with a molecule, it can be scattered or absorbed. For majority of the molecules, the absorption of one photon with energies in the near UV region is not enough to cause ionisation, but it is sufficient to induce vibronic excitations. Multi-photon ionisation (MPI) refers

to a process where a molecule is ionised due to the absorption of multiple photons. The number of photons required to ionise the molecule and/or to from a specific fragment ion is called photon order, which relates to the ion yield Y through [54, 56]

$$Y = c.I^{\alpha} \tag{2.9}$$

where c is a constant, I is the irradiance (or flux density) of the photon beam and α is the photon order. Assuming that n photons are necessary to pump the neutral molecule into an electronic excited state and m photons are required to probe the ionic states of the molecule, the MPI is said to be a (n+m) process. Pump and probe photons may have the same or different energies. The first case is known as one-colour MPI experiment, whereas the latter case is known as two-colour MPI experiment and a prime is used to make the energy distinction, (n+m'). Various schemes of multi-photon ionisation are shown in Fig. 2.7 as well as electron impact ionisation scheme, where ionic states are accessed directly from the electronic GS of the neutral specie. The MPI process is said resonant if the total energy of n pump photons matches the energy difference between an electronic excited state and electronic GS. When that is the case, the technique is called resonance enhanced multi-photon ionisation (REMPI). Otherwise, the process is non-resonant. In general, ionisation from virtual states is not likely because the lifetimes of these states are very short [54]. Ions generated from off-resonant transitions are therefore scarce, unless the pump and probe photons are almost simultaneously absorbed. On the other hand, in REMPI experiments, nuclear dynamics along the electronic excited state can take place before the probe photons are absorbed. The efficiency of the process depends on the laser parameters (e.g. wavelength and flux density) and the excited state lifetimes. Aside from generating excited ions, multi-photon ionisation can also lead to fragmentation of ions. Three main channels are involved in photo-dissociation of ionic species [57]:

- Direct dissociation – the probe photon(s) excite the ion to a pure repulsive electronic excited state. Fragmentation into ion and neutral fragments is inevitable.

- Pre-dissociation – the probe photon(s) excite the ion to a bound electronic excited state, which vibrationally couples with a pure repulsive state via internal conversion, if the states have the same spin multiplicity or intersystem crossing, if the states have different spin multiplicity;

- Spontaneous radiative dissociation – the probe photon(s) excite the ion to a bound electronic state, which subsequently emits a photon and transits to a lower energy repulsive electronic state or to an excited vibrational state of the electronic ground state.

- Internal conversion to a 'hot' electronic ground state – the probe photon(s) excites the ion an electronic state. This initial state subsequently couples with several other electronic states driving the molecular ion to its electronic ground state. As the electronic energy is gradually converted into vibrational energy, dissociation of the ion may occur.

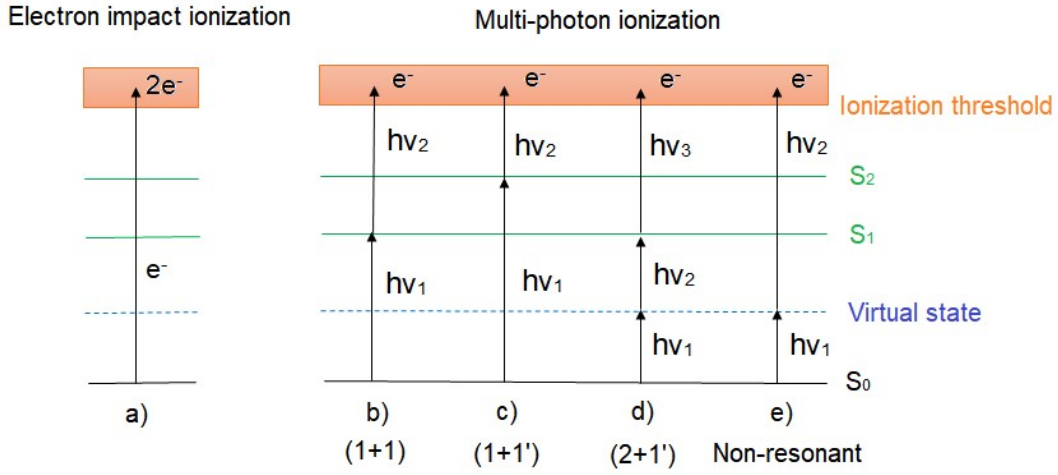

Figure 2.7: Comparison between a) EII and b)–e) MPI schemes. In EII, the ionic states of the ion are directly accessed from the electronic GS of the neutral. MPI may involve b) a resonant vibronic excitation with one photon and ionisation with another photon, both with the same energy (resonant enhanced one-color multiphoton ionisation) c) a resonant vibronic excitation with one photon and ionisation with another photon, with different energies (resonant enhanced two-color multiphoton ionisation) d) A resonant vibronic excitation via an off-resonant state, proceeded by ionisation, with photons of different energy (two-color multiphoton ionisation) e) an off-resonant excitation and ionisation, with photons of different energy (two-color multiphoton ionisation)

2.2.2 Electron impact ionisation (EII)

When electrons with sufficient kinetic energy to excite one of the internal degrees of freedom of a molecule interact with it, some of that energy may be transferred. If the energy transferred is larger than the ionisation energy (IE) of the molecule, a molecular ion can be formed

$$M + e^- \rightarrow M^{+\bullet} + 2e^-$$

Two ionisation energies can be defined: the *adiabatic ionisation energy* (*AIE*) and the *vertical ionisation energy* (*VIE*). *AIE* corresponds to the minimum energy required to produce a molecular ion, that is, to form the ion in the lowest vibronic state. *VIE* corresponds to the energy necessary to vertically ionise the molecule according to the Franck-Condon principle. As the energy of the electron beam is increased, the intensity and variety of ions will also increase because more channels will be available and each one of them generates distinct products. The ions produced by electron impact ionisation encompass the molecular ions, fragment ions, multiply charged ions (at very high electron energies), metastable ions, rearrangement ions and ion pairs [58]. Unlike MPI, EII only generates molecular ions or fragment ions directly from the electronic GS of the neutral; therefore, critical processes occurring in neutral excited states may be identified by comparing results obtained in both type of experiments. Single-photon ionisation (SPI), a process where molecules absorb a single photon with energy above the ionisation energy, provides similar results to EII because cationic states are directly accessed from the neutral GS. An advantage of SPI over

EII is the tighter control of the energy transferred to the target. When a photon is absorbed, all its energy is transferred to the molecule, whereas an electron can transfer any value corresponding to a fraction of its kinetic energy.

2.2.3 Dissociative electron attachment (DEA)

Dissociative electron attachment is a process that occurs when low energy electrons (LEE) interact with a molecule. At such energies, the electrons can be temporarily captured in one of the unoccupied molecular orbitals of the target, forming a transient negative ion (TNI). The TNI can decay through electron auto-detachment or dissociation, giving rise, in the diatomic case shown below, to a neutral and an anionic fragment

$$AB + e^- \rightarrow AB^{*-} \rightarrow AB + e^-$$

$$AB + e^- \rightarrow AB^{*-} \rightarrow A + B^-$$

Both processes are schematically shown in the left panel of Fig. 2.8. The right panel of the same figure evidences that auto-detachment and dissociation may be competitive processes: for short A-B bond distances, the electronic state of the neutral is less energetic than that of the anion and auto-detachment is energetically favoured. However, since the PEC of the anion is purely repulsive, the bond distance of the TNI will elongate, which may also result in the fragmentation into A and B^- fragments. The nuclear dynamic therefore plays an important role in the branching ratios of the two processes. In rare circumstances, the parent anion is stable and none of the mechanisms mention above take place. TNI are formed at specific energies of the incoming electron. For this reason, DEA processes are said to be resonant. Four type of electron attachment resonances can

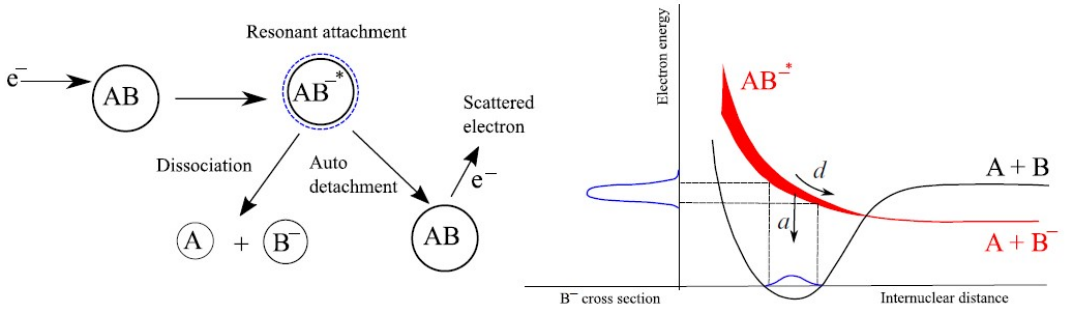

Figure 2.8: Left: Schematic showing the possible processes resultant from interaction of low-energy electron with a molecule AB; Right: potential energy curves of the neutral parent and transient negative anion [59].

be distinguished [60]:

1. *Shape resonances:* the electron is temporarily trapped by the shape of an effective potential. This effective potential results from two components — the attractive polarization potential established between the neutral molecule and the incoming electron and a repulsive

centrifugal potential arising from the angular momentum of the incoming electron. Shape resonances lie energetically above the electronic ground state of the neutral parent and therefore, the molecular parent anion is unstable. The lifetime of such resonances are in the range of $10^{-15} - 10^{-10}$ s and depends on the barrier height and internal energy of the anion.

2. *Core-excited shape resonances:* Core-excited shape resonances are similar to shape resonances with the incident electron now being captured in an electronic excited state of the molecule rather than in the electronic ground state. The incident electron must carry the energy necessary to excite the molecule, and therefore, core-excited shape resonances generally are found at energies higher than those of shape resonances;

3. *Feshbach resonances:* the incident electron electronically excites the molecule. The nuclear charge is less screened in the excited state than in the electronic GS, resulting in a slight positive effective charge that temporarily binds the incoming electron. The electronic state of the anion lies below the excited electronic state of the neutral, but above the electronic ground state. The lifetimes of Feshbach resonances can be very long ($\sim 10^{-5}$ s), particularly if the anion is stabilised in a vibrational energy level whose energy is lower than the energy of the vibrational level $\nu' = 0$ of the electronic excited state of the neutral. In that case, the decay into the electronic excited state of the neutral parent is not energetically favorable;

4. *Nuclear excited (vibrational) Feshbach resonances:* involves coupling of the kinetic energy of incident electron to molecular vibration. The electronic state of the negative ion lies below the electronic state of the neutral molecule and consequently, a stable negative ion may be formed. As the vibrational states of the neutral and anion are separated by very small energy gaps, the anion is formed in a vibrational state ν' with energy above the vibrational energy level ν'=0 of the neutral. Due to this, vibrational Feshbach resonances have the particularity to occur at very low energies ($\sim$ 0 eV), with lifetimes of the order of 10^{-6} s.

2.3 Unimolecular reactions

Molecular ionisation is normally accompanied by vibronic excitation of the ion, particularly in ionisation processes where it is not possible to have a tight control over the energy transferred to the target as in the case of EII. This initial energy imparted to the target is then redistributed among the vibrational degrees of freedom, a process denominated by intramolecular vibrational energy redistribution (IVR), which gives the chance to explore several portions of the PEC/PES. There are key points of the PECs/PESs called transition states (TS) for which the nuclear geometry of the molecule or molecular ion corresponds to a first order saddle point of the electronic energy: it is a maximum along one vibrational degree of freedom called the reaction coordinate, and a minimum along the remaining vibrational degrees of freedom. Bond distances represent in general, reaction coordinates associated with fragmentation and the respective TS is characterised by possessing an imaginary frequency. We will discuss in section 2.4.4 how to find transition states and determine fragmentation pathways with computational chemistry software. TS can be seen as energy barriers

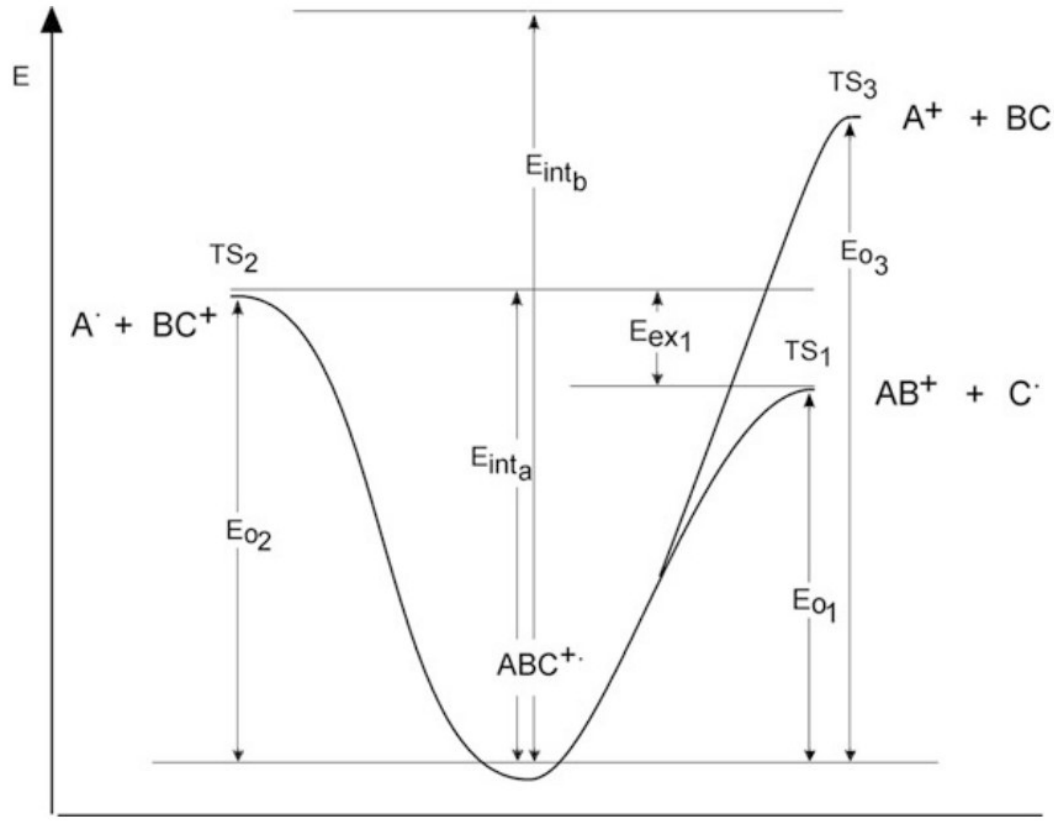

Figure 2.9: Competitive fragmentation pathways of an ABC^+ ion into $AB^+ + C^{\cdot}$, $A^{\cdot} + BC^+$ and $A^+ + BC^{\cdot}$, having energy barriers of E_{01}, E_{02} and E_{03}, respectively [58].

that need to be surmounted to induce chemical changes of the initial products. In a thermochemical point of view, that is achieved when the internal energy in the reaction coordinate is larger than the TS energy. Three different TSs can be observed in Fig. 2.9, representing the fragmentation of a ABC^+ ion into $AB^+ + C^{\cdot}$, $A^{\cdot} + BC^+$ and $A^+ + BC^{\cdot}$ fragments, with energy barriers of E_{01}, E_{02} and E_{03}, respectively. If the internal eenrgy in the reaction coordinate is E_{inta}, the ion may follow either the reaction pathway 1 or 2 but not 3. The difference between the internal energy and the TS energy of the pathway is termed excess energy and is given for pathway 1 as $E_{ex1} = E_{inta} - E_{01}$. If the internal energy in the reaction coordinate is E_{intb}, the ion may follow any of the three reaction pathways. Although the thermodynamical picture tell us which fragment may be formed when a certain internal energy is deposited on a vibrational degree of freedom, it does not elucidate about the kinetics, that is, the time necessary to form these ions and their relative abundances.

2.3.1 Quasi-equilibrium theory (QET)

The quasi-equilibrium theory (QET) is a theoretical method describing the kinetics of unimolecular reactions of ions in mass spectrometric experiments. It extends the theory formulated by Rice-Ramsperger-Kassel-Marcus (RRKM) [61, 62] to describe bimolecular and unimolecular reactions under thermal equilibrium conditions. The way QET does that is by considering a microcanonical

ensemble, where the total energy of the system is fixed, instead of a canonical ensemble, where the temperature is constant. We recall that mass spectrometry experiments are performed under low pressures (high to ultra-high vacuum) and therefore, molecules are no longer found in thermal equilibrium (constant temperature, canonical ensemble), but rather in an ensemble where their total energy is constant (microcanonical ensemble).

The QET assumes that an initial vertical ionisation takes place, driving the molecular ion to a vibronic excited state. In large polyatomic molecules, a large number of electronic excited states of non-repulsive character couple with the initial vibronic state and provide a route to statistically redistribute the electronic potential energy among the vibrational degrees of freedom through raditionless de-excitation (the intramolecular vibrational energy redistribution, IVR). The rate constants of an unimolecular reaction depend on the probability of the electronic energy to be channelled into the vibrational degrees of freedom associated with the transition states leading to the desired products. If the molecular ion has sufficient energy, several reactions or fragmentations may occur in a step-wise manner. The rate constants for unimolecular reactions (dissociation or isomerisation) can be determined using information about the internal energy E, the TS energy (also referred as complex activation energy) E_0 [58]:

$$k(E) = \int_0^{E-E_0} \frac{1}{h} \frac{\rho^*(E, E_0, E_t)}{\rho(E)} \mathrm{d}E_t \tag{2.10}$$

here E_t is the translational energy along the reaction coordinate, which can not be larger than the excess energy, $E - E_0$. ρ(E) is density of states of the reactants with internal energy E and $\rho^*(E, E_0, E_t)$ is the density of states of the TS with an activation energy E_0 and E_t kinetic energy in the reaction coordinate, which in the case of fragmentation, corresponds to the bond being cleaved. The expression can be approximated by a s number of harmonic oscillators [58]

$$k(E) = \left(\frac{E - E_0}{E}\right)^{s-1} \frac{\prod_{j=1}^{s} \nu_j}{\prod_{i=1}^{s-1} \nu_i^*} \tag{2.11}$$

ν_j and ν_i are reactants and TS vibrational frequencies, respectively. The $s-1$ factor accounts for all the vibrational degrees of freedom except for that associated with the bond being fragmented. The inverse of the rate constants corresponds to the mean period of time necessary for that particular reaction to occur.

2.3.2 Fragmentation with and without rearrangement

Unimolecular fragmentation can be separated in two types: fragmentation with and without. The topology of the PEC along the reaction coordinate is different for both cases, and gives rise to different kinetics. For fragmentation of an ion into a smaller ion and neutral species without rearrangement, the TS and the products have sensibly the same energy. The activation energy of the reverse reaction is approximately zero meaning that the products would 'naturally' bind to each other again if the direction followed along the reaction coordinate was inverted. On the other hand,

fragmentation with rearrangement often give origin to relatively stable products, with energies lower than the TS energy: the activation energy of the reverse reaction is not negligible. An example of a PEC associated with a fragmentation with rearrangement is shown in Fig. 2.10. The internal energy of the parent ion $M^{+\cdot}$ is enough to surmount the activation energy of the forward reaction, E_0. The total excess energy $E_{extot} = E_{ex} + E_{0r}$ is converted in vibrational energy E_{vib} and kinetic energy release (KER) of the products $m_1^+ + n$. The activation energy for the reverse reaction E_{0r}, is smaller than the vibrational energy of the products, allowing the occurrence of a reverse reaction. Further fragmentation is expected if the vibrational energy of $m^+ + n$ is larger than any other activation energies existent along other reaction coordinates.

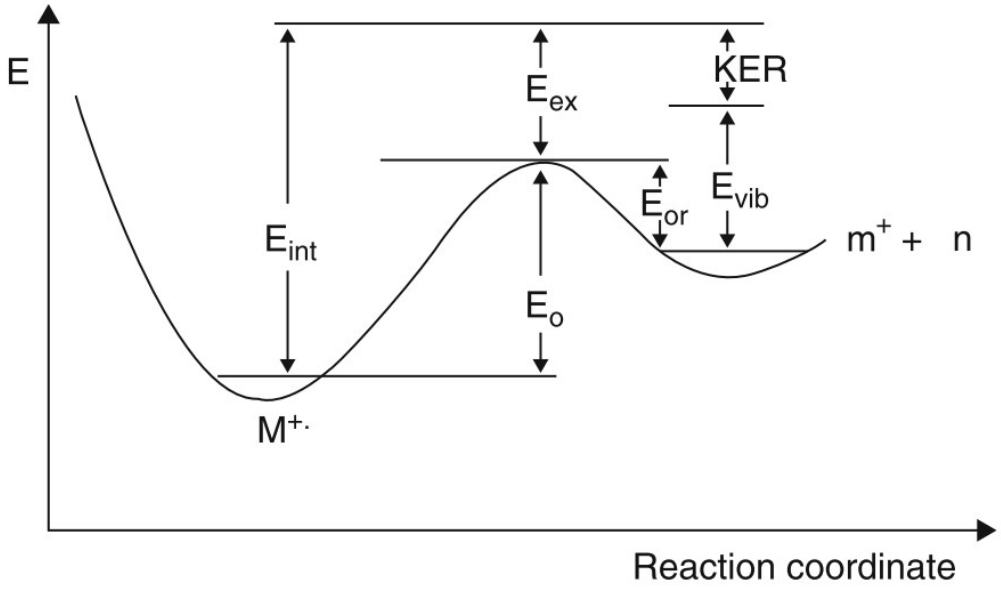

Figure 2.10: A schematic PEC associated to a fragmentation with rearrangement. The parent ion $M^{+\cdot}$ is vibrationally excited with an energy E_{int} which is sufficient to surmount the activation energy of the forward reaction E_0, with an excess of E_{exc}. The energy of the products is much lower than that of the TS energy and therefore the activation energy associated with the reverse reaction E_{0r} is not null. The total excess energy is then converted in vibrational E_{vib} and translation energy, KER, of the products [58].

2.3.3 Prompt and metastable fragmentation

After an ion has been formed in the interaction region of the mass spectrometer, its mass/charge ratio will be analysed by time-of-flight mass spectrometry. Now three situations can be distinguished according to the internal energy of the ion:

- The ion has a very small amount of internal energy. In this case the mean fragmentation time is larger than the time-of-flight (small dissociation rate constants) and the ion arrives intact to the detector.

- The ion internal energy is very close to an activation energy of a reaction. In this case the rate constant is not as low as in the previous case but is not large enough to observe a fragmentation in the interaction region. The fragmentation happens in route to the detector, in the *field free region* (FFR) of the mass spectrometer. These are called *metastable dissociations*. The schematic of a metastable fragmentation taking place in the FFR of a reflectron time-of-flight mass spectrometer is shown in Fig. 2.11 as a blue reaction.

- The internal energy of the ion is large as well as the rate constants for dissociation. Fragmentation occurs very rapidly, yet in the interaction region, and we denominate it by *prompt fragmentation*. The schematic of a prompt fragmentation taking place in the interaction of a reflectron time-of-flight mass spectrometer is shown in Fig. 2.11 as a red reaction.

In a large number of mass spectrometers, the time spent by the ion in the interaction region is no longer than few μs whereas the flight time in the FFR is about tenths of μs. Thus, rate constants associated with the different types of ions are:

- Prompt fragmentation, $k > 10^6$ s^{-1};

- Metastable fragmentation, $10^5 < k < 10^6$ s^{-1};

- Undissociated ions, $k < 10^5$ s^{-1}.

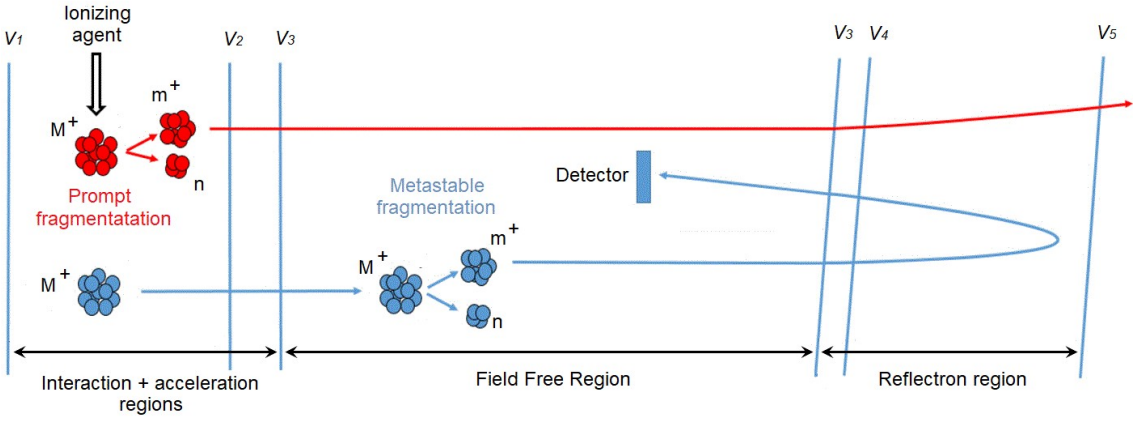

Figure 2.11: Schemtatic of a prompt fragmentation (red reaction) and metastable fragmentation (blue reaction) taking place in the interaction and free field regions of a reflectron time-of-flight mass spectrometer, respectively. Adapted from [63].

When a fragmentation occurs in the FFR, the daughter ion has not the same kinetic energy as the parent ion. Accordingly, their trajectories (represented by blue and red arrows in Fig. 2.11) in the reflection region are different, but information about KER of metastable fragments can be retrieved by varying the reflection voltage of the reflectron region of the time-of-flight mass spectrometer. This subject will be discussed in more detail in section 3.3.4.

2.3.4 Kinetic energy release

The kinetic energy release (KER) composes a part or all the total excess energy which is channelled into the reaction coordinate. If this coordinate represents a bond cleavage, the total excess energy is converted into kinetic energy of the released fragments (thence the name kinetic energy release). The quantification of KER is important to interpret and propose reaction pathways underlying metastable fragmentation. This can be easily comprehended by analysis of Fig. 2.12. When the

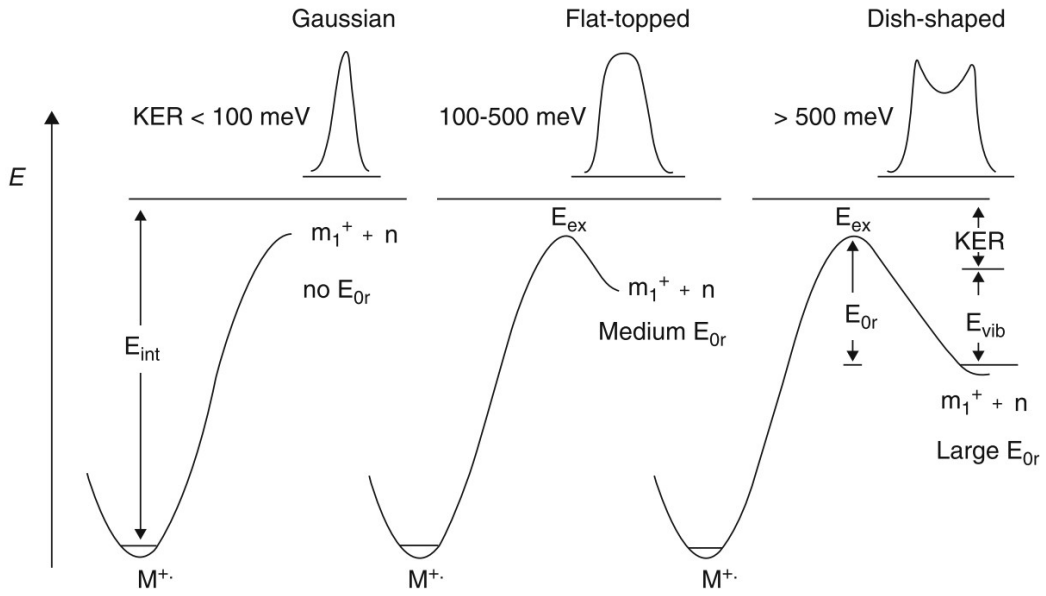

Figure 2.12: Dependence of the metastable ion peak shapes on the activation energies of reverse reactions. Adapted from [58].

activation energy for the reverse reaction is null, the excess energy is completely converted into KER. The ion signal has a gaussian shape with a narrow width, which is proportional to the KER. That corresponds to the PEC and ion signal on the left in Fig. 2.12. Unimolecular reactions whose potential energy curve exhibit a non negligible activation energy for the reverse reaction, produce a flat-topped ion signal, broader than in the first case, because the fragments can now be released with more kinetic energy. That corresponds to the PEC and ion signal on the middle of Fig. 2.12. A large kinetic energy release yields a very broad dish-shaped ion signal, corresponding to the right panel in Fig. 2.12. The determination of these ions shapes and thus the KER, is a simple task in double sector mass spectrometers. In reflectron time-of-flight mass spectrometers, more elaborate methodologies have to be applied as explained in section 3.3.4. In that section, we obtain KERs for fragment ions generated from ionised guanine. Linear time-of-flight mass spectrometers are of no use to obtain information about metastable fragmentation since parent and daughter ions will be superimposed in the mass spectra.

In the next section we introduce a couple of quantum mechanical theories incorporated in a wide variety of computational quantum chemistry software. Computational quantum chemistry programs are exploited in section 3.3.4 to find several unimolecular reactions involving the lowest energy isomers of guanine cations and in section 4.8.2.2 to study the Born-Oppenheimer molecular

dynamics of nitromethane clusters.

2.4 Approximate methods for electronic description and computational quantum chemistry

An important step in quantum chemistry is to solve the time-independent Schrödinger equation within BOA to obtain the electronic WF, from where many of the properties of the molecule can be extracted. However, exact analytical solutions only exist for the hydrogen atom and hydrogen molecular ion. That is due to electron-electron interactions that depend on more than one electron coordinate at a time. Any solution for many-electron systems ($N_e \geq 2$) has to be approached numerically. Several methods have been developed to such purpose and we highlight the most commonly used: *ab initio* methods and density functional theory (DFT). *Ab initio*, as the name suggests, does not rely on any empirical or fitting parameters. DFT on the other hand, incorporates empirical/fitting parameters.

2.4.1 *Ab initio*: Hatree-Fock theory

The Hartree-Fock (HF) theory is one of the simplest *ab initio* methods. It is a mean field theory, meaning that the motion of each electron is described in the mean electrostatic field created by the $N_e - 1$ electrons and N_n nuclei. HF theory misses the Coulomb correlation that describes how the movement of each electron influences the others. Since the effect of correlation on the energy of an atom/molecules is generally not small, HF is not a very accurate method. It serves mostly as starting point to more complex methods, treating electron correlation *a posteriori* (post-HF methods). As stated previously, the exact WF has to be approximated in some way due to the electron-electron Coulomb interaction. In the Hartree method, it is approximated by a product of one electron functions known as orbitals, $\phi_i(\vec{r}_i)$. The product itself is called the Hartree product:

$$\Phi(\vec{r}_1, \vec{r}_2, ..., \vec{r}_{N_e}) = \phi_1(\vec{r}_1)\phi_2(\vec{r}_2)...\phi_{N_e}(\vec{r}_{N_e}) \tag{2.12}$$

where $\vec{r}_i$ are the coordinates of the i^{th} electron. A single Hartree product does not satisfy the Pauli principle, which imposes anti-symmetry of the overall (spatial and spin) electronic wavefunction under permutation of electron pairs. The Hartree-Fock method ensures that this requirement is fulfilled. In the HF method, the exact WF is described through linear combinations of Hartree products, written in the form of Slater determinants [64]:

$$\Phi(\vec{x}_1, \vec{x}_2, ..., \vec{x}_{N_e}) = \frac{1}{\sqrt{N_e!}} \begin{vmatrix} \psi_1(\vec{x}_1) & \psi_2(\vec{x}_1) & \cdots & \psi_{N_e}(\vec{x}_1) \\ \psi_1(\vec{x}_2) & \psi_2(\vec{x}_2) & \cdots & \psi_{N_e}(\vec{x}_2) \\ \vdots & \vdots & \ddots & \vdots \\ \psi_1(\vec{x}_{N_e}) & \psi_2(\vec{x}_{N_e}) & \cdots & \psi_{N_e}(\vec{x}_{N_e}) \end{vmatrix} \tag{2.13}$$

The electron coordinates comprise both space and spin, $\vec{x}_i = \{\vec{r}_i, \vartheta\}$ and the one-electron spin-orbitals ψ_i are given as a product of spatial (orbital ϕ) and spin functions (either α 'up' or β 'down'), for example $\psi_1(\vec{x}_i) = \phi_1(\vec{r}_i)\alpha$, $\psi_2(\vec{x}_i) = \phi_2(\vec{r}_i)\beta$, $\psi_3(\vec{x}_i) = \phi_3(\vec{r}_i)\alpha$, $\psi_4(\vec{x}_i) = \phi_4(\vec{r}_i)\beta$,

and so on ... We only discuss restricted wavefunctions, where each spatial orbital ϕ_i is occupied by two electrons of opposite spin, $i = \{1,2,...,N_e/2\}$. The Slater determinant's columns and rows run over different spin-orbitals and electrons, respectively. Indistinguishable fermions as the case of electrons, are described by total wavefunctions that are antisymmetric with respect to the exchange of any two particles. This requires that no more than two electrons occupy the same spin-orbital (Pauli exclusion principle). Slater determinants ensure the correct symmetry of the total wavefunction.

In the next section, a numerical procedure to solve the HF equations is discussed.

2.4.1.1 Linear combination of atomic orbitals (LCAO) and the Self-Consistent Field (SCF) procedure

We recall that molecular orbitals (MO) represent the spatial regions that electrons can occupy and are often spread over multiple atomic sites. MOs may be expressed as a linear combination of atomic orbitals (LCAO-MO), a procedure developed by Roothaan and Hall in 1951 [65, 66]. One uses a fixed basis set of $N_o \geq \frac{N_e}{2}$ atomic orbitals centered on the different atoms, $\{\varphi_o,\ o = 1,2,...,N_o\}$ to express a number of N_o MOs, $\{\phi_i,\ i = 1,2,...,N_o\}$, of which $\left(N_o - \frac{N_e}{2}\right)$ will be empty orbitals, known as virtual MOs, and $\frac{N_e}{2}$ will be occupied MOs:

$$\phi_i = \sum_{o=1}^{N_o} c_{oi}\varphi_o \tag{2.14}$$

c_{oi} is the contribution of the φ_o atomic orbital to the ϕ_i MO. Constructive or destructive interference of atomic orbitals, originating bonding or anti-bonding MOs, depend on the signs of these coefficients, as shown in Fig. 2.13. The numerical procedure to find the HF wavefunction and respective energy involves the following steps:

1. First, a suitable atomic basis set representing the atomic orbitals φ_o is chosen. Analytical representations for the atomic orbital basis set is given in section 2.4.3. Note that the atomic basis set remains unchanged throughout the calculations.

2. In the first step, a set of trial c_{oi} are chosen and the MOs are constructed accordingly to equation 2.14.

3. The atomic orbital coefficients and the atomic orbitals are used to determine the HF Hamiltonian, and therefore the HF energy.

4. If the HF energy does not vary more than a certain threshold, normally specified by the user in quantum chemistry programs, between successive iterations, that energy and wavefunctions are accepted. The procedure has converged and terminates. If the HF energy changes more than the threshold for convergence, a new set of atomic orbital coefficients are defined, and a new iteration is done.

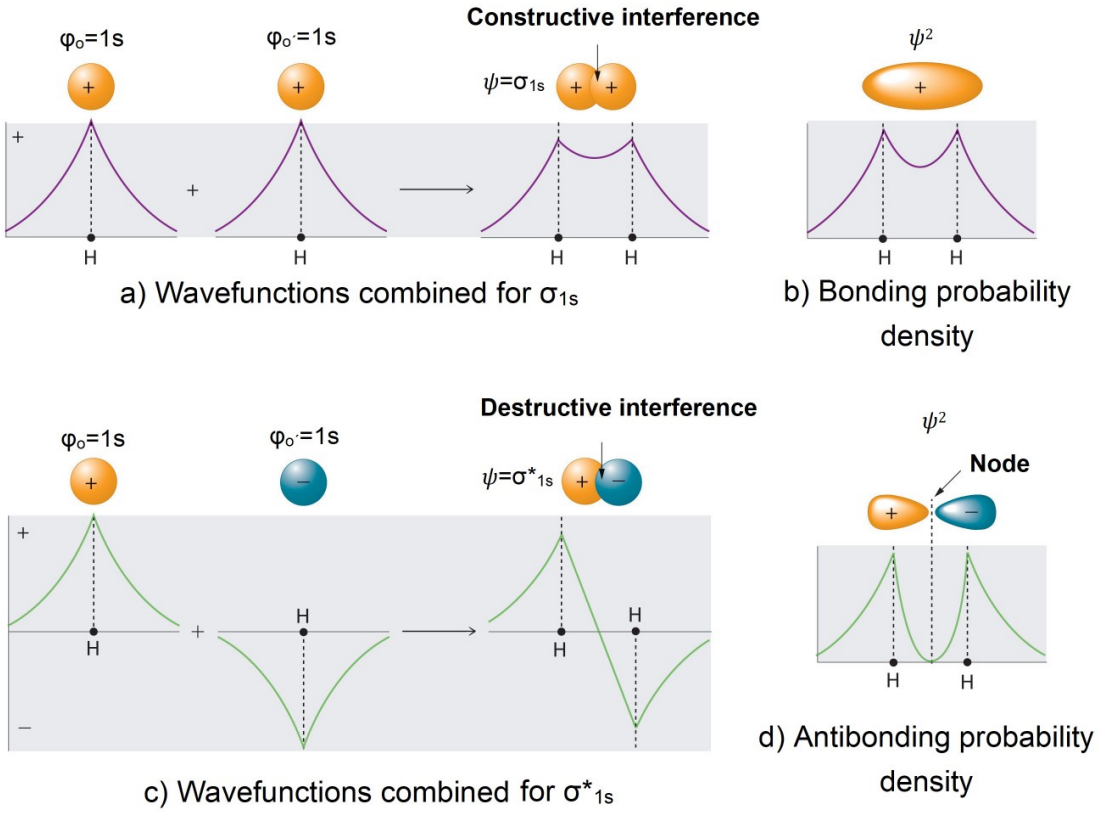

Figure 2.13: Pictorial example of LCAO procedure to produce two MO of H_2 from two H1s atomic orbitals. When the two atoms approach each other, the intereference can be a) constructive, with both coefficients positive or c) destructive, with one coefficient positive and the other negative. We obtain repectively, a b) σ_{1s} bonding orbital, where there is a significant probability of finding the electrons in between atoms and a d) σ^*_{1s} anti-bonding orbital, where the probability of finding electrons in between atoms is null, represented by a node

Although being one of the simplest theories, the HF procedure is more complex than what was here described. The process involves mutual dependencies between parameters. Therefore, it has to be solved iteratively as described above, until a convergence is achieved. Because of that, the procedure is called a self-consistent field procedure.

2.4.2 Density functional theory (DFT)

Density functional theory provides a mean for including dynamic correlation energy in a single determinant ground state wavefunctions, unlike the HF method. DFT and HF methods have roughly the same computational cost, which makes DFT usually a better choice than HF. In DFT, the electronic GS wavefunction and the respective energy are a functional of the electron density $\rho(\vec{r})$ [67] as well as the energy of the corresponding wavefunction, which is written as:

$$E[\rho(\vec{r})] = \int V_{\text{Nuc}}(\vec{r})\rho(\vec{r})\,\mathrm{d}\vec{r} + \frac{1}{2}\frac{e^2}{4\pi\varepsilon_0}\int\int \frac{\rho(\vec{r})\rho(\vec{r}')}{|\vec{r}-\vec{r}'|}\,\mathrm{d}\vec{r}\mathrm{d}\vec{r}' + G[\rho(\vec{r})] \tag{2.15}$$

The first and second terms are the Coulombic nuclei-electron and electron-electron interactions and $G[\rho(\vec{r})]$ is an "universal" functional of the density. The "universal" functional comprises the kinetic energy functional of the electrons T_s and the exchange-correlation functional E_{xc} including the exchange and correlation between electrons, $G[\rho(\vec{r})] = T_s[\rho(\vec{r})] + E_{xc}[\rho(\vec{r})]$ [68]. The electrons move on a potential, normally called the Kohn-Sham potential in honour to the pioneers of DFT, $V_{KS} = V_{Nuc} + \frac{1}{2}\frac{e^2}{4\pi\varepsilon_0}\int \frac{\rho(\vec{r}')}{|\vec{r}-\vec{r}'|}d\vec{r}' + \frac{\delta E_{xc}}{\delta\rho}$ and the time-independent Schrödinger equation becomes:

$$\left(-\frac{\hbar}{2m_e}\nabla^2 + V_{KS}\right)\phi_i(\vec{r}) = \epsilon_i\phi_i(\vec{r}) \tag{2.16}$$

Summing the squared modulus of all the occupied MOs leads to the electronic density:

$$\rho(\vec{r}) = \sum_{i=1}^{occ} |\phi_i(\vec{r})|^2 \tag{2.17}$$

As the electronic density defines the KS potential in eq. 2.16 and this in turn affects the electronic density through MO orbitals in eq. 2.17, the process has to be solved self consistently: one starts with a guess for the density, obtains the MOs and the respective energies, and a new density at the end of that iteration. The procedure is repeated until the density and energies vary less than a specific threshold. This is a self-consistent field procedure similar to the one presented for finding numerical solutions for the HF wavefunction.

The problem of DFT is that the exact form of the exchange-correlation functional is not known. Many approximations to the exchange-correlation functional form exist, some more elaborate than others. The different approximations are summarised as follows :

- *Local spin density approximation (LSDA)*: solely depends on the electron densities.
- *Generalized gradient approximation (GGA)*: depends on electron densities and respective gradients.
- *Meta-generalized gradient approximation (mGGA)*: includes up to second order gradient terms (electron density, electron density gradients, Laplacian of the electron density and orbital kinetic energy density).
- *Hybrid functionals*: Functionals incorporating exact exchange energy (equivalent to HF exchange energy).
- *Double hybrid functionals*: Functionals incorporating both exact exchange and correlation energies (equivalent to HF exchange and post-HF correlation energies).

In general, the inclusion of more terms leads to an improvement of the energies and wavefunction of the system, at expense of increased computational cost. The increase of the accuracy of the functional is seen as climbing a ladder, referred to as the Jacob's ladder: at the bottom, the accuracy matches that of the HF theory, whereas at the top, it matches the desired chemical accuracy (~ 1 Kcal/mol). The different rungs of the ladder are shown in Fig. 2.14, alongside with the new

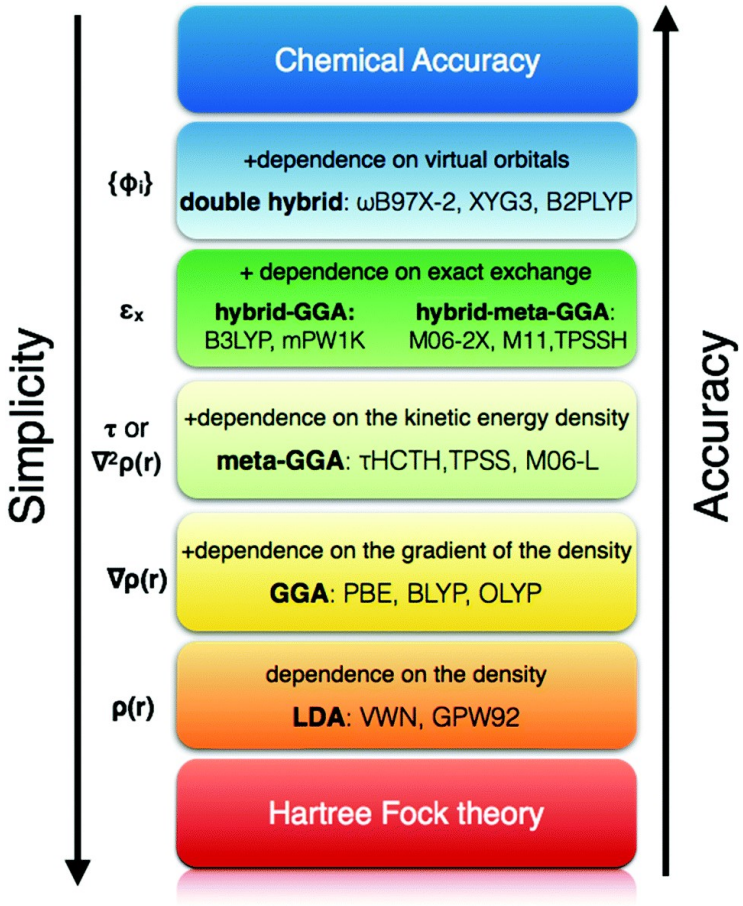

Figure 2.14: Schematic of the Jacob's ladder for DFT. The accuracy increases from the bottom to the top of the ladder. Each exchange-correlation functional is inserted in a rung depending on the of terms used to express it [69].

terms added in each rung and examples of exchange-correlation functionals pertaining to each rung. Some of the functionals are standalone, meaning that they only represent the exchange or the correlation part as the case of the Becke exchange functional (denoted by B), the Becke three paratemer hybrid exchange functional (denoted by B3) or the Lee-Yang-Parr correlation functional (denoted by LYP). The combination of the last two gives origin to the very known B3LYP exchange-correlation functional. Other functionals provide simultaneously exchange and correlation terms as the case of the Tao-Perdew-Staroverov-Scusseria (denoted by TPSS) or the Minnesota 2006 functional with 54% of exact exchange energy (denoted by M06-2X). As can be observed in table 2.1, the M06-2X functional [70] shows a remarkably accuracy in a wide range of benchamark tests like thermochemistry, activation energies of reactions (barrier heights) and thermochemical kinetics. Notably, it also provides a very good description of weakly bonded complexes as Van der Waals and hydrogen bonded systems. The versatility of this functional makes it a good choice to tackle many of the problems in quantum chemistry.

Method	Type	TC177	DBH76	TK253	NCIE53	TKNC306
M06-2X	hyb meta-GGA	1.32	1.22	1.27	0.37	0.97
M05	hyb meta-GGA	2.57	2.19	2.38	1.18	1.98
B3LYP	hyb GGA	3.59	4.50	4.04	2.34	3.47
PBE	GGA	5.20	8.64	6.92	1.79	5.21
BLYP	GGA	4.80	8.52	6.66	3.12	5.48
HFLYP	*ab initio*+GGA	12.73	7.01	9.87	1.36	7.03
HF	*ab initio*	39.18	8.41	23.79	3.55	17.05

Table 2.1: Mean unsigned errors (MUE) of functionals and *ab initio* methods discussed in the present chapter. TC: Thermochemistry; DBH: Diverse barrier heights; TK: Thermochemical kinetics; NCIE: Non-covalent interaction energies; TKNC: Thermochemical of non-covalent. All values are given in kcal/mol. Adapted from [70]

2.4.3 The choice of atomic orbitals basis set

In order to carry out the computational calculations for a given level of theory (HF, DFT or other), a set of atomic orbitals has to be chosen as mentioned in section 2.4.1.1. Very often a Gaussian type orbital basis set or a plane wave basis set is employed. Here only the former is briefly described. The idea of the Gaussian basis set is to mimic the hydrogen like orbitals using contractions/linear combinations of Gaussian functions centered in each atom [71]:

$$\varphi^{cGTO}(\vec{r},\theta,\phi) = \sum_{p=1}^{P} c_p \varphi^{GTO}_{n,l,m_l}(\vec{r},\theta,\phi) \tag{2.18}$$

where the analytic form of each Gaussian type orbital (GTO) is:

$$\varphi^{GTO}_{n,l,m_l}(\vec{r},\theta,\phi) = N|\vec{r}|^l e^{-\zeta|\vec{r}|^2} Y_{l,m_l}(\theta,\phi) \tag{2.19}$$

n, l and m_l are the principal, orbital and magnetic quantum numbers, respectively, N is a normalization factor, $|\vec{r}|$ is the distance from the nucleus (orbital center), ζ is a constant depending on n and on the effective nuclear potential Z_{eff} 'seen' by the electron and $Y_{l,m_l}(\theta,\phi)$ are spherical harmonics. Examples of Gaussian centered basis sets are the Pople's and Dunning's basis sets.

2.4.3.1 Pople's basis sets: Split valence basis set

The Pople's basis set (also known as split valence basis set) normally uses one contracted Gaussian type orbital (cGTO) to describe the sub-shells of core electrons and a varying number of contracted Gaussian type orbitals to describe the sub-shells of valence electrons: a split valence double zeta basis set uses two contracted Gaussian type orbitals to describe each sub-shell of valence electrons; a split valence triple zeta uses three Gaussian type orbitals to describe each sub-shell of valence electrons, and so on. The simpler split valence double zeta basis set is the 3-21G [72], meaning that each core electronic sub-shell is represented by one Gaussian type orbital resultant from the contraction of three primitive Gaussian functions, and the valence electronic sub-shells are represented by two Gaussian type orbitals resultant from the contraction of two and one Gaussian

functions, respectively. The hydrogen like orbitals can be better approximated by including more primitive Gaussian functions in the contraction, for example, the 6-31G split valence double zeta basis set. The 6-311G split valence triple zeta basis set allows even higher flexibility than double zeta basis sets being important in the description of oxygen and fluorine atoms, where electrons can extend to regions far from the nucleus [73].

2.4.3.2 Polarisation and diffuse functions

The basis set discussed above assume a symmetric shape of the atomic orbitals. However, in a molecular environment, the shape of these atomic orbitals can be distorted due to interactions with surrounding electrons. This polarisation effect can be mimicked by adding higher angular momentum orbitals. For example, the 6-31G(d) adds to the 6-31G basis set, extra orbitals of angular momentum $l = 2$ to second row elements, permitting de-localisation of electrons from orbitals p to d.

Diffuse functions manifest the non-valence behaviour of electrons and are expressed by GTOs with very small ζ value, spanning therefore, a considerable spatial region. They are relevant in describing anions, where the additional electrons can be weakly bound far from the atomic nucleus. Inclusion of diffuse functions has shown not to improve significantly GS geometries of anions [74]; however, energies of anions and neutral molecules with lone pairs are expected to be drastically lowered by the inclusion of diffuse functions. Apart from anions, diffuse functions are also important to describe weakly bonded complexes [75]. The 6-31+G basis set for example, requests an additional diffuse GTO centered on heavy atoms.

2.4.3.3 Dunning's basis sets: Correlated consistent basis sets

The Dunning's basis set (also known as correlated consistent basis sets) is designed to provide a certain amount of correlation energy by progressively increasing the angular momentum of the polarisation functions. Depending on the number of functions included, one may have a correlated consistent polarised valence double (D), triple (T), quadruple (Q) ... zeta basis set, cc-pVnZ (n=D, T, Q). Here valence implies that the functions are solely describing valence electrons, which are more prone to interactions with electrons of surrounding atoms. The cc-pVDZ basis set can recover 61−87% of the correlation energy of second row elements [76]. The cc-pVTZ is able to recover 85−97% correlation energy of third row atoms, whereas cc-pVQZ can recover 94−99 % [76]. As can be understood, the difference of recovered correlation energy decreases along the levels: the basis set is said consistent. As the recovered correlation presents a geometric trend along the levels, one can extrapolate energies in the complete basis set limit. It is also possible to augment the basis set with diffuse functions, aug-cc-pVnZ. Dunning's basis sets were optimized with *ab initio* HF and correlated post-HF methods. Therefore, they are suitable for *ab initio* correlated methods. Their applicability to DFT is also possible, but its sub-optimal due to better convergence of DFT energies.

2.4.4 Calculation of transition states and dissociation pathways with computational methods

In section 2.3.1 we introduced the quasi-equilibrium theory and explained how this theory predicts the unimolecular rate constants of dissociation mechanisms. Briefly, to calculate the unimolecular rate constants (equation 2.11), one needs to determine the vibrational levels of the reactants and transitions states. In the present section, determination of reactant and transition state properties is explained in terms of computational chemistry software, more precisely using G09® package [77].

The following steps are routinely employed for determination of dissociation mechanisms of ions:

1. *Determine the optimised structure of the neutral parent*. This is achieved by constructing an input geometry for the program, for example, using Avogadro visualizer software. Avogadro allows the creation of an input file in Gaussian format. The user has to define the level of theory (HF, DFT, ...), basis set (Pople's, Dunning's, ...), charge (0, neutral), multiplicity (1, singlet) and other additional keywords. The keywords *Opt* and *Freq* need to be included. The first requests the program to optimise the input structure to a minimum potential energy configuration using the Berny algorithm, whereas the second requests the calculation of vibrational modes for the optimised geometry. If the geometry is indeed a minimum, no negative vibrational frequencies should be reported.

2. *Determine the optimised structure of the cationic parent*. Taking as input the optimised geometry of the step 1, the user has to run the same type of calculation but now for a cation with charge $+1$ and spin 2 (doublet). The *adiabatic ionisation energy* is obtained by subtracting the energies of the structures obtained in this step and step 1.

3. *Search for a transition state*. To identify a potential TS representing a bond dissociation, the reaction coordinate (bond distance), is first scanned. In a coordinate scanning, the number of steps and step size is defined by the user. The remaining nuclear degrees of freedom are optimised in each step by minimising the total energy and forces acting on the atoms. To perform a coordinate scan, the keyword *Opt=modredundant* has to be added in the input file. The TS geometry is, in the majority of cases, similar to the geometry corresponding to the maximum energy in the potential energy curve of the scan. Therefore, this geometry is used as input structure for the TS search algorithm. The search for the TS is accomplished by using the Berny algorithm, with the keyword *Opt=TS* in the input file. Additionally, force constants have to be estimated (*Opt=estmfc*), numerically calculated in the first step of optimisation (*Opt=calcfc*) or numerically calculated in all the optimisation steps (*Opt=calcall*). Force constants inform the program about the curvature of the PES, enabling it to follow the right direction to find the TS. The quadratic synchronous transit 2 (QST2) and quadratic synchronous transit 3 (QST3) are alternative algorithms used to find TS structures in Gaussian. In QST2 reactants and products structures are provided in the input file. The program attempts to establish a reaction coordinate between these structures and finds the maximum energy structure along it. QST3 proceeds in a similar fashion to

QST2, but it requires an additional input structure corresponding to an approximate TS geometry. Independently of the algorithm used to find the TS, it is common to calculate the vibrational frequencies at the end to verify if the geometry found is indeed a TS (first order saddle point) with one negative vibrational frequency representing the reaction coordinate of interest.

4. *Confirm the reactants and products*. After identifying the TS, it is important to verify that it connects with the desired reactants and products through the reaction coordinate. By default, the intrinsic reaction coordinate (*IRC*) keyword tells the program to perform a forward and backward scan along the reaction coordinate, that is, towards the products and reactants. Again, it is necessary to calculate the force constants by using *IRC=calcfc* keyword.

5. *Optimise the products*. If the Berny algorithm is used to find the TS (Opt=TS), the products are optimised to an energy minimum with *Opt* keyword and vibrational frequencies checked with *Freq* keyword.

6. *Calculate relative energies of the structures*. The zero of energy is set to the reactant's energy and relative energies are then calculated for the TS and products.

2.5 Intermolecular forces and their description

In this section we describe the forces and interactions responsible for the formation atomic and molecular clusters. Contrary to intramolecular forces that have origin in covalent interactions (sharing of valence electrons), intermolecular interactions mainly result from electrostatic interactions, as we will see right next.

2.5.1 Van der Waals interactions

Van der Waals (VdW) forces result from asymmetry in electronic charge distribution in atoms and molecules. Such asymmetry can be permanent in molecules due to differences in electronegativities of the chemical groups composing it or can be induced by electrostatic interactions with other particles. Various types of VdW interactions can be distinguished according to the asymmetry of charge distribution of the interacting particles:

- *London dispersion forces*, when the charge distribution is completely symmetric in both particles. The particles are said to be non-polar.

- *Debye dipole-induced forces*, when one particle has an asymmetric charge distribution (is polar, possessing a permanent electric dipole moment) or is an ion and the other is non-polar.

- *Keesom dipole-dipole forces*, when both particles are polar (have permanent electronic dipole moments).

When particles with no permanent dipole moment approach each other, the repulsion between the electronic clouds polarises both particles, creating an asymmetry in charge distribution. A small

electric dipole moment is induced and a small attractive force is established between them. This is called a London dispersion interaction whose potential is expressed by [78]

$$V^{London}(r) = -\left[\frac{C_6}{r^6} + \frac{C_8}{r^8} + \frac{C_{10}}{r^{10}} + ...\right] \tag{2.20}$$

here r is the distance between the centre of mass of the particles. The first term is dominant and corresponds to the induced dipole − induced dipole interaction. Higher multipoles are generally negligible. C_6=$\frac{3\alpha_e^2 I_E}{4(4\pi\epsilon_0)^2}$ [78] is a constant directly proportional to the isotropic electronic polarisability (α_e) and ionisation energy (I_E) of the particles. Since the rotation of the particles does not alter the dispersion energy, London dispersion forces are not temperature dependent. However, the magnitude of the London dispersion energy greatly depends on the polarisability of the particles, which are generally higher in the case of molecules than atoms. For rare gas atoms, the London dispersion energy lies between −0.9 (helium dimer) and −24 meV (xenon dimer). In molecules, the London dispersion energy is generally smaller than −100 meV [78]. London dispersion energies can be calculated in the context of computational quantum chemistry using empirical dispersion models as the Petersson-Frisch dispersion (PFD) model [79] or the Grimme's dispersion (D3) model [80].

Debye forces result from the interaction between a polar or ionic particle with a non-polar particle. In the case of a polar and a non-polar particles approaching each other, a small electric dipole moment is induced in the non-polar particle. The result is a weak binding between the two with a potential energy described by [78]

$$V^{Debye}(r) = -\frac{2\mu_1^2\alpha_e}{(4\pi\epsilon_0)^2 r^6} \tag{2.21}$$

where μ_1 and α_e are the permanent electric dipole moment and the polarisability of the polar and non-polar particles, respectively. Debye forces are not susceptible to thermal energy because the induced dipole moment can freely adapt to re-orientations of the polar particle. For a polar molecule with μ_1 = 1 D (e.g. HCl) and a non-polar molecule with a polarisability volume of 10^{-23} cm^3 (e.g. benzene) the permanent-induced dipole moment interaction energy is about −8 meV, at a separation distance of r = 0.3 nm.

Finally, two polar molecules can also interact electrostatically via Keesom forces. The dipole moments adopt a co-linear arrangement, with head-to-tail disposition (interaction of sites with positive and negative partial charge in different molecules). However, thermal energy promotes molecular rotation and consequently a misalignment of dipoles. The average interaction energy is given by a Boltzmann-weighted average [78]

$$V^{Keesom}(r) = -2\left(\frac{\mu_1\mu_2}{4\pi\epsilon_0}\right)^2\left(\frac{1}{3k_BTr^6}\right) \tag{2.22}$$

where μ_1 and μ_2 are the dipole moments of the polar molecules and T is the temperature. At room temperature, the average Keesom energy of two molecules with dipole moments of 1 D (e.g. HCl) separated by r = 0.3 nm is ∼ −14 meV.

2.5.2 Other electronic multipole interactions

Some molecules have no asymmetry in charge distribution (a permanent electric dipole moment) but have a charge distribution which is not spherical. These molecules are said to possess higher order multipoles than the electric dipole moment. Quadrupoles and octapoles are cases of higher order electric multipole moments. Benzene is a great example of a molecule possessing an electric quadrupole moment. The π MOs concentrate electronic charge near the carbon atoms, out of the ring plane. This makes the hydrogen atoms slightly positive in comparison with the regions surrounding the carbon atoms. Benzene dimers may form π-stacked, T-shape or parallel displaced structures, due to interaction of the positive partial charge of the hydrogen atoms with the negative partial charge located on carbon atoms of the opposite monomer. These arrangements can be observed in Fig. 2.15. Positive partial charges are represented by a blue colour and negative partial charges as a red colour. The arrows indicate the intermolecular interactions between quadrupole moments. The negative partial charges of perfluorbenzene (C_6F_6) are concentrated on the fluorine atoms and therefore interactions with benzene molecules are achieved by reversed polarity stacking.

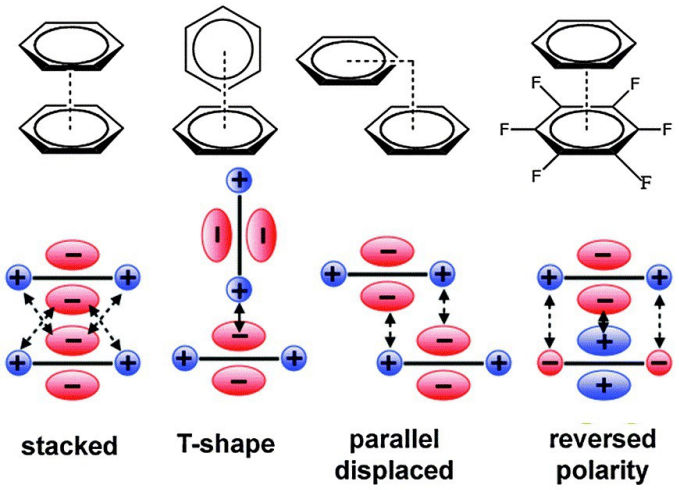

Figure 2.15: Intermolecular geometries/configurations arising from interactions involving the quadrupole moments of the molecules involved [81].

2.5.3 Hydrogen bonding

Hydrogen bonds are established when a hydrogen atom (H), covalently bound to an electronegative atom (X = N, O, F...), interacts with another electronegative element Y with non-bonding electrons (electrons which occupy non-bonding MOs and do not participate in covalent bonds). The positive partial charge on the hydrogen atom, generated by the electronegative element X, is attracted to the negative partial charge on the atom Y. Therefore, hydrogen bonding is mainly electrostatic ($\sim$ 80%) in nature [78]. Hydrogen bonds are generally represented by $X-H\cdots Y$ and the angle formed by X, H and Y is around 180°, $\measuredangle X-H\cdots \mathrm{Y} \approx 180°$. Energies of hydrogen bonds range between -100 and -260 meV and are typically stronger than VdW interactions. In Fig. 2.16 an example

of a hydrogen bond established between a water and ammonia molecules is shown. Electronic charge of the hydrogen atom of the water molecule is delocalised to the electronegative oxygen. This creates a negative partial charge on the oxygen and a positive partial charge on the hydrogen, which interacts with the negative partial charge of the nitrogen of the ammonia molecule. The water molecule is referred as hydrogen donor because it "donates" the hydrogen for the hydrogen bond whereas the ammonia molecule is referred to as hydrogen bond acceptor.

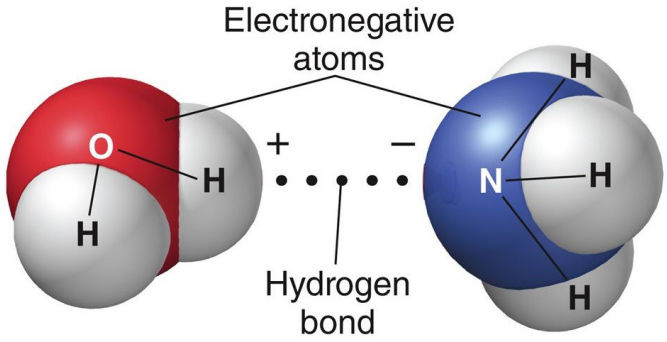

Figure 2.16: Representation of a hydrogen bond between a water molecule and an ammonia molecule. The water molecule is referred as the hydrogen bond donor, whereas ammonia is the hydrogen bond acceptor [81].

2.6 Summary

In this present chapter, we described some physical chemistry principles relevant in the context of this thesis. Molecular excitation and/or ionisation by multi-photon absorption or electron momentum transfer were discussed. The major difference between the two is the access of neutral excited states of the target by multi-photon ionisation. The role of these states in specific ion fragmentation may be assessed by comparing results obtained with both types of experiments. The de-excitation processes taking place after excitation were also analysed. De-excitation processes include luminescence and raditionless decay. The first may happen between electronic states with the same spin multiplicity (fluorescence) or different spin multiplicity (phosphorescence). Due to the high density of excited electronic states in polyatomic molecules, de-excitation from high lying electronic states occurs usually via raditionless decay (internal conversion). Internal conversion is an example of a non-adiabatic process, happening when potential energy curves or surfaces get close to each other. In those cases, the BOA is expected to break down leading to transitions between different electronic states. During the process, electronic potential energy is channelled into vibrational degrees of freedom, producing a vibrationally hot neutral/ion. The quasi-equilibrium theory was introduced to describe the statistical fragmentation of polyatomic ions after electronic-vibrational energy interconversion. A brief introduction to the main concepts and techniques of computational chemistry was given to help the reader following computational simulations presented in the next chapters.

Chapter 3

Dissociative ionisation of guanine and guanosine tautomers: experiments exploiting ILTD and DFT calculations

3.1 Introduction

A significant experimental challenge for developing fundamental understanding of radiation-induced processes in biomolecular systems is producing neutral gas-phase targets of thermally-labile biomolecules without some contribution of thermal decomposition or thermally-driven reactivity. In some types of experiment, only a good target density of the molecule of interest is required and the presence of some other species due to thermal damage is not a major problem. For example, Peña and co-workers were able to study the rotational spectroscopy of uridine successfully despite the fact that their direct laser desorption method produced many other gas-phase species in addition to neutral uridine [82]. However, the presence of thermal damage products in the target is a major problem in dissociative ionisation experiments. This chapter investigates the dissociative ionisation pathways of guanine and guanosine, which are respectively the most thermally-labile nucleobase and nucleoside in DNA and RNA [25, 27]. Our first challenge is therefore to produce viable gas-phase targets and we have chosen a relatively new method to attempt this: *indirect laser-induced thermal desorption* (ILTD). ILTD, firstly developed by Greenwood [31], involves desorbing molecules from a condensed sample on a foil that is heated by CW laser irradiation of its reverse side. It has been used successfully before to produce several gas-phase targets of nucleobases and nucleosides [30, 31, 32, 33], but no studies have been published to date on guanine and those on guanosine did not report a detailed assessment of possible thermal decomposition. This chapter reports the first measurements to assess the possible presence of thermal decomposition products in ILT-desorbed guanine and guanosine.

Further to its propensity for thermal damage in thermal oven sources, guanine carries special interest in the context of this thesis as it exists in a number of different tautomeric forms in the gas phase. Therefore, interpreting its fragmentation pathways in detail represents a challenge,

with different tautomers potentially fragmenting differently. To give ourselves the best chance of recognising such effects, we have preformed experiments revealing both prompt and microsecond-timescale dissociations of guanine$^+$, as well as complementary DFT calculations. With regards to the biological relevance of the molecules studied in this chapter, we recall that guanine is the nucleobase with the lowest ionisation energy and hence it represents the preferential trapping site for holes in DNA upon ionisation of the macromolecule. The depurination of guanosine is a very active *spontaneous* mechanism for genetic alterations of DNA, but investigations regarding the impact of exogenous agents is very scarce. Therefore, the responses of guanine and guanosine to ionising radiation stand out as particularly important to study. Nonetheless, these are the least studied DNA and RNA sub-units in the gas phase. Dissociative ionisation experiments on guanine and guanosine are scarce in the literature. The experiments and calculations in this chapter characterise a number of fragmentatoin pathways of ionised guanine and guanosine molecules for the first time.

In the first section of the present chapter, we describe the *Compact* MPI-TOF mass spectrometry experiment at the OU Molecular and Clusters laboratory. In section 3.2.2 we discuss the details of ILTD sources and compare them with other types of laser desorption methods and conventional heating ovens. The specific ILTD system assembled in the compact MPI-TOF experiment is described and direct measurements of foil temperatures in an ILTD system are presented for the first time. In section 3.3 we investigate the *prompt* (defined here as within several ns) and *metastable* (microsecond timescale) fragmentation of guanine molecules induced by multi-photon ionisation at 225 nm. We calculate, at DFT level, appearance energies of specific fragment ions originating from different tautomers of guanine to help rationalise their presence in the metastable mass spectra but the absence in the prompt mass spectra. In section 3.4 we go a step further in complexity and investigate the ability for our ILTD source to produce intact guanosine targets in the gas-phase. This section also evaluates some possible thermally-driven processes that can affect fragment ion production by MPI of gas-phase biomolecules, notably changes in relative populations of tautomers / conformers and proton transfer photochemistry in neutral excited states, using DFT and TDDFT methodologies, respectively. Finally, we propose a new explanation for the similarities between guanine and guanosine MPI mass spectra based on DFT calculations of the reaction pathways of guanosine.

3.2 Experiment

3.2.1 The compact MPI-TOF mass spectrometry experiment

The compact experiment assembled at the Molecular Clusters Laboratory can be operated in two modes: (1) to study molecules and clusters seeded in supersonic beams or (2) to study molecules brought into the gas phase by ILTD. The system is shown in Fig. 3.1 and comprises two main vacuum chambers: the expansion chamber where CW supersonic beams are formed and the diagnostic chamber where ionisation takes place. The diagnostic chamber also houses the ILTD source and the extraction electrodes of the time-of-flight mass spectrometer. All but one of the

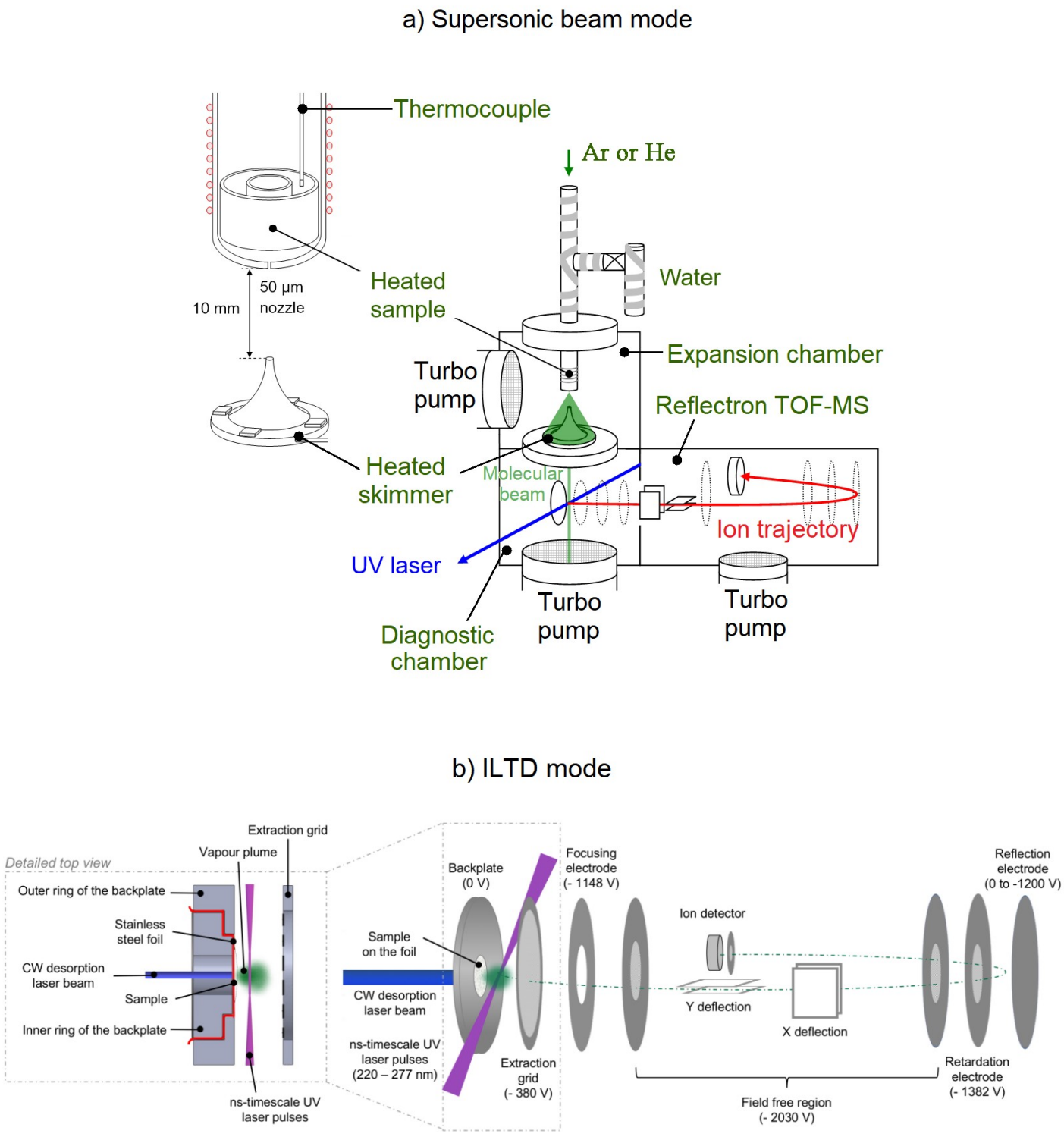

Figure 3.1: Schemes for the two different operation modes of the Compact MPI-TOF experiment: a) Supersonic beam mode and b) ILTD mode. The detailed top view in diagram (b) shows the ILTD source and the extraction grid of the TOF-MS. These are situated in the centre of the diagnostic chamber.

experiments in this chapter were carried out in ILTD mode and the ILTD source is described in section 3.2.2.2. The supersonic beam system is only described briefly in the remainder of this paragraph and full details can be found in B. Barc's PhD thesis [83]. Mounted on the expansion chamber, there is a 50 μm diameter pinhole nozzle that was laser-drilled into the closed end of a stainless steel tube (Lennox Laser). The outside of the tube is heated using a coiled resistive heater with an axial clamp in order to sublimate solid samples in a stainless steel powder cartridge positioned above the nozzle. A K-type thermocouple inserted directly into the powder monitors the sample's temperature. Vaporised molecules are seeded in He or Ar carrier gases, introduced at 0.5−2 bar through a swagelock + VCR gas line. A water reservoir is connected to the gas line for generating hydrated clusters. When hydration is not necessary, the access to the reservoir is closed using a valve. A small portion of the expanding gas mixture that leaves the nozzle passes through a skimmer (*Beam Dynamics model 2*, orifice diameter 400 μm) and the resultant narrow supersonic beam then crosses the ionising UV laser pulses in the diagnostic chamber.

Nanosecond UV pulses (width 7 ns, repetition rate 10 Hz, tunable wavelength 270−220 nm) enter through a DN40CF window on the diagnostic chamber and ionise molecules in the supersonic molecular beam or in the ILTD plume. The laser pulses are generated by a coumarin dye laser (Sirah Cobra Stretch) pumped by the third harmonic of a Nd:YAG laser (Continuum Powerlight II 8000, 355 nm). A grating (groove density 1800 lines per mm) is used to select a single wavelength from the dye laser pulse (which typically covers a 20 nm range within 440-540 nm, depending on the dye used). The wavelength-selected pulse is then frequency-doubled using a BBO crystal. The typical energy per pulse in the experiments in this thesis is 80–200 μJ, and this can be adjusted by varying the time delay between the excitation of the Nd:YAG crystal and the Q-switch (for more details about the laser's operation principles, the reader is referred to [84] and [42]). Pulse energies are monitored using a pyroelectric joulemeter (Spectrum Detector Inc. SPJ−D−8). The spot diameter (3 mm without any focusing) of the laser pulse when it reaches the gas-phase target is controlled using a convex lens mounted on a slider.

The ions produced at the intersection of the laser beam with the molecular target are orthogonally extracted by a voltage difference of −380 V applied between the extraction grid and the backplate. They are subsequently accelerated towards the reflectron TOF-MS by a voltage difference of −1650 V applied between the field region (FFR) and the extraction grid, as shown in Fig. 3.1 (b). The ions are then decelerated and reflected by a set of electrodes towards a microchannel plate (MCP) detector. The reflectron TOF-MS was built by Kore Techonolgy, except for a set of home-built ion extraction electrodes and a home-built voltage controller. It can achieve a mass resolution of m / Δm $\sim$ 1000 in experiments using focused UV pulses. Pre-amplified signals from ions hitting the MCP are timed using a time-to-digital converter (Fast Comtec P7887, minimum bin size 250 ps). A digital pulse generator (Quantum Composers 9250 Series) triggers the UV pulse, the ion extraction pulse, and the start pulse for the TOF analysis. The data acquisition interface was developed in LabVIEW by B. Barc [83] with subsequent adaptations by M. Ryszka [26].

The expansion and diagnostic chambers are deferentially pumped by Pfeiffer Vacuum TMU 521 (argon pumping speed 500 l/s) and Oerlikon MAG W 600 turbomolecular (argon pumping speed 600 l/s) pumps, respectively. Typical pressures in the expansion chamber and diagnostic

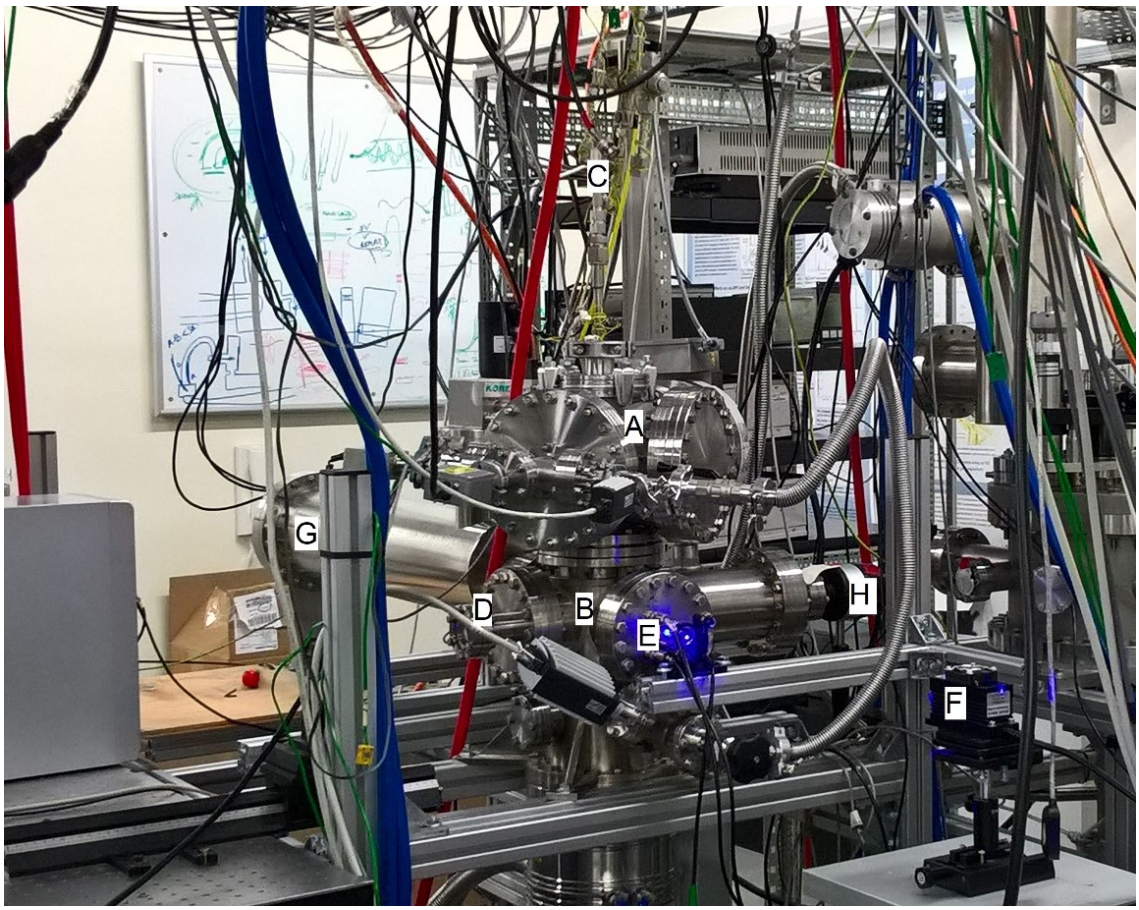

Figure 3.2: Image of the Compact setup at the OU for MPI−TOF experiments on molecules seeded in supersonic jets or desorbed from a foil with ILTD. A: Expansion chamber for establishing a supersonic jet. B: Diagnostic chamber. C: Gas line supplying He or Ar to the supersonic expansion nozzle. D: DN40CF window for the UV pulses that multi-photon ionise molecules in the supersonic jet or the ILTD target. E: DN16CF viewport for the CW desorption laser fot ILTD. F: CW desorption laser. G: reflectron TOF−MS. H: Pyroelectric joulemeter.

chamber during MPI-TOF experiments in supersonic beam mode are 5×10^{-4} mbar and 5×10^{-7} mbar, respectively. The diagnostic chamber pressure during ILTD experiments is typically $5\text{x}10^{-8}$ mbar. The flight tube is evacuated by a Oerlikon TURBOVAC 151 turbomolecular pump (145 l/s). The method applied here to study metastable dissociation of excited ions using the reflectron-TOF mass spectrometer is described in section 3.3.4. Fig. 3.2 shows a picture of the Compact MPI-TOF experiment at the Molecular Clusters Laboratory.

3.2.2 Indirect laser-induced thermal desorption (ILTD)

3.2.2.1 Background of ILTD and comparison with other types of desorption sources

Although thermal ovens allowed researchers to vaporise and investigate various small sized molecules (e.g. some nucleobases and amino acids) it has proved to be difficult or impossible to use such

sources to produce pure intact gas-phase targets of many larger molecules, including some nucleosides [27, 29]. To our knowledge, the largest biomolecule which was vaporised with a thermal oven source with the authors obtaining evidence (but not showing it) for absence of thermal decomposition was the nucleotide deoxycytidine monophosphate [85, 86] but this represents an exceptional result. The low-volatility of highly polar samples can be partially addressed by derivatisation techniques [29, 87], but these inevitably come at the cost of some alterations of the radiation response of the original target. This led researchers to search for alternative vaporisation methods for thermally labile targets with low-volatilty. Laser applications proved to be key in the development of these new methods [5].

The first reports on laser desorption for the production of gas phase targets date from the 1970s. Vastola *et al* vaporised intact ionic salts by directly irradiating the condensed sample with pulses produced by a ruby laser [88]. This is classed as direct laser-induced desorption (DLD) and a variation of this technique was later applied by Posthumus to vaporise polar non-volatile organic molecules, among them nucleotides, using the fundamental harmonic pulses of a Nd:YAG laser [87]. In both works, the sample was dissolved and applied to a metallic probe. The volatile solvent evaporated at ambient temperature and pressure leaving a desorbed film on the metallic surface. The first DLD experiments involved simultaneous desorption and ionisation of the molecules. Since then, numerous DLD systems have been built with lasers that are solely dedicated to target production. Examples include spectroscopy and mass spectrometry studies on amino acids [89, 90], peptides [91, 92], nucleobases [29, 90, 93, 94, 95], nucleosides [29, 96, 97], and nucleotides [98]. However, the direct interaction of the desorption pulses with the sample invariably means that the intact molecules of interest are not the only species in the target [99].

The production of various species (including ions, reaction products, and decomposition products) in addition to the molecule of interest in DLD methods motivated researchers to conduct various studies where energy from the desorption laser pulses was transferred to the sample *indirectly* via an intermediate metal foil. These can be referred to as indirect laser-induced (ILD) desorption methods. The first and most extensively-used type of ILD source is known as *laser-induced acoustic desorption* (LIAD). In LIAD, laser pulses impinging on the reverse side of a metal foil induce the desorption of molecules from a thin condensed sample on the opposite side. This was originally interpreted in terms of rapid local heating by the pulsed laser establishing acoustic waves in the foil that then promote *non-thermal* removal of molecules from the sample [100]. A wide variety of molecules such as amino acids [101], biochromophores [102], viruses, bacteria, and cells [103], and petroleum samples [104] have been brought into the gas phase by LIAD sources. Recently, Küpper's group characterised a LIAD source and found that the desorption had a significant *thermal* component [105]. In line with Kupper's observation, Greenwood and co-workers were among several groups who built LIAD systems for experiments on biomolecules around 10 years ago but did not draw great benefit from the approach. As a result, Greenwood and co-workers replaced the pulsed desorption laser in their LIAD apparatus with a CW desorption laser [30], simplifying the experiment (no need for timing of the desorption laser) and reducing its cost (a simple CW diode laser is much cheaper than common pulsed lasers typically used for LIAD). Whereas LIAD sources functions via a combination of thermal and non-thermal effects,

this new source is purely thermal. Hence we refer to it here as *indirect laser-induced thermal desorption* (ILTD).

One may think that ILTD sources and thermal heating ovens are very similar in nature. However, there are important differences. First, the heating rate of samples in ILTD sources are orders of magnitude larger (we estimate the rate of our ILTD source in section 3.2.2.3) than that of thermal heating ovens (typically 0.01−0.1 K/s). Abdelaziz and co-workers used the hypothetical kinetic diagram shown in Fig. 3.3 to discuss the importance of heating rates for the intact vaporisation of solid samples. Samples with single melting (or sublimation in the case of our application) and

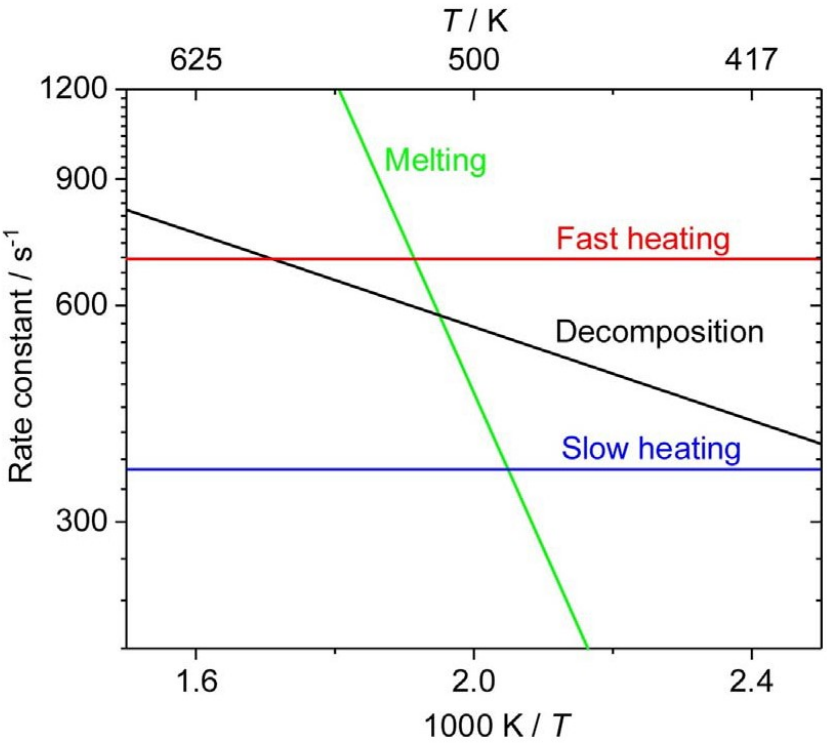

Figure 3.3: Kinetic diagram for decomposition and melting of a hypothetical thermally-labile solid sample. See the explanation in the text. Taken from [25].

decomposition activation energies have a linear kinetics for both processes, represented by green and black lines in the diagram, respectively. Since activation energies for melting a thermally-labile sample are higher than for decomposition, there is a crossing point between the kinetic lines in the diagram. At low temperatures, the decomposition rate is larger than the melting rate, while at high temperatures, the trend is reversed. Quickly heating the sample up to a desired temperature provides a better chance for melting / sublimating it without thermal decomposition, as shown by the intersection between the green and red lines. Heating rates larger than that represented by the red line enables a wider range of temperatures to be used for vaporising the sample without decomposing it. In ILTD, the heating rate depends primarily on the foil properties (e.g. heat capacity, mass, heat transfer coefficient, absorptivity of the laser radiation) and the laser power.

Faster heating rate is not the only advantage that ILTD offers compared with thermal heating

ovens in terms of producing viable gas-phase targets without thermal decomposition. The geometry of ILTD sources is also advantageous: in ILTD the molecules do not interact with any hot surfaces after sublimation, whereas molecules typically collide numerous times with hot oven walls before leaving an oven source. An additional advantage of ILTD is that the ionising beam can pass very close to the foil surface where the gas density is high, giving rise to spectra with good signal-to-noise ratios at low temperature. Also, the closeness of the source to the ionising laser minimises the time that gas phase molecules have available for decomposition in between desorption and interaction with the ionising beam. Similarly, only a small part of the condensed sample is heated significantly in ILTD and this 'hot spot' is exhausted quite quickly. Hence, sample molecules in ILTD remain hot for a much shorter time than they do in an oven source where the entire sample is always heated up. The rapid heating and cooling also help to minimise the amount of time that a condensed sample is hot and possibly thermally decomposing. All these differences reduce the likelihood of thermal decomposition of labile species in ILTD compared with thermal oven sources operating at similar temperatures.

3.2.2.2 Description of the ILTD system

During 2016–2017, a series of ILTD sources were assembled and upgraded in our compact experiment. This work was carried out by Michal Ryszka [26], Rahul Pandey [106], Jana Bocková [84] and I. As shown in Fig. 3.1 (b), the source features a modified backplate of the TOF mass spectrometer. An inner ring with 8 mm-diameter hole inserts into an outer ring such that a stainless steel foil (thickness 10 μm) can be 'gripped' and present a flat surface with respect to the ion extraction region. The backplate system, the extraction pulse grid, the focusing electrode, the first grid of the FFR are collectively described as the 'TOF source' (Fig. 3.4), and are mounted on a single DN100CF flange. A ceramic ring insulates the backplate from the flange (both thermally and electrically — a separate wire allows the backplate to be grounded or biased).

Prior to experiments using ILTD, a solution comprising ~ 20–30 mg of solid sample and a few drops of methanol is spread on the foil with the aid of a spatula. The solvent is left to evaporate for some minutes at room pressure and temperature. The resulting layer of adhered molecules has a thickness of several μm. The ILTD source is then re-installed in the chamber and pumped down to pressures $\leq 10^{-8}$ mbar. Radiation emitted by a CW diode laser (DLM–445–1000, Eksma Optics with an elliptical spot: major axis 4.5 mm and minor axis 1 mm, 445 nm, maximum output power 1 W) passes through a DN16CF viewport (E in Fig. 3.2) located in the centre of the TOF source flange and hits the back of the stainless steel foil. On the opposite side, where the sample is deposited, a plume of neutral molecules is released into the ion extraction region. The CW laser is mounted on a 2D manipulator stage to aid alignment and to move the laser spot onto different parts of the foil. This enables us to desorb molecules from different areas on the sample side of the foil and hence increase the time that measurements can be performed without breaking vacuum to replenish the sample. A lens can be placed in front of the viewport in order to focus the laser beam on the foil. However, this lens was not used in the present experiments as it was observed to have a negligible effect on the MPI-TOF signals. For further details about this and the previous ILTD

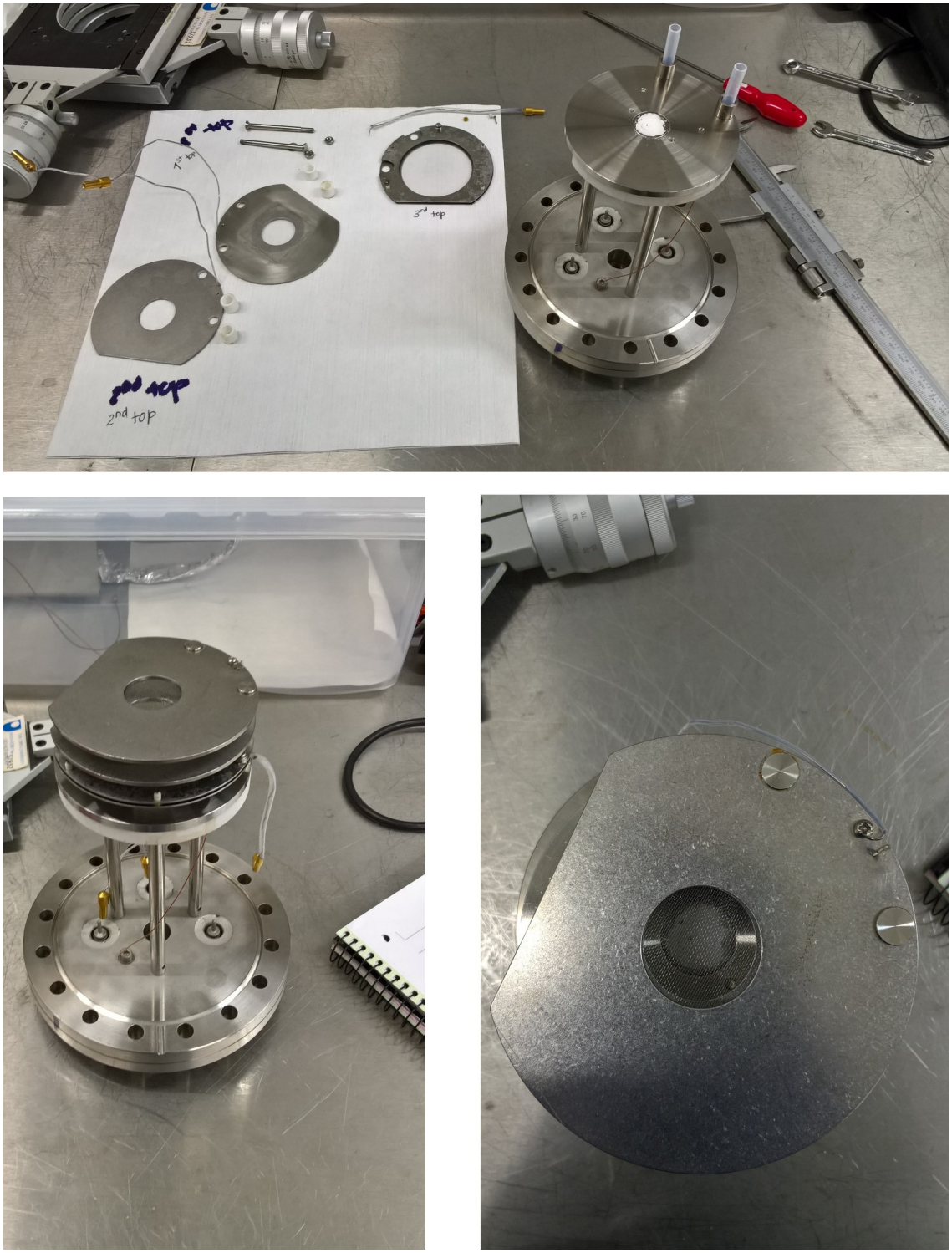

Figure 3.4: ILTD system. Top: disassembled 'TOF source' electrodes. A sample is visible on the stainless steel foil gripped by the backplate system. Bottom: the reassembled TOF source with the adhered sample layer on the foil, ready for installation in the Compact MPI-TOF experiment (ILTD mode).

systems in the Molecular Clusters Laboratory, the reader is referred to [106] and [84].

3.2.2.3 Experimental determination of foil surface temperatures in the OU ILTD system

To date, ILTD sources have been used in experiments on a range of biomolecules (mainly nucleobases and nucleosides) at Queens University Belfast (Greenwood and co-workers) [30, 31], Heriot Watt University (Townsend and co-workers) [32], and at the OU [32, 33]. The sources are all very similar in their essential design; the main differences are in the specifics of the foil mounting system (for example, the foil can be rotated in the most recent ILTD source at Heriot-Watt University in order to allow longer experiments between sample replenishments) and in the specific CW lasers used (small variations in wavelength, maximum power, spot dimensions, and focusing). The previous papers featuring ILTD all showed that a large proportion of the targets comprised intact molecules and none reported clear evidence for any thermal decomposition. Poully *et al.* [30] and Ghafur *et al.* [32] presented further experimental evidence to assess the possible presence of thermal decomposition products in the gas-phase target. The additional MPI measurements performed by Poully and co-workers show that mass spectra of thymidine and adenosine present the parent ion as the most intense feature, strongly suggesting that the molecules were desorbed intact from the foil. The MPI mass spectra of guanosine and cytidine also exhibited a strong signal for the parent ion, but the most intense features are guanine and protonated cytosine ions, respectively. Therefore, the authors could not rule out completely the thermal decomposition of the guanosine nucleoside. Ghafur demonstrated that the ratios of fragment ion / parent ion signals from photoionised uracil (a much less thermally-labile molecule than guanine or guanosine) were independent of the desorption laser power, which provides a strong indication that any thermal damage must be minimal. However, thermal decomposition is not the only process by which changing thermal desorption conditions can lead to changes in dissociative ionisation results. For example, changing the relative populations of different conformers and / or tautomers can also modify fragment ion production [33, 34, 35, 107]. Therefore, it is valuable to complement measurements of this kind with experiments or calculations to characterise of the desorption conditions. In line with the discussion in section 3.2.2, the most important parameters to characterise are the heating rate of the condensed sample and the temperature of the hottest part on the foil that is in contact with the condensed sample. To date, the only reported measurements to estimate foil temperatures in ILTD experiments were based on placing a thermocouple directly in a focused desorption laser beam in air [32]. These tests represent only a rough approximation of a functioning ILTD source and hence the uncertainties on the reported temperatures were large (±30 K). De Camillis [31] noted foil temperatures of ~423−523 K for their experiments on ILT-desorbed nucleosides but gave no details of how this range was estimated or measured. Therefore, we decided to carry out direct measurements of foil temperatures in an ILTD source. Later on in the chapter, these temperature measurements provide our strongest evidence for the lack of thermal decomposition in our ILTD targets of guanine and guanosine.

To all practical purposes, it is not possible to measure the foil temperature while the ILTD

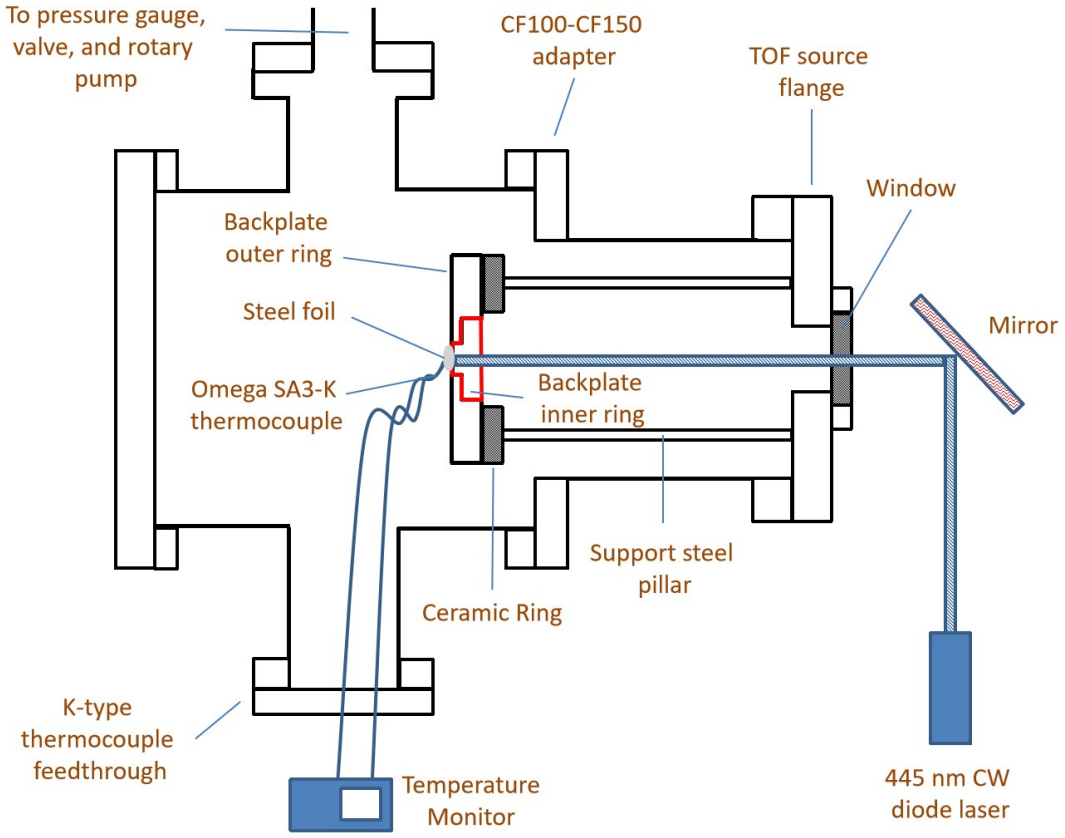

Figure 3.5: Setup used to measure the temperature of the foil in response to different *laser current* values, mirror angles, and chamber pressures.

system is in use to produce a gas-phase target. Therefore, this study was based on running experiments using the ILTD system mounted in a separate chamber. This allowed a thermocouple to be adhered to the part of the foil where a condensed sample would normally be.

The experiments involved measuring the temperature of the ILTD steel foil as a function of the CW laser parameters that are used in our MPI-TOF experiments. The setup is shown in Fig. 3.5. The 445 nm CW diode laser was shined onto a mirror whose angle could be adjusted finely in two dimensions. The reflected laser beam was thus directed through the window in the TOF source flange. The current delivered to the laser head can be varied from 0 to 1 A. This *laser current* is displayed on the controller and determines the laser power. The relationship between *laser current* and laser power was tested using a Gentec-EO power meter. The same meter was used to test the laser power loss due to the mirror and due to the window.

For convenient access to the foil, all the TOF source electrodes were removed except the *backplate* system that grips the foil (as shown in Fig. 3.4 but without a sample). The TOF source flange was connected to a cylindrical chamber which could be evacuated using a rotary vacuum pump. An Omega SA3−K thermocouple was adhered to the steel foil (using the SA3−K's integral adhesive tape) and connected to a temperature monitor outside of the chamber. After turning on the laser, its current was raised to 0.500 A. The mirror's angle was then adjusted until a rise of the foil's temperature was observed, indicating that the laser spot is hitting the foil. Then the mirror's

angle was fine-tuned until the maximum temperature was observed, corresponding to the laser spot being centred as close as possible to the thermocouple's position on the opposite side of the foil. When we use the simple term foil temperature in the rest of this chapter, we are referring to this maximum temperature. This was repeated at several different chamber positions to make sure that the maximum temperature for a specific *laser current* value was determined reliably. It is worth noting that the fine optimisation of the mirror typically raised the temperature by 25−30 K. This indicates a steep temperature gradient across the foil surface, which is consistent with our experience running MPI-TOF / ILTD experiments where moving the CW laser spot as little as 1 mm after a sample had been depleted was enough to recover the highest signal levels observed at a given *laser current*.

The Belfast [31] and Heriot-Watt [32] versions of ILTD used focused CW laser beams, as did some of the early ILTD experiments in the OU Molecular Clusters Lab. As mentioned above, our group abandoned using a focusing lens (which was inconvenient to mount in the space available) because it made no discernible difference to the MPI signal intensity [84]. Possible explanations for this observation include: (i) the maximum foil temperature on the sample side of the foil is not significantly affected by focusing or (ii) a larger hot area without focusing compensates for a lower maximum temperature. To test these ideas, we introduced a lens between the mirror and the chamber to focus the light on the foil. Naturally, this meant that a new fine optimisation of the mirror angle was required to measure the maximum temperature on the foil. The test was performed at a fairly low *laser current* (0.351 A) to minimise the possibility of the partially focused beam damaging the window. A maximum foil temperature of 369 K was obtained with the focusing lens compared with 373 K without it. We expect that the slightly lower temperature obtained with the lens can be explained by some combination of absorption / reflection by the lens and greater difficulty of aligning the smaller spot precisely opposite the thermocouple's position on the foil's reverse side (even though a long and careful mirror angle optimisation was performed). Therefore, we do not view the measured difference of 4 K as being significant. Our prevailing conclusion from this test is that focusing makes little difference to the foil temperature from which molecules are desorbed in ILTD in our setup and this must be related to the specific combination of the unfocused laser spot dimensions and the characteristics of the 10 μm-thick stainless-steel (SS304) foil used (notably 445 nm absorption, radiative emission, and thermal conductivity).

One important observation from the measurements was the rapid response of the measured temperature to a change in the *laser current*. For example, the measured temperature stabilised within a few seconds of turning the laser on with pre-set high laser current of 0.5 A. A similarly fast response was observed for turning off the laser. This result was expected since the foil system must have an extremely small thermal mass and it also suggests an excellent thermal contact with the thermocouple. Moreover, this rapid response is consistent with our observations in MPI-TOF / ILTD experiments. The MPI signal intensity changed and then stabilised within a few seconds of a change in the desorption *laser current* or the desorption laser alignment. Recall that we argue that rapid heating and stabilisation of the sample temperature in the ILTD system is one of the reasons why the method tends to cause less thermal decomposition than heating to an equivalent temperature in a standard oven system.

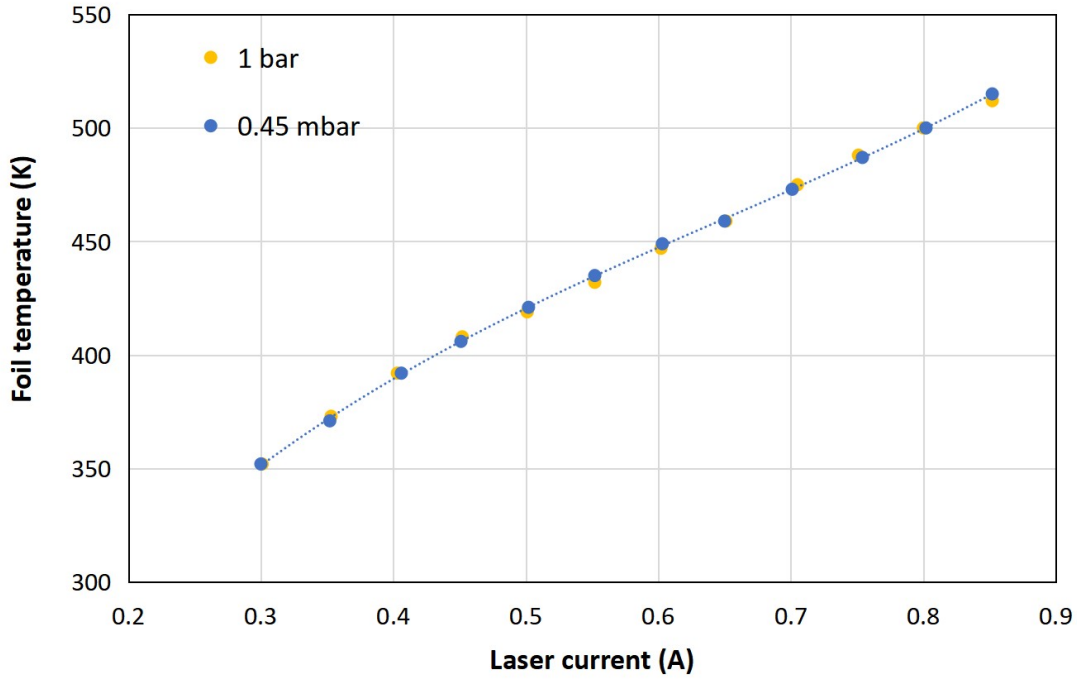

Figure 3.6: Foil temperature vs. *laser current* for two different pressure values. The foil temperatures correspond to the maximum that can be observed after a fine optimisation of the alignment mirror. A polynomial fit is shown for the low-pressure results. The uncertainties on the temperature values are estimated ±2 K, based on the maximum temperatures obtained for separate fine optimisations of the mirror angle. Error bars are not shown for ease of recognizing both data series in the figure.

The experiments described above were carried out without any pumping. The next goal of this set of experiments was to test if the temperature of the foil would change at air vs. under vacuum (for closer analogy with the MPI-TOF / ILTD experiments). Fig. 3.6 shows the thermocouple temperature (after a fine optimisation of the mirror to ensure that maximum temperature was measured) as a function of *laser current* at 1 bar and at 0.45 mbar (the lowest pressure obtained using the present rotary pumping system). The results clearly indicate that pressure does not modify the foil's temperature significantly while performing ILTD. However, the measured temperature decreased by up to 20 K while pumping down the vacuum chamber before returning to its original value once the pressure has stabilized. Hence a forced flow of gas across the foil that has a significant cooling effect, but convection in a gas with a constant measured pressure has negligible effect on the foil temperature.

Before we can use the present data to work out foil temperatures in the MPI-TOF / ILTD experiments, we need to convert the *laser current* into laser power. This is necessary in order to account for the power loss by the mirror in the present experiments, keeping in mind that the MPI-TOF / ILTD experiments did not feature a mirror between the laser head and the foil. A secondary reason for this conversion is to aid comparisons with ILTD applications in other labs

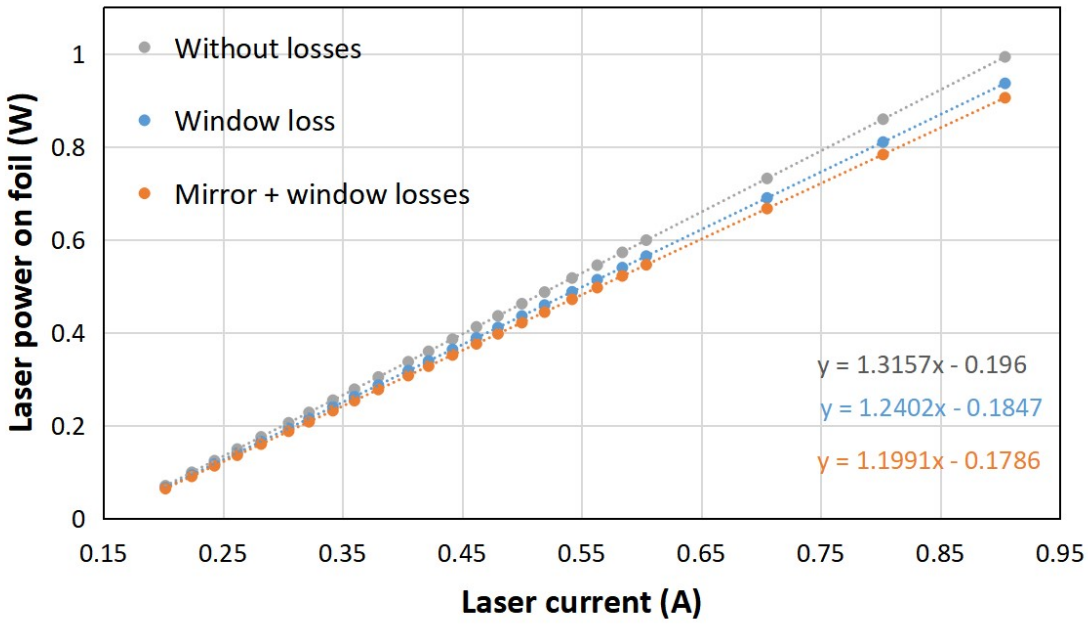

Figure 3.7: Laser power impinging on the foil as a function of laser current. The grey data set represents measurements without window or lens. The orange data set represents the mirror + window arrangement in the current measurements. The blue relation applies to power loss due to window only in the MPI-TOF / ILTD experiments.

(desorption laser power is usually provided in papers, whereas *laser current* is specific to our laser and its controller). The *laser current*–laser power measurements were performed by placing a power meter directly in front of the laser head and varying the *laser current* (grey data points in Fig. 3.7). The accuracy of the meter was confirmed by checking its response against that of separate newly-calibrated meter from a visiting laser engineer.

The next step was to determine the power loss due to the mirror, and also due to the window in the TOF source flange. These losses were determined by carrying out linear fits of the *laser current*-laser power data in Fig. 3.7). The calculation of the difference between the linear fits reveals an average loss of 5.74% due to the window and 3.12% due to the mirror. The formula for *laser current*-laser power conversion for the present experiments is shown in orange. The blue formula applies to the MPI-TOF / ILTD experiments where there is a power loss due to the window only.

Combining the results in Fig. 3.6 and Fig. 3.7 allows us to produce a plot of the foil's maximum temperature vs. the laser power. Fig. 3.8 shows a polynomial response of the foil's temperature to the laser power that impinges on the reverse side of the foil. A non-linear response is expected since the rate of heat loss by radiation and conduction depends on the temperature difference between the foil and its surroundings. Furthermore, the laser power–foil temperature relation is not linear because the emissivity and absorbance of a steel surface are temperature-dependent [108, 109, 110].

It is interesting to compare the present results with the earlier approximation of ILTD foil

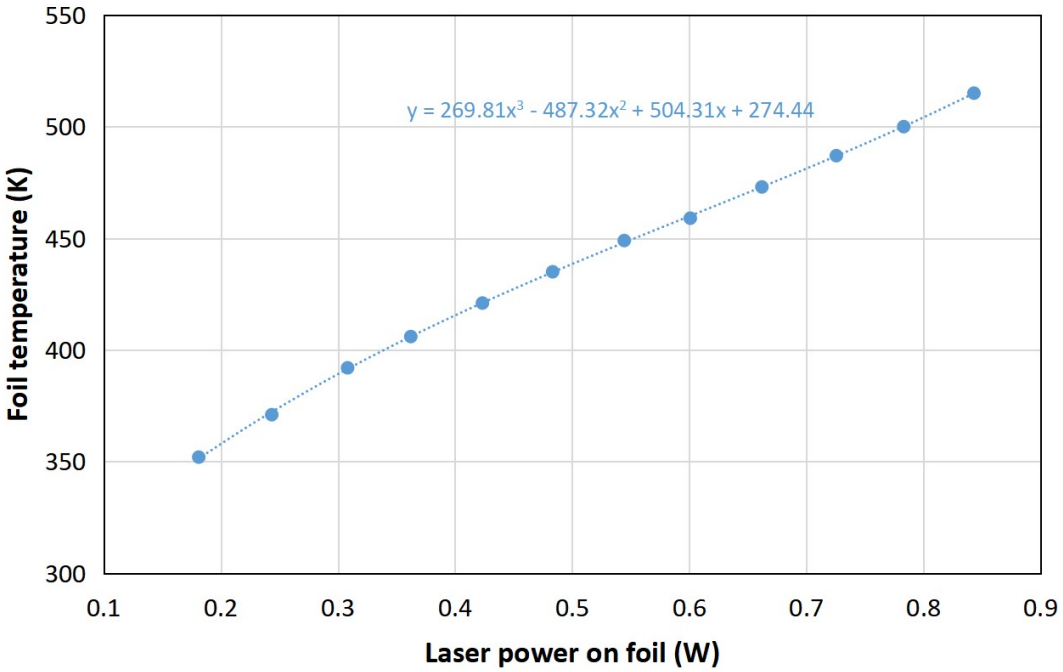

Figure 3.8: Maximum temperature on the foil vs. 445 nm laser power hitting the reverse side of the foil. The uncertainties on the temperature values are estimated ±2 K, based on the maximum temperatures obtained for separate fine optimisations of the mirror angle.

temperature based on focusing the CW laser beam directly on a thermocouple at Heriot Watt University [32]. At a laser power of 0.35 W, the *thermocouple-only* temperature was 424±30 K, whereas the present foil temperature determination is 403±2 K. Hence the results are in agreement to within the respective limits. As the foil allows conduction to the back plate and also presents a larger surface area for radiative emission, it is unsurprising that the *thermocouple-only* method tends to overestimate the temperature on the sample side of the foil during ILTD.

3.3 Guanine: MPI experiments and DFT calculations

3.3.1 General introduction

Guanine is the DNA / RNA nucleobase with the lowest vapour pressure [25] and has previously been reported as being difficult to bring into the gas with a sufficient target density for experimental studies without thermal decomposition [111]. Furthermore, guanine is unique among DNA / RNA bases in that it contains significant populations of various different tautomers [112], whereas the other four exist in just one or two dominant tautomeric forms in the gas-phase. The main purposes of the current section are to: (1) provide new insights into the fragmentation pathways of ionised guanine through metastable dissociation experiments (2) investigate possible tautomeric effects on fragment ion production. Such effects are plausible as distinct fragmentation pathways have previously been observed from keto and enol tautomers of several other molecules [34, 35, 107].

In section 3.3.2, we evaluate evidence for the presence or absence of thermal decomposition in

gas-phase guanine targets from a resistively-heated supersonic expansion nozzle and from an ILTD source. In section 3.3.3, we discuss changes in the relative fragment ion production observed in the prompt MPI-TOF mass spectra of guanine in terms of thermally-driven effects, notably possible changes in tautomer populations. Section 3.3.4 identifies metastable dissociation pathways of excited guanine$^+$ based on analysing MPI-TOF spectra as a function of the reflection voltage of our mass spectrometer. In addition, we complement the experimental results with reaction pathways on ionic states of the five lowest guanine tautomers, calculated at DFT level. Reaction pathways in ionic states of guanine have only previously been calculated for the lowest energy tautomer.

3.3.2 Thermal decomposition assessment of guanine targets vaporised in in a resistively-heated nozzle and in an ILTD source

Temperature onsets concerning thermal decomposition of guanine can be found in two studies in the literature. Wang and You obtained thermogravimetric curves exhibiting a steep step around 783 K involving a weight loss percentage of ~50% [113]. However, the authors did not specify the products of thermal decomposition. On the other hand, Lin *et al.* observed changes in the photoelectron spectra of guanine when heating the sample in a thermal oven above 613 K during 30 minutes, an indication of thermal decomposition [114]. Table 3.1 lists all the previous published experiments on neutral gas-phase guanine targets that we are aware of, highlighting the vaporisation method and any results/comments provided by the authors pertaining to potential thermal decomposition of the target.

Authors [reference] (year)	**Type of experiment**	**Vaporisation technique**	**Results pertaining to possible thermal decomposition shown directly**	**Authors' comments with respect to potential target decomposition or reactivity**
Rice *et al* [115] (1967)	EII including both prompt and metastable fragment ion production	Heating using a direct insertion probe (temperature not specified)	No	No comments.
Hush *et al* [116] (1975)	PeS	Heated sample probe (temperature not specified)	No	Authors argue that where thermal decomposition was suspected, the remaining material in the sample tubes was examined by mass spectrometry.

Authors [reference] (year)	**Type of experiment**	**Vaporisation technique**	**Results pertaining to possible thermal decomposition shown directly**	**Authors' comments with respect to potential target decomposition or reactivity**
Dougherty *et al* [117] (1977)	PeS	Heating (method not specified, 573 K)	No	No comments.
Dougherty *et al* [118] (1978)	PeS	Heated sample probe (temperature not specified)	No	Authors argue that samples were tested for signs of thermal decomposition such as change of colour, charring or time-dependence of a spectrum.
Lin *et al* [114] (1980)	PeS	Heated sample probe (613 K)	No	The authors observed changes in the spectra when heated the sample above 613 K (340 ºC) for more than 30 mins and assigned it to thermal decomposition.
Li *et al* [29] (1989)	MPI mass spectrometry	DLID coupled to supersonic expansion.	No	Authors argue that by adjusting desorption laser parameters, the fragmentation induced by the desorption laser can be controlled.
Nir *et al* [93] (1999)	REMPI spectroscopy	DLID coupled to supersonic expansion.	No	Authors argue that the wavelength dependence of fragments was essentially identical to parent ions which suggests that fragmentation was not a result of the desorption process.
Nir *et al* [119] (2001)	REMPI spectroscopy, SHB	DLID coupled to supersonic expansion.	No	No comments.

Authors [reference] (year)	**Type of experiment**	**Vaporisation technique**	**Results pertaining to possible thermal decomposition shown directly**	**Authors' comments with respect to potential target decomposition or reactivity**
Abdoul-Carime *et al* [120] (2005)	DEA	Heating in an effusive oven (500 K)	No	Authors argue that thermal decomposition was absent as the sample temperature was lower than in Lin *et al* experiments [114] (see above).
Choi *et al* [121] (2006)	IR spectroscopy	Heating in an oven (623 K) + seeding in He nanodroplets	No	Negligible thermal decomposition noted on the basis of the assignments presented in their work. Spectral signatures of potential decomposition products should be possible to spot, however these were absent.
Plekan *et al* [122] (2007)	SPI	Heating in a home-built furnace (643 K)	No	Authors argue that thermal decomposition was absent as the evaporation temperature was similar (20 K higher) to the one previously successfully used by Choi *et al* [121].
Zaytseva *et al* [123] (2009)	PeS	Heating in a home-built furnace (600 K)	No	Absence of thermal decomposition noted on the basis of photoionisation mass spectroscopy measurements.

Authors [reference] (year)	**Type of experiment**	**Vaporisation technique**	**Results pertaining to possible thermal decomposition shown directly**	**Authors' comments with respect to potential target decomposition or reactivity**
Zavilopulo *et al* [124] (2009)	EII	Heating in an effusive oven (420−640 K)	No	Absence of thermal decomposition noted on the basis of no increase in the intensity of H_2O^+ and CO_2^+ fragments (referring to a single mass spectrum at 610 K) and no change of the colour of guanine powder. Authors ascribe changes in the intensity of ion signals with increasing temperature to the vibrational excitation of molecules.
Zhou *et al* [125] (2009)	SPI	Heating in a supersonic expansion nozzle (573, 598 and 668 K), DLID (graphite matrix) coupled to supersonic expansion.	No	No comments.
Minaev *et al* [126] (2014)	EII, DEA	Heating in an effusive thermal multichannel source with a system of collimating slits (≤ 410 K).	No	Authors argue that temperatures ≤ 410 K are below thermolysis limit for guanine.
Ostroverkh *et al* [127] (2019)	EII	Heating in an effusive thermal multichannel source (410 − 630 K).	No	No comments on target decomposition or reactivity. Authors ascribe changes in the relative intensity of ion signals with increasing temperature to the vibrational excitation of molecules.

Authors [reference] (year)	**Type of experiment**	**Vaporisation technique**	**Results pertaining to possible thermal decomposition shown directly**	**Authors' comments with respect to potential target decomposition or reactivity**
AIST spectral database for organic compounds *et al* [128] (1999)	EII at 75 eV	Sample heated to 563 K with the source at 463 K. Authors do not specific the type of source used.	No	No comments by the authors.

Table 3.1: Literature review on volatilisation techniques and tests of target decomposition or reactivity in experiments on guanine. Adapted from [84].

Table 3.1 shows that the previous gas-phase experiments used conventional thermal vaporisation sources (variants of ovens or heated nozzles) or DLD sources. As discussed in section 3.2.2, the former are associated with a larger probability of inducing thermal damage to molecules than ILTD sources, whereas the later invariably produce a range of products in addition to the intact neutral molecule of interest. The conventional heating source papers provide the most useful comparators for ILTD. The sample temperatures ranged from 410 K to 640 K and three works reported having evidence (not shown directly in the papers) for the absence of thermal decomposition based on monitoring ion peaks associated with thermal decomposition products [114, 121, 125].

Our first attempt to study fragment ion production from guanine exploited the supersonic expansion source of the compact MPI-TOF experiment (Fig. 3.9 (a)). Guanine powder loaded in the cartridge was slowly heated (over several hours) and seeded in a supersonic expansion of helium (nozzle pressure 1 bar). MPI mass spectra were recorded at regular intervals as the nozzle temperature increased. Weak ion signals above the background level were began to be observed only at 604−607 K and the corresponding mass spectrum is shown in the top panel of Fig. 3.9. As discussed below, the mass spectrum contains evidence for thermal damage in the neutral target even at this threshold temperature. This led us to attempt guanine target production by ILTD.

A layer of guanine sample adsorbed in the ILTD foil was vaporised and then multi-photon ionised using 225 nm UV pulses with an average fluence of $7{\times}10^6$ W/cm^2. In line with studies using oven sources (see table 3.1), a valuable tool to look for possible evidence for thermal decomposition of a target molecule produced by an ILTD source is to monitor relative fragment ion yields as a function of desorption temperature (itself a function of the CW laser power) [32]. Variation in the relative fragment ion production is observed as a function of the desorption laser power (and hence temperature) may indicate a thermal decomposition of the sample. The relative measurements are necessary due to the temporal depletion of the sample, which leads to a non-constant target density over time. We acquired mass spectra at desorption laser powers ranging from 0.34

W (the threshold for detecting a signal with satisfactory statistics) to 0.81 W. The power was progressively increased between measurements. In the last two acquisitions, the power was decreased from 0.81 W to 0.55 W and then to 0.51 W. Each mass spectrum comprises 1500 ionising pulses at 10 Hz. An example of an MPI-TOF mass spectrum obtained with the ILTD source at a low desorption power (0.36 W, foil temperature 404 K) is shown in the bottom panel of Fig. 3.9.

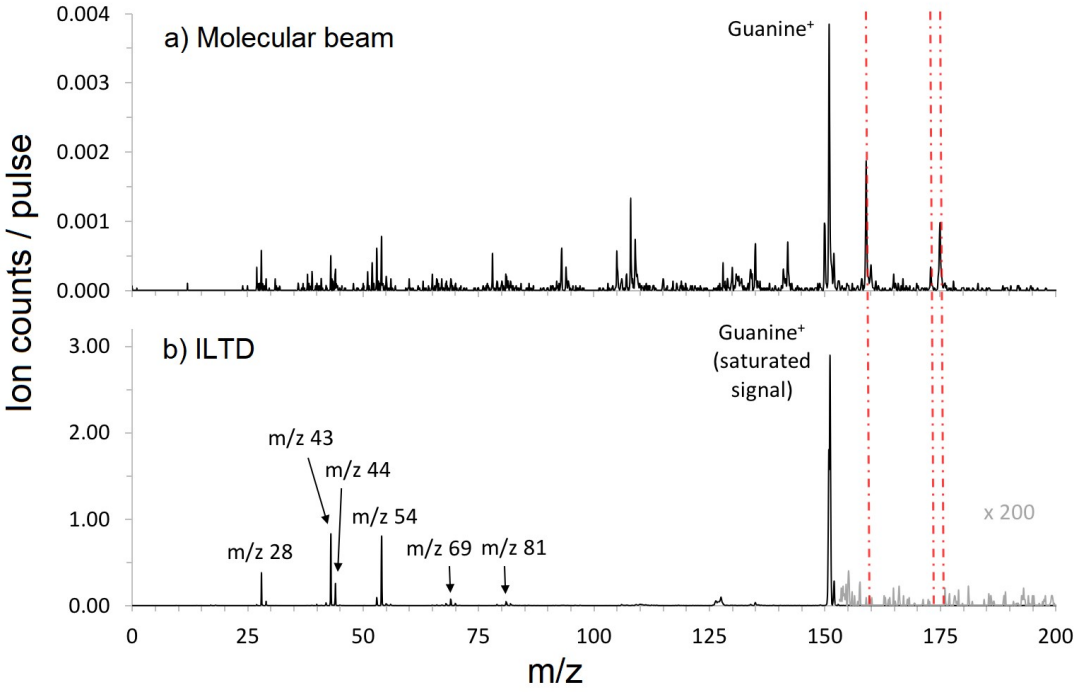

Figure 3.9: Comparison of two 225 nm MPI-TOF mass spectra of guanine produced by a) heating the sample in a nozzle and seeding the vaporised molecules in helium to produce a molecular beam (MPI with UV average laser pulses of 5×10^7 W/cm^2) b) indirect laser-induced thermal desorption (ILTD) using 0.36 W (foil temperature 404 K) of a 445 nm CW laser (MPI with UV average laser pulses of 7×10^6 W/cm^2). Red dash-dotted lines indicate the presence of thermal reactivity products in the molecular beam and their absence in the ILTD experiments. Figure adapted from [84].

An intense feature associated with the parent ion is visible in both TOF-MPI mass spectra in Fig. 3.9: both sources are able to generate intact guanine targets. However, fragment ions with m/z above the parent ion are visible in the molecular beam mass spectrum as well as numerous small fragment ions. The ions with m/z above the parent are not likely to derive from clusters. In fact, the mass spectra of clusters containing other nucleobases generally show a prominent feature for the protonated nucleobase ion signal, which is absent in the molecular beam mass spectrum [129, 130]. Furthermore, strong m/z = 142/141, 105, 94/93 and 78 ion signals are visible in our molecular beam mass spectrum but are very weak or absent in the AIST EII mass spectrum [128]. These observations strongly suggest thermal decomposition/reactivity of the sample in the thermal oven. We visually inspected the guanine sample on the cartridge after the supersonic beam experiments and noticed a discolouration of the sample, suggesting a permanent degradation (note that efficient sample removal from the heated spots on the thin condensed layer prevents an equivalent analysis

in ILTD). It is important to note some further differences between the experiments. Firstly, while we could only obtain signals—containing partially-decomposed guanine—after heating the sample above 600 K in the molecular beam experiments, much lower foil temperatures (399 K for a desorption laser power of 0.34 W) were sufficient for the ILTD experiments. This temperature is distinctly below any temperature (minimum 410 K) that was previously used to produce gas-phase guanine targets from ovens (see table 3.1), including in papers that claim evidence for the absence of thermal decomposition. As ILTD is more suitable for avoiding thermal decomposition than heating in oven sources at a given desorption temperature (see arguments in section 3.2.2.1), the low foil temperature in the present experiments provides the most compelling evidence for the absence of thermal decomposition in our ILTD target. Secondly, the ILTD mass spectrum in Fig. 3.9 contains no peaks that are not also clearly observed in the previous mass spectra of the molecule (e.g. in the AIST EII mass spectrum [128]). This is suggestive of no significant thermal decomposition but is not a proof because some possible neutral products (e.g. H_2O) cannot be multi-photon ionised in our UV laser conditions. Thirdly, the signal intensity in the lower plot in Fig. 3.9 is very high, particularly when we consider that the desorption laser power (0.36 W) is only slightly above the threshold where we started to see reasonable MPI signals. Indeed, it is three order of magnitude larger than the supersonic beam measurement. This indicates that ILTD is an excellent method for producing gas-phase guanine targets—not only is thermal decomposition avoided but also the target density is high. This provides excellent opportunities for studying processes that typically provide weak signals, for example metastable dissociation of excited ions in section 3.3.4. We now evaluate relative fragment ion production as a function of the desorption laser power (and hence temperature) to look for possible evidence of thermal damage at higher desorption laser powers and/or any other thermal effects.

Two mass spectra measured at different desorption powers are shown in Fig. 3.10. The fragment ions were previously assigned in EII and SPI mass spectra of guanine and are discussed in more detail in section 3.3.3. It is possible to observe a distinct enhancement of the metastable fragment ion bands at non-integer values of m/z in range 125−130 compared with the neighbouring prompt ion peaks (e.g. m/z 135) after increasing the laser power to 0.81 W. Production of the most prominent fragment ions in the guanine mass spectra relative to the m/z = 43 fragment ion ($H_3CN_2^+$ / $HCNO^+$) is shown in Fig. 3.11. We chose the m/z = 43 for reference due to saturation of the guanine$^+$ signal in the mass spectra. The ratios are only presented up to a desorption laser power of 0.55 W (foil temperature 449 K) because above this our mass spectra showed evidence for partial saturation of the m/z 43 peak. In this range, we see no clear evidence for changes in the relative production of these fragment ions due to thermal effects (e.g. thermal decomposition or changes in tautomeric populations). With regards to possible thermal decomposition, we also note the following points. Firstly, the temperature on the foil at the highest desorption laser power that we applied in our guanine experiments (0.81 W) was 506 K. This is is much lower than decomposition temperatures reported in the literature concerning vaporisation of guanine in thermal ovens (613 K [114] and 783 K [113]). It is also comfortably within the range of oven temperatures which previous groups have used for guanine, apparently without evidence for thermal decomposition (410 − 640 K). Secondly, After gradually reducing the desorption laser power from 0.81 W to

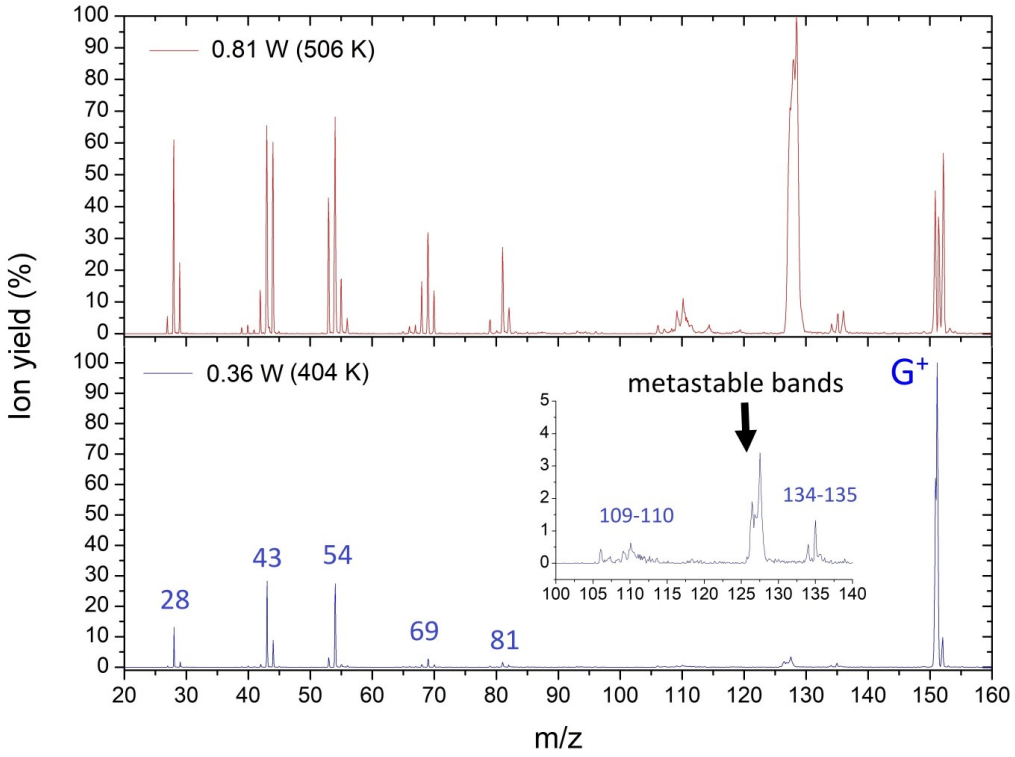

Figure 3.10: Two guanine MPI mass spectra acquired at different desorption powers: blue solid line, 0.36 W (foil temperature 404 K); red solid line, 0.81 W (foil temperature 506K). The gas phase molecules were ionised by 225 nm photons with a fluence of $7{\times}10^6$ W/cm^2. The guanine+ peak is partially saturated in both mass spectra, as are the strongest fragment ion peaks (notably m/z 43 and 54) in the 0.81 W result.

0.51 W, it is possible to recover the initial relative production of fragment ions (the open symbols in Fig. 3.11). This suggests that the adsorbed sample was not permanently modified by high temperatures.

As noted above, manifestation of thermal effects is not restricted to thermal decomposition of the sample. In particular, changes in relative populations of conformers and tautomers are dependent on the target temperatures as well. In this context, the absence of any clear thermal dependence in the fragment ion ratios in Fig. 3.11 could be interpreted in two ways:

1. The relative populations of tautomers / conformers in our gas phase target did not change significantly between foil temperatures of 399 K and 449 K.

2. The relative populations of tautomers / conformers did change in this foil temperature range but the specific structures involved show similar relative production of guanine's main fragment ions.

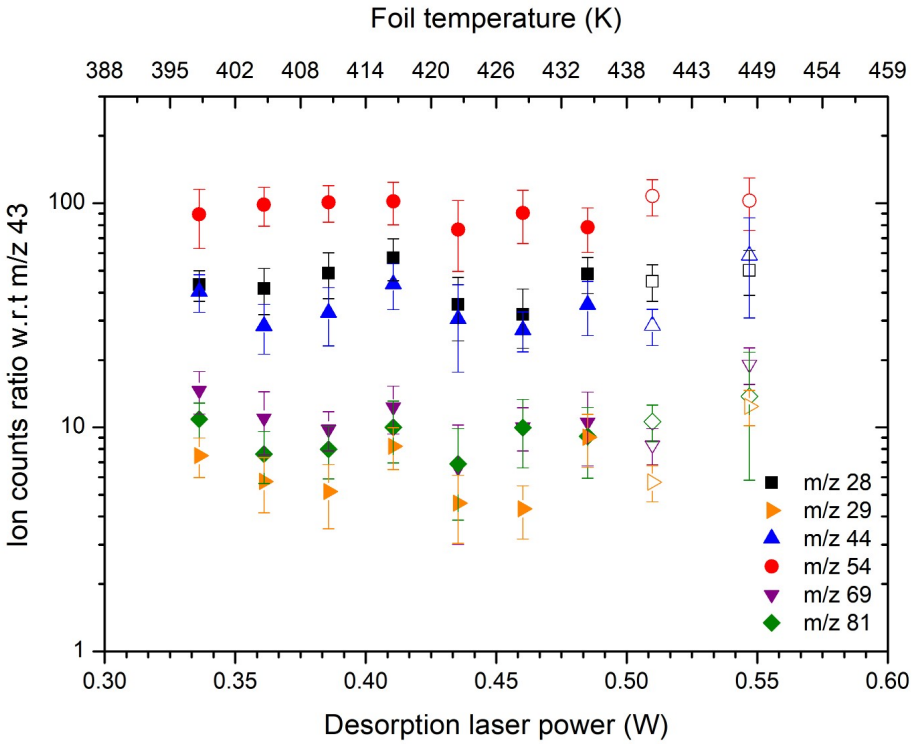

Figure 3.11: Ratio of fragment ion signals relative to the $H_3CN_2^+$ / $HCNO^+$ (m/z = 43) fragment ion signal. Open symbols represent the measurement performed after using the highest desorption power 0.81 W.

To help answer which of these scenarios is most likely to apply to the present experiments, the next section discusses possible changes in the equilibria of guanine tautomers and conformers.

3.3.3 Gas-phase tautomers/conformers of guanine and tautomeric effects on prompt fragment ion production

Guanine possess four labile hydrogens that can bind to seven electronegative sites, making it the DNA / RNA nucleobase with largest number of tautomers in the gas phase [125]. Fig. 3.12 shows schematic diagrams of the different tautomers and conformers reported in the literature, while table 3.2 gives their relative energies. The lowest energy forms predicted by simulations are the keto-N9/7H-amino and enol-N9H-amino structures, although their order depends on the level of theory. Nir and co-workers have produced guanine molecular beams by direct laser desorption of the sample from a graphite substrate using the fundamental harmonic of a Nd:YAG laser, and seeding the molecules in an argon carrier gas [93]. A large number of bands were present in the REMPI spectrum indicating the presence of multiple tautomers. Attempts to identify them using similar desorption conditions were carried by Nir's [119, 131] and Mons' [132] groups employing REMPI and IR-UV hole burning spectroscopy. Both groups identified the presence of keto-N9H, keto-N7H, enol-N9H and enol-N7H tautomers. Later, Choi and Miller compared experimental vibrational transition moment angles (VTMA) of guanine molecules vaporised in an

Tautomer	**Relative energies (meV)**		
	Marian[a]	Zhou *et al.*[b]	Nir *et al.*[c]
1. keto-N9H-amino	58	15	0
2. keto-N7H-amino	0	0	10
3. enol(trans)-N9H-amino	57	98	41
4. enol(cis)-N9H-amino	49	70	73
5. enol(trans)-N7H-amino	121	190	187
6. keto-N7H-imino(trans)	259	256	–
7. keto-N7H-imino(cis)	281	267	–
8. keto-N3H-N7H-amino	298	276	–

Table 3.2: Relative energies of different guanine tautomers. [a]:Obtained at (DFT/MRCI)//B3LYP/TZVP level; [b]: Obtained at B3LYP/6-311++G(d,p) level; [c]: Obtained at MP2/6−311G(d,p) level.

oven and seeded in helium nanodroplets with simulated VTMAs [121]. The authors identified the presence of tautomers $1-4$ (table 3.2) of guanine in the beam. Inconsistencies among the three sets of results were attributed to the presence of 'rare' keto-N7H-imino tautomers in the experiments employing DLD sources. The reasoning that different types of vaporisation sources could affect the tautomeric equilibrium of guanine was further studied and confirmed by Zhou and co-workers [125]. These authors observed a smooth onset around 7.75 eV for the VUV photo-ionisation efficiency (PIE) curves of guanine when vaporised in a thermal oven and a steep onset around 8.2 eV when produced by a DLD source. The lowest energy tautomers of guanine ($1-5$) have AIEs in the range $7.68-7.80$ eV, matching the onset of the PIE curve associated with tautomers produced in the thermal oven. The onset of the PIE curve for tautomers vaporised by the DLD source is associated with the more energetic tautomers $6-8$, whose calculated AIEs are in the range $8.04-8.17$ eV. Tautomeric population may in fact depend not only on the vaporisation method but also on the temperature of the source as mentioned by Choi and Miller [121] and Allegretti and co-workers [34, 107]. However, there are no evidences for such changes in tautomeric populations of gas-phase guanine.

As experimentally shown for selected aldehydes and thioaldehydes by Allegretti and co-workers, mass spectral fragmentation are expected to be tautomer specific with certain ion ratios correlating to the keto and enol populations [34, 107]. Zamir *et al* observed a dependence of the relative fragment ion intensities of β-diketones (acetylcetone, 3-methylacetone, and 3-allyl acetylacetone) on the temperature of the inlet system [35]. For guanine, changes in the tautomeric equilibria with the desorption laser power (foil temperature) are also plausible. Indeed, semi-empirical MD simulations of electron impact ionised tautomers of guanine, permitted Bauer and Grimme to predict an enhanced yield of $H_3CN_2^+$/$HCNO^+$ (m/z = 43) fragment ions from keto tautomers [36]. Therefore, Fig. 3.11 suggests that the relative population of keto / enol tautomers did not change significantly in the present range of ILTD foil temperatures.

A variety of mass spectrometry studies concerning the radiation response of guanine to high energy electrons [115, 126, 127] and photons [122] can be found in the literature. In comparison with EII mass spectra, our MPI data (Fig. 3.10) do not exhibit any new intense feature. In this

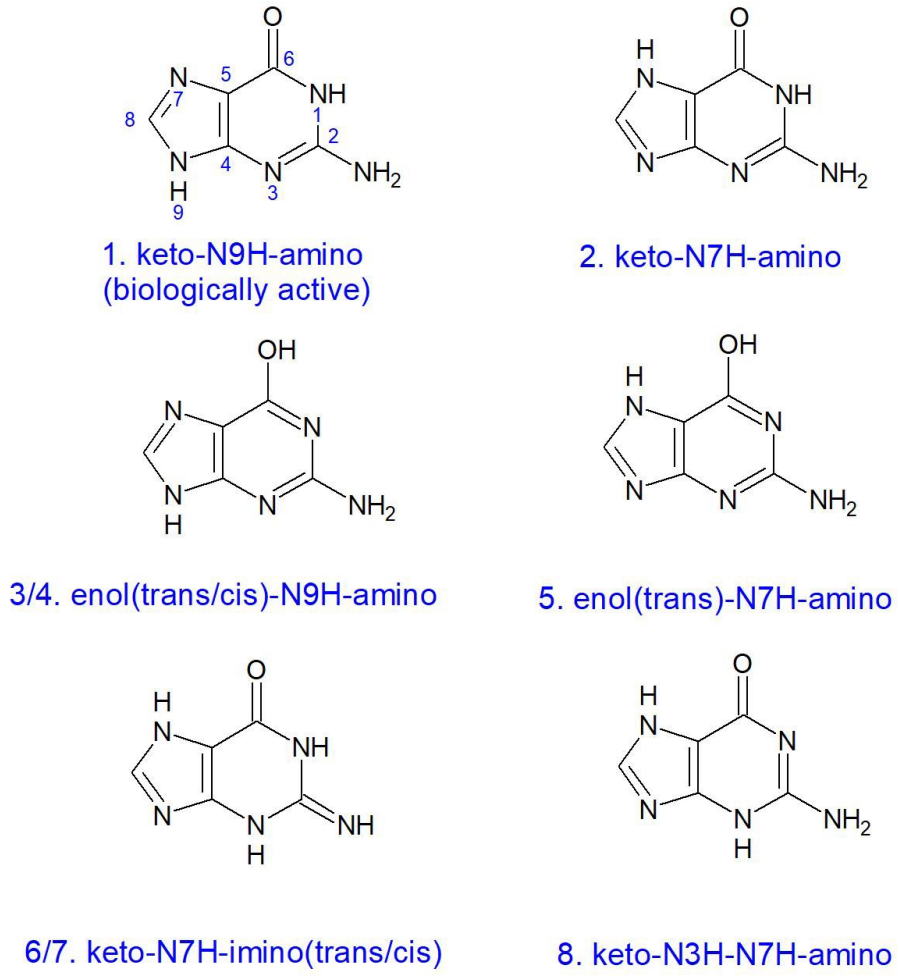

Figure 3.12: Structures and atom labelling of the guanine tautomers / conformers reported in the literature [115].

respect, dynamics in neutral excited states seems not to affect the overall fragmentation pattern of guanine (in contrast with uracil where a new channel was exclusively associated to neutral excited state dynamics [42]). Several authors examined theoretically the topology and dynamics of the PECs associated with the lowest lying singlet neutral excited states (the two $\pi\pi^*$ transitions and the $n\pi^*$ transition) of keto-N9H-amino and keto-N7H-amino tautomers of guanine. Based on the results, the authors expect an ultrafast non-radiative decay to the electronic GS of these structures (within the first hundreds of fs) involving a deformation of the ring [112, 133, 134]. Experimental evidence supporting this ultrafast decay is provided by the absence of features associated with these forms in the UV REMPI spectrum in the nanosecond regime [135]. The enol(*trans*)-N9H tautomer (third in table 3.2) may follow a similar deactivation [135, 136].

Fragment ion ratios obtained in previous EII studies and in our MPI-TOF mass spectra are gathered in table 3.5. Clearly, we have to be cautious in drawing comparisons of relative signal intensities obtained from experiments using mass spectrometers with different (and unknown) acceptance characteristics. Nonetheless, it is worth commenting that the fragment ion ratios in Minaev *et al.'s* and Zavilopulo *et al.'s* EII experiments are broadly similar to each other, despite the

m/z	EII				MPI
	Minaev	Rice	Zavilopulo	AIST database	This work
	410 K	– K	610 K	563 K	399 – 449 K
27, HCN^+	24.2	36.8	22.8	21.7	1.6 ± 0.5
28, H_2CN^+	70.0	87.7	58.6	56.8	44.1 ± 7.9
29, H_3CN^+/COH^+	11.4	7.0	24.1	7.0	5.7 ± 1.7
43, $H_3CN_2^+$/HCNO	100	100	100	100	100
44, $H_4CN_2^+$/H_2NCO^+	51.5	78.9	33.5	31.1	31.5 ± 6.0
53, $HC_2N_2^+$	36.4	37.6	43.3	36.1	12.7 ± 6.6
54, $H_2C_2N_2^+$	60.6	59.6	60.9	57.2	94.5 ± 11.5
55, $H_3C_2N_2^+$	17.5	17.1	20.0	13.4	7.5 ± 3.8
68, $H_2C_2N_3^+$	20.2	13.7	16.7	11.4	3.7 ± 1.0
69, $H_3C_2N_3^+$	24.2	28.1	28.3	23.4	10.3 ± 2.4
70, $H_4C_2N_3^+$	10.8	6.8	11 .7	6.4	3.4 ± 1.1
81, $H_3C_3N_3^+$	24.2	19.3	27.7	23.1	9.5 ± 1.5
82, $H_4C_3N_3^+$	13.5	10.3	10.0	11.7	3.8 ± 1.3
106, $H_2C_4N_4^+$	8.1	6.8	8.3	9.7	2.7 ± 3.0
109, $[G–H_2CN_2/CNO]^+$	63.6	36.8	69.2	63.5	3.8 ± 0.8
110, $[G–HCN_2]^+$	52.7	33.3	83.3	61.9	7.1 ± 1.8
134, $[G–NH_3/OH]^+$	27.3	29.8	31.5	29.4	2.7 ± 1.0
135, $[G–NH_2/O]^+$	23.3	15.3	25.0	18.0	5.9 ± 1.4

Table 3.3: Percentage of fragment ion signal relative to fragment ion m/z=43 obtained from EII mass spectrometry studies employing different vaporization methodologies: **Minaev** [126]: Effusive thermal source at 410 K; **Rice** [115]: Thermal heating (the temperature is not specified); **Zavilopulo** [127]: Effusive thermal source at 610 K; **This work**: ILTD source at different laser powers (temperatures of the foil). The assignment of fragment ions follows previous assignments in the literature [124, 126, 137].

quite large oven temperature difference. As with ratios in the present MPI experiments (Fig. 3.11), this suggests that the relative populations of key tautomers do not change significantly across this temperature range. Secondly, with the exception of m/z 54 signal, the present MPI results show lower production of all fragment ions relative to the m/z 43 peak than was observed in EII. As m/z 43 fragment ion production is expected to dominate from keto tautomers [36], this could suggest preferential MPI of these tautomers in the present experiments. This could indicate longer excited state lifetimes, improved FC factors for photon absorption stages, and / or lower ionisation thresholds or larger populations of the keto tautomers in the target compared with the enol tautomers. The first two are unlikely since upon excitation to the first neutral electronic excited state, enol tautomers do not distort its geometry to reach a conical intersection with the electronic ground state [112]: their excited state lifetimes are expected to be longer, and the FC factors larger than those of keto tautomers.

3.3.4 Metastable fragmentation of guanine

The observation of fragment ions in Fig. 3.10 at non integer m/z values is an indicator of near threshold mechanisms resulting in metastable (or delayed) fragmentation. Metastable fragmentation reflects a slow kinematic process as briefly discussed in section 2.3.3. Mass spectrometry studies of metastable fragmentation are extremely valuable to elucidate the dissociation pathways of excited ions because it can allow ion mass to be defined both before and after dissociation. Metastable dissociation experiments can also provide information on fragment ion energetics, as the microsecond-order time delay implies that the vibrational energy of the precursor ion was very close to the relevant dissociation barrier [138]. The internal energy of the precursor ion is redistributed among the internal degrees of freedom and some part is released as kinetic energy upon fragmentation, resulting in a broadening of the correspondent ion signals.

Only one previous experimental study [115] has analysed metastable dissociation of guanine ions. The exceptionally high signal / noise ratios in the present MPI-TOF experiments on ILT-desorbed guanine enabled us to reveal 13 metastable dissociation pathways of the molecules for the first time, as well confirming three that were previously reported. Metastable dissociation experiments are particularly interesting with regards to guanine because previous works on different molecules have revealed distinct fragmentation patterns of different isomers [139]. Hence a key motivation of the present metastable dissociation study of multi-photon ionised guanine is to look for evidence indicating tautomer / conformer dependent fragmentation of guanine. This work is complemented with DFT calculations exploring the tautomeric dependence of two prominent fragmentations observed in the experiments: HCN loss and HNCO loss from guanine$^+$.

In section 3.3.4.1, we briefly explain the technique that we apply to identify precursor ions and product ions of metastable dissociations in our reflectron-TOF mass spectrometer. Section 3.3.4.2 then explains the method we used to obtain kinetic energy release (KER) data from the metastable peaks in our TOF spectra. Section 3.3.4.3 presents our ion detection data as a function of flight-time and reflection voltage in order to identify specific dissociations of guanine$^+$ as well as specific dissociations of excited fragment ions (sequential fragmentation pathways). The results are discussed in the context of KER analysis of fragment ions peaks and DFT calculations.

3.3.4.1 Identifying fragmentation pathways using a reflectron-TOF mass spectrometer

A range of techniques have been employed previously to study metastable dissociation of excited ions, including double-focusing sector-field [140, 141], modified linear [141, 142], and reflectron [143, 144] time-of-flight (TOF) mass spectrometry, as well as the post-source decay mode of matrix-assisted laser desorption/ionisation mass spectrometry [145]. The present experiments involved measuring MPI-TOF spectra of guanine at a series different reflection voltages. A map comprising all the TOF spectra (with ion flight-time on the x-axis, reflection voltage on the y-axis, and signal intensity colour-coded) was then compared with simulated flight-times, enabling specific metastable dissociations to be identified. The concept of plotting ion flight-time (or a related parameter such as the apparent mass of a metastable peak in a conventional mass spectrum) against

reflection voltage was first reported by Gilmore and Seah [146] and has since been applied to a number of different molecular and cluster targets [19, 138, 143, 147, 148, 149].

For a full description of our variant of Gilmore and Seah's method is provided in the PhD theses of Rahul Pandey and Jana Bockova [84, 106]. Briefly, the method exploits the fact that a fragment ion produced by a dissociation in the field-free region of the mass spectrometer (FFR in Fig. 3.1 (b)) will have lower kinetic energy than its precursor ion. In the present experiments, the time window that ions spend in the FFR is of the order of several tenths of a microsecond to a few ten of microseconds after the laser pulse. The velocity of such a fragment ion in the FFR will be close to that of the precursor ion (modified only by KER) but its mass will of course be reduced. Therefore, it can be reflected by a weaker field than an ion that was produced by a prompt dissociation (defined here as ≤100 ns after ionisation). It follows that an ion produced by a dissociation in the FFR will penetrates less far into the reflectron part of the mass spectrometer than a *prompt ion* would for a given reflectron voltage. If we progressively modify the reflection voltage to more negative voltages (getting closer to the FFR voltage), eventually the field in the reflectron will not be sufficient to reflect a prompt ion back towards the detector and the signal associated with that ion channel will fall to zero. We call this reflection voltage the 'cut-off voltage' and for prompt ions it is equal to the difference between the FFR voltage and the voltage at the position in space where the ionisation took place. This means that measuring the cut-off voltage for prompt ions can be used to determine the crossing point of the ionising laser beam with the ILTD plume. At more negative reflection voltages than the cut-off voltage for prompt ions, the only signals in the TOF mass spectrum will correspond to metastable dissociations. In most cases, it is not possible to identify the poorly resolved TOF features associated with delayed fragmentation events while precursor ions are accelerating towards the FFR. However, all dissociations inside the FFR with a given precursor ion mass and given product ion mass are grouped together to form a distinct peak in the TOF spectrum. The flight-time dependence of such a *metastable peak* on the reflection voltage (up to the metastable channel's own distinctive cut-off voltage) then corresponds to a unique combination of precursor ion mass and product ion mass.

My colleague Jana Bockova developed a simulation in Matlab to identify metastable dissociations visible in our experimental *maps* with ion flight-time on the x-axis, reflection voltage on the y-axis, and signal intensity colour-coded [84]. The initial inputs are the distances within the mass spectrometer, the electrode voltages (except for the reflection voltage), and the crossing position of the laser beam with the molecular beam (determined by measuring the cut-off voltage for prompt ions as described above). The next step is to input one or more *candidate dissociations* (specific combinations of precursor and product ion masses) that might take place in the FFR. The program then generates a map of flight-time against reflection voltage that can be overlaid onto an experimental map. Different candidate dissociations are tested iteratively until a good match is achieved between the simulated and experimental maps. The accuracy of the simulation is checked by calculating the flight times of ions traced to *prompt* dissociations. The simulated flight-times agree with the experimental TOF spectra to within 1%.

3.3.4.2 Determining KER of ions produced by metastable dissociation in a reflectron-TOF mass spectrometer

The analysis of kinetic energy release (KER) of metastable ions is normally done in double sectors or time-of-flight mass spectrometers. In double sectors, the parent ions are first velocity selected by a magnetic sector. The KER distribution of metastable ions involves the variation of the potential difference of the electrostatic analyser [150]. In time-of-flight mass spectrometers, there are two different approaches depending on the type of the mass spectrometer. Linear time-of-flights do not correct for the kinetic energy broadening. Therefore, having accounted for the velocity spread due to the thermal energy and discrimination factors, the KER information can be directly extracted from the ion peak height and width. The simplicity of the procedure is counterbalanced by the restriction that only fragmentations in the acceleration region can be investigated. In other words, metastable fragmentations occurring in the FFR can not be assessed with linear time-of-flights since precursor ions and daughter ions that dissociate in the FFR have the same velocity. This leads to precursor and daughter ions having the same time-of-flight, and the respective features cannot be distinguished in the mass spectrum. Reflectron time-of-flights, on the other hand, permit the investigation of KER in metastable fragmentations in the FFR. As precursor ions and daughter ions fragmenting in the FFR ions have the same velocity, the kinetic energy is larger for the former. Since the penetration depth in the reflectron is proportional to the kinetic energy, parent ions spend more time in this stage than the daughter ions, and two distinguishable features are recorded in the mass spectrum. The extended range of rate constants that can be measured in reflectron time-of-flight mass spectrometers make them ideal to study near threshold dissociations. However, the reflection stage inherently corrects for energy spread of the ions, changing the KER information contained in the ion signal. Laborious ion flight trajectory simulations in reflectrons are routinely adopted to simulate peak shapes in the mass spectrum and extract complete KER distributions. A simpler approach to estimate the mean KER of metastable ions was advanced by Castleman *et al.* in their investigation concerning metastable decomposition of ammonia clusters [151]. The method consists in acquiring two mass spectra where the precursor and metastable ions have the same time-of-flight in the reflectron stage (and consequently, the same time-of-flight). For that, the reflection voltage is tuned in between the measurements. The rationale behind such idea lies on the fact that the daughter ion inherits the initial kinetic energy broadening of the precursor ion. In order to correct it in the exact same way for both ions while keeping the KER information in the daughter ion signal, the time-of-flight has to be the same in the reflectron component. The mean KER, $\langle KER \rangle$, is calculated using parent ion and daughter ion peaks according to [151]

$$\langle KER \rangle = \frac{1}{\langle L^2 \rangle} (qV_{FFR}W)^2 \left(\frac{M_d}{2M_pM_n} \right) \tag{3.1}$$

where $\langle L^2 \rangle$ is the the mean of squared distance travelled by the daughter ion in the FFR, V_{FFR} is the FFR potential, $W = \sqrt{W_d^2 - W_p^2}$ is the width of the daughter ion peak corrected for the initial spread of kinetic energy of the parent [152], M_d, M_p and M_n are the masses of daughter ion, parent ion and neutral fragment, respectively. Estimation of $\langle L^2 \rangle$ requires the derivation of the average

unimolecular dissociation rate constant (k) from the signal intensities of the parent and daughter ions in the mass spectra. The complete set of equations is described in Castleman work [151]. An important aspect that needs to be commented is the control of deposited internal energy on the initial parent ion. Normally, this is achieved by performing photoion-photoelectron coincident (PIPECO) measurements, where detached electrons with a specific kinetic energy trigger the ion mass spectrum acquisition. Such fine control is not possible in the current measurements, and the multi-photon ionised parent ions are generated with a range of internal energies, although with a tighter control than in EII experiments with electron energies significantly above the relevant ionisation thresholds.

3.3.4.3 Results and discussion

In Fig. 3.13 we present MPI-TOF spectra of guanine acquired at a series of reflection voltages, in the form of a map. The reflection voltage was varied in steps of 20 V, from -100 to -700 V. Guanine was desorbed from the foil with a laser power of 0.36 W (404 K) and multi-photon ionised using 225 nm pulses with average fluence $7{\times}10^6$ W/cm^2. Band assignments were made based on the Matlab code described in section 3.3.4.1. The bands with cut-off voltages at -130 V correspond to the undissociated guanine ion and prompt fragment ions. We were able to distinguish 16 different metastable dissociation bands, and signal-to-noise ratios on 10 of these were sufficient to enable precursor and product ion assignments to single-mass-unit precision. In Fig. 3.14 we present the sum of mass spectra at G = -340 V where it is possible to observe some of the very weak metastable bands that are excluded / filtered by the thresholds applied in the 2D coloured map. The bands are listed with assignments in table 3.4 and compared with the metastable fragmentation channels identified in Rice's EII results [115].

Considering the results of the present and previous experiments together (table A.1) yields a striking observation. A total of 10 different bands feature guanine$^+$ as the precursor ion of the metastable dissociation (we can call this a direct metastable dissociation channel of guanine$^+$). This compares with just one *direct* metastable dissociation channel of adenine, uracil, and thymine in Rice's experiments [115, 140] and in previous experiments in our lab [138]. Gas-phase adenine, uracil, and thymine targets are similar in that only one structural form is present with significant a population [153]. Hence the most obvious way to understand the remarkably high number of different direct dissociations of guanine$^+$ compared with the other nucleobases is to link this result to the high number of different tautomers / conformers in neutral gas-phase targets. Indeed, this argument is consistent with recent theoretical predictions of tautomer-dependence in the dissociation pathways of guanine$^+$ [36].

Three of the seven metastable dissociation channels identified in Rice's experiments match ones observed in our MPI-TOF mass spectra [115]. The absence of Rice's other four band in our results may be attributed to different levels energy deposition in the two experiments and / or to differences in the populations of tautomers / conformers in the gas-phase targets. According to our simulations, metastable band A corresponds to a neutral loss of HCN from the guanine precursor ion, a channel that was absent in Rice's mass spectrum. Reaction pathways concerning the HCN

Band in Fig. 3.13	**m/z of precursor ion (m_1) and product ion (m_2)**	**Proposed reaction**	**Identified in metastable dissociation experiments**
	151 → 135	$C_5N_5H_5O^+ \xrightarrow{-NH_2} C_5N_4H_3O^+$	Rice and Dudek [115]
	151 → 134	$C_5N_5H_5O^+ \xrightarrow{-NH_2} C_5N_4H_2O^+$	Rice and Dudek [115]
A	151 → 124	$C_5N_5H_5O^+ \xrightarrow{-HCN} C_4N_4H_4O^+$	Present work
B	151 → 110	$C_5N_5H_5O^+ \xrightarrow{-CN_2H} C_4N_3H_4O^+$	Present work, Rice and Dudek [115]
C	151 → 109	$C_5N_5H_5O^+ \xrightarrow{-CN_2H_2} C_4N_3H_3O^+$	Present work, Rice and Dudek [115]
D	151 → 108	$C_5N_5H_5O^+ \xrightarrow{-HCNO} C_4N_4H_4{}^+$	Present work, Rice and Dudek [115]
E	135 → 106	$C_5N_4H_3O^+ \xrightarrow{-COH} C_4N_4H_2{}^+$	Present work
F	151 → 83	$C_5N_5H_5O^+ \xrightarrow{-C_2N_3H_2} C_3N_2H_3O^+$	Present work
G	134 → 80	$C_5N_4H_2O^+ \xrightarrow{-C_2NO} C_3N_3H_2{}^+$	Present work
	151 → 44	$C_5N_5H_5O^+ \xrightarrow{-C_4HN_3O} CN_2H_4^+$	Rice and Dudek [115]
	151 → 43	$C_5N_5H_5O^+ \xrightarrow{-C_4H_2N_3O} CN_2H_3^+$	Rice and Dudek [115]
H	110 → 82	$C_4N_3H_4O^+ \xrightarrow{-CO} C_3N_3H_4{}^+$	Present work, Rice and Dudek [115]
I	109 → 81	$C_4N_3H_3O^+ \xrightarrow{-CO} C_3N_3H_3{}^+$	Present work, Rice and Dudek [115]
J	151→ 28	$C_5N_5H_5O^+ \rightarrow CNH_2{}^+ / CO^+$	Present work
K	82→ 55	$C_3N_3H_4{}^+ \xrightarrow{-HCN} C_2N_2H_3{}^+$	Present work, Rice and Dudek [115]
L	81→ 54	$C_3N_3H_3{}^+ \xrightarrow{-HCN} C_2N_2H_2{}^+$	Present work, Rice and Dudek [115]
M	81→ 28	$C_3N_3H_3{}^+ \xrightarrow{-C_2N_2H} CNH_2{}^+$	Present work
N	56→ 29	$C_2NOH_2{}^+ \xrightarrow{-HCN} COH^+$	Present work
O	43→ 28	$C_2OH_3{}^+ / HCNO^+ \xrightarrow{-CH_3/-NH} CO^+$	Present work
P	43→ 18	$C_2OH_3{}^+ \xrightarrow{-C_2H} H_2O^+$	Present work

Table 3.4: Summary of the metastable assignments to the bands observed in the present experiments (figures 3.13 and 3.14) and in Rice's EII experiments [115]. Bands G and M-P are very weak. There is a ±1 m/z uncertainty on the identity of the precursor and daughter ions for these bands. The dissociation channels highlighted in red or blue could plausibly be activated sequentially following an ionisation event.

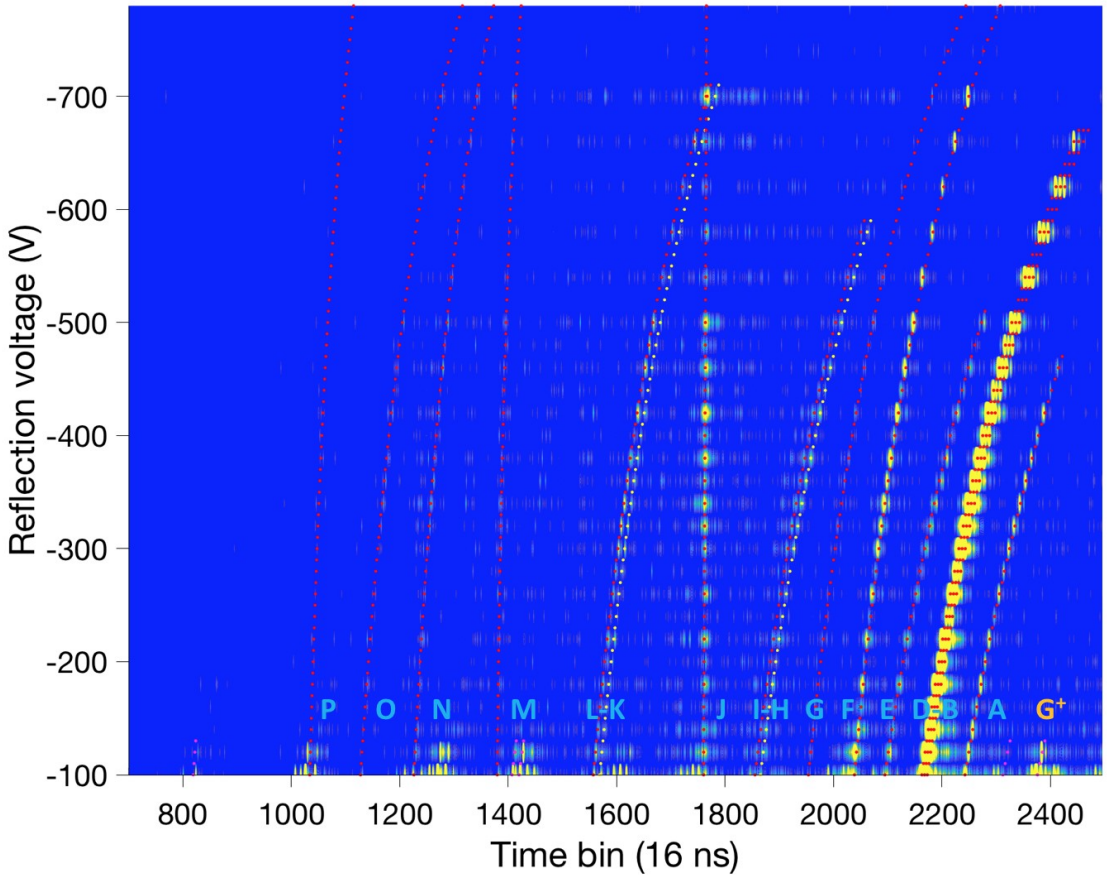

Figure 3.13: Time-of-flight mass spectra of guanine fragment ions against reflection voltage. Experimental signal is represented by yellow bands, whereas simulated bands are given by red dotted lines. Guanine was ionised by MPI at 225 nm with a fluence of 7×10^6 W/cm^2. A letter is assigned to each band (see table A.1 for more details).

loss from the C8–N9 position were previous reported by Cheng [154] and Arani [155] solely for the keto-N9H tautomer. In Fig. 3.15, we present our DFT calculations concerning this reaction, for the five lowest guanine tautomers: keto-N9H, keto-N7H-amino, enol(*trans*)-N9H-amino, enol(*cis*)-N7H-amino and keto-N7H-imino. The most energetic TS for the keto-N9H-amino tautomer is found at 4.66 eV, in good agreement with Cheng and Arani simulations. For the enol(*trans*)-N9H tautomer, a larger dissociation energy is predicted (5.39 eV). Tautomers hydrogenated in the N7 position exhibit dissociation energies substantially lower than the tautomers hydrogenated in the N9 position. The HCN abstraction described in reaction pathways shown in Fig. 3.15 a), b) and c) have an appearance energy of $E_{app} = AIE + DE = 12.12 - 13.63$ eV and require at least 3 photons, while those shown in Fig. 3.15 d) and e) may require only 2 photons. We estimated an unimolecular rate constant of $k = 1.7\times10^3$ s^{-1} and a $\langle$KER$\rangle$ = 15 meV based on the Castleman's method (appendix A.0.2) for the neutral loss of HCN. It would be surprising that such small rate constant would result from tautomers hydrogenated in the N9 position or from the keto-N7H-imino tautomer, since the available energy of three 225 nm photons ($E_{3h\nu} = 3\times5.51 = 16.53$ eV) is much larger than the appearance energy. According to our DFT calculations, these ions could

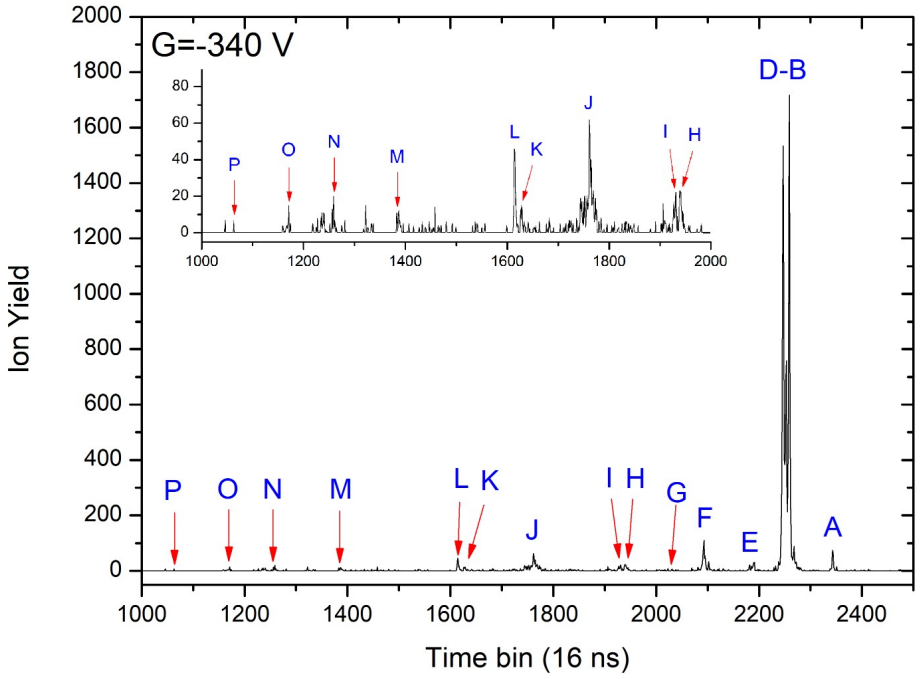

Figure 3.14: Sum of MPI mass spectra of guanine at 225 nm and 7×10^6 W/cm^2 for a reflection voltage of −340 V. The inset plot shows the weak bands M, N, O, P in more details.

be formed with a maximum internal energy of 8.81 eV (keto-N9H-amino), 8.69 eV (enol(*trans*)-N9H-amino), and 8.42 eV (keto-N7H-imino) and for internal energies in range 6.75−8.81 eV, 7.50−8.69 eV and 4.01−8.42 eV, respectively, a prompt fragment $[\text{G-HCN}]^+$ ion signal should be observed in the mass spectra (based on rate constants $k(E)$ calculated with the QET formalism, see appendix A.0.1). However, such prompt ion signal is clearly absent in all the mass spectra. The small unimolecular rate constant and the lack of observation of a prompt $[\text{G-HCN}]^+$ fragment ion in the mass spectra suggest a near threshold dissociation as that produced by 2 photon ionisation of keto-N7H-amino and enol(*cis*)-N7H-amino tautomers.

The most intense metastable bands correspond to loss of cyanamide neutral fragments ($CN_2H_{1,2}$) and HNCO from guanine cation (bands B, C and D in table A.1). The former two channels (assigned with blue / red coloured bands) concern a multi-step fragmentation mechanism, which is dominant in 1-methylguanine and guanine EII mass spectra. Decomposition through mechanism B and C is believed to involve cleavage of C2−N3 and N1−C6 bonds [115], leaving the carbonyl group exposed for subsequent fragmentation. Cheng simulated the reaction pathways concerning bands B and C at DFT level for the keto-N9H-amino guanine cation tautomer and predicted fragmentation energies in the range 2.85 – 3.09 eV, corresponding to an appearance energy of $E_{app} = 10.57 - 10.89$ eV.

The metastable HCNO loss from guanine and methylated derivatives studied by Rice is quite interesting: while guanine and 1-methyl-guanine eject this neutral fragment, 3-methyl and 7-methyl

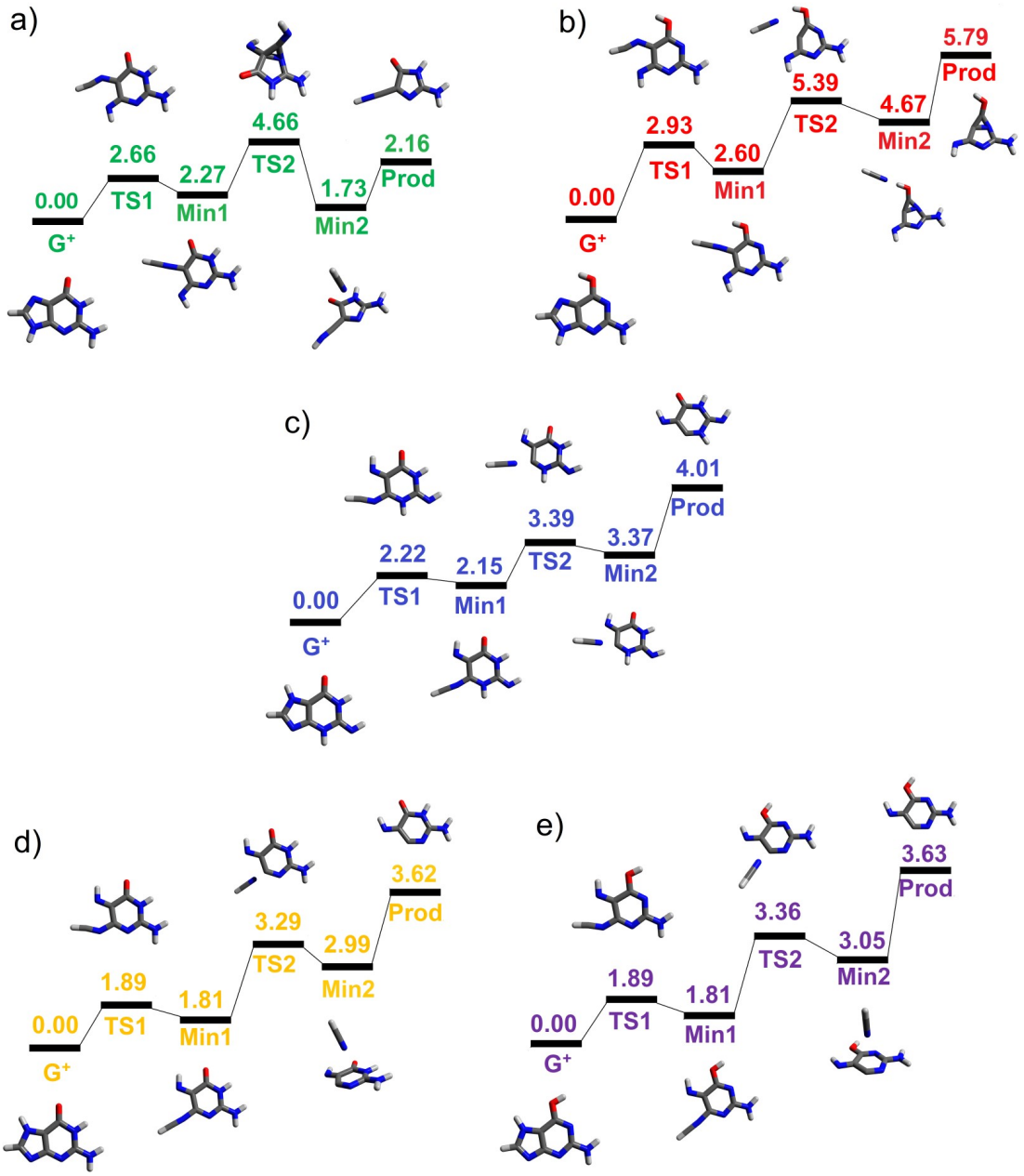

Figure 3.15: Reaction pathways for HCN neutral loss from various guanine tautomer ions: a) keto-N9H-amino; b) enol(*trans*)-N9H-amino; c) keto-N7H-imino; d) keto-N7H-amino; e) enol(*cis*)-N7H-amino. Calculated at DFT level, with the M06-2X functional and 6-311G(d,p) basis set, employing the methodology described in section 2.4.4.

guanine do not. This is indicative that the methylation site is relevant for observing or not the metastable fragmentation. We try to understand if this rationale is applicable to the hydrogenation site of guanine tautomers, by investigating HCNO neutral loss reactions from the lowest five

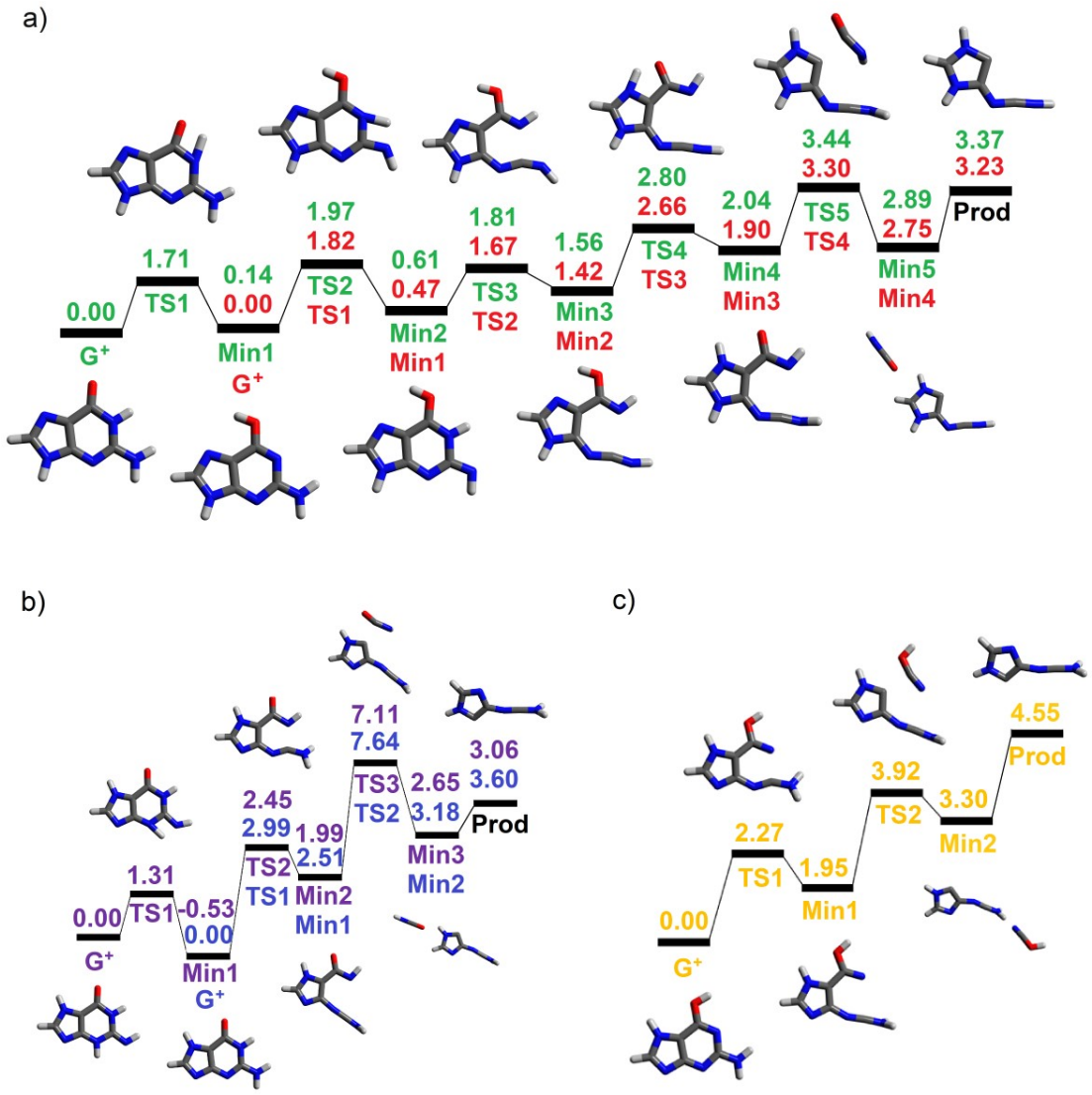

Figure 3.16: Reaction pathways for HNCO neutral loss from various guanine tautomer ions: a) keto-N9H-amino and enol(*trans*)-N9H-amino; b) keto-N7H-imino and keto-N7H-amino; c) enol(*cis*)-N7H-amino. Calculated at DFT level, with the M06-2X functional and 6-311G(d,p) basis set, employing the methodology described in. Energies are given in eV and include zero-point corrections.

tautomers of guanine. These pathways are shown in Fig. 3.16. Cheng and co-workers have previously determined reaction a) for keto-N9H-amino tautomer, which involves the dislocation of the hydrogen from the N1 to the N7 position. It is worth noting that the appearance energy of reaction paths in a) ($E_{app} = 11.14 - 11.16$ eV) match the available energy of 2 photons ($E_{2h\nu} = 11.02$ eV). We estimate a mean kinetic energy release of 7 ± 3 meV for the HCNO neutral loss from the guanine precursor ion, with a mean rate constant $k = (1.06 \pm 0.35) \times 10^4$ s^{-1} (appendix A.0.2).

Ionisation of enol(*trans*)-N9H-amino and keto-N9H-amino tautomers via 2 photons generate guanine ions with a maximum of 3.18 eV and 3.30 eV, respectively. This internal energy is just the right amount to verify the loss of HCNO from guanine ions with the mentioned kinetics (see appendix A.0.1). The enhancement of the metastable band observed in the mass spectra of Fig. 3.10 when the desorption laser power is increased to 0.81 W, can be interpreted as an increase of the unimolecular rate constant due to internal excitation of the neutral target. The reactions for the remaining tautomers, enol(*cis*)-N7H-amino, keto-N7H-imino and keto-N7H-amino, are more energetic and require absorption of 3 photons. In this scenario, and according to our DFT calculations, the maximum internal energy of the ionised tautomers is 8.72 eV (enol(*cis*)-N7H-amino), 8.42 eV (keto-N7H-imino), and 8.71 eV (keto-N7H-amino). For the enol(*cis*)-N7H-amino and keto-N7H-amino tautomers, the internal energy is not enough to observe a dissociation with a mean rate constant of 1.06×10^4 s^{-1} (appendix A.0.1). For the keto-N7H-imino, it is sufficient to observe a prompt fragment ion in the mass spectra but that is not observed in our MPI-TOF mass spectra. The data we have available suggest that metastable bands associated with HNCO loss in our MPI-TOF mass spectra derives from ionisation of guanine tautomers hydrogenated in the N9 site with 2 photons.

In summary, the rich metastable fragmentation pattern obtained in the present work results from two factors. Firstly, it is due to the intense target density produced by the ILTD source, enabling even very weak channels to be detected. Secondly, it stems from the variety of guanine tautomers present in the gas plume, each one having different metastable dissociation channels activated following ionisation in conditions leading to a given range of deposited energies.

Tautomer	**Adiabatic ionisation energy, eV**		**$G^+ \rightarrow$[G-HCN]$^+$/[G-HCNO]$^+$ dissociation (appearance) energy, eV**
	This work	Zhou [125]	
Keto-N9H-amino	7.72	7.68	4.66 (12.38) / 3.44 (11.16)
Keto-N7H-amino	7.82	7.80	3.62 (11.44) / 7.64 (15.46)
Enol(*trans*)-N9H-amino	7.84	7.75	5.79 (13.63) / 3.30 (11.14)
Enol(*cis*)-N7H-amino	7.81	7.76	3.63 (11.44) / 4.55 (12.36)
Keto-N7H-imino	8.11	8.12	4.01 (12.12) / 7.11 (15.22)

Table 3.5: Adiabatic ionisation energies of different guanine tautomers (including zero-point corrections). Dissociation and appearance energies for reaction pathways leading to bands A and D are also given. The uncertainty for ionisation energies is ±0.11 eV, for dissociation energies ±0.05 eV, and for the appearance energies ±0.16 eV.

3.4 Guanosine: MPI experiments and DFT calculations

3.4.1 General introduction

Guanosine is one of the four nucleosides within DNA, and it is composed of a sugar unit bonded to the N9 position of guanine (see Fig. 3.17 for the structure and atomic labelling of guanosine).

Until now, studies investigating the radiation response of this molecule are very scarce, and those reported in the literature do not provide strong evidences for the lack of thermal decomposition of the gas-phase targets. Therefore, the first aim of the current MPI-TOF experiments is to look for evidence pertaining the degree of decomposition of ILT-desorbed guanosine. This is addressed in section 3.4.2.1 and features an analysis of the product ions, the source temperature, and the fragment ion production as function of the desorption laser power.

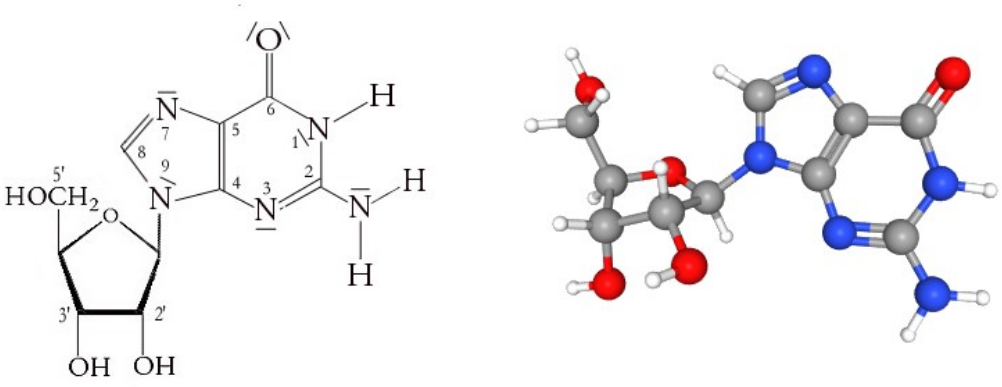

Figure 3.17: Atom labelling of guanosine and respective ball and stick representation [156]. The atomic labelling in the nucleobase is the same as the atomic labelling of guanine given in the previous section.

In the subsequent sections we investigate, by means of DFT calculations, thermally-driven mechanisms that could explain the reduction of fragment ion / guanosine ion yields observed in our MPI-TOF mass spectra as a function of increasing desorption laser power. In particular, section 3.4.2.2 addresses the possible role played by changes in tautomer and conformer populations of guanosine in the electronic GS, while section 3.4.2.3 focuses on energy barriers associated with quenching mechanisms in neutral excited states.

Finally, in section 3.4.3, we calculate reactions pathways at DFT level for the dominant fragment ions observed in our MPI mass spectra of guanosine and draw comparisons with other mass spectra of guanosine in the literature, as well as with mass spectra of guanine.

3.4.2 Investigating thermally-driven effects on ion production from multi-photon ionised guanosine

3.4.2.1 Thermal decomposition assessment

In the present experiments, ILT-desorbed guanosine molecules multi-photon ionised using 270 nm pulses with an average fluence of 3.0×10^7 W/cm^2. Our previous studies of multi-photon ionised pyrimidine-based nucleosides revealed increased relative detection of intact nucleoside ions at longer MPI wavelengths [33, 84]. Therefore, we chose this wavelength — the longest available with good stability from our laser system at the time of the measurements — for our experiments on guanosine to give us the best chance of detecting the intact parent ion. MPI mass spectra

were acquired with laser desorption powers ranging of 0.30 W to 0.45 W (corresponding to foil temperatures of 388−426 K) to investigate how thermal energy affects the relative fragment ion production.

To our knowledge, only one study in the literature has investigated the thermal decomposition products of guanosine. In that study, by Wang and You, thermogravimetric and differential scanning calorimetry curves representing the relative molecular weight of the sample as a function of temperature were obtained for nucleobases and nucleosides [113]. Guanosine powder samples were heated up to 1073 K at a rate of 10 K/min in a nitrogen atmosphere. The residues were then separated by HPLC and identified by IR absorption spectroscopy. The authors observed thermal decomposition stages at approximate temperatures of 524 K and 733 K. Their results show that thermal decomposition products of guanosine involve cleavage of the N-glycosidic bond to form guanine (151 a.m.u., detected as soluble residues) and decomposition of the sugar ring (detected as insoluble residues) [113].

In common with the scarcity of studies addressing the thermal decomposition products of guanosine, radiation response investigations of this nucleoside in the gas phase are very rare. Moreover, only Poully's and co-workers reported tests for possible thermal damage of the targets [30]. Although the results strongly suggest intact vaporisation of thymidine and adenosine targets, it was not possible to completely rule out some thermal decomposition of guanosine due to its weak relative signal in the MPI mass spectrum. To our knowledge, the full set of published experiments on neutral gas-phase guanosine targets are listed in table 3.6.

Authors [reference] (year)	**Type of experiment**	**Vaporisation technique and temperatures, if provided**	**Tests for thermal decomposition presented**	**Comments with respect to potential target decomposition or reactivity**
Li and Lubman [29] (1989)	One-colour REMPI at 266 nm	DLID coupled to supersonic expansion	No	No comments by the paper's authors.
Nir *et al* [97] (2000)	REMPI spectroscopy (290−287 nm)	DLID from a graphite substrate coupled to supersonic expansion	No	No comments by the paper's authors.
Nir *et al* [157] (2004)	REMPI spectroscopy + UV-UV SHB (290−285 nm), IR-UV SHB	DLID from a graphite substrate coupled to supersonic expansion	No	No comments by the paper's authors.
Abo-Riziq *et al* [96] (2007)	REMPI spectroscopy, IR-UV SHB	DLID from a graphite substrate coupled to supersonic expansion	No	No comments by the paper's authors.

Authors [reference] (year)	**Type of experiment**	**Vaporisation technique and temperatures, if provided**	**Tests for thermal decomposition presented**	**Comments with respect to potential target decomposition or reactivity**
NIST [158] (2014)	EII MS	Unknown	No	No comments from the database compilers or measurement team.
Poully *et al* [30] (2015)	Proton-collision induced ionisation MS	ILTD (532 nm)	Yes	The authors present MPI of the nucleosides that strongly suggest intact vaporisation of adenosine and thymidine. They could not exclude the possibility of thermal decomposition of guanosine due to a relatively weak signal of the parent ion.
De Camillis *et al* [31] (2015)	Two-colour (267+800 nm) MPI-MS with fs lasers, delay close to 0 fs.	ILTD (445 nm and approximate foil temperature 423−523 K)	No	The authors do not exclude the possibility of thermal decomposition, noting the low yields of parent ions. The authors provide an approximate foil temperature range but do not explain how the temperatures were determined or estimated.
AIST spectral database for organic compounds [159] (1999)	EII-MS at 75 eV.	Sample heated to 483 K with the source at 493 K. Author's do not specify the type of source used.	No	No comments by the authors. Guanosine$^+$ detection is extremely weak compared with the MS in refs [30] and [31], suggesting some thermal decomposition.

Table 3.6: Literature summary of volatilisation techniques and information relevant to target decomposition in experiments on neutral guanosine. See the list of acronyms at the beginning of the thesis for full names of experimental methods.

Fig. 3.18 shows a typical 270 nm MPI mass spectrum from the present set of experiments (top) and a two-colour (overlapping 267+800 nm fs laser pulses) MPI mass spectrum obtained by De Camillis *et al* with an ILTD source at Queen's University of Belfast (bottom). The two mass spectra in the figure show good agreement with each other in terms of the main ion peaks and their approximate relative intensities. The significant parent ion feature at m/z = 283 (labelled Gu$^+$ on the figure) shows that both ILTD applications were able to, at least, vaporise some of the sample

without thermal decomposition. The observation of extra ions in our mass spectrum in the range

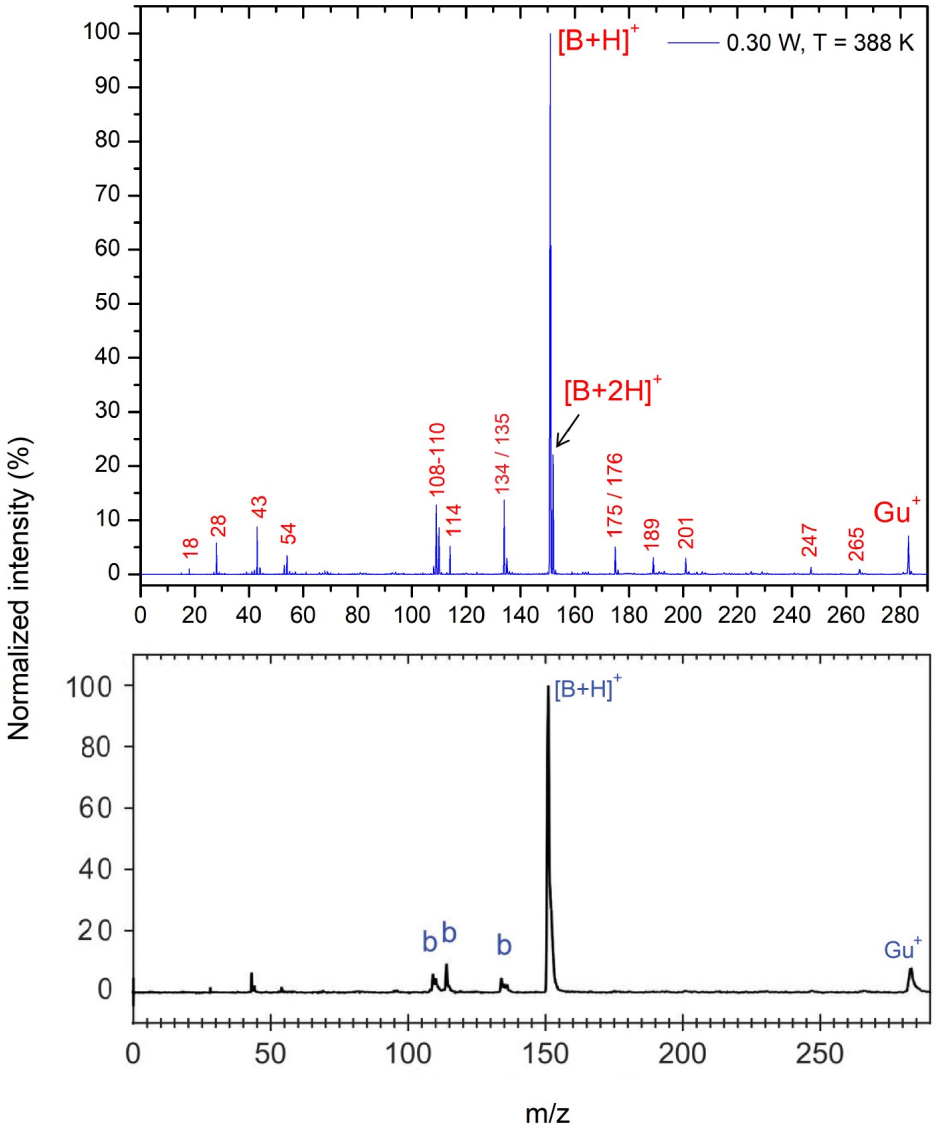

Figure 3.18: Mass spectra of guanosine. Top: our one-colour MPI experiment with 270 nm pulses and fluence of 3.0×10^7 W/cm^2. The desorption laser power of 0.30 W corresponds to 388 K at the hottest part of the foil in contact with the sample. Bottom: De Camillis *et al's* two-colour MPI experiment using simultaneous 267+800 nm pulses from a fs laser. Desorption laser power is not specified, but the authors note foil temperatures of approximately 423−523 K in their paper about all four DNA nucleosides [31]. The letter b stands for base fragment ions.

m/z = 151−283 can be attributed to the higher signal-to-noise ratio and mass resolution of our mass spectrometer. Based on Wang and You's results, the presence of ions with m/z = 151 (guanine) in our MPI mass spectrum could be a possible indicator of thermal decomposition of guanosine. It is worth noting however, that fragment ions with m/z = 151 where previously identified by

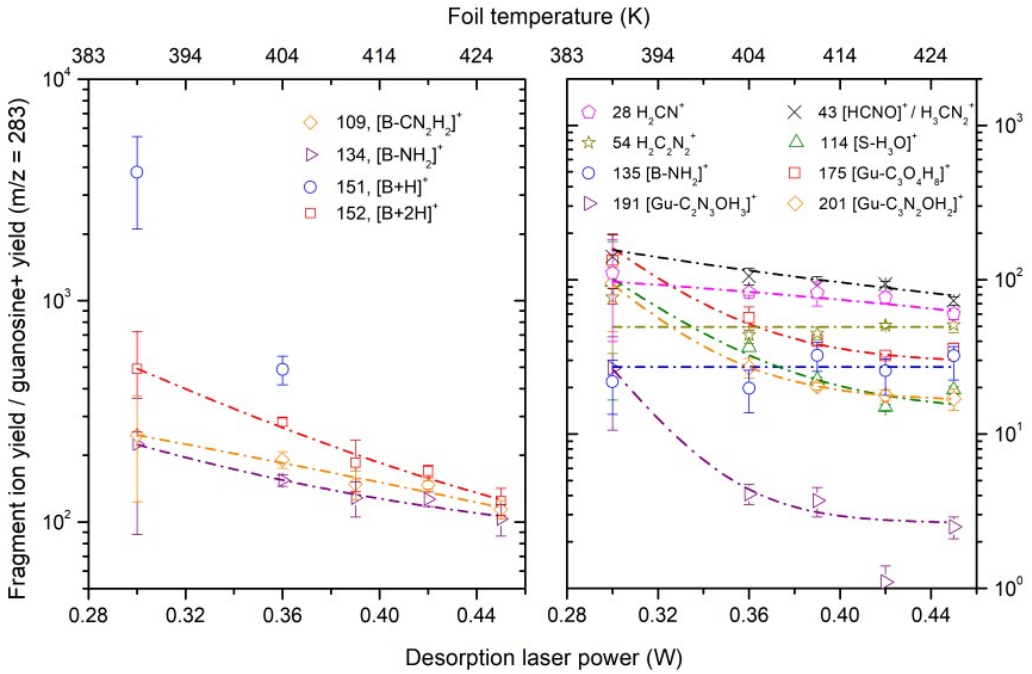

Figure 3.19: Ratios of fragment ion yield over guanosine$^+$ yield plotted against desorption laser power for the major (left) and minor (right) ion peaks in the present MPI-TOF mass spectra. Relative yields for the $[B+H]^+$ fragment ion are not given for desorption powers ≥ 0.36 W due to saturation of the signal. Dashed-dotted lines are exponential fits to data points. The error bars are given by the standard deviation of the ratios.

Feketeová and co-workers in collision-induced dissociation mass spectra of intact guanosine and copper-guanosine ion complexes produced by ESI sources [160]. Thence, the presence of guanine ions (labelled $[B+H]^+$ in Fig 3.18 according to the scheme explained below) in our MPI-TOF results (or indeed any other mass spectra) does not necessarily imply thermal decomposition of guanosine in the target. The other thermal decomposition products of guanosine reported by Wang and You, are not visible in the MPI mass spectrum, with the exception of m/z = 114. However, some thermal decomposition products — namely those without the base part of the nucleoside still essentially intact to provide the chromophore — will not be multi-photon ionisable in the present laser conditions. A more reliable indicator of negligible thermal decomposition in the present ILTD target is the low foil temperature (388 K in the Fig. 3.18) compared with the onset temperature for thermal decomposition determined by Wang and You (524 K). Moreover, the heating rate in the present experiments (~100 K s^{-1}) was around three orders of magnitude faster than in Wang and You's experiments (10 K min^{-1}) and faster heating rates are associated with reduced thermal decomposition compared with melting or sublimation [25]. It is also worth noting that the foil temperatures in the present experiments were far lower than the sample temperature of 483 K for the EII mass spectrum in the AIST database.

To investigate the dependence of fragment ion production on thermal desorption conditions, we plotted in Fig. 3.19 the yields for specific fragment ions signal / the guanosine ion signal against

desorption laser power (and hence foil temperature). Here B refers to the base part of the nucleoside after *simple* cleavage of the N-glycosidic bond (i.e. with no hydrogen transfer associated with the cleavage). Hence, $[B+H]^+$ represents the base part with an additional hydrogen transferred from the sugar, resulting in the same chemical formula as guanine+ (m/z = 151). All ions with signals >3% of the strongest peak in the mass spectrum are included in the graphs. The relative yield for the m/z = 151 fragment ion is only provided for desorption powers up to 0.32 W since that ion signal becomes saturated above that power. With the exception of the weak fragment ion with m/z 135, all of the fragment ion signals decrease compared with the guanosine$^+$ signal as the desorption laser power increases. This somewhat surprising result will be discussed further below but the key point here is that the opposite trend would normally be expected if significant thermal decomposition was taking place. Hence, the present study provides new evidence that supports the absence of significant thermal decomposition in targets ILT-desorbed guanosine, even though it is not possible to rule it out completely.

Aside from its relevance to assessing possible thermal decomposition in the target, the relative fall in fragment ion production as a function of desorption laser power in Fig. 3.19 is interesting and might be explained by one or more of the following possibilities:

- **The fragment ions may originate from both clusters and monomers of guanosine**. If the desorption rate (not determined absolutely in our experiments) is sufficiently high, then it is possible that multiple collisions in the expanding plume could lead to internal cooling and some clustering [161]. Clustering, in general, will tend to reduce the production of fragment ions because some of the internal energy deposited during ionisation goes into breaking up the cluster instead of breaking up its constituent molecules. Hence, it is plausible that increasing clustering with increasing desorption power — itself a normal thing to expect, if indeed we do have any clustering, because a greater desorption laser power leads to a higher density of desorbed molecules and hence more intermolecular collisions — will lead to an increase in the guanosine ion signal vs. the signals for fragment ions from guanosine. However, we believe that this mechanism is unlikely in our experiments because we do not observe any cluster ions or fragment ion that can be clearly assigned to clusters. Furthermore, no evidence of cluster formation has been reported previously from any ILTD sources [30, 31, 32, 33, 84].

- **The relative populations of guanosine tautomers/conformers may change with temperature**. Tautomer and/or conformer transitions may occur in the electronic GS or in neutral excited states of nucleosides as evidenced in our experiments on uridine [33] and previously predicted by Delchev [162]. As discussed in the guanine section of this chapter, different tautomers may have distinct fragmentation patterns. Hence, the observed decrease in the relative fragment ion yield with desorption laser power could possibly be linked to certain higher-energy tautomers being less prone to fragmentation upon MPI than lower energy tautomers. Determination of guasonine tautomer and conformer populations in the electronic GS are evaluated through DFT calculations in section 3.4.2.2.

- **Photo-physical and photo-chemical mechanisms may be activated by thermal energy in the neutral excited states**. The extra thermal energy can help to activate reactions, notably involving proton transfer, in neutral electronic excited states, accessed during the MPI process. The reaction products may have higher threshold energies for dissociative ionisation, hence fragment ion production would be reduced compared with guanosine ion production. Mechanisms involving hydrogen transfer in neutral excited states are investigated in section 3.4.2.3.

3.4.2.2 Investigating mechanisms that could be responsible for reduced fragment ion production by guanosine MPI as a function of the desportion laser power: tautomer and conformer populations

Perhaps somewhat counter-intuitively, the number of guanosine tautomers is reduced compared to guanine due to the blockage of the N9 position by the N-glycosidic bond. With this site on guanine blocked, only two tautomers of guanosine can exist: the keto and the enol forms. Although the number of tautomers is significantly reduced, the N-glycosidic bond brings in a new conformation space for guanosine. De Vries and co-workers have only identified the presence of the enol tautomer with a *syn* conformation (5'OH$\cdots$N3 hydrogen bond) in their jet cooled laser desorbed molecular beam by performing REMPI and IR-UV SHB spectroscopies [97, 131, 157]. The lack of evidence of keto tautomers was rationalised in terms of higher ionisation energies or short lived excited states [131]. They also investigated, in two different works, the energies of *syn* and *anti* conformers of enol guanosine and keto 3'OH-deoxyguanosine by *ab initio* methods [97, 157]. They found that the *syn* conformers have a lower energy than *anti* conformers and that the difference in energy between them is approximately the same for both tautomers (0.07 eV for keto 3'OH-deoxyguanosine and 0.09 eV for enol guanosine). So and Alavi performed theoretical calculations of vertical excitation energies of nucleosides [163]. The optimised keto guanosine structure at B3LYP/6-311++G(d,p) features a hydrogen bond between the sugar hydroxyl group 2'OH and the base nitrogen site N3 (2'OH$\cdots$N3, *anti* conformation). The dissimilarities among these structures may lead us foresee distinct electronic excited states or ionisation energies, as mentioned by De Vries. Thence, the thermally-driven effect observed in the relative fragment ion production could possibly result from relative changes in populations of these tautomers and conformers. In this section we present DFT calculations that help us to assess the likelihood of a significant change in tautomer and conformer populations as a function of desorption laser power in the present experiments.

We optimised the keto-*syn*, enol-*syn*, keto-*anti*, and enol-*anti* guanosine forms at DFT level, with the M06-2X functional and a 6−31+G(d) basis set. The reasons for having performed our own calculations are: (1) The low level of theory used in Nir's works, (2) The different levels of theory used by Nir and So and Alavi, which make the results not directly comparable, (3) We will use these geometries for other types of calculations in subsequent sections. For the input geometries, we used similar input structures as those investigated in Nir *et al* and So and Alavi's works [97, 157, 163]. The optimised geometries are displayed in Fig. 3.20 along with the relative energies

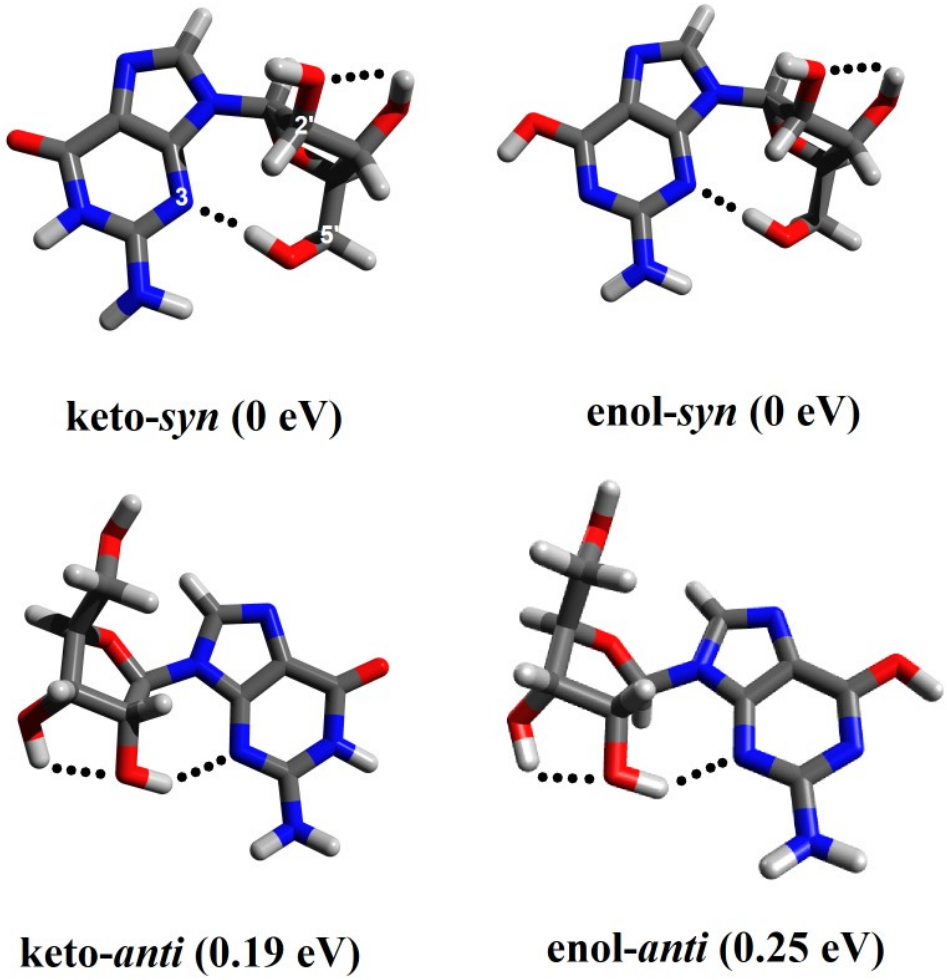

Figure 3.20: Structures and relative zero-point energies of keto and enol tautomers of guanosine. For the keto and enol tautomers, the two distinct *syn* (with a 5'OH···N3 hydrogen bond) and *anti* (with a 2'OH···N3 hydrogen bond) conformers are also presented. Various conformers of the enol tautomer have been described by Nir *et al* but here we only present the lowest energy structure reported in their work [157]. This conformer is more stable than the *anti* conformer, the next lowest-energy structure, by 0.09 eV, calculated at the HF/6-31G(d,p) level. The *syn* conformer of the keto tautomer of 3'OH-deoxyguanosine was predicted by Nir *et al* to be more stable than the *anti* conformer by 0.07 eV at HF/6-31G(d,p) level [97].

with zero-point corrections.

The *syn* conformers are isoenergetic and more stable than the *anti* conformer by 0.19 eV and 0.25 eV for keto and enol tautomers, respectively. Both *syn* conformations establish a 5′OH···N3 bond with length 1.87 Å. The keto-*anti* and enol-*anti* structures have longer hydrogen bond lengths, 2.13 Å and 2.09 Å, respectively.

In order to evaluate the population of tautomers and conformers in a gas target as a function

of the temperature, we calculated the Boltzmann distributions considering the relative thermal energies of the different structures at different temperatures. The bar graph shown in Fig. 3.21 represents the population of the tautomers and conformers at different temperatures.

The populations of keto-*anti* and enol-*anti* tautomers are less than 1%, even at the highest temperature considered: 450 K. Even across the large temperature range considered (250−450 K), the relative populations of the keto-*syn* and the enol-*syn* tautomers changed by only 3%. Hence, the changes in the relative fragment ion yield observed in Fig. 3.19 are clearly larger than the relative changes in the population of tautomers and conformers of guanosine calculated at DFT level. Therefore, if we assume that the foil temperature (388−426 K) is solely responsible for the distribution of different structures, the reduction in the fragment ion production cannot be explained only based in changes of populations of different structures in the electronic GS.

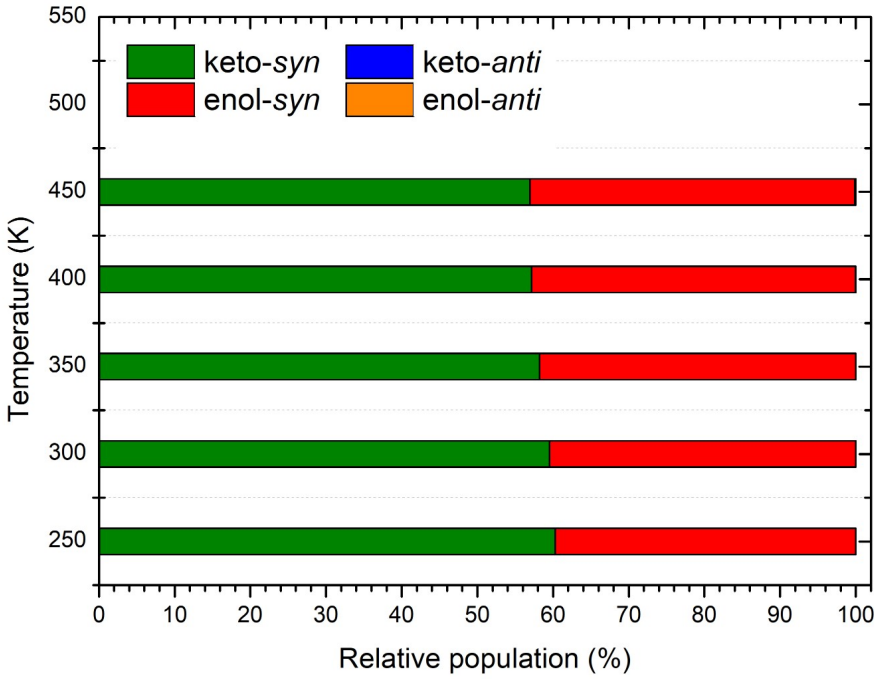

Figure 3.21: Boltzmann distribution for the different tautomers/conformers of guanosine, calculated based on the relative thermal energies in the 250−450 K range. The population of keto-*anti*+enol-*anti* is negligible compared with populations of the remaining two tautomers (<1% at 450 K). Note that the foil temperatures in the present experiments on guanosine ranged from 388 to 426 K (see Fig. 3.18).

3.4.2.3 Investigating mechanisms that could be responsible for reduced fragment ion production by guanosine MPI as a function of the desportion laser power: thermally-enhanced reactivity in neutral excited states

Efficient quenching mechanisms have been reported as responsible for the observed ultrafast de-excitation of electronically excited molecules with intramolecular hydrogen bonds and hydrogen-bonded clusters. For example, lifetimes of nucleosides in water are found to be shorter than in gas phase [31, 164]. Furthermore, the Watson-Crick guanosine-cytidine and guanine-cytosine pairs exhibit a faster de-excitation than the respective nucleosides and nucleobases either in solution and gas phase [165, 166]. For the last system, de-excitation occurs efficiently through a barrierless proton transfer mechanism assisted by charge transfer (CT) states [167]. Tuna *et al.* reported the same phenomenon in adenosine [168]. Given the fact that the four structures of guanosine scrutinised in the present work establish hydrogen bonds between their base and sugar parts (described in the Fig. 3.20 caption), it is reasonable to suppose that such states may also play a role in photo-deactivation and reactivity of guanosine. Photo-chemical processes such as these in neutral electronic excited states may be activated by the absorption of the first UV photon in our experiments and then lead to an altered fragmentation pattern upon ionisation.

As mentioned in previous sections of this chapter, vaporisation of diverse nucleosides (guanosine, adenosine, cytidine and thymidine) using an ILTD source similar to ours was first accomplished by De Camillis and co-workers [31]. They investigated the neutral excited state dynamics of these nucleosides using two-colour (267+800 nm) time-resolved pump-probe experiments. Their results show a decrease in excited state lifetimes of nucleosides, compared with the corresponding isolated nucleobases, with the notable exception of guanosine. It is intriguing why guanosine does not behave just like the other nucleosides. Are there efficient quenching mechanisms in guanosine that are absent in the guanine nucleobase, for example proton transfer assisted by CT states, and that may alter the structure of the molecule? In this section, we explore the electronic excited states of guanosine tautomers, in particular the CT states, and investigate if they play an active role in the photochemistry of guanosine under the current experimental conditions. As far as we are aware, unimolecular reactions in neutral excited states of nucleosides have only been previously studied theoretically by Delchev for uridine [162] and by Tuna for adenosine [168]; no results have been reported for guanosine.

In order to locate the lowest CT states of the two most stable guanosine tautomers, keto-*syn* and enol-*syn*, we adopted the same methodology as the one presented in Tuna's work [168]. First, a relaxed potential energy scan of the 5'O−H bond distance in steps of 0.1 Å was performed in the neutral GS at M06-2X/6-31+G(d) level of theory. The vertical excitation energies at each point were calculated with TDDFT employing the same functional and basis set. The M06-2X functional with the 6-31+G(d) basis set were chosen for this investigation because they have shown a good overall performance in predicting electronic state spectroscopy data as determined by several benchmark tests [70]. This scan allowed us to predict at which 5'O−H bond distance the energy of the lowest CT drops below the energy of the valence states localized on the nucleobase: this is 1.49 Å in the keto-*syn* tautomer and 1.39 Å in the enol-*syn* tautomer. The optimisation of the

lowest CT state was performed for longer 5'O–H bond distances and the energies are represented by open blue circles in Fig. 3.22 a) and b) for the keto and enol tautomers, respectively. Due to the steep energy increase of the CT state and its mixing with states of different character at shorter 5'O–H bond distances, a linear coordinate interpolation was performed in that range for all the states. The geometry end points of the interpolation correspond to the S_0 global minimum (crossed open red square) and the optimised S_1 state where the CT character appears (crossed open blue circle). To estimate the TS energy associated with the hydrogen transfer reaction, the adiabatic potential energy curve (PEC) of the S_1 state is required. This is depicted by open blue circles in Figs. 3.22 c) and d) for keto and enol tautomers, respectively.

Analysing the top panels of Fig. 3.22, we observe that the lowest singlet excited states of keto-*syn* guanosine are similar to those of the isolated guanine nucleobase, both in qualitative and quantitative terms [133]. A destabilization of the $n\pi^*$ dark state is observed for the enol tautomer, presumably arising from the interaction of the 5'OH group with the lone pair of the N3 atom.

The bottom panels clearly show energy barriers located around R(O–H)=1.30/1.40 Å and $5.00-5.25$ eV, resultant from the coupling of $\pi\pi^*$ and CT states. According to the calculations performed in the last section, the stretching vibration frequencies of the 5'O-H bond are ω = 3530 cm^{-1} and ω = 3512 cm^{-1} for keto-*syn* and enol-*syn* structures of guanosine, respectively. Considering that the fundamental vibrational level (v" = 0) involving the 5'O-H stretch lies 0.22 eV above the minimum of the potential energy well ($\frac{1}{2}h\omega_{5'O-H}$), one can conclude that the absorption of one 270 nm photon (4.59 eV) is not sufficient to overcome this energy barrier. For that, at least the first level (v" = 1) of the 5'OH stretching vibration would need to be populated. Since the characteristic temperature of these motions is $\sim$ 5000 K, the proton transfer mechanism assisted by CT states can be ruled out under the current experimental conditions. This indicates that this CT state does not play a role in the relative changes in fragment ion production as a function of desorption power shown in Fig. 3.19. However, this mechanism could plausibly be responsible for changes in fragment ion production at shorter wavelengths. As an extension to this work, it would be very interesting to repeat the experiments in section 3.4.2.1 at lower wavelengths (e.g. at 220 nm, 5.56 eV, which is comfortably above this barrier and also accessible using our pulsed laser).

We conclude in this section that changes in conformer and tautomer populations of the target are unlikely explanations for the observed thermally-driven effects on the ion production. A new reaction has been identified in electronic excited states but the barriers for this specific reaction are too high to contribute to the present results. Nonetheless, the identification of this reaction highlights the plausibility of existing other excited-state reactions that could play a role in the observed thermal effects on relative peak heights, for example tautomer and / or conformer transitions. Indeed, energy barriers associated with conformer transitions were shown to be smaller in neutral excited states than in the electronic ground state of uridine [162]. Evidences for such transitions in uridine were also obtained experimentally, by observing changes in the fragment ion production in MPI-TOF mass spectra as a function of the source temperature [33].

In section 5, we present a new DEA / EII / MPI apparatus that will enable us to perform EII experiments on ILT-desorbed molecules for the first time. In fact, attempting EII experiments on ILT-desorbed guanosine as a function of the desorption laser power will be particularly important

Figure 3.22: Potential energy curves along 5'O−H bond distance of keto and enol tautomers of guanosine with a *syn* conformation. In a) and b), a linear coordinate interpolation was performed between the S_0 optimized geometry (crossed red open square) and the first point of the S_1 state with CT character (crossed blue open circle). Red open squares represent the energy of the S_0 state at the optimised S_1 geometry. In panels c) and d), the red open squares represent the energy of the optimised S_0 state. S_1 depicts the adiabatic PEC for the first neutral excited state and the red full squares the energy of the S_0 state at those geometries. The fundamental (ν" = 0) and first excited (ν" = 1) vibrational levels of the 5'O−H stretching motion are represented by solid black lines.

to better understand the thermally-driven effect we are observing: if a reduction in the fragment ion production is not verified as it is in the MPI-TOF experiments, the thermally-driven effect is MPI-specific and can be attributed to dynamics in neutral excited states. Moreover, EII will also be valuable in terms of testing for thermal decomposition because any species in the neutral target will be ionised in these experiments. The fact that the present MPI scheme will not ionise any possible thermal decomposition products that do not have a chromophore is a significant limitation

in the present tests for thermal decomposition.

3.4.3 Investigating exceptionally strong guanine ion production by guanosine ionisation

In this section we investigate routes in ionic states leading to singly and doubly hydrogenated base ions. As can be observed in in Fig. 3.18, these are the major features in our MPI mass spectrum. The propensity for nucleosides to fragment along the N-glycosidic bond with single and double hydrogen transfer from the sugar part to the base part has been evidenced in other mass spectrometry studies [29, 30, 31, 169, 170], but reaction pathways describing the mechanism have never been calculated or proposed.

We start the discussion by noting that most of the small fragment ions from the sugar side of guanosine$^+$ are expected to be mainly neutral and hence not visible in the present experiments. This is because the positive charge on guanosine$^+$ is localised on the base part of the ion since the it is where the highest occupied molecular orbitals are found (see appendix B). Indeed, most of the fragment ions below m/z =151 in the guanosine MPI mass spectrum at 270 nm are visible in the guanine MPI mass spectrum at 225 nm (with exception of a fragment ion with m/z = 114, which is also visible in De Camillis *et al's* MPI mass spectrum, and we attribute to $[S-H_3O]^+$). The fragment ions in our guanine and guanosine MPI mass spectra are shown in table 3.7. The similarity of both mass spectra below the guanine$^+$ m/z value seems initially surprising since replacing one of the hydrogens of guanine by a ribose ring would normally be expected to modify the fragmentation pattern. Furthermore, different guanine tautomers can fragment differently (see sections 3.3.3 and 3.3.4) and the sugar in guanosine locks the base only in two tautomeric forms. In particular, keto and enol tautomers were shown to have a major influence on mass spectra of some molecules (including guanine) [34, 36, 107], however it should be noted that these two tautomers are still accessible in guanosine (as shown in section 3.4.2.2 above). The absence of hydrogens at N7/N9 positions does not seems to substantially affect the prompt fragmentation pattern of guanosine. The most obvious way of interpreting the guanosine fragmentation pattern below m/z 151 is by assuming that those fragment ions are formed through a guanine-like intermediate ion because this is the major feature in the mass spectrum and the fragment ions produced by both targets are similar. Greenwood and co-workers assigned all the features below m/z 151 in their mass spectrum to base fragment ions but did not discuss the specifics of the routes. The proposal that guanine ions can be intermediate products in sequential fragmentation routes of guanosine ions is a novelty.

To understand why such a large proportion of guanosine$^+$ ions fragmented to form guanine$^+$ (either as a stable product or as part of a sequential fragmentation process), we calculated several potential energy curves along chemical bond distances. More precisely, we exploited how the stretching of the 5'O−H, N−glycosidic, 2'C−H, 3'C−H, 2'C−O, and 4'C−O bonds affects the reactivity of guanosine$^+$. The PEC's were calculated at M06−2X/6-31+G(d) level and the coordinates of interest were scanned in steps of 0.1 Å without constrains on the remaining degrees of freedom. Maxima geometries in the PEC's were then used as input to find the transition states with

m/z	Assignment	Visible in guanosine MPI-MS	Visible in guanine MPI-MS
283	Gu^+ [29, 30, 31]	Yes	No
265	$[Gu\text{-}H_2O]^+$ [30]	Yes*	No
247	$[Gu\text{-}2H_2O]^+$	Yes*	No
201	$[Gu\text{-}C_3N_2OH_2]^+$ / $[Gu{-}C_2N_3O]^+$	Yes*	No
189	$[Gu\text{-}C_2O_4H_6]^+$	Yes*	No
176	$[Gu\text{-}C_3O_4H_7]^+$ / $[Gu{-}C_4N_3O_4H]^+$	Yes	No
175	$[Gu\text{-}C_3O_4H_8]^+$ / $[Gu{-}C_4N_3O_4H_2]^+$	Yes	No
153	^{13}C isotopes of $[B+H]^+$/$[B+2H]^+$	Yes*	No
152	$[B+2H]^{+,a}$	Yes	Yes (guanine isotope)
151	$[B+H]^+$ [29, 30, 31]	Yes	Yes
136	$[B\text{-}N]^+$	Yes*	No
135	$[B\text{-}NH]^+$	Yes*	Yes*
134	$[B\text{-}NH_2]^+$	Yes	Yes*
114	$[S\text{-}H_3O]^+$	Yes	No
110	$[B\text{-}CN_2]^+$	Yes	No
109	$[B\text{-}CN_2H]^+$	Yes	No
108	$[B\text{-}CNO]^+$	Yes*	No
81	$C_3N_3H_3^+$	No	Yes*
69	$C_2N_3H_3^+$	Yes*	Yes*
68	$C_2N_3H_2^+$	Yes*	Yes*
55	$C_2N_2H_3^+$	Yes*	Yes*
54	$C_2N_2H_2^+$	Yes*	Yes
53	$C_2N_2H^+$	Yes*	Yes*
44	$CN_2H_4^+/H_2CNO^+$	Yes*	Yes
43	$CN_2H_3^+/HCNO^+$	Yes	Yes
42	CN_2H_2+/CNO^+	Yes*	Yes*
41	CN_2^+H	Yes*	No
29	CN^+H_3/COH^+	Yes*	Yes*
28	CNH_2^+	Yes	Yes

Table 3.7: Fragment ions observed in the MPI mass spectrum of guanosine and guanosine. The guanosine sample was desorbed at 0.30 W (foil temperature 388 K) and ionised with 270 nm photons at a fluence of $3{\times}10^7$ W/cm^2. The guanine sample was desorbed at 0.36 W (foil temperature 404 K) of and ionised with 225 nm photons at a fluence of $5{\times}10^7$ W/cm^2. *: Weak channels with an intensity larger than 0.5% and smaller than 5%, relative to the most intense feature in the mass spectrum. ^{a}: This signal is too strong to be attributable solely to isotopes of $[B+H]^+$.

the Berny algorithm and with estimations of the force constants. For more difficult cases, where the transitions states could not be found by this method, we requested the numerical calculation of the force constants or used the QST3 method for finding TSs (see section 2.4.4). Levola and co-workers have previously investigated uridine, thymidine and uridine derivatives and concluded that the 2'OH group destabilises the sugar ring of uridine, making its cleavage preferential over the direct N-glycosidic bond [169]. Indeed, our calculations revealed that opening the sugar ring at the 4'C–O bond in the keto-*syn* structure of guanosine$^+$ remarkably triggers an exothermic reaction

leading to fragmentation into a hydrogenated base ion (i.e. a guanine ion) and a neutral linear dehydrogenated sugar.

The reaction pathway is shown in red in Fig. 3.23 and solely presents one TS, reflecting the migration of a hydrogen, within the sugar, from the C3' to C4' position; after that, the glycosidic bond cleavage happens spontaneously as well as the hydrogen transfer from the 2'OH group to the N9 position in the base and a hydrogen transfer from the 3'OH to the 2'O. This reaction is particularly relevant for the statement made above regarding the possibility of guanine ions acting as intermediate species for fragment ions with m/z below 151 in the guanosine mass spectrum. This is because one of the products is the keto-N9H-amino guanine ion which is formed through an exothermic reaction, giving the chance for further fragmentation and/or reaction within the time window for ion detection.

A second reaction pathway leading to formation of a hydrogenated base ion was found and is shown in green in Fig. 3.23. The mechanism involves an initial hydrogen transfer from the C2' carbon to the N3 nitrogen of the base, followed by the N-glycosidic bond cleavage. Unlike the previous mechanism, both the hydrogen transfer and the N-glycosidic bond cleavage are endothermic, but the energies are lower than the TS energy of the first mechanism. The blue mechanism represents a reaction whose products are hydrogenated guanine and double dehydrogenated sugar. According to the pathways presented in the figure, the single hydrogen transfer (max. TS in the green reaction is 1.51 eV) is energetically more favourable than the double hydrogen transfer (max. TS in the blue reaction is 2.61 eV), and this is broadly consistent with the most intense feature in the mass spectra being $[B+H]^+$ and not $[B+2H]^+$. Even though, we cannot guarantee that there are not other reactions pathways leading to $[B+H]^+$ or $[B+2H]^+$ with smaller energies due to the large number of degrees of freedom of guanosine. The remaining reactions investigated are not shown because they did not lead to fragmentation of the N-glycosidic bond cleavage with transference of hydrogen(s) from the sugar part to the base part.

The ionisation of guanosine and 2'OH-deoxyguanosine by electron impact produces single hydrogenated base as the major fragment ion [158, 159, 171]. We suspect that the 151+ peak in the EII mass spectra of guanosine [158, 159] contains some signal from guanine in the target produced by thermal decomposition in view of (i) the extremely weak or absent guanosine$^+$ signal, (ii) the lack of information on the vaporisation sources (most likely ovens), and (iii) the high temperature of the guanosine sample in the AIST measurement (483 K). Adenosine (the other purine nucleoside in DNA and RNA) and the respective 2'OH-deoxyadenosine analogue, exhibits the single hydrogenated base fragment ion as the strongest feature in EII mass spectra as well [172, 173]. For these two molecules, the $[B+H]^+/[B+2H]^+$ ion signal ratio is strongly affected by the presence/absence of the 2'OH group: the presence of the 2'OH group decreases the $[B+H]^+/[B+2H]^+$ ratio. Changes in single and double hydrogenated base ion signal ratios are observed between pyridine ribo− and deoxyribonucleosides too [174, 175, 176, 177]. The extent is even larger than for adenosine/2'OH-deoxyadenosine case [170]: the major fragment ion in the cytidine mass spectrum is the double hydrogenated base ion, whereas for deoxycytidine it is the single hydrogenated base ion [174, 175]. Uridine and deoxyuridine/thymidine present the same trend [170, 176, 177]. Thus, the most intense fragment ion appearing in the mass spectra is strongly

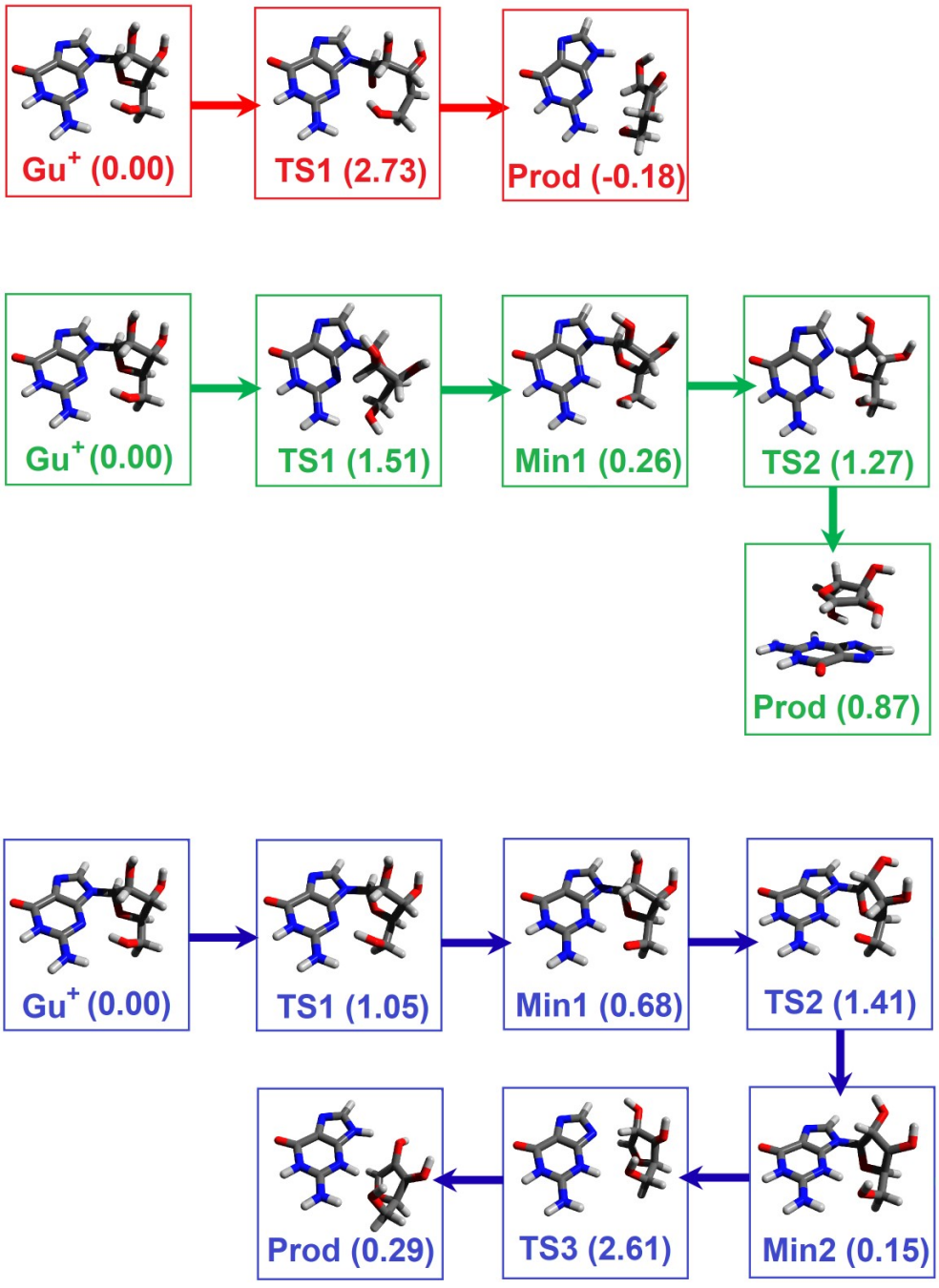

Figure 3.23: Reaction pathways of keto-*syn*-guanosine. The pathways shown in green and red produce a guanine fragment ion and a dehydrogenated neutral sugar. The pathway shown in blue produces a double hydrogenated guanine ion and a doubly dehydrogenated neutral sugar.

determined by the chemical structure of the nucleoside's sugar. As the pyridine ribonucleosides adopt preferentially an *anti* conformation [162, 178], while pyridine deoxyribonucleosides and purine ribonucleosides adopt preferentially a *syn* conformation [157, 178, 179, 180], the relative intensity of $[B+H]^+/[B+2H]^+$ signals somehow reflects the population of *syn* and *anti* conformers. The decrease of the $[B+H]^+/[B+2H]^+$ ratio with the desorption laser power shown in Fig. 3.19 is consistent with a growth of the population of *anti* conformers.

We have seen in section 3.4.2.2 that the change in the relative percentage of guanosines' tautomers/conformers with temperature in the electronic GS is much smaller than the reduction the relative fragment ion signal, particularly for the $[B+H]^+$ fragment ion. However, changes in the conformer populations are not restricted to occur in the electronic GS. Indeed, such transitions have been predicted to be energetically more favourable in electronic excited states of uridine than in the electronic GS [162]. One colour MPI experiments performed in uridine at the Molecular Clusters Laboratory manifest a variation in the sugar fragment ion yield with the laser desorption power and UV photon wavelength, indicating that a critical process is occurring in the electronic excited states, which was ascribed to conformer transitions [84]. As the energies associated with N-glycosidic bond rotation of *syn* conformers of guanosine are very low (approximately 50 cm^{-1} according to the vibrational frequency analysis performed after the optimisation of the structures in the previous section) its characteristic temperature is also very low (on the order of $\sim$ 100 K). The increase in the thermal energy may excite the these vibrational levels, improving the transition rate associated with conformer transitions in the electronic excited states. This hypothesis can be tested in future calculations of the PECs of the excited states along the N-glycosidic bond rotation as well as experimentally by monitoring the relative fragment ion production as a function of the photon wavelength.

3.5 Summary

In this chapter, we used an ILTD source to vaporise guanine and guanosine samples and investigated their radiation damage induced by one colour multi-photon ionisation with 225 nm and 270 nm pulses, respectively. We described ILTD in detail, discussed its advantages compared with other source types for certain types of experiments, and presented the first temperature vs. laser power calibration for an ILTD source.

The thermal decomposition assessment of guanine did not reveal strong signs of fragmentation prior to ionisation. This conclusion is mainly based on the much lower foil temperatures used in the ILTD experiments (maximum 399 K) compared with temperatures reported for the onset of thermal decomposition of guanine (above 613 K) and on the constant fragment ion production in the 399–449 K range. Metastable dissociation of guanine was also investigated by acquiring mass spectra at different reflection voltages and simulating the time-of-flights of the ions with a Matlab code. The metastable map exhibits a total of 16 channels. We performed, for the five lowest tautomers of guanine, DFT calculations concerning 2 of these channels (neutral loss of HCN and HCNO). The calculations and experimental data revealed a tautomer-dependent metastable fragmentation, with tautomers hydrogenated in the N7 position contributing to the loss of HCN

and tautomers hydrogenated in the N9 position contributing to HCNO loss. This investigation on radiation response of guanine highlights the importance of separating and probing individual tautomers, conformers or isomers of a molecule because each one of them can have a distinct fragmentation pattern.

Similarly to guanine, the thermal decomposition assessment on guanosine did not reveal strong evidence for decomposition of the target. The temperature of the foil during the ILTD experiments is also much lower (maximum 426 K) than the temperatures reported in the literature for the onset of thermal decomposition of guanosine (524 K). The relative production of fragment ions decreases with increasing desorption laser power. We proposed explanations for this and tested some of them by means of theoretical calculations. The first is a relative change in tautomer and conformer populations of guanosine. We determined the Boltzmann populations for the 4 lowest energy structures using their relative thermal energies calculated at DFT level and verified that this argument could not explain entirely the changes observed in the relative fragment ion production. Secondly, we investigated the possibility that the observed reduction in relative fragment ion production with increasing desorption laser power could be linked to proton transfer reactions in neutral exited states. These reactions alter the initial structure of guanosine (an isomeric-like transition) and may change the fragmentation routes of the molecule after ionisation. Although we identified one proton transfer reaction for keto− and enol−*syn* structures of guanosine, the respective barrier heights are higher than the available photon energy, thence not accessible in the current experiments. Based on several mass spectra of nucleosides, we recognised that the $[B+H]^+/[B+2H]^+$ ratio is affected by the relative population of *syn* and *anti* conformers. Transitions between structures of this type were shown to be facilitated in the neutral electronic excited states of uridine. We noted that such transitions could explain the changes in fragment ion production, including the $[B+H]^+/[B+2H]^+$ ratio. In this respect, it would be valuable to perform theoretical calculations to investigate conformeric transitions in the neutral electronic excited states of guanosine and reaction pathways in the ionic states of the *anti* conformers.

Finally, we tried to comprehend the strong ion signal for hydrogenated base in the MPI-TOF mass spectra of guanosine through calculation of reaction pathways of the keto-*syn* structure at DFT level. We verified that a particular pathway, involving the opening of the sugar ring, triggers a complex exothermic rearrangement in the molecule and culminates with guanine keto-N9H and a linear dehydrogenated sugar as products. We suspect that the guanine-N9H product can further decompose and produce the fragment ions observed in the guanine mass spectrum. The similarities between guanine and guanosine mass spectra below m/z 151 support this hypothesis. The best way to test this in a future work is to analyse the metastable dissociation of guanosine and to identify the precursor and daughter ions of each band.

3.6 Acknowledgments

The indirect laser thermal desorption system was first developed by M. Ryszka, T. Cunha and R. Pandey, previous PhD students working at the Molecular Clusters Laboratory. The system was upgraded and optimized by my PhD colleague J. Bocková. D. Bou Debes (PhD student at the OU)

and I analysed the foil temperature measurements, which were performed by S. Eden. I performed the experiments of laser desorbed guanine with the collaboration of J. Bocková and D. Mészáros, an internship student at The Molecular Clusters Laboratory. J. Bocková simulated the flight times of metastable ions in Matlab and assigned the metastable bands with the help of K. Nixon (a researcher from Wolverhampton University who recently moved to the Open University). I worked with J.C. Poully (visiting researcher from the Caen University) to construct the reaction pathways associated with the loss of HCN and HCNO fragments from guanine tautomers. I performed the the analysis of the mass spectra to extract kinetic energy releases and rate constants. I also carried the calculations of unimolecular rate constants within the quasi-equilibrium theory, using the information of the reaction pathways. The measurements of laser desorbed guanosine were performed by me and my colleague J. Bocková. I analysed the experimental data. The DFT and TDDFT calculations were performed by me with the support of J.C. Poully. J. Bocková, K. Nixon, S. Eden, and I participated in the discussion of the work.

Chapter 4

Manipulation of neutral CW molecular beams using Stark deflection

4.1 Manipulation of neutral atoms and molecules: an overview

Gas-phase molecular beams may encompass several structures of the same molecule as discussed in the previous chapter. Additionally, if internal energy is removed from these molecules, they can aggregate into clusters with different sizes and arrangements. Such 'lack of purity' can prevent us from drawing precise conclusions about the radiation response of a single structure. Indeed, the impurity of the gas-phase target for our experiments on guanosine (almost certainly containing two different guanosine structures but also possibly containing small populations of thermal decomposition products) in the previous chapter limited the conclusions we could draw from the results. Therefore, there is great potential benefit to manipulate neutral molecular beam prior to an irradiation experiment. The ideal outcome of such a manipulation is to achieve a pure target. However, if that is not achievable, the ability to change the populations of different species within a mixed beam in a controlled manner still provides a powerful tool to aid interpretations. In this chapter, we present a new Stark deflection approach that operates in the latter way to help trace specific fragment ions to specific neutral precursors in an irradiated beam.

Back in 1922, Stern and Gerlach [181] were able to deflect silver atoms by making them pass through a non-homogeneous magnetic field. The intrinsic angular momentum (spin) of silver's outer shell electron is responsible for the atom's permanent magnetic dipole moment. The non-homogeneous field produces a net force on these 'small silver magnets', deflecting them from a straight path. Upward deflection occurs for co-aligned spins whereas downward deflections occur for anti-aligned spins. Stern and Gerlach were the pioneers of atomic beam manipulation of quantum selected states. However, the manipulation of neutral molecular targets requires a different approach because most electronic ground states are closed shell configurations, totalling a null spin angular momentum, S=0 (singlet states). One property that many molecules possess and can be exploited in this context however, is non-uniform charge distribution. Molecular composition may encompass chemical groups with different electronegativities that result in a permanent electric dipole moment. Conformers or isomers of the same molecule generally have different electric

dipole moments due to a distinct spatial disposition of the atoms. Molecular clusters also have distinct electric dipole moments depending on their size and the way the component molecules bind to each other. Strong non-homogeneous electric field are capable of trapping molecules and clusters in *pendular states* where the rotation of the electric dipole moment is confined to a small angle along the field direction [182]. The species then feel a force according to their dipole moment, their rotational state and the local electric field gradient in space. This acceleration can be used to change the trajectory of specific species in a molecular beam and this is called *Stark deflection*.

Stark deflected beams are generally produced by supersonic expansion sources because rotational cooling enhances the deflection amplitude, giving a better chance of separating the various species. Recently, Küpper *et al* applied Stark deflection to a molecular beam containing water monomers and clusters, achieving a purification of 93% for the dimers [41]. Earlier achievements by Küpper and collaborators include the separation of *cis* and *trans* isomers of 3-aminophenol and 3-fluorphenol molecules [40, 183] and purification of dry and hydrated pyrrole and indole clusters [184, 185]. Stark deflection has also been used to determine electric properties of clusters. Heiles [186] showed that bimetallic lead-rich alloy clusters are barely deflected when compared with the tin-rich alloy counterpart. The analysis of the experimental data by first-order perturbation theory confirmed the enhanced dielectric properties of the latter system. The same procedure has been adopted to study charge transfer processes between alkali atoms and C_{60} molecules [187] and to investigate how temperature influences the electric dipole moment magnitude of weakly bound complexes [188]. All the studies highlighted above employed pulsed supersonic expansion nozzles where the molecules are seeded in high pressure carrier gases (up to hundreds of bars). This enables a very large flow of gas to expand into a pumped chamber during the short period of the nozzle valve being open (typically a few tens of microseconds). If the *duty cycle* (the ratio of valve open time / the pulsing period) is low then a very low pressure can be maintained despite the large gas flow during the pulses. Rotational cooling increases with greater gas flow and lower pressure in the pumped *expansion chamber*. Hence pulsed supersonic beams enabled the groups cited above to achieve sufficiently low rotational temperatures (normally in the range of a few Kelvin to a few tenths of a Kelvin) to achieve significant deflection of their target species away from the central axis of the beams and to ensure that different species are deflected by distinct distances (i.e. the *spreading out* of a specific species' trajectory due to various occupied rotational states is kept to a minimum). Pulsed supersonic beams are therefore the natural choice for using pulsed lasers to probe the deflected species, notably applying action spectroscopy methods. However, they are much less suitable for investigations involving collision processes with very low cross sections, such as dissociative electron attachment (DEA) experiments. In such cases, working with CW supersonic beams offer the key benefit of high duty cycles (typically close to 1 if not 1), maximising the signal / noise ratio achieved in a given experimental time period. For example, typical DEA measurements last several hours or days even with high duty cycles so working with pulsed supersonic beams (which must have low duty cycles, otherwise the cooling advantage compared with CW beams is low) is generally impractical. A key goal for the Molecular Clusters Group is to perform DEA experiments on molecules and clusters in Stark-deflected beams (see chapter 5) and hence it is attractive to optimise and characterise the manipulation of CW beams of molecules

/ clusters in our Stark deflection system.

As far as we are aware, manipulation of CW beams using Stark effect has only been performed with the purpose to filter some relatively small molecules (e.g. formaldehyde [189, 190] (deuterated) ammonia [189, 191] and water isotopologs [192]) according to their velocities and rotational states, using a *Stark quadrupole filter*. Zeeman deflectors can solely deflect paramagnetic molecules, like pure beams containing molecular oxygen [193] and have been, as consequence, much less disseminated than Stark deflectors. Momentum transfer methods offer an alternative to deflection experiments in non-homogeneous fields. In such experiments, a scattering beam normally composed of rare gas atoms, collide with the molecular beam in an orthogonal direction, deviating it from the initial trajectory. The deflection angle is inversely proportional to the target mass, thence enabling the detection of different molecular cluster sizes by choosing the appropriate angle of detection [194]. The disadvantage of this procedure compared with Stark deflection is the lack of discrimination of different cluster arrangements of a given size. However, despite its great potential, the usefulness of Stark deflectors in manipulating different species in CW beams has never been demonstrated in the literature.

In this chapter, we present data from two sets of electron impact ionisation experiments on nitromethane molecules and clusters in Stark-manipulated CW beams. Nitromethane (CH_3NO_2) is a rotor with a large electric dipole moment (3.46 D) and hence it appears to be suited as a test-case for Stark manipulation applications. Indeed, a previous theoretical work identified the molecule as suitable for Stark deceleration [195]. However, it can also be viewed as presenting an experimental challenge because it is larger than any molecule that has previously been Stark-manipulated in CW beams in the published literature (the largest is formaldehyde, CH_2O [189, 190] as mentioned above). Furthermore, no Stark deflection experiments on clusters in CW beam have been reported before. Nitromethane is a volatile liquid which is straight-forward to seed in a supersonic expansion and forms clusters readily [196]. Finally, nitromethane was chosen because it is a common test-case molecule for dissociative electron attachment (DEA), one of the main goals of the Molecular Clusters Group. The first experiment is discussed in section 4.8.1 and comprises the manipulation of nitromethane molecules seeded in helium CW supersonic beams. The aim of this study is to evaluate the performance of a home-built C++ code to predict the deflection profiles of molecules / clusters in our Stark deflector. For that, we monitor the fragment ion yield of the nitromethane ion signal as a function of the movable skimmer position and compare it with the simulations. In the second experiment, presented in section 4.8.2, we manipulate nitromethane molecules and clusters seeded in argon CW supersonic beams. The aim of this study is to understand if we can assign *neutral* precursor(s) to a given ion based on the suppression of its signal in the EII-TOF mass spectrum in the middle region of the molecular beam as a function of the Stark deflector voltage.

4.2 Fundamental physics behind Stark deflection

The Stark effect describes a change in the energy levels of an atom, molecule, or cluster due to a charge distortion in the presence of an external electric field. In the absence of an external electric

field, the Hamiltonian for a free rigid rotors is written as [197]

$$\hat{H}_{rot} = \hbar^2(A\hat{J}_a^2 + B\hat{J}_b^2 + C\hat{J}_c^2) \tag{4.1}$$

where $\hat{J}_a$, $\hat{J}_b$ and $\hat{J}_c$ are the total angular momentum operators, projected on the inertial axis (a,b,c). A, B and C are rotational constants associated with the moments of inertia I_a, I_b and I_c through $A=\frac{\hbar}{2\pi I_a}$, $B=\frac{\hbar}{2\pi I_b}$ and $C=\frac{\hbar}{2\pi I_c}$. The rRotors are subdivided into four categories:

1. Linear top if I_a=0 and I_b=I_c;

2. Spherical top if I_a= I_b=I_c;

3. Symmetric top if $I_a \neq I_b$ and I_b=I_c;

4. Asymmetric top if $I_a \neq I_b$ and $I_b \neq I_c$;

Analytical solutions for the non-perturbed linear and symmetric rotors exist. They are composed of spherical harmonics $|J\ M\rangle$ and Wigner matrices $|J\ K\ M\rangle$, respectively [197]. The K quantum number specifies the projection of J onto inertial axis, while M denotes the projection onto a given space axis. Solutions for the Schrödinger equation involving asymmetric rotors rely on numerical methods, because K is no longer a good quantum number. Approximate solutions for asymmetric rotors are found by using linear combinations of symmetric rotor wavefunctions [198]. The Stark Hamiltonian incorporate the contribution of the energy shifts due to the presence of an external electric field with intensity $\vec{E}$, acting on a molecule or cluster with a permanent electric dipole moment $\vec{\mu}$ [195, 198]:

$$\hat{H}_{Stark} = -\vec{\mu}.\vec{E} \tag{4.2}$$

The permanent electric dipole moment tends to couple/align with the electric field direction. The degree of alignment is improved by increasing the electric field strength. Furthermore, molecules populating lower rotational levels align more easily than rotationally hot molecules. The Stark effect thus depends on the populated rotational levels of the molecule or cluster and on the external electric field strength. We recall that the external electric field in a Stark deflector is non-homogeneous and therefore, the Stark energy shifts vary in space. Because the electric field is a conservative, changes in electric potential energy have to be counterbalanced by changes in translational kinetic energy so that the mechanical energy is kept constant. The transformation of electric potential energy into translational kinetic energy is the origin of Stark deflection: molecules or clusters in specific rotational states accelerate towards regions where their electric potential energy decreases. If the acceleration is towards higher electric fields, the rotational state is denominated *high-field seeking state*. Otherwise the molecule accelerates towards lower electric fields and the rotational state is called *low-field seeking state*. The electric force is proportional to the electric potential energy gradient:

$$\vec{F}_{el} = -\vec{\nabla}W(\vec{E}) = \mu_{eff}\vec{\nabla}\vec{E} \tag{4.3}$$

where W is the electric potential energy and μ_{eff} is the *effective electric dipole moment* defined by $\mu_{\text{eff}} = -\frac{\partial W(E)}{\partial E}$. Stark deflection generally involves the acceleration of molecules or clusters usually in a transverse direction relative to the supersonic beam propagation, while *Stark deceleration*, another application based on the Stark effect employing pulsed electric fields, involves the deceleration of targets in a longitudinal direction relative to the propagation axis. We recommend the review from Meerakker *et al.* to a more detailed description of neutral beam manipulation based in Stark effects [199].

4.3 The Stark deflection apparatus at the OU

The Stark deflection experiment was mainly built by Michal Ryszka and is described in detail in his PhD thesis [26]. It is composed by 4 chambers, each one differentially pumped and featuring skimmers to allow a beam to pass between them (Fig. 4.1). The first chamber (the expansion chamber) contains a stainless steel nozzle. The nozzle position can be adjusted using a X-Y-Z manipulation stage so the beam alignment can be refined without breaking vacuum. An external VCR / swagelok system connects the gas-line tube to a reservoir for volatile liquid samples and to He, Ar or Kr carrier gas supplies. The reservoir can be by-passed by closing a set of valves.

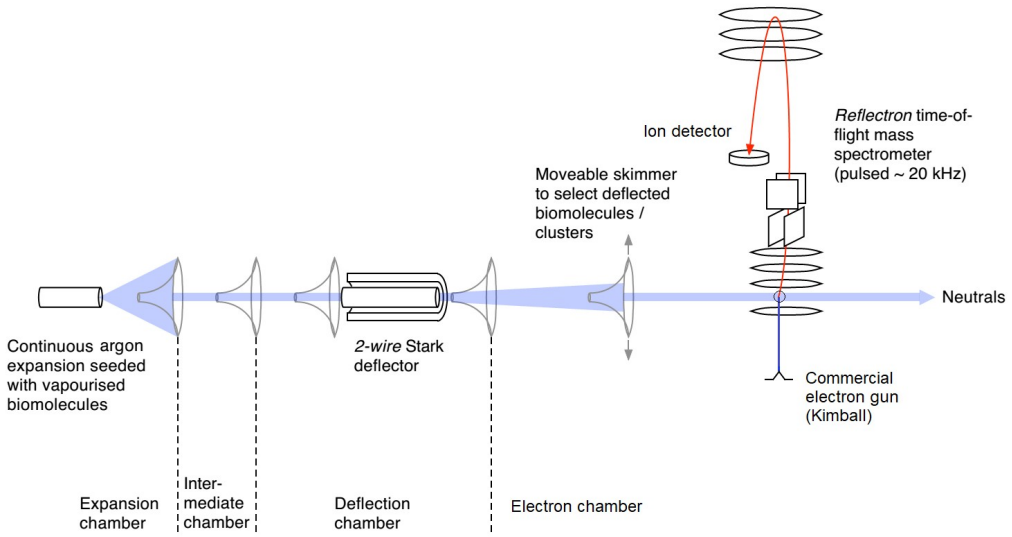

Figure 4.1: Schematic of the Stark experiment.

Solid samples can be placed in a cartridge located inside the nozzle. A resistive heating coil placed around the nozzle and fed by a variac, increases the temperature of the sample to a desired value, which is monitored by a K-type thermocouple (see Fig. 4.2 for more details). A CW supersonic expansion is established when the gas mixture passes through the nozzle orifice and enters in the expansion chamber. To enhance the rotational cooling of the molecules in the CW supersonic beam, we used a more refined nozzle that the laser-drilled nozzles (Lennox Laser) of the compact experiment. The assembly is composed by a platinum / iridium alloy (95 : 5 %) disc with a fine orifice (Agar Scientific) as shown in detailed section of Fig. 4.2. We have a set of discs with

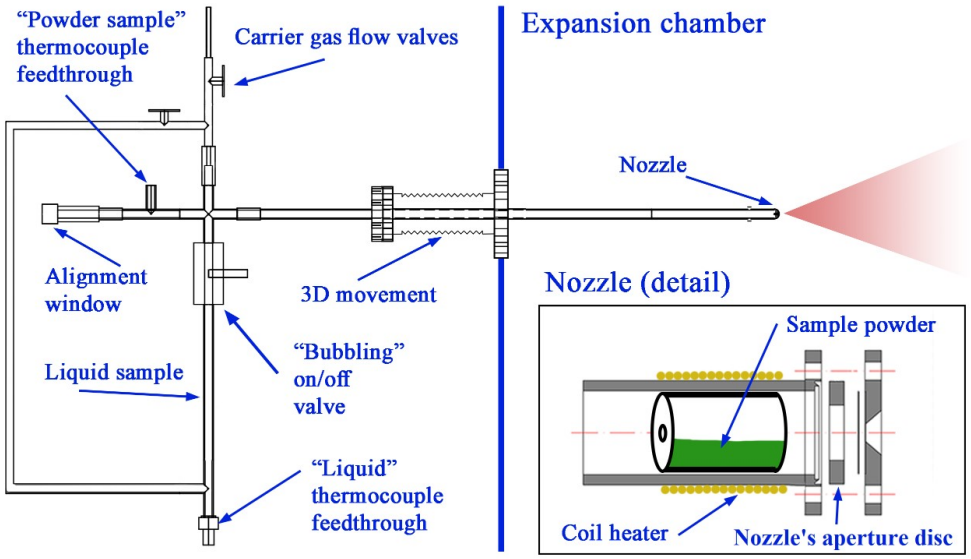

Figure 4.2: Schematic of the gas line mounted in the first chamber of Stark apparatus. The insert shows a cut of the nozzle where the cartridge for solid samples is mounted (not used in the present chapter).

different diameters (between 20 and 70 μm) which enable us to change the nozzle aperture diameter. The shape of orifices is nearly circular to minimise turbulence in the expansion. The expansion chamber is pumped by an Oerlikon Turbovac Mag W 2200 iP turbomolecular vacuum pump (2100 l/s pumping speed for nitrogen) and backed by an Oerlikon Trivac D 65B (65 m^3/h), resulting in pressures of $10^{-4} - 10^{-5}$ mbar while the supersonic expansion is flowing. In addition, when lower pressures are necessary, an Edwards and a Leybold turbomolecular pumps can be turned on to evacuate this chamber, totalling 4000 l/s of pumping speed. Terminal properties of the beam greatly depend on the vacuum conditions in the expansion chamber, as we will discuss in depth in the following sections. A small portion of the supersonic expansion passes through a conical skimmer (Beam dynamics model 2 skimmer, $\varnothing$ 2 mm) placed $1-4$ cm downstream from the nozzle before entering the second chamber, called the *intermediate chamber*. The intermediate chamber is pumped by an Oerlikon Turbovac SL 700 turbomolecular vacuum pump (690 l/s of pumping speed for nitrogen), achieving pressures of 10^{-6} mbar while the supersonic beam is flowing. The beam passes through a second conical skimmer ($\varnothing$ 1 mm) and reaches the *deflection chamber*, where the Stark deflector is installed. The deflection chamber is pumped by an Oerlikon SL 700 turbomolecular vacuum pump and the pressure during experiments is of the order of 10^{-8} mbar.

The Stark deflector has a geometry that is referred to *2-wire* (see Fig. 4.4) was built by Kupper's group. It consists of a steel rod and a trough with 3 mm and a 3.2 mm radius, respectively, and length 150 mm. The rod and trough are separated by a gap of 1.4 mm. After electrode conditioning routines, the maximum voltage that can be applied between the rod and the grounded trough without risking discharges is 12 kV. The supersonic beam passes through a third conical skimmer (diameter 1 mm) mounted in front of the Stark deflector (shown in Fig. 4.1 but not in Fig. 4.4). This skimmer defines the supersonic beam dimensions and position immediately prior to deflection (key

input information for simulating the deflector's operation). The skimmer mounted immediately after the Stark deflector (diameter 1 mm and shown in both Fig. 4.1 and Fig. 4.4) is important for aligning of the Stark deflector with the rest of the experiment but does not perform a significant role beyond that. An extension tube is installed after the deflection chamber to increase the distance travelled by molecules or clusters after the leaving the Stark deflector and hence exaggerate the spatial separation of species that were deflected differently. The extension can be considered as the first part of the *electron chamber* (Fig. 4.3). A gate valve mounted in between the deflection and electron chambers permits the interruption of the beam flow from the former to the latter. Background mass spectra are usually acquired by closing this valve. After travelling 50 cm from the back of the Stark deflector, the supersonic beam reaches a skimmer (diameter 1 mm) mounted on a 3-way movement (*movable skimmer*). The movable skimmer selects the portion of the beam to probe, either by MPI or EII. A continuous electron beam (150−200 eV in the present experiments), generated by a Kimball ELG-2 commercial electron gun, crosses the selected part of the molecular beam in the extraction region of a reflectron time-of-flight mass spectrometer (Kore Technology, matching the characteristics of the mass spectrometer in the compact MPI-TOF experiment). Extraction pulses with −380 V amplitude and repetition rate 20 – 30 kHz, extract the resultant ions towards the flight tube. Ions are detected by a chevron MCP. The electron chamber is pumped by an Oerlikon Turbovac SL 700 and backed by a Oerlikon Scrollvac SC 30D dry pump.

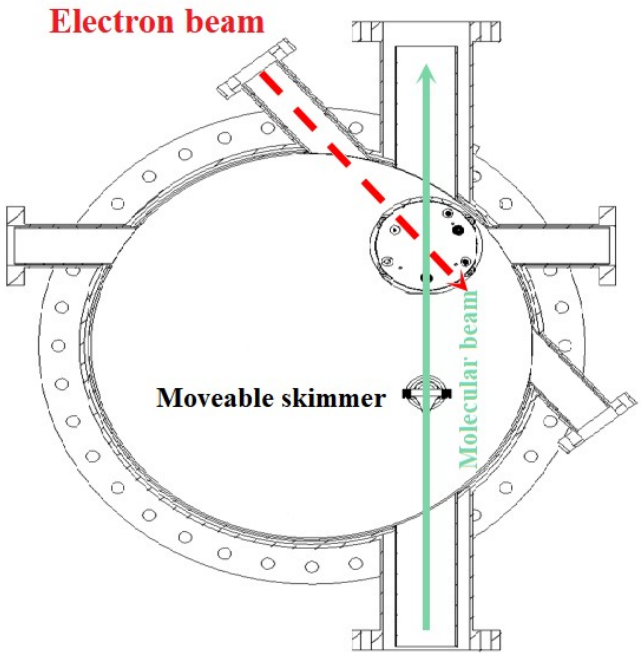

Figure 4.3: Top view of the electron chamber. The electron beam produced by the Kimball electron gun (red dashed line) crosses the supersonic beam (green solid line) in the extraction region of the TOF mass spectrometer. The movable skimmer can be moved in a direction perpendicular to the cross section of the figure. Adapted from [106].

4.4 Stark deflector electric field

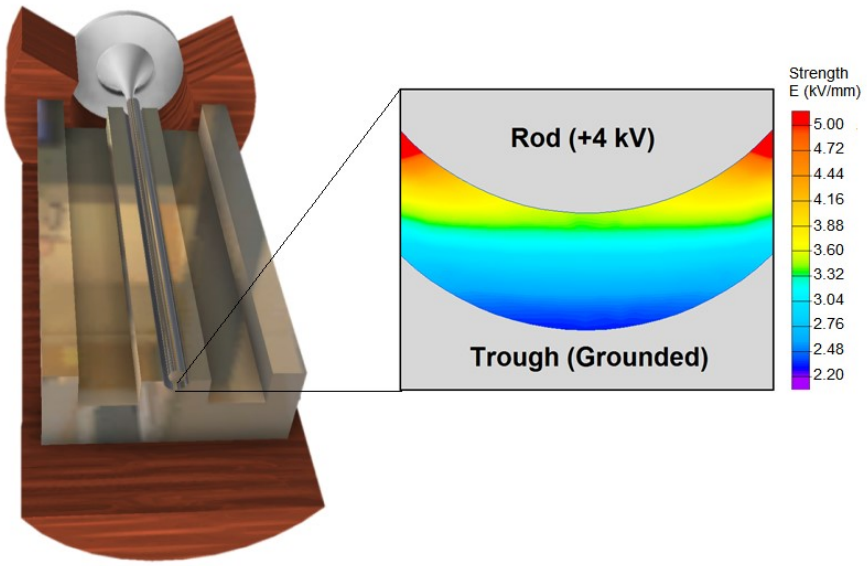

Figure 4.4: Stark deflector CAD on the left and pictorial representation of the electric field in the gap between rod and trough. Electric field values are given in kV/mm.

The knowledge of electric fields inside the deflector is crucial to model the dynamics of deflected species through equation 4.3. Solutions for the electrostatic fields of the Stark deflector were obtained through finite element analysis using the Quickfield 6.3 student version software. First, we constructed the cross section geometry of the rod-trough gap. Then, we applied a mesh with 237 nodes (0.18 mm spacing between nodes) and defined the voltages in each boundary. We set the relative electric permittivity to 1. A graphical example of the electric field strength at 4 kV is given in Fig. 4.4. The electric field strength varies linearly with distance from the bottom-most part of the trough to the bottom-most part of the rod. Therefore, we interpolated the electric field values with a first order polynomial.

4.5 Stark energy shifts

Aside from the electric field in the deflector, Stark energy shifts are also necessary to calculate the forces acting on molecular targets and ultimately, the deflection dynamics. Kupper and co-workers published a program (called *CMIStark*) to calculate Stark shifts of molecules and clusters under electric field perturbations [198]. The program receives input data concerning the electric dipole moment decomposition along inertial axis and the rotational constants of the molecule or cluster. Three modules compose the program: the first is responsible for calculating the shifts; the second prints the information in a command line; and the last shows the results on a graph. The calculation module allow us to choose the range of rotational quantum numbers to include in the

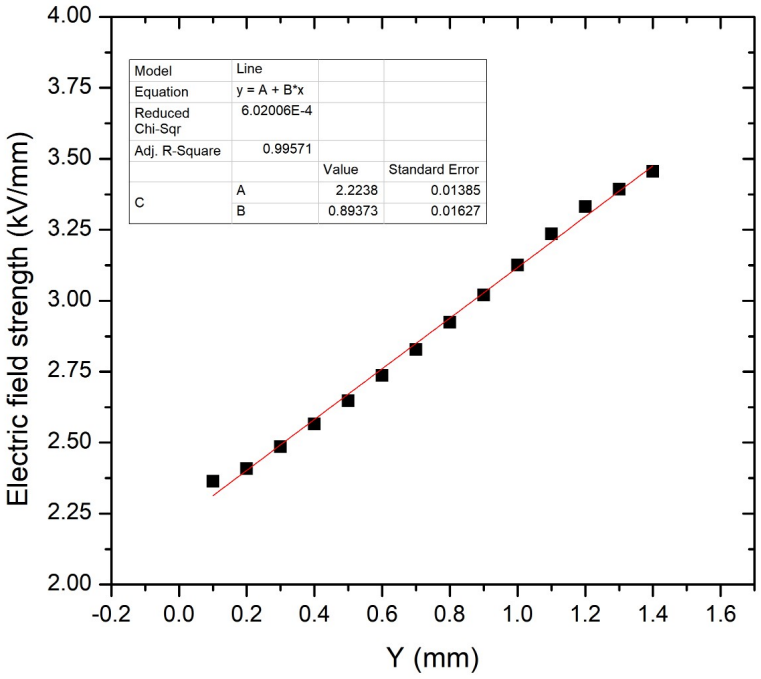

Figure 4.5: Electric field strength inside the Stark deflector, along the vertical direction (Y) for an applied voltage of 4 kV on the rod. Calculated using Quickfield 6.3 student version.

calculation: $-J_{min}$, $-J_{max}$, $-K_{min}$, $-K_{max}$, $-M_{min}$ and $-M_{max}$. We added a line of code (python) to the command line printing module in order to generate a text file containing the electric potential energy as a function of the electric field. This file will be used in our home-built code to calculate the deflections.

An example of Stark energy curves calculated using the CMIStark programme is shown in Fig. 4.6. Our curves, on the right panel are compared with those calculated by Schwettmann *et al* and exhibit a remarkable agreement. This ensures that we are using the programme in an appropriate manner to calculate the Stark energy curves of molecules and clusters.

4.6 Supersonic molecular beams

The supersonic beam properties play a critical role in determining the deflection dynamics inside the Stark deflector and are dictated by the conditions in the nozzle and its immediate surroundings in the expansion chamber. This section presents the key important concepts required to understand and characterise supersonic beams. We start by describing under which conditions a supersonic expansion occurs and specifying the different zones of a supersonic jet. Then, we discuss translational cooling and beam properties of pure and mixed expanded gases. Rotational and vibrational cooling and clustering are described in the last sections.

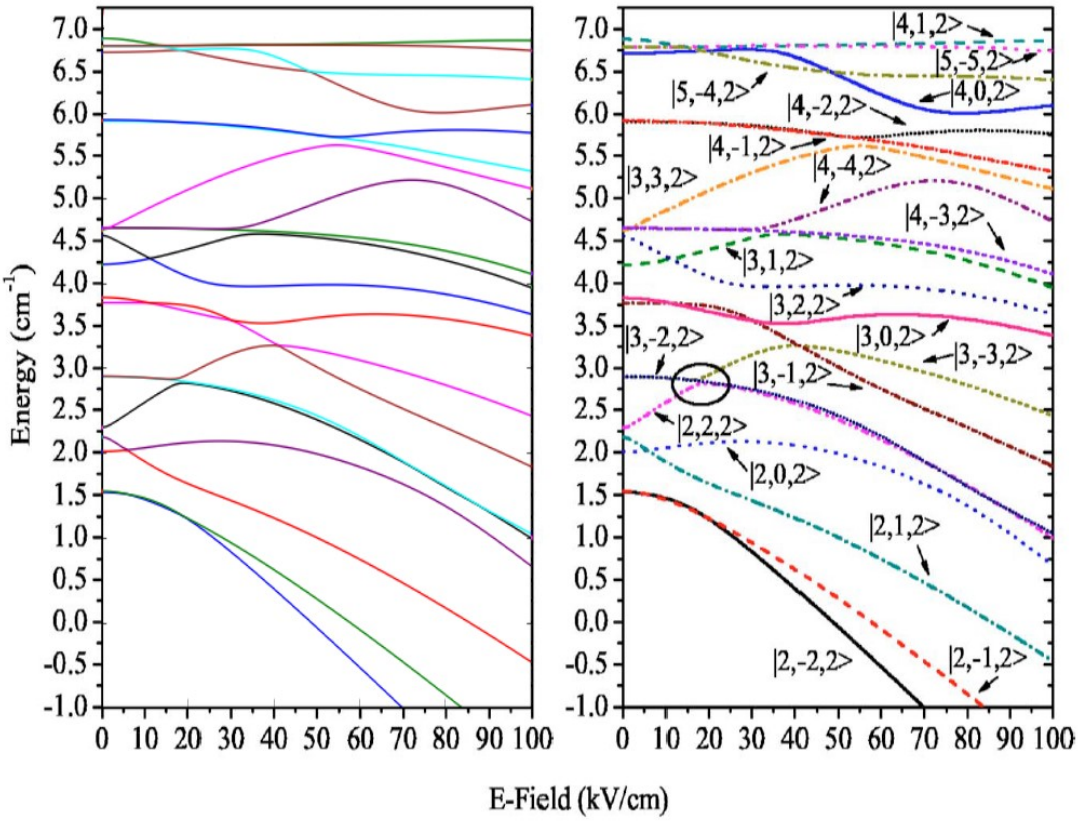

Figure 4.6: Stark energy curves for some of the nitromethane rotational states. Right: calculated by Schwettmann *et al* [195] using the nomenclature |J, τ, M⟩, where τ is a pseudo-quantum number with integer values between -J and +J for fixed J and M. Left: Calculated by our group using the CMIStark programme and using the rotational constants and the electric dipole moment given in Schwettemann work.

4.6.1 Supersonic expansion

Supersonic expansions are formed when a gas expands through an orifice whose diameter (D) is much larger than the mean free path of the gas particles (λ_0):

$$\lambda_0 << D$$

During the expansion, the gas density drops and three distinct regimes can be identified:

- A *viscous flow regime* close to the nozzle, where collisions between atoms and / or molecules are so frequent that a thermodynamic equilibrium is maintained. The equations of ideal gases are valid in this regime.

- An *intermediate regime*, where collisions are less frequent. Due to differences in the collisional cooling efficiency of internal and translational degrees of freedom, the temperatures associated with different degrees of freedom begin to decouple and thermodynamic equilibrium is broken.

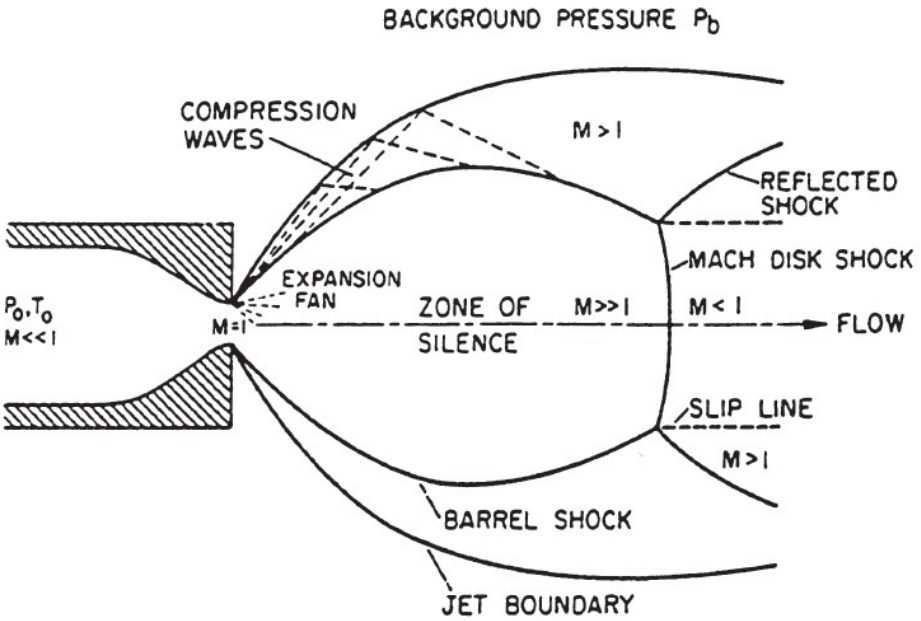

Figure 4.7: Scheme of the different zones comprising the expanded beam. M denotes the Mach number. Reproduced from [200].

- A *free molecular flow regime* where collisions are so rare that cooling effectively ceases.

Given the continuous nature of the expansion, the transition locations between these three regimes are not precisely defined. However, the molecular regime is expected to be reached after a distance of approximately 20 D, which corresponds to 0.4−1 mm with respect to the nozzles used in this thesis. Atoms and molecules in the jet, ultimately collide with residual gas and randomize their velocities, forming the *barrel shock* and *Mach disk* zones (Fig. 4.7). The barrel shock zone surrounds the beam centreline while the Mach disk, is a shock wave nearly perpendicular to the beam propagation direction. The location of the Mach disk (x_M) with respect to the nozzle orifice depends on the ratio of the source pressure (P_0) over the *background pressure* (P_B, equal to the measured pressure in the expansion chamber while the supersonic beam is flowing in our experiments) [200]:

$$x_M = 0.76D\sqrt{\frac{P_0}{P_B}} \tag{4.4}$$

In the *zone of silence* (the volume enclosed within the barrel shock and the Mach disc shock), the gas moves with an average velocity which is larger than the speed of sound: hence, the jet is supersonic. To *extract* a supersonic beam and allow it to travel a much longer distance with the aid of differential pumping, a skimmer must be placed in the zone silent zone. The skimmer's shape must be designed to introduce minimal extra turbulence (aerodynamic sides and sharp orifice edges). x_M varies between 4.8 cm and 16.8 cm in the present experiments, hence the 1−4 cm nozzle-skimmer separation is comfortably within the zone of silence.

4.6.2 Translational cooling of an expanding gas

The numerous between particles as the gas flows through the nozzle orifice result in conversion of some of the enthalpy of the gas (defined as the sum of its internal energy and the work required to achieve its pressure and volume) to translational energy in a single direction so that [201]:

$$H(x) + TE(x) = \text{constant} \tag{4.5}$$

where x is the position in the beam propagation direction, H(x) is the molar enthalpy at x, and TE(x) is the molar translational energy of the gas in the x direction. This is called an isentropic expansion, where the maximum flow velocity (vmax i.e. the flow velocity if the expansion achieves full conversion of enthalpy to translational energy in one direction) attained is given by equation 4.6. The maximum flow velocity can also be described as the terminal velocity of the beam. [200]:

$$v_{max} = \sqrt{\frac{2R}{M}\frac{\gamma}{\gamma-1}T_0} \tag{4.6}$$

where R is the molar gas constant, M is the molar mass, T_0 is temperature of the gas at the nozzle, and γ=c_p/c_v is the specific heat ratio of the gas species. The initial Maxwell-Boltzmann

Gas	γ	**Terminal velocity (m/s)**	
		300 K	393 K
He	5/3	1744	2021
Ar	5/3	558	647
Kr	5/3	385	441

Table 4.1: Terminal velocities for He, Ar and Kr at 300 and 393 K. Values calculated using equation 4.6

distribution of velocities is transformed into a narrow velocity distribution. For ideal monoatomic gases, γ=5/3 and the maximum velocity after the expansion is around 1.6 times larger than the mean thermal velocity before the expansion. The width of the velocity distribution is directly proportional to the translation temperature of the gas (Fig. 4.8), which drops along the beam streamline, as well as the pressure and density. Since temperature has a direct influence in the speed of sound, supersonic regimes are characterized by Mach numbers greater than 1 [201]:

$$M_n(L) = \frac{v(T(L))}{s(T(L))} > 1 \tag{4.7}$$

where $v(T(L))$=$\sqrt{\frac{2R}{M}\frac{\gamma}{\gamma-1}[T_0 - T(L)]}$ is the average flow velocity, $s(T(L))$=$\sqrt{\frac{\gamma RT(L)}{M}}$ is the speed of sound and $L = \frac{x}{D}$ is a reduced source distance, in units of nozzle apertures. Knowing the Mach numbers along the beam propagation enable us to estimate the beam's translational temperature

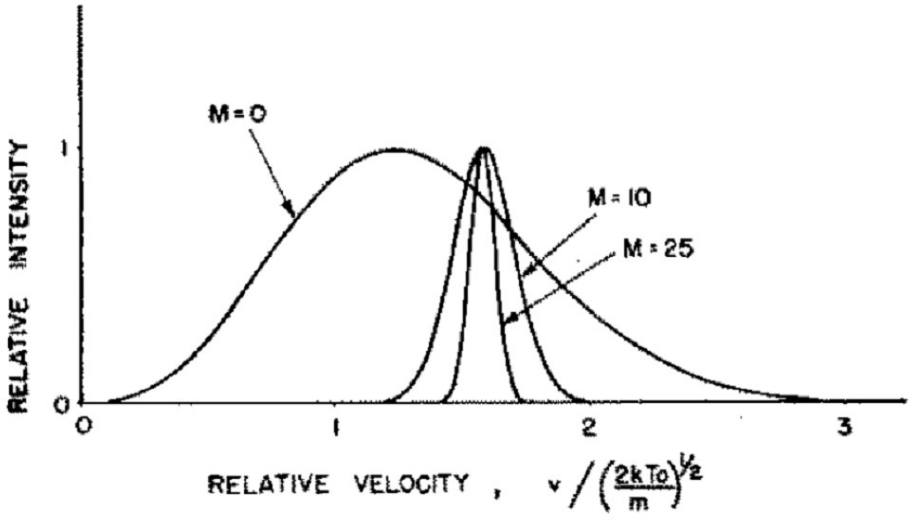

Figure 4.8: M=0 represents a Maxwell-Boltzmann velocity distribution, while M=10 and M=25 represent two velocity distributions of supersonic jets. Widths of supersonic distributions reflect the translational temperature of the beam: the narrower the width, the lower the translational temperature and larger the Mach number. Reproduced from [202].

(T(L)), pressure (P(L)) and density ($\rho(L)$) [200]:

$$T(L) = T_0\left(1+\frac{\gamma-1}{2}M_n(L)^2\right)^{-1} \tag{4.8}$$

$$P(L) = P_0\left(1+\frac{\gamma-1}{2}M_n(L)^2\right)^{-\frac{\gamma}{\gamma-1}} \tag{4.9}$$

$$\rho(L) = \rho_0\left(1+\frac{\gamma-1}{2}M_n(L)^2\right)^{-\frac{1}{\gamma-1}} \tag{4.10}$$

Andersen and Fenn obtained, through flow analysis in a converging nozzle, a formula for the Mach number in the *viscous flow regime*, valid for $L > 4$ with the form $M_n(L) = 3.2L^{2/3}$ [202]. The terminal Mach number, the Mach number when the expansion terminates, is expressed by

$$M_T = G\left(\frac{\lambda_0}{D\epsilon}\right)^{-(\gamma-1)/\gamma} = G(\sqrt{2}\sigma\rho_0 D\epsilon)^{(\gamma-1)/\gamma} \tag{4.11}$$

G is a constant solely depending on γ, ϵ is the collisional effectiveness parameter, representing the maximum fractional exchange in the mean random velocity per collision and σ is the collision cross section [201, 202]. A value of ϵ=0.25 was experimentally determined by Andersen and Fenn in pure argon supersonic expansions [202]. Lighter gases, such as helium, show much lower collisional effectiveness parameters as concluded by McClelland and co-workers in supersonic expansions of helium/iodine mixtures [203]. Grouping equations 4.8 and 4.11, we conclude that colder translational temperatures are obtained if:

- The initial gas temperature T_0 is reduced;

- Gases with fewer degrees of freedom are used — ideally monatomic gases;

- The product $\rho_0 D$ is increased. At constant temperature, this corresponds to an increase in the product $P_0 D$.

4.6.3 Seeded beams

A seeded molecular beam can be formed by vaporising molecules into a carrier gas (typically a noble gas). The properties of the gas mixture are expressed as a weighted average of the properties of the seeded and carrier gases. If the fraction of seeded molecule is very small, its terminal properties of the beam are similar to the pure carrier gas. If the driving pressure is high, carrier gas atoms will impact multiple times in the heavier seeded molecules, accelerating them to almost the same terminal velocity and temperature. Otherwise, carrier and seeded gases reach different terminal translational temperatures and velocities, the so called velocity slip effect. Amirav reported that mixtures containing light carrier gases (e.g. He or Ne) are more susceptible to velocity slipping effects and incomplete cooling than heavy carrier gases (e.g. Ar, Kr or Xe) [204].

4.6.4 Rotational and vibrational cooling

As noted above, the frequent number of collisions in the initial stage of the expansion (the viscous stage) maintains a thermodynamic equilibrium between internal and translational degrees of freedom. However, as the expansion evolves, the gas density (and consequently the collision rate) drops, leading to a decoupling between the internal and translational degrees of freedom. Typically, vibrational degrees of freedom decouple first because vibrational-translational (V−T) relaxation is a slow process requiring a large number of scattering events [205, 206]. Rotational-translation relaxation is a much faster process and thence, rotational degrees of freedom decouple later. Hence a supersonic expansion generally produces a beam with $T_{vib} > T_{rot} > T_{trans}$. For example, Amirav *et al.* were able to cool down tetracene ($C_{18}H_{12}$) in Ar (P_0D=3.2 − 4 mbar.cm) to vibrational and rotational temperatures of T_{vib}=50 K and $T_{trans} \approx T_{rot}$=3 − 7 K. However, even molecules with such low rotational temperatures may populate several rotational states since the energy gaps between energy levels tend to be smaller in larger molecules and clusters. Indeed, the difficulty of producing supersonic beams with low levels of rotational excitation limits the size of molecules and clusters that can be separated effectively using Stark deflection.

4.6.5 Clustering

Apart from being a great source of cold molecular beams, supersonic expansions also allow the formation of clusters. Dipole bonded (e.g. Van der Waals or hydrogen-bonded) complexes can be formed via three body collisions, with the third body carrying out the binding energy of the cluster. This mechanism increases the rotational and translational temperatures of the beam in comparison to a situation without condensation. While two-body collisions promoting the cooling of the expanding gas are proportional to $P_0 D/T_0$, three-body collisions scale with $P_0^2 D/T_0^2$. In order to

increase the chance of clustering, with the same mass throughput, the reservoir pressure should be increased and the nozzle orifice diameter should be decreased, such that p_0D^2 remains constant. Yang and co-workers verified that the size of CH_4 clusters formed in gas mixture expansions was doubled when the nozzle temperature was decreased from 27 ºC to −30 ºC [207]. However, the vast number of experiments performed by our group in supersonic beams shows that the driving pressure has a minor effect on clustering. In our experiments to increase clustering: (1) we use Ar instead of He, (2) we increase the temperature of the sample(s) and hence the abundance of molecules that can cluster together and (3 - but less significant) increase the pumping in the expansion chamber.

4.7 Simulation of deflection profiles

The interpretations of our experimental results depend critically on our ability to predict the deflection profiles for each rotational state of specific molecules and clusters in our experiment. A key part of this PhD was the development a C++ code for this purpose, which be found in appendix C. As the code is very extensive, we report here briefly the main functions and procedures. When executing the program from the command line, the user is asked for the initial parameters:

- The carrier gas (He, Ar or Kr), pressure and temperatures in the nozzle: P_0 (in bar) and T_0 (in K);
- The mass (in a.m.u.) and name of the seeded molecule or cluster;
- The time step for integration of Newton's equation of motion Δt (in μs);
- The deflector voltage (in kV);
- The output file from the CMIStark software containing the Stark curves for each rotational state of the molecule or cluster;
- The rotational temperature to use in the Boltzmann distribution of rotational states.

The inputs are stored in appropriate variables. The first step calculates the terminal translational temperature and the maximum and mean velocities of the beam, assuming that it is composed by a pure monoatomic gas. The program then reads the CMIStark output file that contains the Stark energy curves for each rotational state, counts the number of states and allocates the respective memory for electric field strengths and Stark energies in the arrays *state_field* and *state_energy*. A second passage through this file has the purpose of copying the field strengths and Stark energies, attributing a Boltzmann factor $e^{-W|_{E=0}/k_BT_{rot}}$ according to the unperturbed rotor energy $W|_{E=0}$, and perform the dynamics in a state-by-state manner. The starting conditions are defined as a

point source centred in the middle of the deflector (Y = 0 mm, where Y is the direction of the deflection axis), moving with the maximum velocity (v_x) of the beam. The electric field at a certain vertical position (Y) is calculated by an auxiliary function called *determine_local_field*. The electric fields are implemented for 1, 2, 4, 6, 8, 10 and 12 kV voltage difference between rod and trough, through the first order polynomial obtained from the Quickfield results (e.g., fit in Fig. 4.5 for 4 kV applied on the rod). Electric fields for other voltages may be easily integrated. After knowing the field strength at the actual vertical position, the acceleration is calculated by an approximate differentiation form of equation 4.3:

$$\vec{a} = \frac{\vec{F}_{el}}{M_{mol}} = -\frac{\vec{\nabla} W}{M_{mol}} \approx -\frac{\Delta W}{M_{mol} \times \Delta y}$$

The values for ΔW are searched in the *state_energy* array, such that the electric field at the actual position is in between both. Δy is given by *DER_STEP*, a value that needs to be changed for each voltage in order to scale the distances. The dynamics is performed with a Verlet algorithm [208]. At each time step, a *collision condition* is verified: if the vertical position is greater than 0.7 mm or smaller than −0.7 mm, the molecule or cluster crashes into the deflector rod or trough and the dynamic cycle is interrupted for that rotational state. Otherwise, a new cycle is tested until the molecule or cluster leaves the deflector enters in a free field region. By knowing the transverse velocity (v_y) and vertical position at the exit of the deflector, the vertical position of the molecule or cluster and the Y position of the movable skimmer is calculated by simple geometric arguments. After having calculated the dynamics for all the rotational states on the CMIStark output file, the program terminates with the generation of a comma separated value (.csv) extension file, containing the positions and velocities in each instant inside the deflector and the final position of the molecule when reaching the movable skimmer. Boltzmann factors are printed in a dedicated column. The .csv file then needs post-processing, namely, the normalization of the Boltzmann factors and the respective summation contributing to a given deflection. In the end, a normalized intensity as function of vertical deflection is obtained. However this profile does not take into account the initial profile of the molecular beam (i.e. its divergence and width). This correction is made *a posteriori*, by convoluting an undeflected profile measured experimentally with the simulated deflection profile. Similar corrections have been applied before by other groups [209, 210]. The convolution program is selected by prog==1 and the points of measured undeflected profiles are contained in the matrices *undef_beam1[][2]* for the helium and *undef_beam2[][2]* for the argon experiments discussed in this thesis. New undeflected beam profiles should be used in each set of experiments to allow for small variations in nozzle alignments.

4.8 Results

4.8.1 Manipulation of neutral nitromethane molecules seeded in helium

The aim of the experiments in this section was to measure a complete Stark deflection profile of nitromethane molecules. Helium was the chosen carrier gas for two reasons. Firstly, the Stark deflector provided by Küpper combined with its separation from the probe beam (matching his

group's experiments on 3-aminophenol [40]) is ideally suited to achieve deflections of several mm of molecules seeded in helium beams. The most-deflected molecules in slower supersonic beams will tend to crash into the deflector (as shown in section 4.8.2). This effect cannot be compensated effectively by using extremely weak deflecting fields because Stark curves often have steep and complex shapes below around 20 kV/cm which makes controlled Stark deflection extremely difficult (see Fig. 4.6). Secondly, we did not want significant clustering in the present experiments because this would complicate our test of the agreement between the experimental and simulated deflection profiles. Helium expansions lead to much less efficient clustering than argon expansions (as discussed in section 4.6.5).

The nitromethane reservoir (see Fig. 4.2) was left at room temperature during the present experiments and we used the nozzle with a disc aperture of 20 μm. The vapour pressure of nitromethane at room temperature is 36 mbar, representing 6 % of the beam composition. The He driving pressure was 560 mbar (the lowest we could regulate). Combining a small orifice with a low driving pressure and substantial pumping at 4000 l/s enabled us to achieve an expansion chamber pressure of 8×10^{-6} mbar during the experiments. Keeping this pressure as low as possible was important to achieve the most effective rotational cooling possible.

We performed measurements at 0, 4, and 8 kV applied on the Stark deflector. In these measurements the skimmer right after the Stark deflector was removed (it only served to laser-align all the skimmers in the experiment). The movable skimmer was moved in the deflection direction (Y) in steps of 0.5 mm and an electron beam of energy 150 eV and emission current 20 μA ionised the portion of the molecular beam that passed through it. The mass spectrometer voltages were optimised looking for maximum difference in signal between 0 and 4 kV on the deflector. This resulted in a different set of optimal voltages than the ones that yielded the highest absolute signals. This 'maximum Stark deflection' optimisation of the mass spectrometer can be rationalised in terms of finding conditions that preferentially sample ions that originated from the rotationally-coldest molecules in the beam. Such a selection is plausible because the rotationally-coldest molecules will tend to have experienced more collisions in the expansion and hence will tend to have velocities that are closer to the helium atoms in the beam (less *velocity slip*). Modelling the mass spectrometer acceptance with respect to ion velocity and position is very difficult in the present experiments because (i) we do not have a detailed characterisation of the electron beam shape and (ii) the time between extraction pulses was sufficient for ions to travel to different parts of the TOF source prior to extraction. However, while we do not know the specific mechanics of this optimisation, the key message to draw from it is that the rotational temperature of the molecules sampled in this experiment is almost certainly lower than the rotational temperature of the molecular beam as a whole. Four mass spectra were acquired for each position of the movable skimmer at a given deflection voltage. We measured a total of six background mass spectra, two at each voltage, by closing the gate valve between the Stark and the electron chambers.

Input parameters for simulation of the deflection profiles were taken from literature: rotational constants are available from experimental microwave spectroscopy data (A=13.34 GHz B=10.54 GHz and C=5.87 GHz [211]), while the electric dipole moment decomposition was obtained from [195].

The experimental undeflected and deflected profiles are shown in Fig. 4.9 as blue crosses and red open circles, respectively.

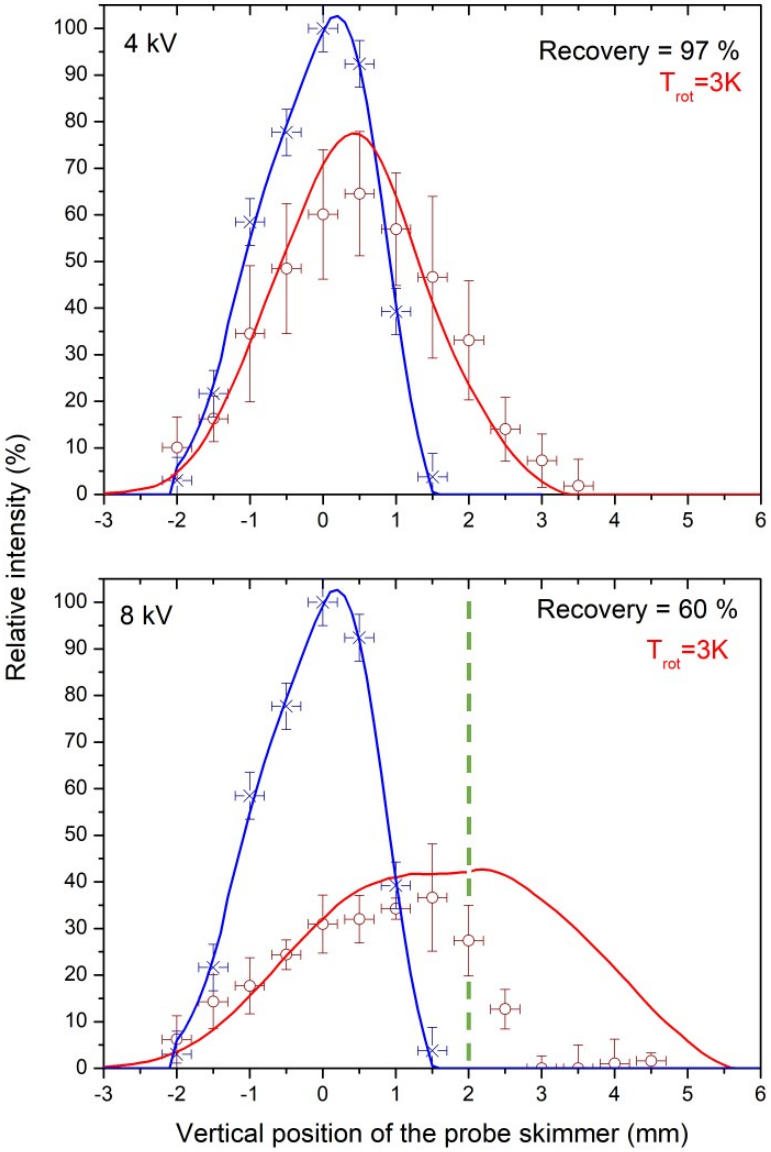

Figure 4.9: Deflection profiles of nitromethane ion signal seeded in helium at 4 kV and 8 kV. Blue crosses correspond to the intensity of the undeflected beam. The solid blue curve was obtained from a fit to the points. Red open circles correspond to the measured intensity of the deflected beam and the solid red lines represent the simulated deflected profiles. The recovered percentage of the nitromethane ion signal is given for both cases. The vertical dashed green line represents the movable skimmer position at which our simulations begin to disagree with the experimental points.

The width of the undeflected profile (approximately 3.5 mm) is the expected width (3.6 mm) of a divergent beam at the movable skimmer calculated based on the relative positions of the nozzle,

the skimmer in front of the Stark deflector and the movable skimmer, and the respective orifice diameters'. This is reassuring and shows that the electron beam is distinctly wider than the diverged molecular beam. The deflected profiles exhibit a clear shift of the beam maximum position by 0.5 mm at 4 kV and 1 mm at 8 kV, relative to the undeflected profile. The beam is also broadened from a width of 3.5 to 5 mm. A reasonable agreement between the experimental and simulated profiles (represented by solid red lines) can only be expected when the signal recovery percentage is high (e.g., the 4 kV profile). For low signal recovery percentages, the agreement is only reasonable for movable skimmer positions up to 2 mm from the beam centreline, as shown by the vertical green dashed line at 8 kV. A narrow electron beam may be responsible for the undetected signal.

Using the formula 4.11, the terminal Mach number of a pure helium beam with the specified initial conditions should be around 2.9 and the respective terminal translational temperature that follow from equation 4.8 is 76 K, a value that is much higher than the rotational temperature predicted from matching simulated profiles with experimental data points. The effective collisional parameter of helium ϵ_{He}=0.02 was derived by McClelland assuming that rotational and translational temperatures of the diluted iodine molecules and the diluent helium atoms were approximately the same. Thence, the value of the effective collisional parameter is expected to be specific for that case and not transferable to other gas mixtures as the nitromethane + helium. Helium-to-iodine mass ratio is much smaller than helium-to-nitromethane and therefore, a more efficient cooling is expected for the later gas mixture. In fact, when we use an effective collisional parameter similar to the argon, ϵ=0.25, the expected terminal translational temperature is 12 K, providing a closer agreement with the rotational temperatures of our simulations. We recall that we tuned the TOF mass spectrometer voltages to probe the rotationally-coldest and fastest portion of our molecular beam. Anyway, we do not aim to determine the rotational or translational temperatures of the molecules seeded in the supersonic beam. The main purpose of the present work is to assess the performance of the home-built C++ code in simulating the deflection profiles of the molecules / clusters in the supersonic beam after crossing the Stark deflector. With this respect, we conclude that the deflection simulations agree with the experimental data points of the deflection profiles up to 2 mm of the skimmer position. This is a great limitation in terms of our deflection experiments. Instead of attempting to deflect and probe molecules far off from the beam centreline, the best way of using our Stark deflector is by analysing the suppression of ion signal in the beam centreline, where our C++ code predicts well the deflection profiles. In the next section, we evaluate if this methodology enable us to identify the origin of fragment ions in respect to neutral precursors of nitromethane monomers and clusters.

4.8.2 Tracing reaction products to specific neutral clusters of nitromethane in Stark deflected beams

Our aim in this section is to use Stark deflection to gain insights into the origins of different ionisation products from a mixed beam. No attempts to do this have been published to date using CW beams. The previous section shows that the present construction of the Stark deflection experiment is not well suited to probing species that have been deflected by significantly more

than the width of the undeflected beam. This essentially limits us to experiments based on ionising molecules and clusters that remain on the axis of the supersonic beam, while others are Stark deflected away. In general, the molecules and clusters which are least affected by the Stark deflector voltage will be those in higher rotational states and / or with low dipole moment / mass ratios. This necessity to stay on the supersonic beam axis is certainly a limitation but it also brings advantages. Most importantly, it opens the way for using slower-moving carrier gases than helium, notably argon. This means that molecules and clusters spend longer in the Stark deflector and a small vertical acceleration will lead to a bigger deflection at the movable skimmer position. Therefore a small Stark effect causes much greater *Stark removal* in an argon beam than it does in a helium beam. Molecules / clusters deflecting too far and / or crashing into the deflector is not a problem in Stark removal. Hence, Stark effects can be harnessed in molecular beams with higher rotational temperatures when we work with argon than with helium. This is particularly valuable for us because working with CW beams makes it very difficult to attain low rotational temperatures. Secondly, clusters form more readily in argon expansions than helium expansions and one of the Group's main goals is study reactions within specific cluster configurations.

In the present experiments, we used 500 mbar of argon to seed nitromethane molecules in a supersonic beam produced in a nozzle with an orifice diameter of 20 μm. The nitromethane sample was kept at room temperature. The pumping speed on the expansion chamber was 2100 l/s giving a working pressure of 4×10^{-5} mbar. The movable skimmer was kept static at $Y = 0$ mm, where the maximum signal of NM^+ is observed. The mass spectrometer voltages were optimised to obtain maximum ion signals, opposing to the optimisation performed in section 4.8.1 where we tried to obtain the maximum ion suppression. The supersonic beam was crossed by an electron beam of 200 eV and the resultant fragment ion were analysed by TOF mass spectrometry. One mass spectrum was recorded at each deflector voltage, which ranged from 0 to 12 kV, in steps of 0.5 kV. Two background mass spectra were acquired at the beginning and at the end of the scan, by closing the gate valve in between the Stark chamber and electron chamber. To account for small variations of the emission current of the electron gun, we normalised the mass spectra so that the Ar^+ signal had the same intensity in all of them. This approach enables us to monitor the variation of different ion signals as a function of the deflection voltage, which we can attribute to the removal of neutral precursors molecules or clusters from the beam.

Two mass spectra acquired with 0 kV and 12 kV applied on the Stark deflector are presented in Fig. 4.10. Two observations stand out from the figure. The first is the presence of nitromethane clusters, giving rise to fragment ions above the monomer (m/z value 61), notably protonated nitromethane ($(NM)H^+$, m/z = 62), methylated nitromethane ($(NM)CH_3^+$, m/z = 76) and nitromethane dimers ($(NM)_2^+$, m/z = 122). These ions were previously observed in the EII-MS of nitromethane clusters in helium nanodroplets (further discussion in section 4.8.2.2). Secondly, there is substantial suppression of monomer signals, but relatively minor suppression of cluster fragment ions when a voltage of 10 kV is applied in the Stark deflector. The contrast is surely linked with the different properties of precursor neutrals (e.g. electric dipole moment / mass and rotational constants), which directly affect the deflection amplitude.

In order to investigate if specific neutral precursors of different fragment ions can be identified,

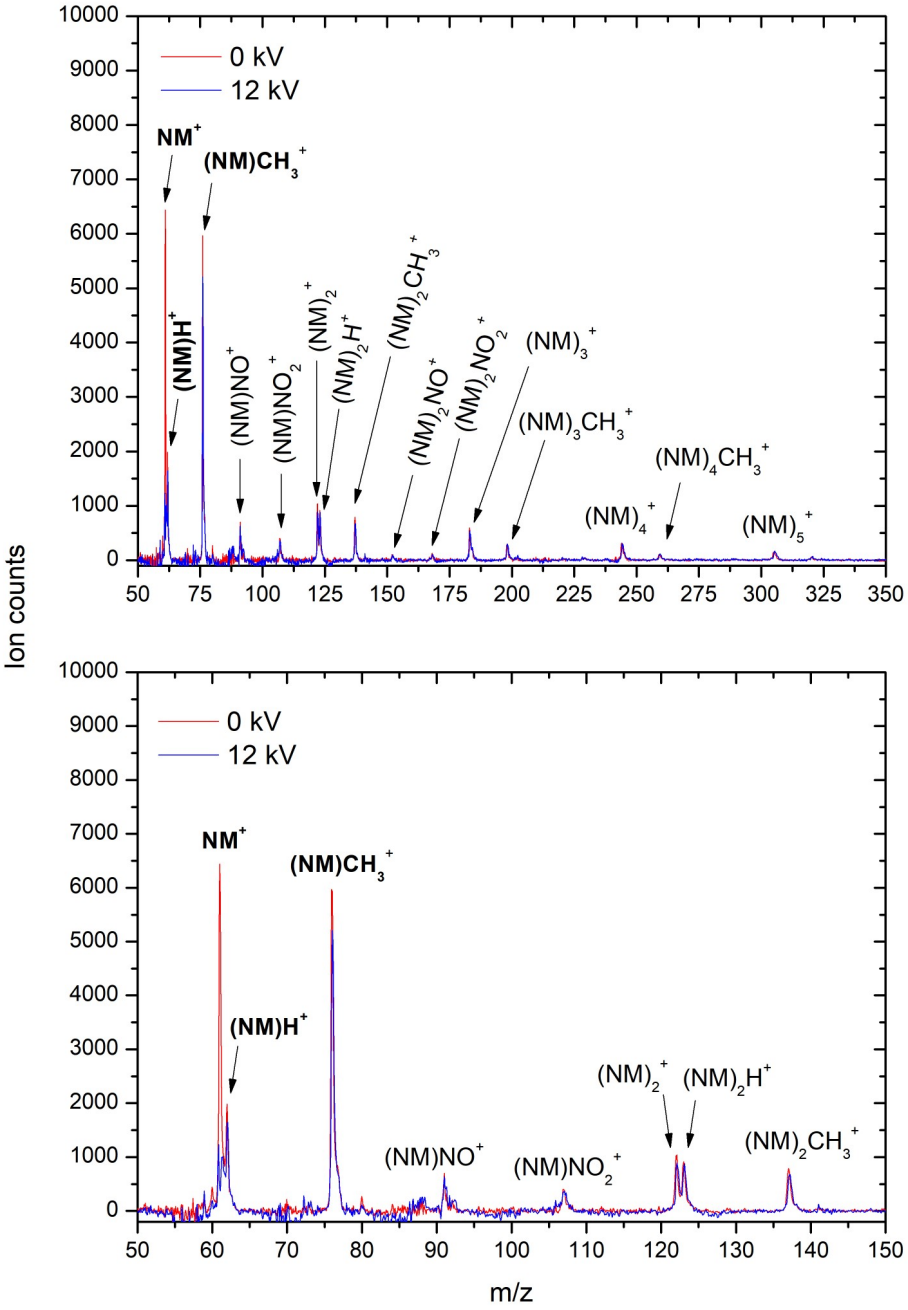

Figure 4.10: Electron impact ionisation mass spectra of nitromethane seeded in argon at 0 kV (red) and 12 kV (blue) deflection voltages. The upper panel shows an extended m/z range, where cluster ions up to the pentamers can be observed. Prominent signals for fragment ions from clusters are visible at m/z=62 (protonated nitromethane, $(NM)H^+$) and m/z=76 (methylated nitromethane, $(NM)CH_3^+$). The bottom panel shows that the NM^+ ion signal exhibits a larger degree of removal than cluster fragment ions and the dimer ion ($(NM)_2^+$), and this is attributed due to the distinct Stark effects of the respective neutral precursors.

we need to determine electric dipole moments and rotational constants of different sizes and conformations of clusters. Li and co-workers obtained three optimised geometries of nitromethane dimers at MP4SDTQ/6-31G*//HF/6-31G* level [212]. We performed our own optimisations at DFT level, with M06-2X functional and an aug-cc-pVDZ basis set. This functional has shown to be superior to others in describing non-covalent systems [70]. Empirical dispersion was included by applying the Peterson Frisch model. The input geometries were similar to the ones reported by Li. The absence of negative frequency values ensured that optimised geometries correspond to minimum energy structures and not to saddle points. The optimisation procedure converged towards only two structures. We refer to the first as the *side-by-side dimer* (SSD), where the molecules are anti-parallel to each other, and interact via dipole-dipole forces (Keesom interaction). We refer to the second as the *collinear dimer* (CD), where the molecules align one after the other, also interacting via dipole-dipole forces. Similarly to Li's energy calculations, the most stable conformer at M06-2X/aug-cc-pVDZ+PFD is the SSD. We went further and performed geometry optimisations for trimers, obtaining a total of three structures: the side-by-side trimer (SST), the collinear trimer (CT) and the triangular trimer (TT). All the structures can be found in Fig. 4.11. Electric dipole moments, rotational constants and relative energies are given in table 4.2.

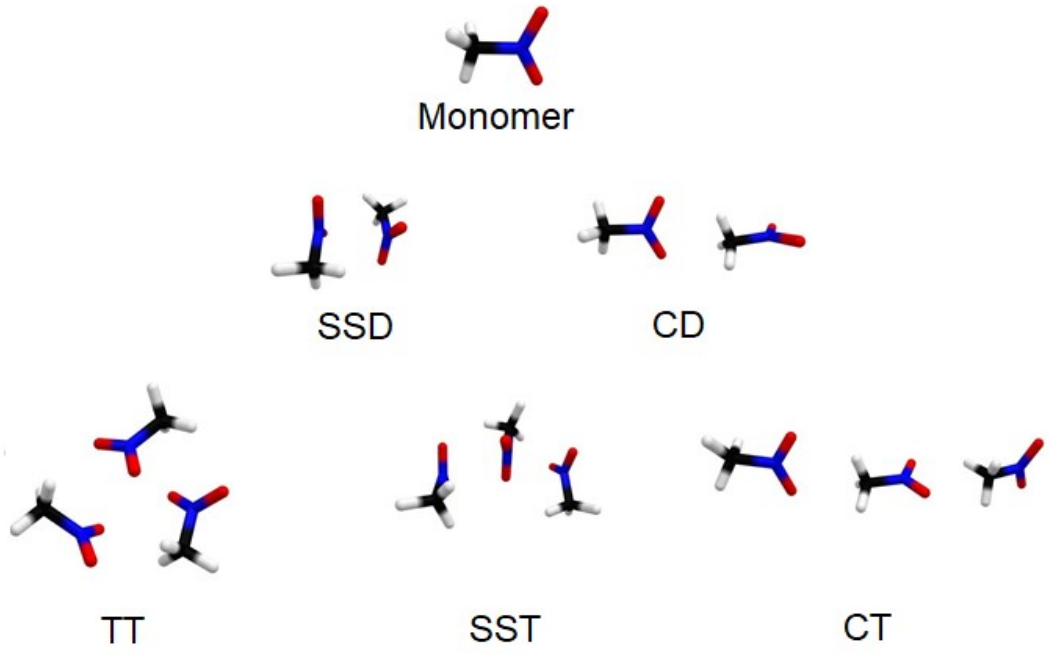

Figure 4.11: Geometries of the optimised monomer, dimer and trimer structures at M06−2X/aug−cc−pVDZ level.

These parameters were used to generate the Stark energy shifts with the CMIStark software. The density of rotational states increases for larger clusters, as can be understood by the smaller rotational constants. For that reason, we requested the calculation of a larger number of rotational

states for clusters ($J \leq 70$) than for monomers ($J \leq 30$). The experimental NM^+, $(NM)H^+$ and

Structure	μ	A	B	C	Rel. energy
	D		GHz		meV
Monomer[a]	3.46	13.34	10.54	5.87	–
Side-by-side dimer (SSD)	0.55	2.98	1.56	1.49	0
Collinear dimer (CD)	8.11	6.01	0.59	0.58	150
Triangular trimer (TT)	2.01	1.16	0.76	0.55	0
Side-by-side trimer (SST)	3.36	1.58	0.47	0.45	112
Collinear trimer (CT)	12.71	3.61	0.16	0.16	505

Table 4.2: Electric dipole moment, rotational constants and relative energies of the optimized nitromethane monomer, dimers and trimers. Relative energies include zero-point corrections.[a]: The electric dipole moment value was taken from [195] and the rotational constants from [211].

$(NM)CH_3^+$ signals are shown in Fig. 4.12, along with simulated removal curves for nitromethane monomer (dashed lines in the upper panel), SSD and CD structures for a selection of possible rotational temperatures (dashed and full lines in the bottom panel, respectively). NM^+ ions are suppressed more than cluster fragment ions, in agreement with Fig 4.10. None of the simulated removal curves for pure nitromethane fit the experimental points over the full range of voltages. This is an indication that there is some contribution from neutral clusters precursors to the NM^+ ion signal. Indeed, good agreements are achieved for mixtures of NM monomers and a specific dimer, the side-by-side dimer. Assuming that the monomer and SSD to have the same rotational temperature, the best agreements were observed for rotational temperatures between 10 and 20 K. In general, the cooling efficiency depends on the cluster size, that is, the rotational temperature of monomers and dimers will not necessarily be the same. It is worth noting that Küpper and co-workers predicted slightly different rotational temperatures for indole and indole-water species in their helium pulsed supersonic beam [184]. Furthermore, while velocity slip effects are much less significant in seeded Ar beams than seeded He beams, we cannot rule out the possibility that the present optimisation of the mass spectrometer favours sampling different velocities and hence different rotational temperatures of different species in the beam. Therefore, we tested how one of the fits in the upper plot of Fig. 4.12 would be modified by assuming a substantial difference in rotational temperature between the monomers and clusters in the supersonic beam. As shown in Fig. 4.13, a very good agreement between the experimental and simulated removal curves is also achieved when considering T_{rot} = 10 K for monomers and T_{rot} = 50 K for SSD (the maximum rotational temperature that can be simulated for these species without severely compromising the accuracy). This shows that the present conclusion that monomer ions do not come exclusively from neutral monomers in the present experiments is not dependent on assuming equal rotational temperatures for monomers and clusters in the beam.

The results from the previous and current section show us that efficient rotational cooling of nitromethane monomers can be attained, when seeded both in helium and argon. Indeed, formation of VdW complexes in heavy carrier gases (e.g. Ar) does not occur before rotational-vibrational cooling has been achieved [204]. Formation of VdW complexes in light carrier gases is quenched

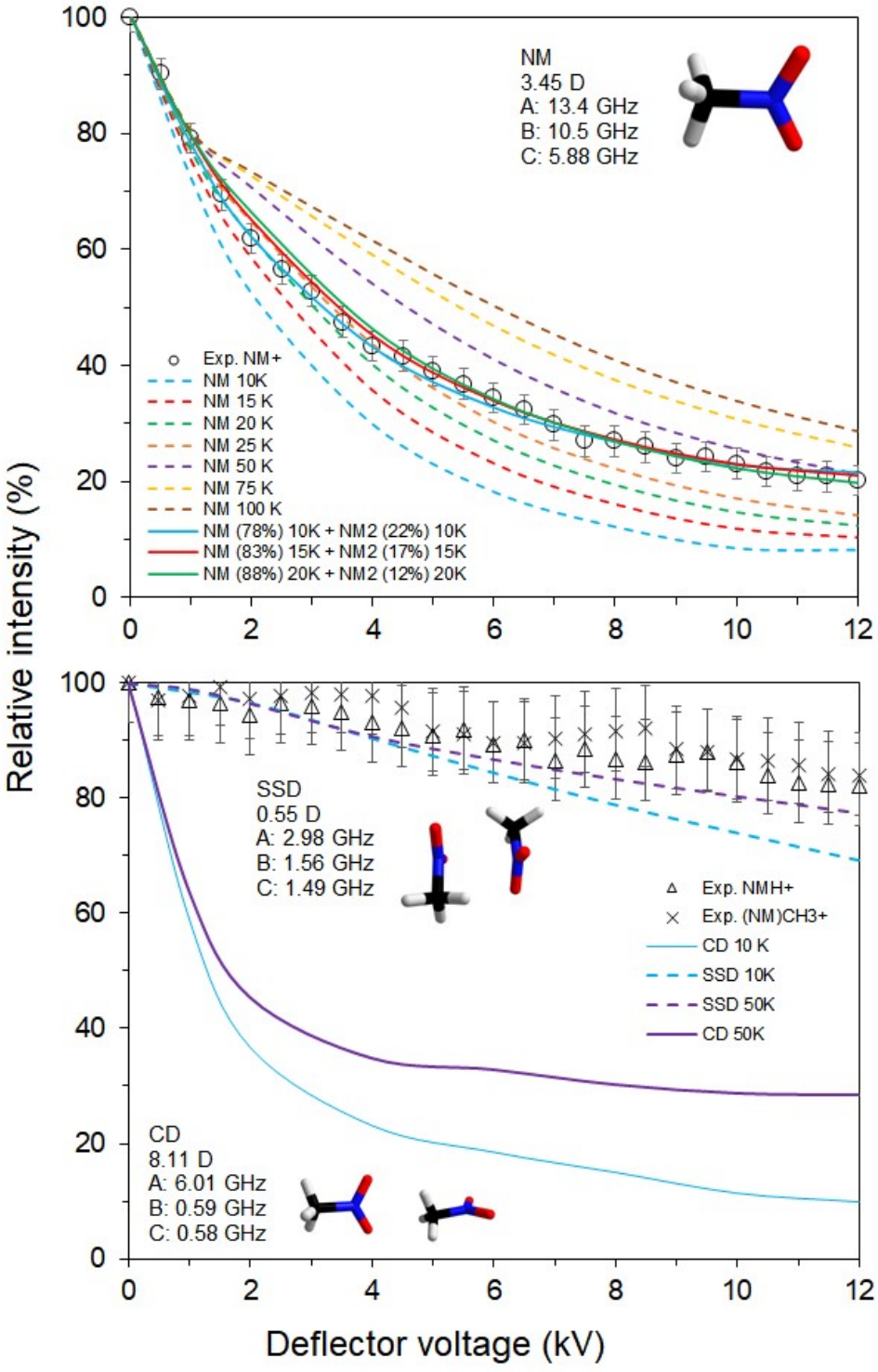

Figure 4.12: Upper panel: simulated removal curves of nitromethane monomers (dashed) and combinations of monomers and side-by-side dimers (full) at different rotational temperatures. Experimental points of NM^+ ion signal are given by open circles; Bottom panel: removal curves of side-by-side dimers (dashed) and collinear dimers (full). Experimental points of $(NM)H^+$ and $(NM)CH_3^+$ ion signals are given by open triangles and crosses, respectively. Removal curves for the dimer ion itself and for the protonated dimer ion are not presented due to large fluctuations linked to relatively low signal-to-noise ratios.

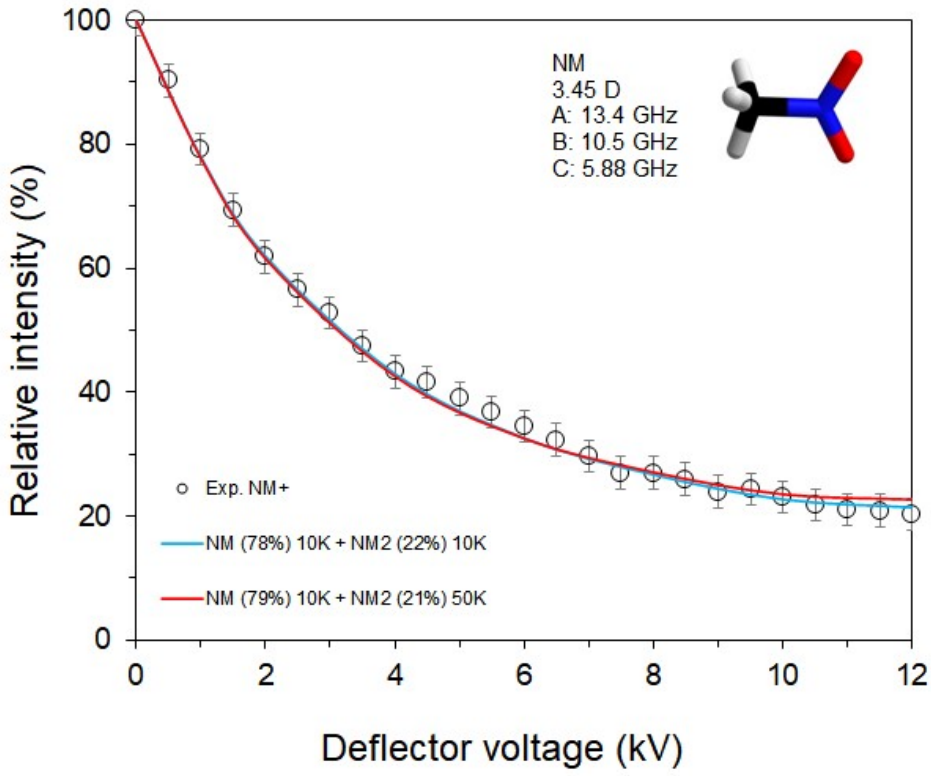

Figure 4.13: Simulated removal curves of mixed nitromethane monomers and side-by-side dimers with the same rotational temperature of 10 K (blue) and a rotational temperature of 10 K for the monomer and 50 K for the SSD (red). The experimental points of nitromethane ion signal are shown as open black circles.

due to velocity slip effects in the initial step of the expansion, resulting in high energy collisions between carrier gas and seeded molecules. The velocity slip is progressively reduced along the expansion, a necessary condition to form clusters. However, the density also decreases reducing the probability for three body collisions. Therefore, clusters are hardly formed in light carrier gases [204]. This explains the presence of clusters when nitromethane is seeded in argon and the absence when it is seeded in helium, with similar initial conditions.

The bottom panel in Fig 4.12 concerns ion signal removal from clusters. Simulated removal curves for CD structures are completely different to the experimental points. Deviations for the SSD simulations from the exact experimental values may arise from higher rotational temperatures of these dimers or additional contributions from larger clusters (or both). Based on simple μ/m arguments, the removal curves of pure trimers of nitromethane with a triangular (TT) and side-by-side arrangement (SST) will be located in between that of monomers and SSD. Collinear trimers (CT) have an enormous dipole moment and hence would be removed even more efficiently, taking the simulated curve even further from the experimental data points. Thence, the detected $(NM)H^+$ and $(NM)CH_3{}^+$ signals are not likely to derive from trimers.

Complexes of SSD with weakly bound argon atoms may be a source for (NM)H+ and $(NM)CH_3{}^+$

fragment ions too since heteroclusters are generally formed when molecules are seeded in argon [213]. We estimated the removal curves for SSD+Ar_n (n =1,2) clusters at T_{rot} = 10 K and 50 K (see Fig. D.1 in appendix D). These curves were obtained by scaling the SSD curves by 1.32× (m_{SSD+Ar}/m_{SSD}) and 1.66× (m_{SSD+Ar_2}/m_{SSD}) and assuming no change in the dipole moment or rotational constants. Although small changes (<5%) in the electric dipole moment have been previously verified for benzonitrile-argon clusters with respect to the isolated molecule, the coupling with the electric field was distinct and so were the transmission efficiency through a Stark discriminator [214]. Remarkable agreements are predicted for most of the nitromethane-argon complexes, but based on the example given above, care should be taken in making strong statements about them. Indeed, the generation of argon-molecular complexes required higher driver pressure for the argon carrier gas than that employed in our work [215, 216, 217]; moreover we could not identify any argon-nitromethane cluster ion signal in our mass spectra, and so, we attribute the $(NM)H^+$ and $(NM)CH_3{}^+$ ion signals to fragmentation of pure SSD and not argon-SSD mixed clusters.

The large energy difference between the SSD and CD optimised structures (150 meV) makes it unsurprising that SSD are more common in our beam than CD. Nonetheless, in the next section we explore the isomerisation dynamics between CD and SSD dimers. The purpose is to understand why we can observe fragment ions resultant from side-by-side dimers but not for collinear dimers: is there a favourable CD→SSD conformational change after the supersonic expansion? If so, is the backward conformation reaction expected? In section 4.8.2.2 we evaluate, through DFT calculations, the plausibility of NM^+, $(NM)H^+$ and $(NM)CH_3^+$ ions to fragment from side-by-side dimer ions. Both sets of calculations give us even more confidence in the conclusions from comparing the experimental results with the simulations.

4.8.2.1 CD→SSD neutral conformational dynamics

The large energy difference between SSD and CD is not sufficient to rule out the presence of CDs in the supersonic beam. Indeed, if large energy barriers exist between the energy minima, clusters may get trapped in CD configurations during the supersonic expansion. Therefore, we decided to assess the relaxation dynamics of CD into SSD at room temperature and at the lowest conceivable temperature in the present molecular beam: 10 K.

Conformation dynamics were performed within the self-consistent charge density functional tight-binding formalism [218, 219] with the DFTB+ software [220, 221]. DFTB is an approximation of DFT, where no matrix elements are computed. This speeds up the calculation procedures when compared with standard DFT. For the DFTB simulations, we first optimised the CD geometry with the gDIIS algorithm and the Slater-Koster files found in the 3ob-3-1 package [222] (these contain the parameters that describe the interaction between neighbouring atoms). A full third order correction to the Hamiltonian was included, using the following Hubbard derivatives: O= −0.1575, H= −0.1857, N= −0.1535 and C= −0.1492 [220, 223]. Intermolecular interactions were incorporated by Grimme's DFTD3 [80] empirical dispersion function with Becke Johnson damping [224], using a_1=0.5719, a_2=3.6017, s_6=1 and s_8=0.5883 parameters. The molecular dynamics (MD) comprise thirty trajectories in a NVE (constant number of particles, volume and

energy) ensemble, with a total of 10 ps each (20000 steps, 0.5 fs time step). We ran two sets of calculations with different initial temperatures: T_0 = 300 K and T_0 = 10 K. The NVE ensemble was chosen in order to maintain a constant energy of the system, mimicking the conditions after the expansion have ceased. Bend and dihedral angles between the C−N bonds of each molecule were extracted from MD files using the Travis software [225]. These parameters inform about the relative orientation between each molecule in the dimer. The panels on the left in Fig 4.14 show exactly these angles for each MD trajectory (thin coloured solid lines) and the mean value (thick black solid line) for an initial temperature of 300 K. The panels on the right refer to an initial temperature of 10 K.

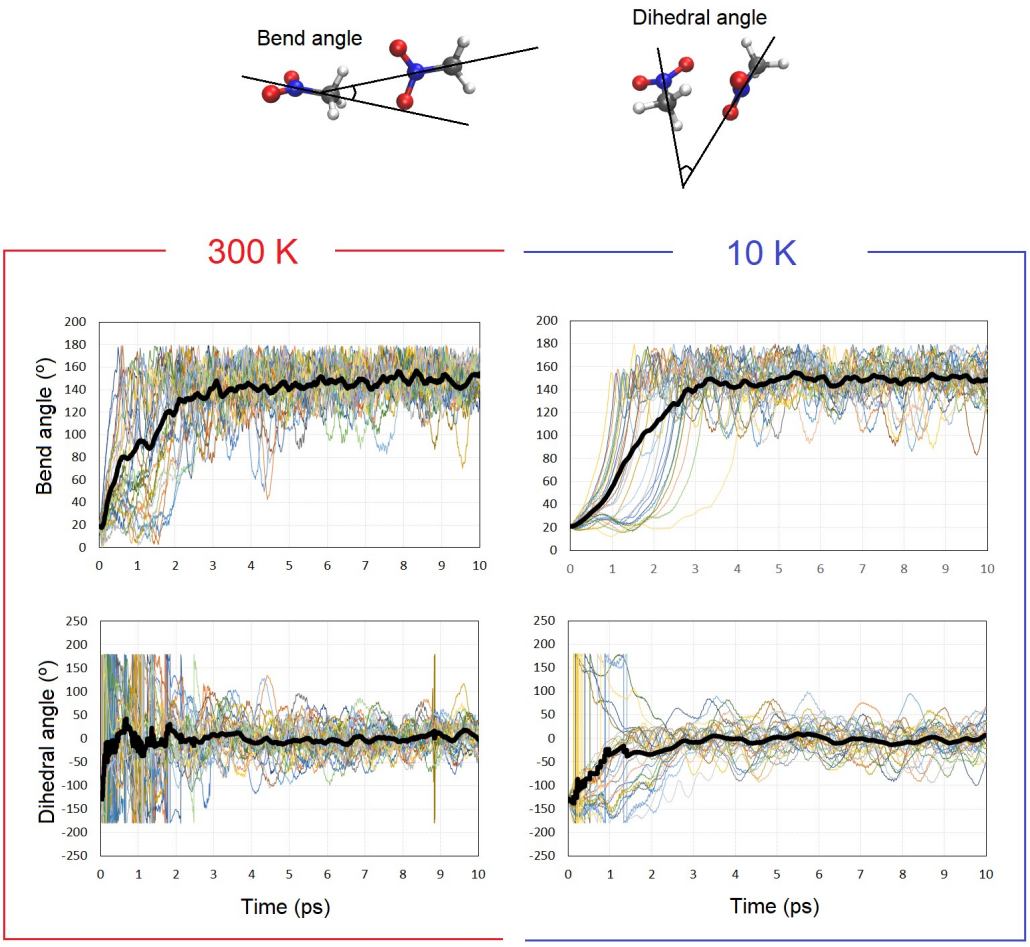

Figure 4.14: N-C-N bend and N-C-N-C dihedral angles established between molecules in nitromethane dimers as function of MD simulation time, at an initial temperature of 300 K (left panels) and 10 K (right panels). The starting point of the simulation is the collinear dimer (CD) with optimised bend and dihedral angles of the 19° and -110°, respectively. The bend and dihedral angles of the side-by-side dimer are approximately 140° and 0°, respectively. Hence the simulation indicates rapid relaxation from the CD to the SD.

At 300 K, the figures shows that the molecules change their initial parallel direction to an opposite direction, in the first 2 ps. As the mean value of the dihedral angle fluctuates around

0º, the electric dipole moment of the dimer is very small after 2 ps: a CD→SSD conformation change occurs within this time window. At 10 K, the conformational change is delayed by only 1 ps; it occurs 3 ps after MD initialisation. The decrease in potential energy provided by this transition (SSD is more stable than CD) induces an increase in kinetic energy (temperature), since a microcanonical ensemble was considered. A reverse transition is not observed for both initial temperatures within the time window of the MD simulation. Based on these results, we infer that CD structures will be very scarce or absent in the molecular beam since a conformational change from CD to SSD would be expected in a short timescale. This is consistent with the fact that we see no evidence for fragment ions deriving from CD clusters in the Stark removal curves (Fig. 4.12).

4.8.2.2 BOMD in the electronic ground state of side-by-side dimer cation

The fragmentation pattern of nitromethane clusters embedded in helium nanodroplets have been previously reported by Ferreira da Silva *et al* [196]. The group showed that protonated and methylated nitromethane are the main fragment ion products resultant from electron impact ionisation, with intensities approximately one order of magnitude larger than monomer and dimer ion signals. Here, the bare nitromethane ion signal is slightly larger than protonated and methylated nitromethane ion signals (see Fig. 4.10) and this may be due to different size distribution of clusters and / or to additional ionisation mechanisms—Penning ionisation and charge transfer—in the nano-droplet environment. Many pure hydrogen bonded molecular clusters exhibit a tendency to relax via proton transference after ionisation. For example, Slavíček *et al* showed, by means of non-adiabatic dynamic simulations, that proton transfer is the dominant mechanism happening after photo-ionisation of the lowest orbitals of pure water dimers [226]. Heinbuch and co-workers have generated molecular beams of pure formic acid clusters seeded in helium and identified the fragment ions resultant from soft X-ray irradiation. They showed that the major fragmentation channel corresponds to a loss of dehydrogenated formic acid molecules, $(HCOOH)_{n+1} \rightarrow (HCOOH)_n H^+ + COOH$, with branching ratios beginning at 48.1% for n = 1 and increasing above 90% for n ≥ 2 [227]. Shinohara and co-workers studied the behaviour of pure clusters of ammonia upon photo-ionisation and were able to detect both protonated and unprotonated ammonia ion signals. The authors concluded that the photon energy had a great influence on the relative ratios of ammonia dimers and protonated ammonia monomer: an increase of 2 eV of the energy of the photons beyond the appearance potential of the protonated ammonia monomer favoured the formation of this ion [216]. Lee *et al* [228] and Vaidyanathan *et al* [215] employed supersonic sources to produce molecular beams of methanol seeded in helium. Dominant series of protonated methanol fragment ion resulted from the electron impact ionisation of the methanol clusters. Two possible pathways leading to protonated methanol within the dimer were identified, one of them barrierless and the other one involving a small energy barrier (< 0.4 eV) [228]. Even in cluster systems not possessing hydrogen bonds, as the case of our dipole-dipole bonded side-by-side dimer, proton transfer have shown to be a very important mechanism [229]. Some authors have discussed the absence of unfragmented clusters in terms of poor Franck-Condon factors: after vertical ionisation, the cluster undergoes large changes in geometry, normally involving a proton transfer within the

unfragmented cluster [216, 217]. Since the optimum geometry of the cluster ion is marked by proton transfer reactions, a protonated cluster ion is formed after fragmentation of the cluster ion. As a first step towards elucidating the energetics of chemical reactivity of side-by-side dimers, we optimised some key structures, which are represented in Fig. 4.15. This schematic is consistent

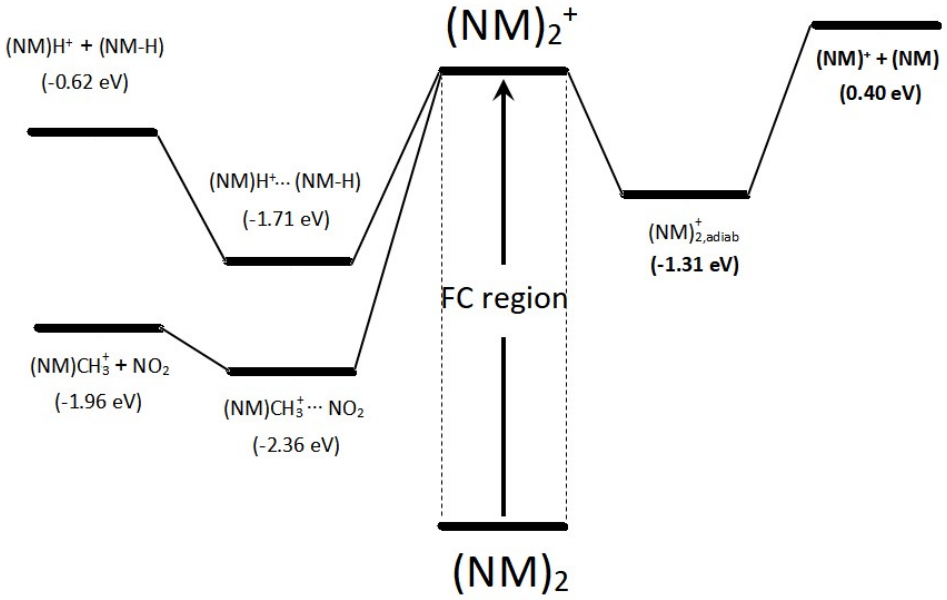

Figure 4.15: Optimised structures of $(NM)CH_3^+$, $(NM)H^+$ and NM^+ products and respective intermediates after ionisation of the SSD. Energies are given relative to the vertical ionised SSD energy, $(NM)_2^+$. Note that the optimisation of the vertical ionised SSD converges to the $(NM)_{2,adiab}^+$ structure; therefore, it is a local minimum. Lower energy structures, namely $(NM)H^+\cdots(NM{-}H)$ and $(NM)CH_3^+\cdots NO_2$ may connect to the vertically ionised SSD through transition states (TS) in the multidimensional potential energy surface (PES).

with the relative ratios observed in Fig. 4.10. The relative energies of the key fragment ion + neutral pairs from the SSD ion can be summarised as follows: $(NM)^+ > (NM)H^+ > (NM)CH_3^+$. Based on our removal curves for NM^+, the SSD only contributes to approximately 10–22% of the NM+ signal in our experiments with no voltage on the deflector. The low intensity of $(NM)_2^+$ in present mass spectra (Fig. 4.10) compared with the $(NM)H^+$ and (NM)CH3$^+$ signals indicates that the vertically ionised SSD is formed with a large internal energy compared with the TS for the respective dissociations. However, the simple optimisation of structures is not enough to predict the outcomes of ion fragmentation within the time window for detection. Therefore, we performed Born-Oppenheimer molecular dynamics (BOMD) in the electronic ground state of the SSD cation to pinpoint the kinetic details of its chemical reactions. The BOMD has some advantages over reaction pathways calculation for example the time needed to observe a certain reaction (kinetic information) and the exploration of portions of the PES that are normally not investigated in reaction pathway calculations.

Molecular dynamics (MD) simulations were performed in three steps: i) thermalisation, ii)

sampling and iii) production runs. In step i), the SSD cluster was thermalised with a self-consistent charge density functional theory tight-binding (SSC-DFTB) [218, 219] at 150 K in a canonical ensemble (NVT, constant number of particles, volume and temperature), using a Nosé-Hoover chain thermostat [230, 231, 232]. The time window for thermalisation was 50 ps, with 1 fs time steps. The DFTB+ software [220, 221] was used for thermalisation. In step ii), thirty geometry snapshots were taken at every picosecond after the initial thermalisation period. These structures were used as input for the production runs, simulated with BOMD at DFT level, M06−2X/6-31+G(d) [70, 233, 234]. We considered a microcanonical ensemble (NVE) with a temperature of 3200 K per vibrational mode, corresponding to an internal energy of 6.8 ± 1.2 eV, following the value recommended by Grimme and co-workers of 0.6 eV per atom [235, 236, 237]. This energy was randomly distributed among all the vibrational modes of the SSD ion, mimicking a statistical intermolecular vibrational energy redistribution (IVR) process. This approximation is justified due to the large density of Van der Waals vibrational modes of the cluster, which ensures enough time for a complete IVR before the occurrence of vibrational pre-dissociation (VP) [238]. Each trajectory comprises a total of 1000 mass-weighted time steps and a total of 30 trajectories were simulated. The fragmentation assessment was based on distances between heavy atoms, setting 5 Å as the threshold for dissociation. Fragment partial charges were evaluated using the Mulliken charge decomposition method [239]. Branching ratios were calculated by summing the partial charges of an ion over all trajectories and dividing by the number of trajectories. Production runs were performed in Gaussian09 [77].

The branching ratios obtained in the BOMD simulations are summarised in table 4.3. With the exception of (NM)NO^+, the simulation qualitatively predicts all the fragment ions present in the mass spectra. This gives us greater confidence that the present experimental study allied to the simulated Stark removal curves have correctly traced the observed (NM)H^+ and (NM)$CH3^+$ products to ionised SSD precursors. Even at such large internal energies, it is interesting that the major ion formed is the undissociated parent $(NM)_2^+$ ion, closely followed by the methyl fragment ion CH_3^+ (not assessed in our experiments due to the large background ion production at this m/z value). The NM^+ production represents 17% of the fragmentation channels. Only then appear the methylated and protonated nitromethane ions, with 13.7% and 6.9%, respectively. The under-estimation of intensity of protonated and methylated nitromethane fragment ions in our BOMD simulation compared with the experimental results may result from the restriction to a narrow range of internal energies. Alternatively, it may be linked to a parallel intermolecular vibrational energy redistribution and vibrational pre-dissociation events, which are known to proceed in a sequential manner in clusters with large density of states [238]. Indeed, the large density of VdW vibrational states and the large energy difference between the dissociated dimer ion and vertically ionised dimer ion (0.40 eV as shown in Fig. 4.15) are consistent with significant contributions of vibrational pre-dissociation taking place on timescales longer than intermolecular vibrational energy redistribution. This argument certainly has consequences for the observed ratios since chemical reactions within the cluster have a larger probability to occur prior to the rupture of the VdW structure: fragment ions such as CH_3^+ and NM^+ should have a reduced intensity in detriment to other reactive species, e.g. (NM)CH_3^+, $(NM)^+$, etc.

Fragment ion	BOMD Yield (%)	Present experiments	Innsbruck results [196]
CH_3^+	20.0	Not discernible due to large signals from background ions	Not shown
NO^+	5.4	Observed but not traced to any specific precursor	Not shown
CH_3O^+	1.3	Not visible above the background noise	Not shown
CH_3NO^+	5.8	Observed but not traced to any specific precursor	Not shown
NO_2^+	3.2	Observed but not traced to any specific precursor	Not shown
NO_2H^+	0.1	Not visible above the background noise	Not shown
NM^+	17.0	Observed and traced to monomers and SSD	Observed without evidence for origin
$(NM)H^+$	6.9	Observed and traced to SSD	Observed without evidence for origin
$(NM-H)CH_3^+$	3.4	Not visible above the background noise	Not shown
$(NM)CH_3^+$	13.7	Observed and traced to SSD	Observed without evidence for origin
$(NM)NO_2^+$	2.6	Observed but not traced to any specific precursor	Observed without evidence for origin
$(NM)_2^+$	20.6	Observed but not traced to any specific precursor	Observed without evidence for origin

Table 4.3: Ions' branching ratios resultant from the BOMD in the electronic ground state of the SSD ion.

4.9 Summary and future work

In the present chapter we have demonstrated that the Stark removal method can be used to trace the origin of fragment ions to specific neutral cluster precursor in mixed CW beams. This is a significant step forward because Stark manipulation methods have only been used once before to successfully identify fragment ion origins and those previous experiments applied pulsed supersonic beams. Indeed, Stark deflection of CW beams has never previously been applied to analyse such large molecules as nitromethane or any molecular clusters. Our proof-of-principle experiments have also revealed evidence supporting different rotational temperatures of different species in the beam. In the present experiments, the differences in the dipole moment / mass ratios between the neutral precursor candidates were sufficiently large that the analysis could tolerate some differences in rotational temperature. However, such differences will pose a major problem

in applications where candidate species with more similar Stark deflection characteristics need to be distinguished. Strategies to address this problem will therefore be requires to exploit the method to its full potential, most likely involving simulations of rotational cooling in the specific expansion conditions applied.

4.10 Acknowledgments

The Stark deflection of nitromethane seeded in helium was the first set of experiments performed and analysed during the course of the current PhD. At that time, my supervisor Samuel Eden, provided a lot of help, spending a large amount of time in the laboratory, explaining me how to operate with the mass spectrometer and Stark deflector. We analysed the experimental data together. I then started to work on the C++ code, discussing the details with Prof. Dr. Samuel Eden whenever I found appropriate. The experimental data regarding electron impact ionisation of nitromethane seeded in argon was acquired by Michal Ryszka, a previous PhD student at The Molecular Cluster Laboratory, and the respective data analysed by him and Prof. Dr. Samuel Eden. I worked with Dr. Jean Christophe Poully on the DFT calculations, to estimate the properties of monomers and clusters and to simulate the reactivity of the cationic SSD. I simulated the Stark removal curves based on the DFT calculations and on the C++ code. I also acknowledge Tiago Cunha who suggested me to use the CMIStark software for calculating Stark energy shifts and provided me with a few examples about how to run the program. I also acknowledge Rahul Pandey for having shared with me experimental data of 3-aminophenol seeded in argon, which I used as a further test to evaluate the performance of the C++ code. Finally, I would like to thank to Jochen Küpper and his group for providing the Stark deflector.

Chapter 5

Development of a new DEA / EII / MPI experiment on ILT-desorbed molecules and molecules / clusters in Stark deflected beams

5.1 General introduction

In the present chapter, we describe a new multi-purpose apparatus assembled in the Molecular Cluster Laboratory that replace the previous interaction chamber in the *Stark deflection* experiment. The reasons justifying this change are:

1. The Kimball electron gun on the old chamber did not produce viable electron beams below around 50 eV. This ruled out EII near threshold and, of course, DEA.

2. The high resolution electron beam system in the old chamber produced too low currents (nA) to give adequate signals with the low target density in the supersonic beam. This problem was compounded by poor transmission of ions from the crossing point of the supersonic beam / electron beam into the extraction volume of the mass spectrometer.

   The new chamber addresses both of these challenges by using a single high-current electron gun system with a collimating magnetic field. The system can produce μA-order electron beams down to few eV — sufficiently low to access many DEA resonances. Pulses of electrons pass directly through the extraction region of the mass spectrometer. There is no sacrifice compared with to the Kimbal gun and our attempted experiments with the high resolution gun had never produced adequate ion signals to study DEA in a meaningful way.

3. The old chamber could only be used to investigate supersonic beam targets. The new one also allows ILTD targets to be studied. To achieve this we had to modify the standard designs of our ILTD source (first fiber-optic laser beam delivery for ILTD) and of our TOF source (new steps to prevent electron interactions with the condensed sample).

The new apparatus is designed to study targets produced either by seeding molecules in supersonic expansions or by releasing plumes of molecules using *indirect laser-induced thermal desorption* sources. Negative or positive ions produced in collision with electrons or by UV multi-photon ionisation can be analysed by reflectron time-of-flight mass spectrometry. The comparison of MPI and EII data provide insights about neutral excited states of biomolecules, when performed under the same experimental conditions: fragment ions present in the MPI but absent in the EII mass spectrum can be attributed to dissociation or isomeric transitions in neutral excited states [32]. Furthermore, the interpretation of neutral excited state dynamics is relevant for understanding some DEA processes, namely, core-excited shape and core-excited Feshbach resonances that involve electronic excitation of the transient negative ion. Therefore, it is desirable to construct an apparatus like the one presented in this chapter, that enables fast and simple switching between these kinds of experiments without upsetting molecular / cluster target conditions. The spatial separation of neutral species by Stark deflection is still possible for supersonic expanded beams in the new multi-purpose apparatus. This is the first experiment that will probe ILT-desorbed molecules with anything other than an ionising laser. It will also enable the study of DEA to molecules / clusters from Stark-manipulated beams for the first time.

The experiment is now completely designed and built and the electron gun and mass spectrometry systems have been tested. Testing of the new ILTD system and further optimisation of the electron beam at low energies is currently in progress. Fig. 5.1 shows the current status of the *crossed beam chamber* of the new DEA / EII / MPI experiment. These components will be discussed throughout the chapter, which is structured as follows. We begin by describing the chambers and the mass spectrometer in section 5.2. The magnetic properties of chamber materials are of particular importance in order avoid disrupting the magnetic field that collimates the electron beam. Then, in section 5.3, we describe the new ILTD source and refer the major differences relatively to the ILTD source mounted on the compact experiment. In section 5.4 we describe the assembly of the electron gun and Faraday cup in the interaction chamber. We also mention the principle of collimation of electrons with magnetic fields and how we shielded the electron beam from electric fields from the ion optics of the TOF mass spectrometer. In section 5.4 we provide details about the procedure adopted for optimising the voltages of the EG for performing EII experiments. The optimisation of other important parameters for operating the EG at low energies, such as the duty cycle and the delay between the release of electrons and the pulse for extraction of the ions, is described in section 5.4.2. In section 5.4.2.1 we used the optimised EG to perform EII experiments on Stark deflected methanol molecules and clusters. We optimised the TOF mass spectrometer voltages based on the detected ion signals.

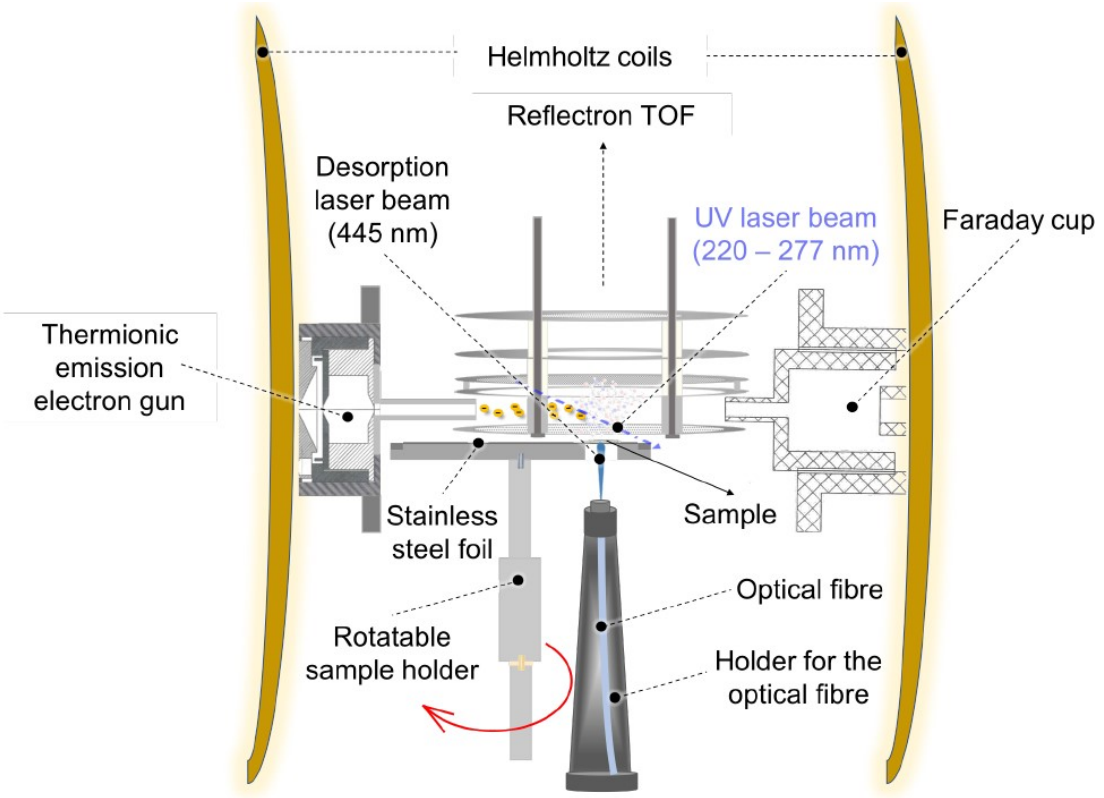

Figure 5.1: Components featuring the crossed beam chamber of the new DEA / EII / MPI experiment. Briefly the main parts of the experiment that are not shown in the interest of simplicity: (i) the inlet system for effusive calibration gas and (ii) the supersonic beam that can cross the electron beam or the UV laser beam as an alternative target to the ILTD system. Figure taken from [84].

5.2 Movable skimmer chamber, crossed-beam chamber and reflectron time-of-flight mass spectrometer

The SS304 interaction chamber of the *Stark deflection* apparatus was replaced by a smaller, custom made, SS316L chamber produced using a combination of stainless steel types (SS316 and SS316LN). The exchange reduced magnetic permeability and dimensions of the chamber. The first factor is crucial to manipulate low energy electron (LEE) because their trajectories are very sensitive to magnetic fields. By constructing as many parts of the experiment as possible from materials with the lowest-possible magnetic permeability, we can minimise the contributions of unwanted magnetic fields (due to parts becoming magnetised with time) and we can also minimise the disruption of the collimating magnetic field due to magnetic field lines becoming concentrated in materials with higher permeability. Naturally, the most important parts to construct using materials with low permeability are those closest to the electron gun and the electron beam. The permeabilities of the materials used in the new experiment are listed in table 5.1. The choice of the material is a compromise between the required magnetic properties, mechanical properties, vacuum compatibility, cost, and availability within reasonable lead times (for example, we could find

no commercial supplier of suitable SS316LN tubing). The smaller size is required for the chamber to fit within the available Helmholtz coils that establish the collimating magnetic field. Larger Helmholtz coils would be very difficult to fit within the available space in the laboratory. The new chamber is based on five SS316 cylinders that intersect at a single central point. It features SS316 DN160CF open flanges at the bottom and top, as well as opposite pairs of DN100CF and DN40CF flanges around the body, as we can see in Fig. 5.3. The closest open flanges to the electron gun and the beam (A and E) are 316LN; the less critical open flanges are 316L.

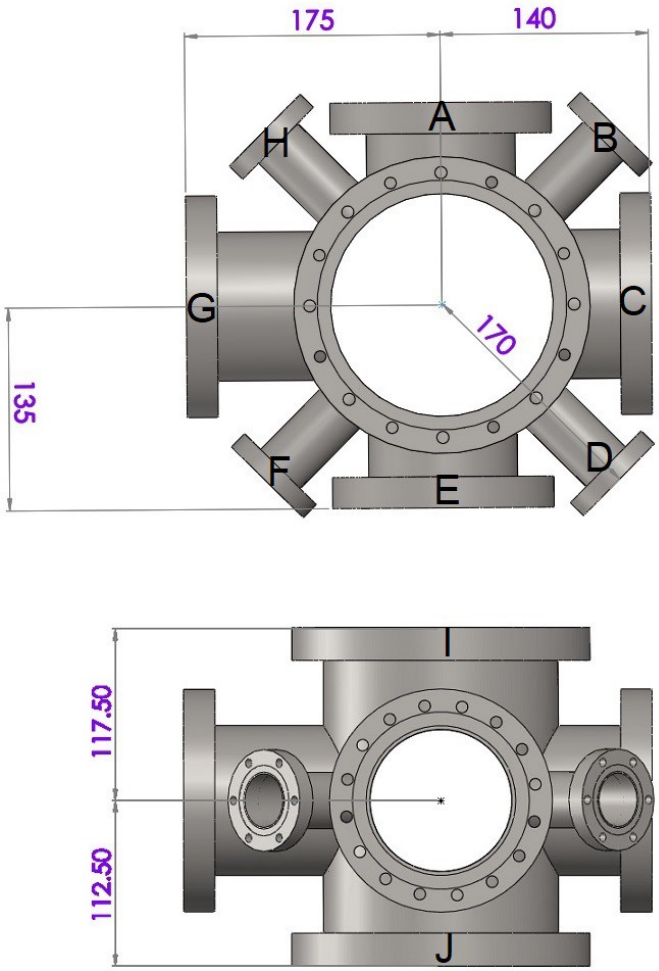

Figure 5.2: CAD drawing of the new SS316L chamber. Dimension are given in mm. The top image is a view from above and the bottom image is a view from the slide. Key flange purposes include: G: Stark-manipulated molecular beam entrance, E: electron gun insertion, H: UV laser pulse entrance, I: mass spectrometer mount, and J: ILTD source insertion.

This *crossed-beam chamber* houses the central components of the experiment: a custom ILTD source, an electron gun (EG), a Faraday cup, a calibration gas inlet, and a new set of extraction electrodes for the mass spectrometer. A SS316LN DN160CF–DN100CF zero length adapter,

placed on the top flange (flange I, Fig. 5.3), links the reflectron time-of-flight mass spectrometer to the crossed beam chamber. The adapter was bought from LewVac with a rectangular bore. The bore was machined by OU mechanical workshop staff according to our CAD drawings, so that X and Y deflectors of the mass spectrometer (SS304) could pass through. These deflectors help to direct extracted ions onto trajectories that end at the MCP detector. The set of electrodes comprising the ion extraction and focusing optics of the mass spectrometer are made of titanium and are mounted on four titanium pillars screwed to the adapter. The grids are made of high transparency (88%) SS316 mesh. Gold meshes were also considered but they are very fragile and easily damaged, which would require the removal of the whole mass spectrometer for the respective replacement. A chevron microchannel plate (MCP) ion detector is mounted at the end of the reflectron time-of-flight mass spectrometer.

Material	μ_r	**Key components**
SS304	≤ 1.3	Mass spectrometer, UV window flanges, electrical feedthrough flanges, molecular beam alignment window flange, moveable skimmer chamber, and ILTD foil.
SS316L	≤ 1.1	Tubing in crossed-beam chamber, open flanges in crossed-beam chamber except A and E (see fig. 5.3).
SS316LN	≤ 1.005	Open flanges A and E in crossed-beam chamber, all closed flanges around the crossed-beam chamber except those mentioned above.
Titanium	≤ 1.00005	All TOF source parts except grids and ceramics, and all LITD system parts close to the electron beam except the foil.
Aluminium	≤ 1.000022	Bolts, nuts, and washers on the crossed-beam chamber, and support frame.

Table 5.1: Relative magnetic permeabilities of materials used in the new apparatus.

UV pulses for multi-photon ionisation experiments enter and exit through DN40CF UV viewports (SS304) installed on flanges H and D (Fig. 5.3). Note that it was not possible to source affordable UV window flanges made from a material with lower permeability. If necessary, very sensitive electron beam experiments could be preformed using blank SS316LN flanges in the future. The pulse energy is measured by a joulemeter (Spectrum Detector Inc. SPJ-D-8) placed in front of flange D. Flanges B and F are used to mount miniature high voltage (MHV) connectors (SS304) to supply voltages to the ion optics. Given the reduced dimensions of the crossed beam chamber, the movable skimmer had to be placed in a separate chamber which we call the *movable skimmer chamber*. This chamber comprises three crossed cylinders. These cylinders terminate with two pairs of opposite DN100CF open flanges and one pair of opposite DN40CF open flanges. The moveable skimmer chamber connects to flange G of the crossed beam chamber (Fig. 5.3). Both chambers, are supported by aluminium frames. In the new design, the distance between the back of the Stark deflector and the movable skimmer is slightly shorter (457 mm) than in the previous apparatus (477 mm). On the other hand, the distance between the movable skimmer and

the electron beam is longer in the new experiment (324 mm) than it was in the previous (126 mm).

A notable point about the crossed beam chamber is that it has no available port for a vacuum pump or a pressure gauge. This is partly due to spatial constraints and the large number of other essential components. However, this design feature also reflects the intention of mounting turbo pumps and gauges (both magnetic field sources) a significant distance away from the electron gun and the electron beam. An Oerlikon Leybold TURBOVAC SL700 (with N_2 pumping speed of 690 l/s) evacuates both chambers via the movable skimmer chamber. The pump is attached to the chamber through a mechanical system composed of two elbows, a DN100CF−DN160CF reducing nipple and a collar manufactured in the OU workshop. The collar rests on a small aluminium frame, promoting mechanical stability for the pump. The flight tube is pumped by an Oerlikon Leybold TURBOVAC 151 (with N_2 pumping speed of 145 l/s). Both turbomolecular pumps are backed by an Edwards XDS100 Dry Scroll Vacuum Pump. The pressure in the experiment is monitored by a Leybold IONIVAC ITR 90 pressure gauge connected to the movable skimmer chamber.

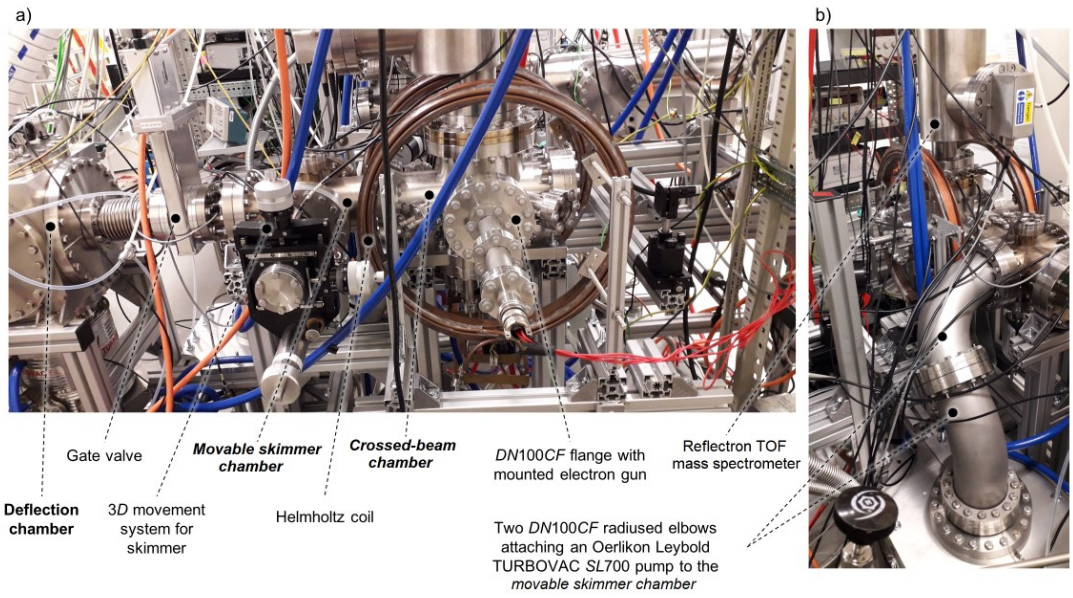

Figure 5.3: Photographs of the new DEA / EII / MPI experiment. a) Side view of the experiment. The supersonic beam generated in the expansion chamber propagates from the left to the right. b) The support system for the turbobomolecular pump of the movable skimmer chamber. Adapted from [84].

The UV pulses to multi-photon ionisation measurements can be directed into the crossed beam chamber via the same tandem laser system described in the compact experiment section. This will be particularly valuable for testing and optimising the new ILTD system, keeping in mind that EII experiments have never been performed successfully on ILT-desorbed molecules before. Furthermore, comparing fragment ion production by MPI with EII can provide evidence for structural changes in electronic excited states [33]. The UV laser pulses cross the compact experiment and are redirected to the middle of the interaction region of the new apparatus by an optical system, composed by a silica plano-convex lens (50 cm focal distance) and a vacuum UV

enhanced mirror (120 – 700 nm, average reflectance ≥ 88 %) mounted on an aluminium plate, in front of flange A. The joulemeter is placed in front of flange D, fixed on an optical post mounted in the aluminium frame. The optimisation of the optical system will be addressed in a future work, based on multi-photon ionisation ion signal intensities.

5.3 The custom *indirect laser-induced thermal desorption* source

The *indirect laser-induced thermal desorption* source of the new experiment has a different design than that mounted on the Compact experiment, mainly due to the following reasons:

1. We aim to do DEA experiments on ILTD targets. DEA is a low-cross section process and electron beam currents are generally low at DEA energies to minimise beam divergence due to space charge. This means that we will get very weak signals compared with our MPI experiments and hence will require much longer acquisition times to achieve good signal to noise ratios. Therefore each preparation of sample on the foil needs to provide a target that lasts much longer. In line with Dave Townsend's ILTD system [32], we will achieve this using a large rotatable foil.

2. Due to the fixed positions of the Stark deflector experiment and the UV pulsed laser, as well as the dimensions of the mass spectrometer and the Helmholtz coils, the only possible position to mount the ILTD source is from below the crossed-beam chamber. This effectively rules out delivering the desorption laser beam via a window. Therefore, our new design features CW laser delivery via an optical fibre (the first time this has been done for ILTD).

3. Whereas it is straight-forward to prevent photons in a multi-photon ionising laser beam from interacting with the condensed sample on the foil, this is much more difficult to achieve using an electron beam. It is essential to prevent any stray electrons from the beam from hitting the condensed sample because these will drive unwanted chemical reactions and / or desorption. The new design addressed this problem by placing a negative bias voltage on the foil to repel electrons and using a grid to shield the central part of the electron from being deflected by this bias voltage. Furthermore, the TOF source electrodes will be heated to prevent layers of biomolecules condensing on the TOF electrodes.

The remainder of this section describes the custom ILTD source in more detail. The ILTD source is mounted on the bottom blank flange of the crossed-beam chamber. The system comprises a titanium disk and ring with ∅ 80 mm that locks the stainless steel foil in place. The disk has an arc-shaped aperture to expose the foil to the desorption laser radiation (Fig. 5.4).

The disk is screwed to a titanium pillar that connects to a rotary manipulator in the opposite end. With this system, fresh sample can be desorbed simply by rotating the foil. Given the large surface area of the foil, sample lasts longer compared with the ILTD source of the compact experiment.

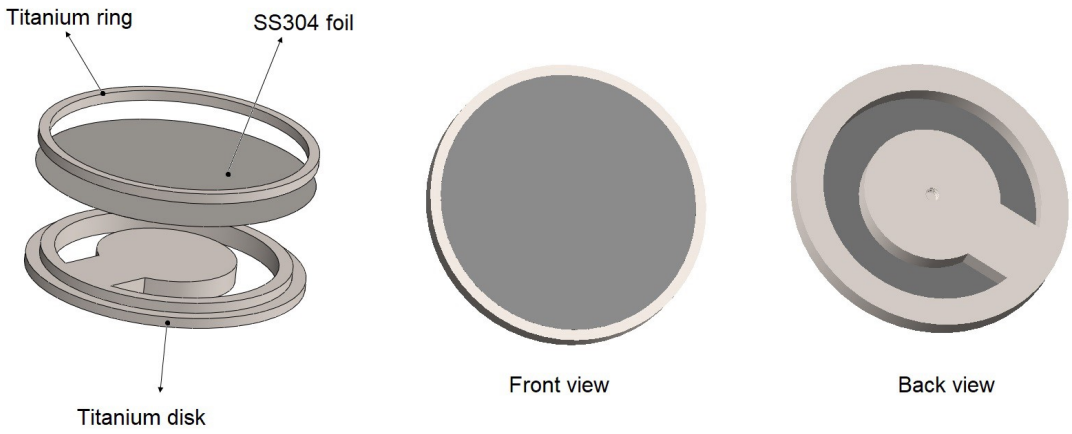

Figure 5.4: CAD drawing of the *indirect laser-induced thermal desorption* source assembled in the new apparatus. The ILTD source is composed by a titanium disk and ring, which lock the SS304 foil. The larger surface of the foil permits longer acquisition times compared with the ILTD source existent in the compact experiment.

In the current design, the SS304 foil of the ILTD source (A in Fig. 5.5) is ~ 3 mm away from the first electrode of the ion optics (grid D in Fig. 5.5). A bias voltage, more negative than the sum of the electron beam energy and the pulsed extraction voltage, polarises the foil, preventing electrons from the electron beam from hitting the foil. This ensures that electrons only interact with desorbed molecules.

Figure 5.5: Left: View of ILTD source and ion optics from a DN100CF flange. A: Sample plate; B: Holder with fibre optic; C: Calibration gas inlet; D: Backplate of ion optics; E: Faraday cup. Right: Bottom flange partially-disassembled (note that the fibre optic holder and the calibration gas inlet are not present). The black knob allows the rotation of the ILTD source.

To avoid condensation of the sample in the grids of the ion optics during the measurements

with the ILTD source, the crossed-beam chamber is heated using heating tapes around it. The idea is to prevent electrons in the beam from interacting with molecules condensed on the electrodes of the ion optics — most of all on the grid just above the foil. Otherwise, we would start seeing desorbed ions from these electron interactions — exactly what we are trying to avoid by putting a bias voltage on the foil. Furthermore, preventing the condensation of molecules on electrodes near the electron gun also avoids deflection of the electron beam due to the building up of charges and creation of unwanted electric fields that disrupt the normal behaviour of the electron beam. With this regard, the vaporisation of molecules is not a pure *indirect laser-induced thermal desorption* process, but rather a combination of *indirect laser-induced thermal desorption* with conventional heating. The temperature range that we expect to heat the crossed-beam chamber is 353−363 K. Heating to approximately this temperature has proved to be enough in our molecular beam experiments to prevent any condensation of nucleobases (and various other biomolecules) onto our heated skimmers. This estimated temperature is based on the fact that each skimmer base is connected to a holder at 373 K but the skimmer orifice will certainly have a lower temperature than this due to limited thermal conductivity and due to cooling by the carrier gas flow. However, on the rare occasions that the skimmer heaters broke, our attempts to remove the condensed layers by heating to these temperatures were unsuccessful — even when the skimmers were left hot for more than a week. Moreover, our foil temperature measurements allied to our previous MPI experiments using ILTD (Chapter 3 and references [32, 33]) show that we needed to raise the foil temperature to at least 393 K to obtain a discernible vapour target. Therefore, we can be confident that heating to the chamber to approximately 373 K will be adequate to prevent condensation on electrodes but insufficient to remove the sample from our foil. This is however, a different way of working to any previous ILTD application. We will use low laser powers to desorb molecules from a foil that was initially at approximately 373 K instead of room temperature. The temperature of the electrodes of the ion optics due to heating of the chamber is monitored by a T-type thermocouple, which has non-magnetic properties, attached to the titanium disk of the ILTD source.

The desorption process is initiated by the same diode laser used in the compact experiment (Eksma Optics, DLM−445 – 1000). Since the flange with the ILTD source is mounted on the bottom open flange of the crossed-beam chamber, we cannot directly irradiate the foil as we do in the compact experiment. Therefore, we decided to guide the light through an optical fibre system, which facilitates the alignment and improves safety. An optical system composed of the CW laser, iris diaphragms, a lens, and the optical fibre, is mounted on the optical table. The light spot is collimated to the desired size with the irises and focused with the lens (200 – 2500 nm, 8.7 mm focal distance) into the core of the optical fibre (200 – 1100 nm, 600 μm core diameter, 3 m long, SMA terminations). The opposite termination of the optical fibre is attached to a DN40CF fibre optic feedthrough (SS304, 200 – 1100 nm, 600 μm core diameter, SMA terminations, standing temperatures up to 373 K) found in the bottom flange of the crossed-beam chamber. A vacuum compatible optical fibre (200 – 1100 nm, 600 μm core diameter, 0.15 m, SMA terminations, maximum 473 K) guides the light inside the chamber towards the foil. The fibre is sustained by a titanium holder built in the OU workshop (B in Fig. 5.5). The optical fibres and the optical

feedthrough were acquired from Anglia Instruments UK. It is worth noting that sourcing these components was not a straightforward task. Preliminary tests to assess the robustness of the optical components (fibre optics and optical feedthroughs) were necessary since we are using them outside the normal range of specifications. This can explain why ILTD had not been attempted using fibre optics previously. The tests and assembly of the optical components were successfully executed by my PhD colleague Jana Bocková and details are provided in her thesis [84]. Images of the bottom flange of the crossed-beam chamber with the optical fibres and the ILTD source is shown in Fig. 5.5.

5.4 Electron gun and Faraday cup

The new experiment hosts an OU-home built thermionic emission electron gun and a Faraday cup, mounted in opposite DN100CF flanges (flanges E and A of fig. 5.3). These components were inherited from E. Krishnakumar, and have been utilised previously in velocity mapping image experiments, achieving currents of few nA at low energies [240, 241]. The filament of the electron gun works under the thermionic emission principle: the refractory metal filament emits electrons due to thermal energy, which is increased by passing an electric current through it. The Richardson-Dushman law expresses the emitted current density, J_e, as a function of temperature T

$$J_e = A_G T^2 e^{-\frac{W}{k_B T}} \tag{5.1}$$

A_G is a constant and W is the work function of the material. The filament of our electron gun is made of tungsten (Agar Scientific AGA054), whose parameters are $A_G = 60$ A.cm^{-2}.K^{-2} and $W =$ 4.54 eV.

The dimensions and the electronic scheme of the electron gun are shown in Figs. 5.6 and 5.7, respectively. An ISO-TECHIPS1603D power supply delivers 2.2 A to the filament, heating it sufficiently to trigger thermionic emission ($\sim$ 2500 K). Electrons are then accelerated by applying a voltage difference between the filament (at negative potential) and the anode (grounded). The filament voltage is supplied by an Aim−TTiEX752M power supply and defines the energy of the electrons. A pair of 1 MΩ resistors is mounted in parallel with the filament, in a Wheatstone bridge configuration, to ensure that the tip of the filament is at same potential as the point between the resistors. The EG has three elements (triode) with a Pierce geometry [242]. The cathode is set at the filament voltage with the addition of a small bias voltage (delivered using an Aim−TTiEX752M power supply). Varying the bias voltage controls the surface emission area and, as consequence, the intensity and aberrations of the electron beam [243]. A second electrode called the grid in this type of gun (even though the electrode is gridless in this specific design) has the purpose of focusing and pulsing the electron beam. Aim−TTi TGP110 pulse generator produces a $0-5$ V pulse, which is then amplified and delivered to the grid. The amplified pulse is added to the filament voltage and a focusing bias; the lower voltage allows the beam to leave the electron gun and the higher voltage prevents it from doing so. It is also possible to use the EG in continuous mode. In that case, the grid acts solely as an electrostatic lens with the bias voltage supplied by a Farnell LS

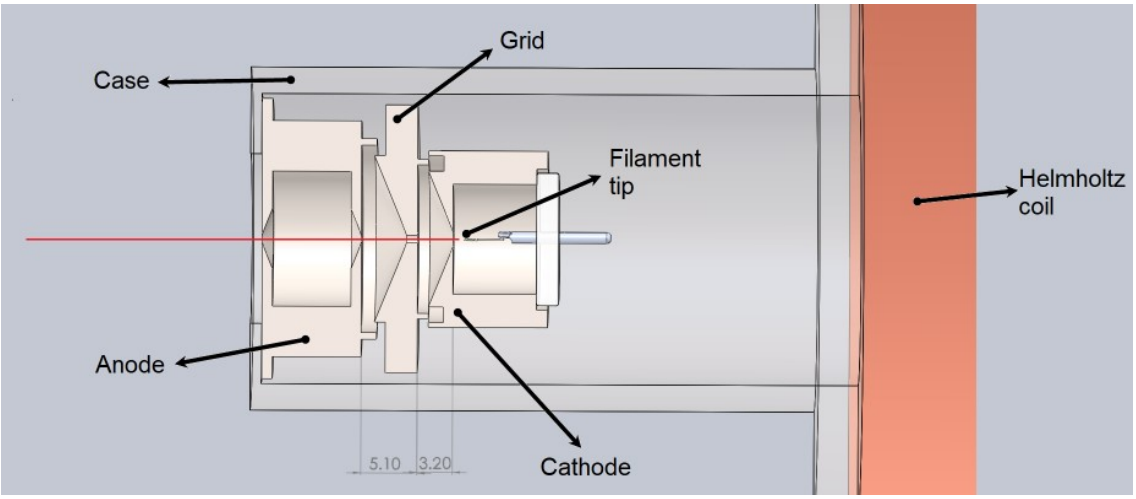

Figure 5.6: Electron gun scheme. The diameter of cathode aperture is 1.6 mm, whereas the diameter of grid and anode apertures is 1 mm. The red line indicates the trajectory of the electrons.

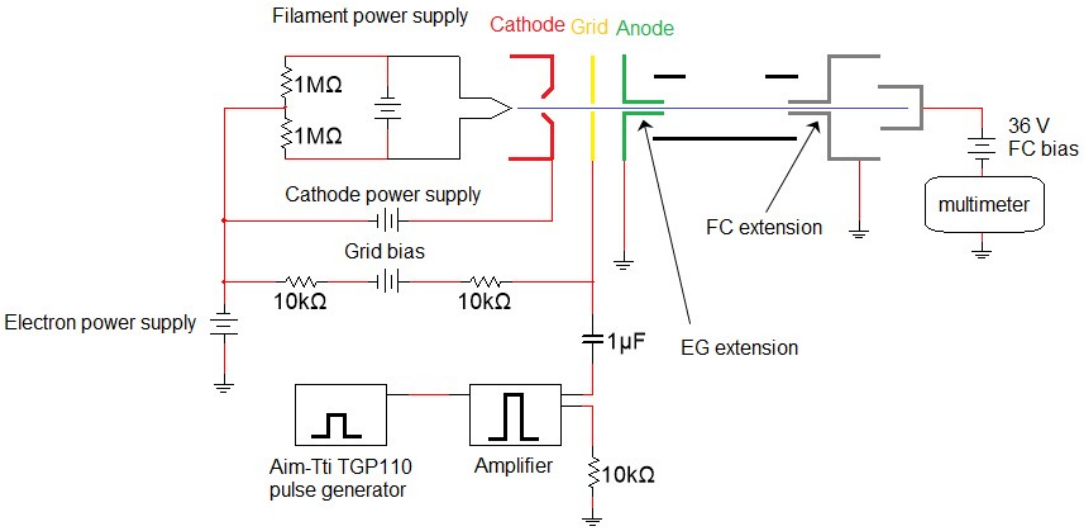

Figure 5.7: Electronic scheme of the electron gun and Faraday cup. Adapted from [240]

30 – 10 power supply. The three components, cathode, grid and anode, are electrically insulated by ceramics. Space-charge and remnant electromagnetic fields can negatively affect the trajectories of the electrons, specially the ones with low energy, which start to deviate from the beam centreline. With the current electron gun design, to achieve decent currents in the interaction region of the mass spectrometer and have the chance to observe processes with very low cross-sections, we need to collimate the electron beam with magnetic fields. Inside the electron gun, the resultant electromagnetic force (Lorentz force) acting on the electrons is

$$\vec{F} = q(\vec{E} + \vec{v} \times \vec{B}) \tag{5.2}$$

with $\vec{E}$ being the electric field vector, $\vec{v}$ the velocity vector of the electrons and $\vec{B}$ the magnetic field vector. Hence, an electron with a velocity component that is transversal with respect to B

field direction (set up to match the intended beam direction) will travel in tight spirals around the magnetic field direction but it will not deviate further away from the central axis of the beam. This is why a collimating B field is such a powerful tool in electron beam technology. A pair of coils are mounted coaxially with the EG and FC (mounted in flanges A and E of Fig. 5.3) in a Helmholtz geometry to generate an uniform magnetic field inside the crossed-beam chamber. In the Helmholtz geometry, the distance separating the coils is equal to its radius. Both coils are cooled by a closed water system and are mounted on an aluminium support with a screw system built in the OU workshop, enabling the independent adjustment of the position and tilting angle. The magnetic field intensity inside the crossed-beam chamber is estimated by using the Biot-Savart law

$$B = \left(\frac{4}{5}\right)^{3/2} \frac{\mu_0 N I}{R} \tag{5.3}$$

where μ_0=4$\pi \times 10^{-7}$ T.m.A^{-1} is the permeability of free space and I is the current circulating on each coil. To estimate the number of turns of the copper wire in each coil, we measured the wire diameter ($d = 1 \times 10^{-3}$m), the radius of each coil (R_c = 0.24 m) and the total resistance of the wire ($R = 10.8\ \Omega$). Knowing the resistivity of copper at room temperature ($\rho = 1.68 \times 10^{-8}\ \Omega$.m), the number of turns is obtained

$$N_{turns} = \frac{\pi\left(\frac{d}{2}\right)^2 \times R}{\rho \times 2\pi R_c} \approx 335$$

After the installation of the coils, we measured the magnetic field inside the crossed-beam chamber with a GM04 gauss-meter and a transverse probe (Hirst Magnetic Instruments). We supplied a current of 2 A to each coil with two GW INSTEKSPS−606 power supplies and measured a 2.3 mT, which compares to 2.5 mT obtained from equation 5.3. The magnetic field intensity may be increased up to 5.2 mT (4.5 A in each coil) to further narrow the precession motion of the electrons and enhance the electron current that reaches the extraction region of the TOF mass spectrometer. Electron currents are measured by a U1232A Handeheld Digital multimeter (Keysight Technologies, with 0.01 μA sensitivity) connected to the Faraday cup. The EG and the FC were fitted on titanium plate holders, fixed with four titanium rods to the respective blank flanges. The plates are locked to the rods using titanium M2 hexagonal screws.

Early tests of the electron with the working voltages applied to the TOF source electrodes resulting in negligible currents detected in the FC. This was attributed to the field produced by the focusing ring leaking into small gap between the exit of the EG and the TOF extraction volume. Two titanium extensions, one for the electron gun and another for the FC, were therefore produced in the OU workshop to solve the problem. The extensions penetrate directly in between the electrodes of the extraction region as shown in Fig. 5.8 for shielding the electrons from the TOF source fields above the pulser grid.

The experiment lacks an electron energy monochromator. Therefore, electron energy resolution cannot be lower than the thermal energy, ±0.5 eV with the filament at ~ 2500 K. The disadvantage of low electron energy resolution is offset by high electron beam currents (e.g. up to several μA) which will be important for experiments probing low-cross section processes (notably DEA) on low-density targets.

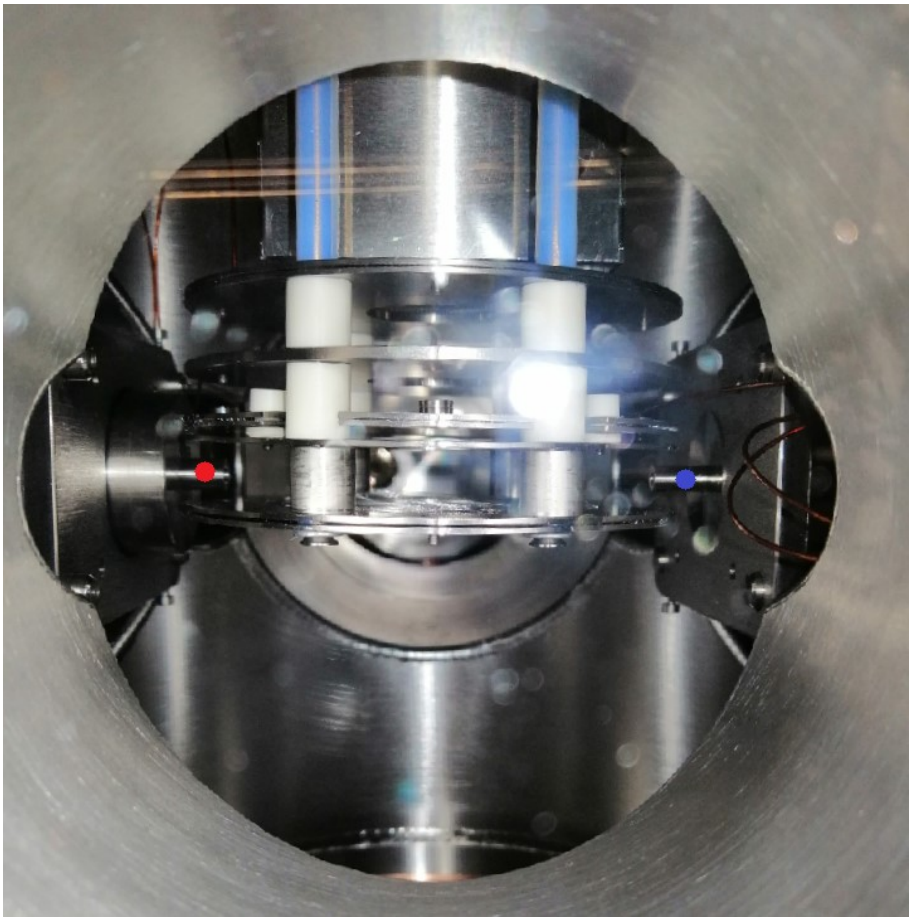

Figure 5.8: Electron gun and Faraday cup extension (red and blue dots, respectively) to shield the electron beam from field leaks from the TOF source electrodes above the pulser grid.

5.4.1 Electron gun and time-of-flight mass spectrometer optimisation in preparation for electron impact ionisation experiments

Generation of high energy electron (HEE) beams is easier to achieve with high beam currents than for LEE beams due to faster electrons being deviated less by residual electric fields and space charge. Therefore, the most straightforward tests we can perform involve to apply HEE beam currents suitable for EII experiments. In the first instance, a 70 eV CW electron beam was characterised. This energy approximately corresponds to the maximum EII cross section for most molecules reported in spectral libraries. During the Helmholtz pair alignment, we noticed that the current reaching the FC could be improved by slightly tilting the coils, so they were no longer parallel to each other. We interpreted this as being a direct effect of stray magnetic fields. To reduce them, the stainless steel bolts, nuts, and washers that were used close to all CF flanges, were replaced by aluminium counterparts. The changes produced a positive effect on beam collimation and the asymmetry between coils diminished. Ion gauges and turbomolecular pumps were strategically placed far from the electron beam and the magnetic field produced by the coils to minimise their interference with the trajectories of the electrons. The closest components that could contribute to stray magnetic fields in the vicinity of the electron beam are the foil of the

ILTD source (however its very low mass means that this is very unlikely to be significant), the steering deflectors of the reflectron time-of-flight mass spectrometer, the fibre optic components, the viewports, and the electrical feedthrough flanges, all of them manufactured in SS304. SS316L is also far from being the most appropriate material to use in the new experiment. So the grids, the tubing of the chamber, and some of the flanges could also contribute to stray magnetic fields. It is only really SS316LN that we can "trust" as well as truly non-magnetic materials such as titanium and aluminium.

The optimisation process of the EG proceeded in the following steps:

1. The currents reaching the FC and hitting the grid were measured as a function of the current passing through the EG filament. Based on previous initial optimizations, the cathode and grid voltages were set to 29 V and 31 V, respectively, with respect to the beam voltage at which the EG was floated (-70 V with respect to ground). The current in the Helmholtz coils was set to 4.5 A, (the maximum based on Krishnakumar and Mason's procedures [240]). Fig. 5.9 shows that the detection of electron current in the FC begins at 2.20 A applied in the EG filament, and a maximum is reached for 2.25 A. For filament currents above 2.25 A, the electron current detected in the FC drops. On the other hand, the current measured on the grid decreases for a filament current of $2.20-2.25$ A, reaches a local minimum and increases from thereon. The increase of current density with the filament current (and thus, the filament temperature) induces space-charge effects, leading more electrons to collide with the electrodes of the EG and consequently to a drop in the current measured in the FC.

2. The FC current was optimised as a function of grid voltage, setting the filament current to 2.25 A, the cathode voltage to 29 V, and the current on Helmholtz coils to 4.5 A. The FC current approached a plateau while the grid current increases approximately monotonically, when the grid voltage is increased (Fig. 5.9 (b)). We attribute this to an improvement in the focusing of the electrons for more positive voltages on the grid. However, more positive grid voltages also attract electrons more strongly onto the electrode itself, leading to the observed increase in the grid current. We could not observe the maximum in the EG current due to the limitation of the voltage supplied by the power supply (maximum 32 V).

3. The current measured in the FC was optimised as a function of the cathode voltage, setting the filament current to 2.25 A, the grid voltage to 31.8 V (corresponding to the highest FC current in Fig. 5.9 (b)) and the current passing in the Helmholtz coils to 4.5 A. As shown in Fig. 5.9 (c), the current measured in the FC increases when the cathode voltage is increased from 0 to 30 V and then remained approximately constant between 30 V and 35 V (the highest cathode voltage tested). The grid current evolves in an opposite manner, decreasing from $0-30$ V and remaining constant after that.

4. The current measured in the FC was optimised as a function of the current passing through the Helmholtz coils (see Fig. 5.9 (d)), setting the filament current to 2.25 A, the voltage in the grid to 31.8 V and the voltage in the cathode to 33.5 V (value for which the current detected in the FC is maximum, Fig. 5.9 (c)). Increasing the Helmholtz coils current produces a more intense magnetic field capable of improving the electron beam collimation and therefore, the current measured in the FC. It is interesting to note that the current measured in the FC does not start to increase at the same voltage that the grid current starts to decrease. This points to a very divergent electron beam: when the current in the Helmholtz coils is lower than 3 A, a portion of the electrons emitted by the filament pass through the hole in the grid electrode but divergence after that is too extreme to detect the beam on the FC. For currents above 3 A, the electron beam is collimated adequately to escape the EG and to be detected in the FC.

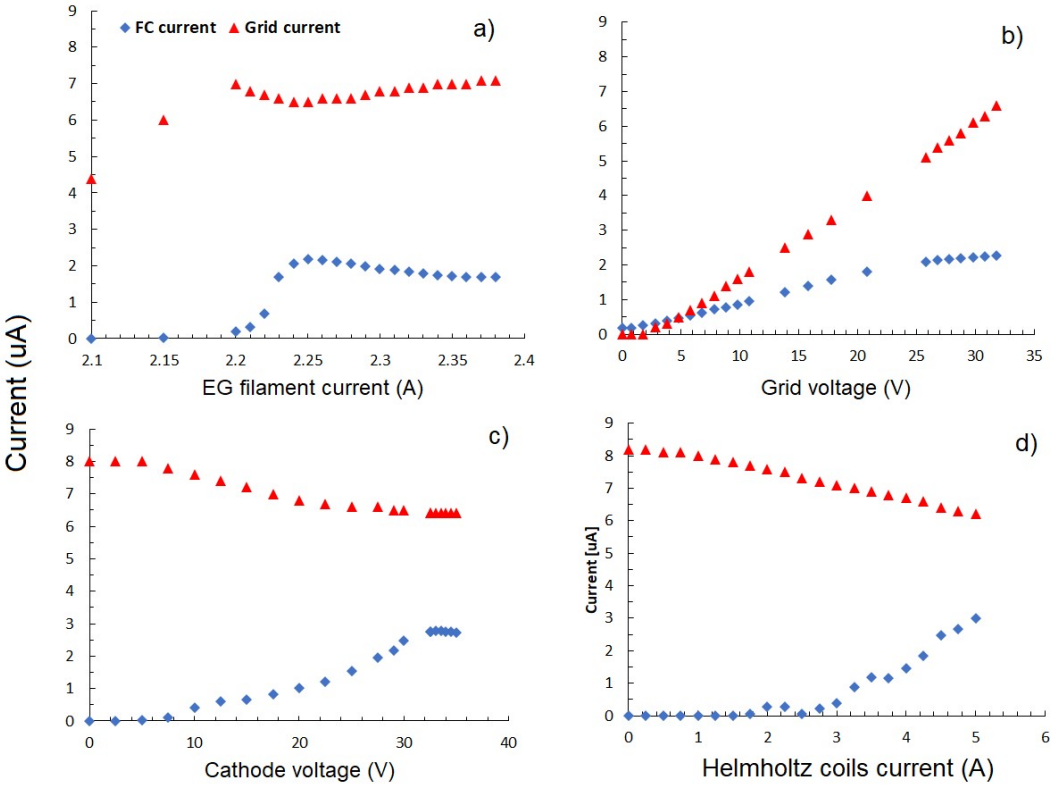

Figure 5.9: Optimisation of EG parameters at 70 eV. Red triangles and blue diamonds refer to currents measured on the grid and FC, respectively, as a function of: a) Current passing through the filament (cathode voltage 29 V and grid voltage 31.8 V, Helmholtz coils current 4.5 A); b) Voltage applied to the grid (EG current 2.25 A, cathode voltage 29 V, and Helmholtz coils current 4.5 A); c) Voltage applied to the cathode with respect to −70 V (EG current 2.25 A, grid voltage 31.8 V, and Helmholtz coils current 4.5 A); d) Current applied to the Helmholtz coils (EG current 2.25 A, cathode voltage 29 V, and grid voltage 31.8 V). All voltages given are with respect to the beam voltage that the electron gun is floated at (-70 V).

The electrodes of the time-of-flight ion optics were designed in SolidWorks and built in the OU workshop. Contrary to the ion optics of the compact experiment, the new ion optics do not have a

solid electrode. Instead, a ring with a high transparency SS316 grid is used, enabling ILT-desorbed molecules to migrate towards the interaction region. Inspired by grid systems employed by Limão-Vieira and co-workers at NOVA, a "sandwich" system was implemented in the electrodes to lock the grids in place and ensure the best possible grid flatness. This represents an improvement in comparison with the original electrodes of KORE, where grids were glued using carbon cement. The TOF source and the respective assembly with the crossed-beam chamber in shown in Fig. 5.10.

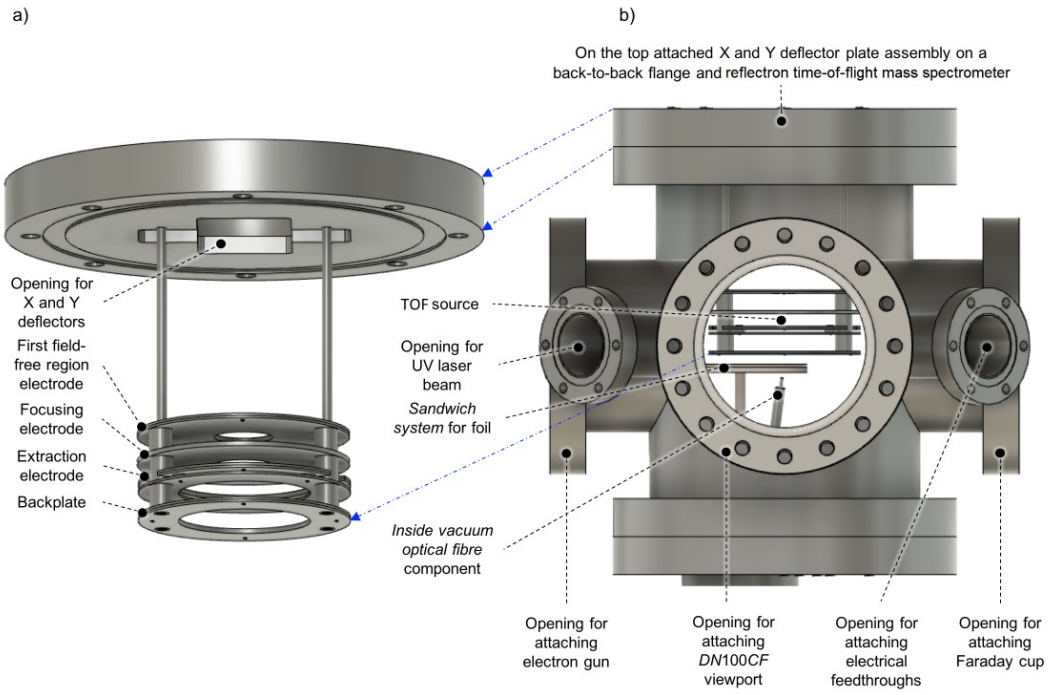

Figure 5.10: a) TOF source of the new DEA / EII / MPI appartus. b) Front view of the crossed-beam chamber with the TOF source assembled on the top.

We tested the new apparatus by performing EII experiments at 70 eV, on methanol molecules seeded in helium. Methanol has a high vapour pressure at room temperature (120 mbar) and seeding molecules in helium expansions generally provides higher EII- or MPI-TOF signals (based on the Group's experience using the compact experiment and the previous version of the Stark experiment). This also served the important purpose of testing our alignment of the new electron beam with the Stark deflected molecular beam. The mass spectrometer voltages were optimised to maximise the overall intensity of the ion signals. EII-TOF mass spectra acquired with 0 and 10 kV applied on the rod of Stark deflector are shown in Fig. 5.11. The experimental Stark removal points concerning the methanol and the protonated methanol ion signals are shown as inset. The degree of removal of methanol ion signal (17% at 10 kV) is greater than that attained for protonated methanol (only 7% at 10 kV). The greater removal of MeH^+ than Me^+ is clearly due to MeH^+ coming from ionised clusters with lower dipole moment / mass ratios. This observation is broadly consistent with the much more extensive nitromethane study in section 4.8.2. Note that nitromethane and methanol have similar dipole / mass ratios (0.057 D / a.m.u. and 0.053 D / a.m.u. respectively). The greater suppression of nitromethane$^+$ at 10 kV in Fig 4.12 (77 %) compared with that of

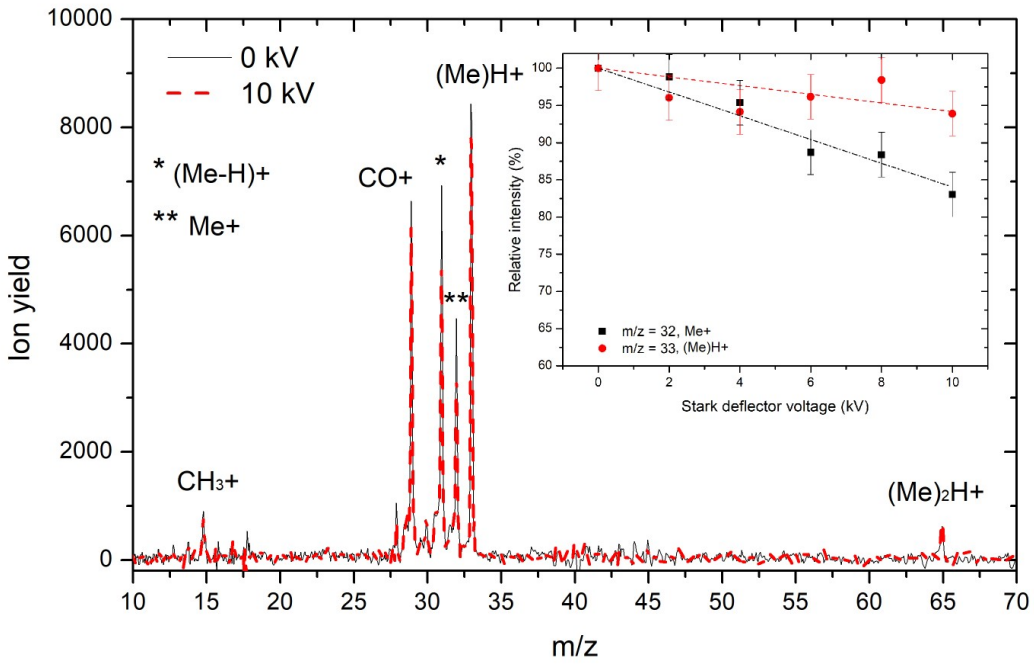

Figure 5.11: EII-TOF mass spectra of methanol seeded in helium at 70 eV. A supersonic beam was generated in a 50 μm nozzle by seeding 120 mbar of methanol in 1.1 bar of helium. The nozzle and the sample's reservoir were kept at room temperature. The expansion chamber was evacuated with a speed of 3300 l/s. The black solid line represents a mass spectrum where the Stark deflector was off (0 kV) and the dashed red curve represents a mass spectrum with 10 kV difference between rod and trough of the Stark deflector. Experimental Stark removal points are shown as inset.

methanol$^+$ at 10 kV in Fig. 5.11 is mainly attributed to the fact that the methanol molecules in the helium beam would have spent much less time in the deflector than the nitromethane molecules in the argon beam. However, different levels of rotational cooling and clustering in each beam will also have contributed to the different Stark removal curves.

5.4.2 Testing the electron gun performance in preparation for dissociative electron attachment experiments

The preparation of the electron gun for dissociative electron attachment experiments requires three main steps. Firstly, the EG parameters need to be optimised to work with a pulsed electron beam. Secondly, it is necessary to install a calibration gas inlet system. Thirdly, it is necessary to optimise the electron beam at low electron energies where stray magnetic and electric fields become more disruptive of the beam. The following sections, sections 5.4.2.1 and 5.4.2.2, present our progress with pulsing the electron beam and installing the calibration inlet. The experimental electron beam optimisation at low electron energies falls into future work.

5.4.2.1 Pulsing of the electron gun

Pulsing the EG is valuable for EII experiments since if we do not do it so, then some ionisations could take place during the extraction pulse and the ions produced in such collisions can add to the background signal in the resultant EII mass spectrum. However, pulsing the electron gun is even more important in DEA experiments. Otherwise, the mass spectrometer will extract and guide the electrons towards the MCP detector shortening its lifetime. Pulsing the EG requires the application of a square signal to the grid, with a given amplitude (equal to the difference between *off* and *on* voltages), a period, a duty cycle and a delay between the extraction pulse. The off and on voltages control the exit of electrons from the EG. According to Fig. 5.9 b), the off voltage needs to be 0 V (although negative values may be optimal), while the on voltage needs to be around 31 V (although more positive values may be optimal). Such amplitude cannot be achieved with the standard pulse generators available in the laboratory. To circumvent this, a square pulse is generated with 10 V of amplitude, using an Aim−TTi TGP110 pulse generator, which is then amplified by an home-built amplifier (R. Seaton and colleagues from Intra-Faculty Electronics and Computing Facility at OU). When the grid pulse is applied (on voltage), the electrons leave the EG and interact with molecules. During this period, the extraction electrode of the reflectron time-of-flight mass spectrometer is grounded and no ions or electrons are extracted. Electrons are then blocked by grounding the grid (off voltage) of the EG, and negative ions are extracted towards the detector by applying a positive voltage on the extraction electrode (+380 V) of the mass spectrometer. The extraction rate is set to ∼ 20 kHz, limited by the maximum frequency of the BEHLKE GHTS 30 pulser, which delivers the pulses for the extraction electrode. The duty cycle of the grid pulse and the respective delay with respect to the extraction pulse were optimised by monitoring the evolution of ion signals in EII experiments on methanol seeded in a helium supersonic beam (see the 0 kV mass spectrum in Fig. 5.11). We focused our attention on the strongest peak in the mass spectrum after the background subtraction (in the protonated methanol ion signal, m/z=33), whose variation with the aforementioned parameters is shown in Fig. **??**. Stronger signals were obtained with a duty-cycle of 1/5 and coincident grid and extraction pulses; however, to avoid presence of electrons in the interaction region during the extraction, a delay of 1 μs was used. The time required for 70 eV electrons to transverse the extraction region of the mass spectrometer is roughly 18 ns, much smaller than the delay employed between pulses.

5.4.2.2 The calibration gas inlet system

The gas inlet system serves to introduce a calibration gas in the main chamber. This calibration gas will define the energy scale of LEEs. DEA to O_2 is known to form a broad and intense peak of O^- ions at 6.5 eV [241]. Such peak can be used as reference for energy calibration of the electron beam. With this system it is also possible to measure absolute DEA cross sections using relative flow techniques (RFT). The determination of absolute cross sections by RFT involves the comparison of signal intensities between the target and a standard specie for which the cross section is known,

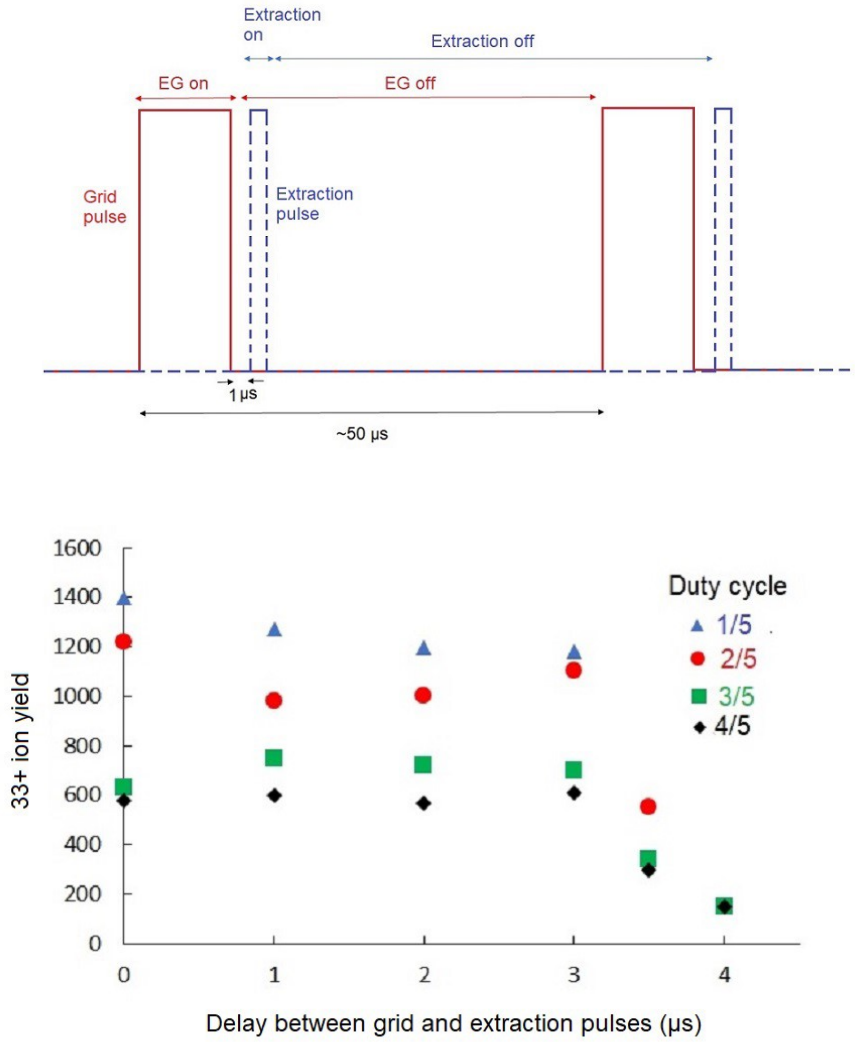

Figure 5.12: Top: Pulsing scheme for the grid of the EG and the extraction grid of the ion optics. Bottom: Optimisation of 33^+ ion signal resultant from fragmentation of methanol clusters seeded in He, upon collision with 70 eV electrons.

under the same experimental conditions [244]:

$$\sigma_t = \sigma_s \frac{N_t}{N_s} \frac{I_s}{I_t} \frac{p_s}{p_t} \frac{K_s}{K_t}$$

here t and s subscripts refer to target and standard species, respectively, N is the intensity of each ion, I is the averaged electron beam current, p is the pressure of the gas in the gas line and K is the ion detection efficiency. The gas inlet system is shown in Fig. 5.5 and comprises a SS304 DN16CF flange, where a stainless steel ($1/4$ inches of inner diameter) tube was welded in the outside. A titanium tube (6 mm inner diameter) was used in the vacuum side to minimise residual magnetic fields. The tube was bent to redirect the gas towards the interaction region of the mass spectrometer. The gas flow is controlled by an external DN16CF LewVac fine control variable leak valve.

5.5 Summary and future work

This chapter described the importance of installing the new DEA / EII / MPI apparatus in the Molecular Clusters Laboratory at the Open University. A detailed description of the the new components and changes made to the previous Stark experiment were given. The key progress and achievements described in this chapter are:

1. The replacement of the large volume SS304 interaction chamber featuring a high-energy-resolution / low-beam-current electron beam system within a mu metal shield with a small volume SS316L crossed-beam chamber designed for a low-energy-resolution / high-beam-current electron beam system with collimating external magnetic field. The chamber was assembled in a dedicated aluminium frame, and laser aligned with the remaining chambers of the Stark deflection setup. Preliminary EII experiments on Stark-manipulated methanol molecules and clusters in a helium beam demonstrate the successful alignment.

2. The inclusion of a custom ILTD source in the new crossed-beam chamber. The larger surface area and the rotatable system will permit irradiation of gas-phase targets for longer periods of time, compared with the ILTD source of the compact MPI-TOF experiment (described in chapter 3). The CW desorption laser beam is transmitted through a fibre optic system, reducing the radiation hazards and facilitating the alignment.

3. The EG and FC were installed and the performance of the EG was optimised for EII experiments at 70 eV. The optimisation process involved a self-consistent variation of voltages in the components of the EG and the current of the Helmholtz coils, in order to maximise the current measured in the FC. Then, we optimised the EG parameters to work in pulsed mode and high energy, based in electron impact ionisation experiments of methanol seeded in helium.

Despite of all the changes and improvements implemented, further work is still necessary, namely:

1. Optimisation of the UV mirrors and lens positions based on multi-photon ionisation ion signals and optimisation of mass spectrometer voltages for targets produced with the ILTD source. These steps are planned to be addressed in multi-photon ionisation experiments of laser desorbed uridine;

2. Performing tests with the ILTD source while heating simultaneously the interaction chamber to temperatures ~ 80 ºC;

3. Perform dissociative electron attachment experiments. The experimental characterisation and optimisation of the electron gun to operate in the low energy is necessary. The results of the simulations are a good starting point for this step. It is also fundamental to calibrate the electron energy scale using the O_2 gas. Finally, optimisation of the mass spectrometer voltages to transport and detect the negative ions.

5.6 Ackowledgments

Dr. Sam Eden proposed the idea of building a new apparatus combining the EG, FC, and the Helmholtz coils belonging to Prof. E. Krishnakumar and Prof. Nigel Mason, and part of the Stark deflection experiment incorporating a new ILTD source. Dr. Sam Eden, Jana Bocková and I worked on the general aspects of the experiment. Then we delegated tasks. The aluminium frame was designed by J. Bocková and D. Mészáros (an internship student at the Molecular Cluster Laboratory at The Open University). They assembled the aluminium frame support and interaction chamber and mounted the support for the Helmholtz coils. I was responsible for sketching the new ion optics electrodes for the mass spectrometer and the zero-length adapter connecting the new interaction chamber with the mass spectrometer. The alignment of the interaction chamber with the Stark deflection chamber was done by me and J. Bocková. Thomas Webley, the laboratory manager, gave us a valuable help to place the mass spectrometer on top of the interaction chamber, without upsetting the alignment. J. Bocková designed and tested the bottom flange containing the components for the ILTD source and the optical fibre system. The EG and FC were designed by Prof. E. Krishnakumar and built by C. Hall and the staff of Research Design and Engineering Facility at the OU. Prof. E. Krishnakumar provided useful suggestions regarding how to shield the electron beam from the leaking potentials of the electrodes of the ion optics. Me and J. Bocková built the protoboard with the electronics to supply the voltages to the EG (based on the schematics provided by Prof. E. Krishnakumar) with the support of D. Pound from Intra Faculty Electronics and Computing Facility at the OU. The holding systems for the EG and FC were designed by J. Bocková. I worked in the optimisation of the EG and FC with J. Bocková, D. Mészáros, I. Jana (an internship student in the Velocity Map Imaging Laboratory at the OU), Dr. K. Nixon and T. Hajj (an internship student in the Molecular Clusters Laboratory at the OU). The optimisation of the extraction optics and mass spectrometer voltages were done by me and J. Bocková. The drawings of the support system for the new turbomolecular pump attached to the 6 way cross chamber were produced by J. Bocková and installed by J. Bocková and T. Hajj.

Building an apparatus as the one described in this chapter required staff from diverse areas. We would like to thank to the Research Design and Engineering Facility at the OU, in particular to C. Hall and K. Dewar by providing advices about the materials and design of individual components, to A. Jones by the manufacturing of the ILTD source, the EG and the FC holding systems and respective extensions and to M. Abbott by building the electrodes of the ion optics and part of the support system of the new turbomolecular pump attached to the 6 way crossed chamber. We would like also to acknowledge the Intra Faculty Electronics and Computing Facility at the OU, in particular to D. Pound, by the help provided in the installation of the electronics for the EG and FC. All the design work was discussed with and supported by Dr. S. Eden.

Chapter 6

Conclusions and outlook

This PhD thesis focused on two major challenges in studying the radiation response of isolated neutral biomolecules and molecular clusters. The first concerns producing viable gas-phase targets of thermally-labile biomolecules without contamination by thermal dissociation products. The second concerns identifying tautomer-specific and cluster-specific radiation-induced reactions in experiments with multiple structures in the target. To address these challenges, we tested the capability of an ILTD source to vaporise guanine and guanosine, we compared prompt and metastable fragmentation experiments on these molecules with DFT calculations of tautomer-specific reaction pathways, and we and investigated the capability of a Stark deflector to manipulate nitromethane molecules and clusters seeded in CW supersonic jets. Finally, we report on the development of a new DEA / EII / MPI experiment assembled at the Molecular Clusters Laboratory to investigate the radiation response of clusters and molecules produced by ILTD or seeded in Stark-manipulated supersonic beams. In section 6.1 of the present chapter, we list the main contributions of this thesis. In section 6.2, we make a summary of the conclusions drawn in each chapter and propose further work that will enhance our comprehension about radiation-induced processes in neutral biomolecular targets of increasing complexity.

6.1 Highlights

We consider that the major contributions of this PhD thesis are:

1. **Demonstration of the value of ILTD for experiments on the most thermally-labile nucleobase and nucleoside**. We report direct measurements of foil temperatures from an ILTD source for the first time. Comparing the temperature of the ILTD foil with thresholds reported in the literature for thermal decomposition provided strong evidence for the absence of thermal decomposition in our ILT-desorbed guanine target. The same approach also supported the absence of thermal decomposition in our ILT-desorbed guanosine target, although this is less conclusive due to the scarcity of comparable studies in the literature. The high signal / noise ratios achieved in our MPI-TOF experiments on both of these targets indicates

that ILTD has considerable potential for experiments on neutral gas-phase biomolecules on the scale of nucleobases and nucleosides.

2. **Providing new insights into the fragmentation pathways of excited guanine ions in the gas phase**. Experimental identification of metastable pathways of guanine upon multi-photon ionisation with 225 nm photons. We identified 13 metastable dissociation pathways for the first time, as well confirming three that were previously reported in electron impact ionization experiments [115]. Taking together the present and previous experiments, a remarkable total of 10 different direct metastable dissociations of guanine$^+$ have now been identified, compared with just one each from previous experiments on adenine, uracil, and thymine [115, 138]. The large number of different direct dissociations of guanine$^+$ is likely to be at least partly due to the variety of different tautomers in neutral targets. To test this idea, we calculated reaction pathways and the respective unimolecular rate constants for some of the observed fragment ions. Based on these calculations, we were able to assign tautomer-dependent fragmentation pathways in our MPI experiments: metastable HCN abstraction to tautomers hydrogenated in the N7 position and metastable HCNO loss to tautomers hydrogenated in the N9 site.

3. **Proof-of-principle that Stark removal can be used to trace radiation-induced reaction products to specific neutral precursors in a mixed CW beam**. We developed a C++ code to predict deflection profiles of molecules and clusters inside our Stark deflection apparatus as a function of rotational temperature. By comparing experimental and simulated Stark removal curves (the removal of specific neutrals from the central axis of the beam as a function of the voltage on the Stark deflector), we were able to identify the neutral precursors of fragment ions deriving from electron impact ionisation of nitromethane molecules and clusters in a supersonic beam. We concluded that the detected nitromethane ions originate from both neutral monomers and a specific dimer arrangement (the side-by-side dimer), while methylated and protonated nitromethane ions derive mainly from side-by-side dimers. This demonstrates considerable potential of the method to investigate reactivity in clusters or in specific tautomers. However, evidence suggesting different rotational temperatures of different species in the beam presents challenge for the method's development.

4. **Design, assembly and partial optimisation of a new apparatus with the ultimate goal of performing the first DEA experiments of ILT-desorbed molecules and Stark-manipulated molecules**. The key progress at this stage has been the optimisation of the apparatus (alignment of the chambers, EG parameters, TOF voltages) for working in electron impact ionisation mode with molecules seeded in supersonic beams.

6.2 Summary and conclusions

6.2.1 Chapter 3 – Dissociative ionisation of guanine and guanosine tautomers: experiments exploiting ILTD and DFT calculations

In chapter 3 we presented results of multi-photon ionisation of ILT-desorbed guanine and guanosine molecules. We investigated potential markers of thermal decomposition of the targets: looking for ions in the MPI-TOF mass spectra that could be assigned to thermal decomposition products, comparing the foil temperatures oven temperatures in experiments in the literature, and analysing relative fragment ion production as a function of the CW desorption laser power (and hence, the foil temperature). We did not find any evidence for thermal decomposition of the targets. The fragment ion production for guanine is constant in the range of foil temperatures investigated (399−449 K). For guanosine, we observed a significant reduction in fragment ion production compared with guanosine$^+$ production as a function the foil temperature. To help understand this result, we assessed possible thermally-driven changes in tautomer / conformer populations and possible thermally-assisted photo-chemical reactions (notably proton transfer) in neutral excited states through DFT and TDDFT calculations, respectively. We concluded that neither of these mechanisms could plausibly be responsible for such a large variation in the fragment ion production. We suspect that the responsible thermally-induced mechanism is related with changes in tautomer / conformer populations in the neutral excited states rather than in the electronic ground states. For some nucleosides (uridine) the energy barriers for conformeric transitions were found to be smaller in the neutral excited states than in the electronic ground state, enabling thermally-assisted photophysical changes upon absorption of one UV photon. Such conformer transitions in neutral electronic excited states could explain the changes in the fragment ion production observed as a function of the laser desorption power if the *anti* conformers of guanosine are less prone to dissociation than the *syn* conformers.

The metastable pathways of guanine were investigated by mapping the intensity of ion signals against the time-of-flight and the reflection voltage of the TOF mass spectrometer. The precursor and daughter ions of the observed metastable channels were assigned by comparing the experimental map a Matlab simulation code. To interpret the results, we calculated fragmentation pathways, at DFT level, in the ionic states of the five lowest tautomers of guanine, and the respective rate constants. The results supported tautomer-dependent fragmentations of guanine$^+$: the metastable loss of HCN in our MPI experiments is assigned dominantly to tautomers hydrogenated in the N7 position while the HCNO loss is assigned dominantly to tautomers hydrogenated in the N9 position.

Finally, we investigated at DFT level, some reaction pathways of cationic keto-*syn* guanosine leading to N-glycosidic bond cleavage with single and double hydrogen transfer from the sugar to produce guanine$^+$ (the most intense feature in our MPI mass spectra and indeed in all guanosine mass spectra in the literature) and protonated guanine. We observed that breaking the 4'C−O sugar bond triggered spontaneous hydrogen transferences within the sugar and between the sugar and the base, ultimately leading to the N-glycosidic bond breakage and formation of a singly hydrogenated base ion (guanine$^+$) and a singly dehydrogenated sugar. The products are found to

be exothermic relative to the reactants and we suspect that they can further decompose giving rise to most of the ions previously observed in our guanine MPI-TOF mass spectra at 225 nm. This mechanism could explain why guanosine and guanine produce very similar MPI-TOF mass spectra. A reaction pathway involving the transference of the 2'C hydrogen from the sugar to N3 position on the base with subsequent cleavage of the N-glycosidic bond was also found to form a singly hydrogenated base and singly dehydrogenated sugar. This reaction pathway has transitions states with lower energies than the transition state of the first mechanism and may be responsible for the large guanine$^+$ signals in our MPI-TOF, and perhaps, in the most of the mass spectra.

6.2.2 Chapter 4 – Manipulation of neutral CW molecular beams using Stark deflection

Chapter 4 described the potential of Stark deflection in manipulating CW beams of neutral targets. Nitromethane molecules seeded in helium were deflected in two different electric field gradients (with 4 kV and 8 kV on the deflector rod) and probed by electron impact ionisation. A C++ code was written to predict deflection of molecules populating different rotational states. The program was able to reproduce the experimental deflection profiles and the low rotational temperature (3 K) required to achieve a good agreement can be rationalised in terms of the mass spectrometer being optimised in those specific measurements to preferentially sample a rotationally-colder subset of molecules in the beam. The maximum intensity of the deflected molecular beam was shifted 1.0 mm upwards relative to the undeflected beam and the beam was broadened by 2 mm. The C++ code does not show a good agreement with the experimental results for deflections larger than 2 mm and we suspect that this is a consequence of a narrow electron beam. Therefore, we are restricted to compare the simulations with the experimental data points in the vicinity of the beam centreline. For that reason, we developed a new (to our knowledge) approach which we call Stark removal with the aim of tracing fragment ions to specific neutral precursors. This approach was tested by investigating the origin of some fragment ions resultant from electron collisions with molecules and clusters of nitromethane seeded in a CW argon beam. The results revealed that the nitromethane ion signal derives mainly from monomers and (a smaller percentage) from a specific conformation of dimer, which we call the side-by-side dimer. Moreover, fragment ions deriving from clusters, (NM)H$^+$ and (NM)CH$_3^+$, are dominantly traced to ionised side-by-side dimers as well. The best agreement between the experiments and the simulation was achieved for a 10 – 20 K for the monomers and a higher temperature for the side-by-side dimers (approximately 50 K). This is an important outcome of the study as it demonstrates a challenge—taking into account possible variations in rotational temperatures of different species in the beam—that needs to be overcome in order to exploit the method to its full potential.

Thermochemical and dynamic calculations were performed to better understand the reactivity of side-by-side dimers after ionisation. The relative appearance energy for certain ion products agrees with their relative yield in the mass spectra. On the other hand, molecular dynamic simulations overestimated small fragment ions like CH$_3^+$ and underestimated larger fragment ions as (NM)H$^+$ and (NM)CH$_3^+$. This is rationalised in terms of dynamic timescales for intermolecular

vibrational energy redistribution and vibrational pre-dissociation: intermolecular vibrational energy redistribution proceeds on timescales shorter vibrational pre-dissociation and this sequence favours the formation of cluster fragment ions. Since the BOMD simulations cannot capture the sequentiality of these processes, cluster fragment ions are underestimated in detriment of small fragment ions.

The success of the present experiments indicate that Stark removal methodology can be a valuable tool identifying the neutral precursors of specific fragment ions in experiments that benefit from CW operation or pulsing with high duty cycles—notably DEA.

6.2.3 Chapter 5 – Development of a new DEA / EII / MPI experiment on ILT-desorbed molecules and molecules / clusters in Stark deflected beams

In chapter 5, we described the new DEA / EII / MPI apparatus assembled in the Molecular Cluster Laboratory. This apparatus will provide the unique capability of being able to study high- and low-energy electron beam interactions with ILT-desorbed molecules. Furthermore, it is designed to allow the first DEA experiments on molecules or clusters in Stark-manipulated beams. We replaced the large magnetically-shielded interaction chamber of the Stark apparatus with a smaller-mainly SS316L chamber (the crossed-beam chamber) in order to accommodate an electron beam system with an external collimating magnetic field. The achievements regarding this experiment are the following:

- Design and complete assembly of the apparatus. We designed and installed an ILTD source and a new TOF source for the mass spectrometer. We also installed an OU-built electron gun, Faraday cup, and Helmholtz coils (designed by E. Krishnakumar). The chamber was laser aligned with the remaining chambers of the Stark deflection apparatus.

- The new ILTD source is attached to a rotatable system and features a larger surface area than the ILTD source assembled in the compact experiment. This extends the time of measurements without having to break vacuum to replace the sample. A fibre optic system guides the CW desorption laser light towards the foil, improving safety and repeatability of the alignment.

- The optimised parameters for pulsing the electron gun were determined by monitoring ion signals resultant from electron impact ionisation at 70 eV of methanol molecules seeded in helium. The mass spectrometer voltages were optimised during this experiment as well.

6.3 Future work

A number of questions regarding the main topics of the current thesis remain unanswered. In relation to the results obtained from the ILTD source, the following points should be addressed:

- Calculate the energy barriers for the N-glycosidic bond rotation in the neutral excited states of guanosine and conclude whether the thermally-driven effect in the fragment ion production is compatible with changes in conformations in these states.

- Calculate reaction pathways for guanosine *anti* conformers leading to single and double hydrogenated base and single and double dehydrogenated sugar products. Of particular interest are the reaction pathways calculated in the present thesis for the *syn* conformer of guanosine. The comparison of the energy barriers for these pathways for both conformers will clarify which one is more robust to radiation and perhaps explain the thermally-driven effect on the fragment ion production of guanosine.

- Investigate the metastable fragmentation of guanosine to better understand its fragmentation pathways and, in particular, if guanine ions participate in the sequential fragmentation of the molecular ion.

- Evaluate the ability of the ILTD source to vaporise targets larger than nucleosides (e.g. nucleotides). This was not discussed in the present thesis but was partially tested in the compact experiment [84], where we tried to vaporise uridine monophosphate samples. We observed an increase in its volume and consistency during the evacuation of the chamber. We attribute this to a solvent effect or to the partial negative charges localised on the phosphate groups. We need to test alternative solvents to methanol for producing the layer of nucleotide samples.

Regarding the Stark deflection experiments, we need to check if we can use the C++ code to simulate, Stark deflected profiles in MPI experiments far from the beam centreline. We note that the direction of the UV laser pulses and the spot size can be adjusted easily through the optical system of the new experiment, unlike the electron beam produced by Kimball electron gun. In addition, we need to test the capability of the Stark removal approach to investigate mixtures of species that do not show such dramatic differences in dipole moment / mass as the two stable dimer configurations of nitromethane do. This is likely to require new strategies to determine or predict the differences in rotational temperatures of monomers and clusters in the studied supersonic beam. The key next steps for the advancement of the new DEA / EII / MPI apparatus are:

- Optimise the new ILTD source for electron beam experiments, with the TOF source externally heated to prevent sample condensation on the grids and electrodes.

- Optimise the EG parameters to operate at DEA energies (<10 eV).

Bibliography

[1] E. Alizadeh, T. M. Orlando, and L. Sanche. "Biomolecular damage induced by ionizing radiation: The direct and indirect effects of low-energy electrons on DNA." In: *Annual Review of Physical Chemistry* 66 (2015), pp. 379–398. DOI: 10.1146/annurev-physchem-040513-103605.

[2] G. Gómez-Tejedor and M. Fuss. "Radiation damage in biomolecular systems." In: *Radiation damage in biomolecular systems*. Springer Science+Business Media, 2012. Chap. Preface. DOI: 10.1108/02640470510611517.

[3] H. Rabus and H. Nettelbeck. "Nanodosimetry: Bridging the gap to radiation biophysics." In: *Radiation Measurements* 46.12 (2011), pp. 1522–1528. DOI: 10.1016/j.radmeas.2011.02.009. URL: 10.1016/j.radmeas.2011.02.009.

[4] J. Oro, S. L. Miller, and A. Lazcano. "The origin and early evolution of life on Earth." In: *Annual Review of Earth and Planetary Sciences* 18 (1990), pp. 317–356. DOI: 10.1146/annurev.ea.18.050190.001533.

[5] V. G Stavros and J. R. R Verlet. "Gas-Phase Femtosecond Particle Spectroscopy : A Bottom-Up Approach to Nucleotide Dynamics." In: *Annual Review of Physical Chemistry* 67 (2016), pp. 1–22. DOI: 10.1146/annurev-physchem-040215-112428.

[6] B. Boudaiffa, P. Cloutier, D. Hunting, M. A. Huels, and L. Sanche. "Resonant Formation of DNA Strand Breaks by Low-Energy (3 to 20 eV) Electrons." In: *Science* 287.5458 (2000), pp. 1658–1660. DOI: 10.1126/science.287.5458.1658.

[7] B. Alberts, A. Johson, J. Lewis, D. Morgan, M. Raff, K. Roberts, and P. Walter. *Molecular Biology of the Cell*. 5th. New York: Garland Science, 2008, p. 1709.

[8] Zephyris. *DNA structure*. URL: https://creativecommons.org/licenses/by-sa/3.0/deed.en.

[9] S. Surget, M. P. Khoury, and J. C. Bourdon. "Uncovering the role of p53 splice variants in human malignancy: A clinical perspective." In: *OncoTargets and Therapy* 7 (2013), pp. 57–67. DOI: 10.2147/OTT.S53876.

[10] W. M. Baird, L. A. Hooven, and B. Mahadevan. "Carcinogenic polycyclic aromatic hydrocarbon-DNA adducts and mechanism of action." In: *Enviromental and Molecular Mutagenisis* 45 (2005), pp. 106–114. DOI: doi:10.1002/em.20095.

[11] M. F. Goodman and R. Woodgate. "Translesion DNA polymerases." In: *Cold Spring Harbor Perspectives in Biology* 5.10 (2013), pp. 1–20. DOI: 10.1101/cshperspect.a010363.

[12] H. Wang, X. Mu, H. He, and X. D. Zhang. "Cancer Radiosensitizers." In: *Trends in Pharmacological Sciences* 39.1 (2018), pp. 24–48. DOI: 10.1016/j.tips.2017.11.003.

[13] F. D. Lewis, X. Liu, J. Liu, S. E. Miller, R. T. Hayes, and M. R. Wasielewski. "Direct measurement of hole transport dynamics in DNA." In: *Nature* 406.6791 (2000), pp. 51–53. DOI: 10.1038/35017524.

[14] A. Sobolewski and W. Domcke. "Molecular mechanisms of the photostability of life." In: *Physical Chemistry Chemical Physics* 12.19 (2010), pp. 4897–4898. DOI: 10.1039/C005130F.

[15] I. W. G. on the Evaluation of Carcinogenic Risks to Humans. In: *Radiation*. Vol. 100 D. Lyon, France: International Agency for Research on Cancer, 2012.

[16] J. Kohanoff, M. McAllister, G. A. Tribello, and B. Gu. "Interactions between low energy electrons and DNA: a perspective from first-principles simulations." In: *Journal of Physics: Condensed Matter* 29.38 (2017), pp. 1–29. DOI: 10.1088/1361-648X/aa79e3.

[17] Y. Frongillo, T. Goulet, M. J. Fraser, V. Cobut, J. P. Patau, and J. P. Jay-Gerin. "Monte carlo simulation of fast electron and proton tracks in liquid water - II. Nonhomogeneous chemistry." In: *Radiation Physics and Chemistry* 51.3 (1998), pp. 245–254. DOI: 10.1016/S0969-806X(97)00097-2.

[18] I. Foffa, M. Cresci, and M. G. Andreassi. "Health Risk and Biological Effects of Cardiac Ionising Imaging : From Epidemiology to Genes." In: *International Journal of Environmental Research and Health* 6 (2009), pp. 1882–1893. DOI: 10.3390/ijerph6061882.

[19] J. Bockova, A. Rebelo, M. Ryszka, R. Pandey, T. da Fonseca Cunha, P. Limão-Vieira, N. J. Mason, J. C. Poully, and S. Eden. "Mapping the complex metastable fragmentation pathways of excited 3-aminophenol +." In: *International Journal of Mass Spectrometry* 442 (2019), pp. 95–101. DOI: 10.1016/j.ijms.2019.05.006.

[20] J. Gu, J. Leszczynski, and H. F. Schaefer. "Interactions of electrons with bare and hydrated biomolecules: From nucleic acid bases to DNA segments." In: *Chemical Reviews* 112.11 (2012), pp. 5603–5640. DOI: 10.1021/cr3000219.

[21] M. Neustetter, J. Aysina, F. F. Da Silva, and S. Denifl. "The Effect of Solvation on Electron Attachment to Pure and Hydrated Pyrimidine Clusters." In: *Angewandte Chemie* 54.31 (2015), pp. 9124–9126. DOI: 10.1002/anie.201503733.

[22] N. J. Kim, H. Kang, G. Jeong, Y. S. Kim, K. T. Lee, and S. K. Kim. "Anomalous fragmentation of hydrated clusters of DNA base adenine in UV photoionization." In: *Journal of Physical Chemistry A* 104.28 (2000), pp. 6552–6557. DOI: 10.1021/jp000813+.

[23] B. Barc, M. Ryszka, J. C. Poully, E. Jabbour Al Maalouf, Z. El Otell, J. Tabet, R. Parajuli, P. J. M. Van Der Burgt, P. Limão-Vieira, P. Cahillane, M. Dampc, N. J. Mason, and S. Eden. "Multi-photon and electron impact ionisation studies of reactivity in adenine-water clusters." In: *International Journal of Mass Spectrometry* 365-366 (2014), pp. 194–199. DOI: 10.1016/j.ijms.2014.01.007.

[24] A. L. de Barros, A. Medina, F. Zappa, J. M. Pereira, E. Bessa, M. H. Martins, L. F. Coelho, W. Wolff, and N. V. de Castro Faria. "A simple experimental arrangement for measuring the vapour pressures and sublimation enthalpies by the Knudsen effusion method: Application to DNA and RNA bases." In: *Nuclear Instruments and Methods in Physics Research: Section A* 560.2 (2006), pp. 219–223. DOI: 10.1016/j.nima.2006.01.026.

[25] A. Abdelaziz, D. H. Zaitsau, A. V. Buzyurov, S. P. Verevkin, and C. Schick. "Sublimation thermodynamics of nucleobases derived from fast scanning calorimetry." In: *Physical Chemistry Chemical Physics* 22.2 (2020), pp. 838–853. DOI: 10.1039/c9cp04761a.

[26] M. Ryszka. "Radiation Induced Processes In Biomolecules And Clusters In Controlled Beams." Doctoral dissertation. The Open University, 2016.

[27] M. S. Wilson and J. A. McCloskey. "Chemical Ionization Mass Spectrometry of Nucleosides. Mechanisms of Ion Formation and Estimations of Proton Affinity." In: *Journal of the American Chemistry Society* 97.12 (1975), pp. 3436–3444. DOI: 10.1021/ja00845a026.

[28] M. Fang, J. Ivanisevic, H. P. Benton, C. H. Johnson, G. J. Patti, L. T. Hoang, W. Uritboonthai, M. E. Kurczy, and G. Siuzdak. "Thermal Degradation of Small Molecules: A Global Metabolomic Investigation." In: *Analytical Chemistry* 87.21 (2015), pp. 10935–10941. DOI: 10.1021/acs.analchem.5b03003.

[29] L. Li and D. M. Lubman. "Resonance enhanced multiphoton ionization of nucleosides by using pulsed-laser desorption in supersonic beam mass spectrometry." In: *International Journal of Mass Spectrometry and Ion Processes* 88.2-3 (1989), pp. 197–210. DOI: 10.1016/0168-1176(89)85016-5.

[30] J. C. Poully, J. Miles, S. De Camillis, A. Cassimi, and J. B. Greenwood. "Proton irradiation of DNA nucleosides in the gas phase." In: *Physical Chemistry Chemical Physics* 17.11 (2015), pp. 7172–7180. DOI: 10.1039/c4cp05303f.

[31] S. De Camillis, J. Miles, G. Alexander, O. Ghafur, I. D. Williams, D. Townsend, and J. B. Greenwood. "Ultrafast non-radiative decay of gas-phase nucleosides." In: *Physical Chemistry Chemical Physics* 17.36 (2015), pp. 23643–23650. DOI: 10.1039/c5cp03806e.

[32] O. Ghafur, S. W. Crane, M. Ryszka, J. Bockova, A. Rebelo, L. Saalbach, S. De Camillis, J. B. Greenwood, S. Eden, and D. Townsend. "Ultraviolet relaxation dynamics in uracil: Time-resolved photoion yield studies using a laser-based thermal desorption source." In: *Journal of Chemical Physics* 149.3 (2018). DOI: 10.1063/1.5034419.

[33] J. Bockova, A. Rebelo, M. Ryszka, R. Pandey, D. Mészáros, P. Limão-Vieira, P. Papp, N. Mason, D. Townsend, K. Nixon, V. Vizcaino, J. Poully, and S. Eden. "Thermal desorption effects on fragment ion production from multi-photon ionized uridine and selected analogues." In: *Molecules (Under review)* ().

[34] D. L. Ruiz, M. D. M. Schiavoni, S. L. Laurella, J. M. Giussi, J. J. P. Furlong, and P. E. Allegretti. "Spectrochimica Acta Part A : Molecular and Biomolecular Spectroscopy The evidence for the occurrence of tautomeric structures for selected aldehydes and thioaldehydes." In: *Spectrochimica Acta A: Molecular and Biomolecular Spectroscopy* 78.5 (2011), pp. 1397–1402. DOI: 10.1016/j.saa.2011.01.017.

[35] L. Zamir, B. S. Jensen, and E. Larsen. "An investigation of tautomeric equilibria by means of mass spectrometry." In: *Organic Mass Spectrometry* 2.1 (1969), pp. 49–61. DOI: 10.1002/oms.1210020106.

[36] C. A. Bauer and S. Grimme. "Automated quantum chemistry based molecular dynamics simulations of electron ionization induced fragmentations of the nucleobases uracil, thymine, cytosine, and guanine." In: *European Journal of Mass Spectrometry* 21.3 (2015), pp. 125–140. DOI: 10.1255/ejms.1313.

[37] W. Wolff, H. Luna, E. C. Montenegro, W. Wolff, H. Luna, and E. C. Montenegro. "Isomeric signatures in the fragmentation of pyridazine and pyrimidine induced by fast ion impact Isomeric signatures in the fragmentation of pyridazine and pyrimidine induced by fast ion impact." In: *Journal of Chemical Physics* 143 (2015), p. 044314. DOI: 10.1063/1.4927233.

[38] A. M. Rijs and J. Oomens. "IR Spectroscopic Techniques to Study Isolated Biomolecules." In: *Topics in Current Chemistry* 364 (2015), pp. 1–42. DOI: 10.1007/128.

[39] Y. Hu, J. Guan, and E. R. Bernstein. "Mass-selected IR-VUV (118 nm) spectroscopic studies of radicals, aliphatic molecules, and their clusters." In: *Mass spectrometry Reviews* 32 (2013), pp. 484–501. DOI: 10.1002/mas.

[40] F. Filsinger, J. Küpper, G. Meijer, J. L. Hansen, J. Maurer, J. H. Nielsen, L. Holmegaard, and H. Stapelfeldt. "Pure samples of individual conformers: The separation of stereoisomers of complex molecules using electric fields." In: *Angewandte Chemie* 48.37 (2009), pp. 6900–6902. DOI: 10.1002/anie.200902650.

[41] H. Bieker, J. Onvlee, M. Johny, L. He, T. Kierspel, S. Trippel, D. A. Horke, and J. Küpper. "Pure Molecular Beam of Water Dimer." In: *Journal of Physical Chemistry A* 123.34 (2019), pp. 7486–7490. DOI: 10.1021/acs.jpca.9b06460.

[42] B. Barc, M. Ryszka, J. Spurrell, M. Dampc, P. Limão-Vieira, R. Parajuli, N. J. Mason, and S. Eden. "Multi-photon ionization and fragmentation of uracil: Neutral excited-state ring opening and hydration effects." In: *Journal of Chemical Physics* 139.24 (2013). DOI: 10.1063/1.4851476.

[43] K. A. Kistler and S. Matsika. "Multi-scale Quantum Models for Biocatalysis vol.7." In: *Multi-scale quantum models for biocatalysis*. Ed. by D. M. York and T.-S. Lee. Dordrecht Heidelberg New York London: Springer Science+Business Media, 2009. Chap. 11-Quantum, pp. 285–339.

[44] M. Born and K. Huang. *Dynamical theory of crystal lattices*. Ed. by N. F. Mott, E. C. Bullard, and D. H. Wilkinson. 1st. Oxford University Press, 1968, p. 432.

[45] T. Kato. "On the adiabatic theorem of quantum mechanics." In: *Journal of the Physical Society of Japan* 5 (1950), pp. 435–439. DOI: 10.1143/JPSJ.5.435.

[46] M. A. L. Marques, N. T. Maitra, F. M. S. Nogueira, E. K. U. Gross, and A. Rubio. In: *Fundamentals of time-dependent density functional theory*. Springer-Verlag, 2012. Chap. 14: Non-Born-Oppenheimer dynamics and conical intersections, pp. 279–299. ISBN: 978-3-642-23517-7. DOI: 10.1007/978-3-642-23518-4.

[47] J. P. Malhado, M. J. Bearpark, and J. T. Hynes. "Non-adiabatic dynamics close to conical intersections and the surface hopping perspective." In: *Frontiers in Chemistry* 2 (2014), pp. 1–21. DOI: 10.3389/fchem.2014.00097.

[48] S. Faraji, S. Matsika, and A. I. Krylov. "Calculations of non-adiabatic couplings within equation-of-motion coupled-cluster framework : Theory, implementation, and validation against multi-reference methods." In: *Journal of Chemical Physics* 148 (2018), p. 044103. DOI: 10.1063/1.5009433.

[49] J. Von Neumann and E. Wigner. "On the behaviour of eigenvalues in adiabatic processes." In: *Physikalische Zeitschrift* 30 (1929), p. 467. DOI: 10.1142/9789812795762_0002.

[50] J. Franck. "Elementary processes of photochemical reactions." In: *Transactions of the Faraday Society* 21 (1925), pp. 536–542. DOI: 10.1039/TF9262100536.

[51] E. Condon. "A theory of intensity distribution in band systems." In: *Physical Review* 28.6 (1926), pp. 1182–1201. DOI: 10.1103/PhysRev.28.1182.

[52] V. P. Gupta. *Principles and Applications of Quantum Chemistry*. London San Diego Waltham Oxford: Elsevier, 2016.

[53] J. D Coyle. "What is organic chemistry." In: *Introduction to organic photochemistry*. John Wiley & Sons, 1986. Chap. 1, pp. 1–37.

[54] J. Lindon, G. Tranter, and D. Koppenaal. "Luminscence theory." In: *Encyclopedia of spectroscopy and spectrometry*. 2nd. Elsevier, Academic Press, 2010, pp. 628–634.

[55] D. A. Skoog, F. J. Holler, and S. R. Crouch. *Principles of Instrumental Analysis*. 7th ed. Boston, USA: Cengage Learning, 2018, p. 397.

[56] J. Morellec, D. Normand, and G. Petite. "Resonance shifts in the multiphoton ionization of cesium atoms." In: *Physical Review A* 14.1 (1976), pp. 300–312. DOI: 10.1103/PhysRevA.14.300.

[57] E. F. van Dishoeck and R. Visser. "Molecular Photodissociation." In: *Laboratory Astrochemistry*. John Wiley & Sons, Ltd, 2014. Chap. 4, pp. 229–254.

[58] J. Gross. *Mass Spectrometry*. Third. 5. Springer, 2017, pp. 1–968. DOI: 10.1021/ac00269a027.

[59] I. I. Fabrikant, S. Eden, N. J. Mason, and J. Fedor. *Recent Progress in Dissociative Electron Attachment: From Diatomics to Biomolecules*. 1st ed. Vol. 66. Elsevier Inc., 2017, pp. 545–657.

[60] L. Christophorou, D. McCorkie, and A. Christodoulides. In: *Electron–Molecule Interactions and their Applications*. Ed. by L. Christophorou. Vol. 1. Academic Press, Inc., 1984. Chap. 6-Electron attachment processes, pp. 477–617.

[61] O. K. Rice and H. C. Ramsperger. "Theories of unimolecular gas reactions at low pressures." In: *Journal of the American Chemical Society* 49.7 (1927), pp. 1617–1629. DOI: 10.1021/ja01406a001.

[62] R. A. Marcus. "Unimolecular dissociations and free radical recombination reactions." In: *Journal of Chemical Physics* 20.3 (1952), pp. 359–364. DOI: 10.1063/1.1700424.

[63] P. Ferrari, E. Janssens, P. Lievens, and K. Hansen. "Thermal radiation and fragmentation pathways of photo-excited silicon clusters." In: *Journal of Chemical Physics* 143.22 (2015), p. 224313. DOI: 10.1063/1.4936917.

[64] R. F. P. Atkins. *Molecular quantum mechanics*. 5th. Oxford, UK: Oxford University Press, 2010, pp. 1–537.

[65] C. Roothan. "New developments in molecular orbital theory." In: *Reviews of Modern Physics* 23 (1951), pp. 69–89.

[66] G. G. Hall. "The Molecular Orbital Theory of Chemical Valency . VIII . A Method of Calculating Ionization Potentials." In: *Procedings of the Royal Society A* 205 (1951), pp. 541–552. DOI: 10.1098/rspa.1951.0048.

[67] P. Hohenberg and W. Kohn. "Inhomogeneous electon gas." In: *Physical Review* 136.3B (1964), pp. 864–870. DOI: 10.1007/BF01198136.

[68] W. Kohn and L. J. Sham. "Self-consistent equations including exchange and correlation effects." In: *Physical Review* 140.4A (1965), pp. 1133–1138. DOI: 10.1046/j.1365-4362.2002.01376.x.

[69] Q. Peng, F. Duarte, and R. S. Paton. "Computing organic stereoselectivity – from concepts to quantitative calculations and predictions." In: *Chemical Society Reviews* 45 (22 2016), pp. 6093–6107. DOI: 10.1039/C6CS00573J.

[70] Y. Zhao and D. G. Truhlar. "The M06 suite of density functionals for main group thermochemistry, thermochemical kinetics, noncovalent interactions, excited states, and transition elements: Two new functionals and systematic testing of four M06-class functionals and 12 other function." In: *Theoretical Chemistry Accounts* 120 (2008), pp. 215–241. DOI: 10.1007/s00214-007-0310-x.

[71] S. F Boys. "Electronic Wave Functions . I . A General Method of Calculation for the Stationary States of Any Molecular System." In: *Proceedings of the Royal Society A* 200 (1950), pp. 542–554. DOI: 10.1098/rspa.1950.0036.

[72] Binkley, J. S., Pople, J. A., Hehre, W. J. "Self-Consistent molecular orbital methods. XXI. Small split-valence basis sets for the first-row elements." In: *American Chemical Society* 102 (1980), pp. 939–947. DOI: 10.1021/ja00523a008.

[73] R. Krishnan, J. S. Binkley, R. Seeger, and J. A. Pople. "Self-consistent molecular orbital methods . XX . A basis set for correlated wave functions." In: *Journal of Chemical Physics* 72 (1980), pp. 650–654. DOI: 10.1063/1.438955.

[74] T. Clark, J. Chandrasekhar, G. W. Spitznagel, and P. V. R. Schleyer. "Efficient Diffuse Function- Augmented Basis Sets for Anion Calculations . III .* The 3-21 + G Basis Set for First-Row." In: *Journal of Computational Chemistry* 4.3 (1983), pp. 294–301. DOI: 10.1002/jcc.540040303.

[75] J. E. D. Bene and H. D. Mettee. "Ab initio computation of the enthalpies of some gas-phase hydration reactions." In: *Journal of Physical Chemistry* 87 (1983), pp. 3279–3282. DOI: 10.1021/j100240a020.

[76] T. H Dunning. "Gaussian basis sets for use in correlated molecular calculations . I . The atoms boron through neon and hydrogen Gaussian basis sets for use in correlated molecular calculations . I . The atoms boron through neon and hydrogen." In: *Journal of Chemical Physics* 90 (1989), pp. 1007–1023. DOI: 10.1063/1.456153.

[77] M. J. Frisch, G. W. Trucks, H. B. Schlegel, G. E. Scuseria, M. A. Robb, J. R. Cheeseman, G. Scalmani, V. Barone, G. A. Petersson, H. Nakatsuji, X. Li, M. Caricato, A. V. Marenich, J. Bloino, B. G. Janesko, R. Gomperts, B. Mennucci, H. P. Hratchian, J. V. Ortiz, A. F. Izmaylov, J. L. Sonnenberg, D. Williams-Young, F. Ding, F. Lipparini, F. Egidi, J. Goings, B. Peng, A. Petrone, T. Henderson, D. Ranasinghe, V. G. Zakrzewski, J. Gao, N. Rega, G. Zheng, W. Liang, M. Hada, M. Ehara, K. Toyota, R. Fukuda, J. Hasegawa, M. Ishida, T. Nakajima, Y. Honda, O. Kitao, H. Nakai, T. Vreven, K. Throssell, J. A. Montgomery Jr., J. E. Peralta, F. Ogliaro, M. J. Bearpark, J. J. Heyd, E. N. Brothers, K. N. Kudin, V. N. Staroverov, T. A. Keith, R. Kobayashi, J. Normand, K. Raghavachari, A. P. Rendell, J. C. Burant, S. S. Iyengar, J. Tomasi, M. Cossi, J. M. Millam, M. Klene, C. Adamo, R. Cammi, J. W. Ochterski, R. L. Martin, K. Morokuma, O. Farkas, J. B. Foresman, and D. J. Fox. *Gaussian09 Revision D.01*. Gaussian Inc. Wallingford CT. 2016.

[78] R. L. Johnston. *Atomic and molecular clusters*. New York: Taylor & Francis, 2002.

[79] A. Austin, G. A. Petersson, M. J. Frisch, F. J. Dobek, G. Scalmani, and K. Throssell. "A density functional with spherical atom dispersion terms." In: *Journal of Chemical Theory and Computation* 8.12 (2012), pp. 4989–5007. DOI: 10.1021/ct300778e.

[80] S. Grimme, J. Antony, S. Ehrlich, and H. Krieg. "A consistent and accurate ab initio parametrization of density functional dispersion correction (DFT-D) for the 94 elements H-Pu." In: *Journal of Chemical Physics* 132.15 (2010). DOI: 10.1063/1.3382344.

[81] R. P. Matthews, T. Welton, and P. A. Hunt. "Competitive pi interactions and hydrogen bonding within imidazolium ionic liquids." In: *Physical Chemistry Chemical Phyics.* 16 (2014), pp. 3238–3253. DOI: 10.1039/C3CP54672A.

[82] "The nucleoside uridine isolated in the gas phase." In: *Angewandte Chemie - International Edition* 54.10 (2015), pp. 2991–2994. DOI: 10.1002/anie.201412460.

[83] B. Barc. "Hydrated clusters of nucleic acid bases in supersonic beams probed by multi-photon ionization (MPI) mass spectrometry." Doctoral dissertation. The Open University, 2012. DOI: 10.21954/ou.ro.0000f115.

[84] J. Bocková. "Scaling complexity in the study of radiation damage in biomolecules." Doctoral dissertation. The Open University, 2019.

[85] J. Kopyra. "Low energy electron attachment to the nucleotide deoxycytidine monophosphate: Direct evidence for the molecular mechanisms of electron-induced DNA strand breaks." In: *Physical Chemistry Chemical Physics* 14.23 (2012), pp. 8287–8289. DOI: 10.1039/c2cp40847c.

[86] J. Kočišek, B. Sedmidubská, S. Indrajith, M. Fárník, and J. Fedor. "Electron Attachment to Microhydrated Deoxycytidine Monophosphate." In: *Journal of Physical Chemistry B* 122.20 (2018), pp. 5212–5217. DOI: 10.1021/acs.jpcb.8b03033.

[87] M. A. Posthumus, P. G. Kistemaker, H. L. Meuzelaar, M. A. Posthumus, M. C. Ten, and N. de Brauw. "Laser Desorption-Mass Spectrometry of Polar Nonvolatile Bio-Organic Molecules." In: *Analytical Chemistry* 50.7 (1978), pp. 985–991. DOI: 10.1021/ac50029a040.

[88] F. J. Vastola, R. O. Mumma, and A. J. Pirone. "Analysis of organic salts by laser ionization." In: *Organic mass spectrometry* 3 (1970), pp. 101–104.

[89] I. Dimicoli, M. Mons, B. Tardivel, and Q. Zhao. "A simple laser vaporization source for thermally fragile molecules coupled to a supersonic expansion : application to the spectroscopy of tryptophan." In: *Chemical Physics Letters* 320 (2000), pp. 282–288.

[90] R. Tembreull and D. M. Lubman. "Pulsed Laser Desorption of Biological Molecules in Supersonic Beam Mass Spectrometry with Resonant Two-Photon Ionization Detection." In: *Analytical Chemistry* 59.8 (1987), pp. 1082–1088. DOI: 10.1021/ac00135a004.

[91] J. R. Cable, M. J. Tubergen, and D. H. Levy. "Laser Desorption Molecular Beam Spectroscopy: The Electronic Spectra of Tryptophan Peptides in the Gas Phase." In: *Journal of the American Chemistry Society* 109 (1987), pp. 6198–6199.

[92] R. Cohen, B. Brauer, E. Nir, L. Grace, and M. S. de Vries. "Resonance-Enhanced Multi-photon Ionization Spectroscopy of Dipeptides." In: *Journal of Physical Chemistry A* 104 (2000), pp. 6351–6355.

[93] E. Nir, L. Grace, B. Brauer, and M. S. De Vries. "REMPI spectroscopy of jet-cooled guanine." In: *Journal of the American Chemical Society* 121.20 (1999), pp. 4896–4897. DOI: 10.1021/ja984088g.

[94] E. Nir, M. Müller, L. I. Grace, and M. S. de Vries. "REMPI spectroscopy of cytosine." In: *Chemical Physics Letters* 355 (2002), pp. 59–64.

[95] A. Gahlmann, S. T. Park, and A. H. Zewail. "Structure of isolated biomolecules by electron diffraction - Laserdesorption: Uracll and guanine." In: *Journal of the American Chemical Society* 131.8 (2009), pp. 2806–2808. DOI: 10.1021/ja808720j.

[96] A. Abo-Riziq, B. O. Crews, I. Compagnon, J. Oomens, G. Meijer, G. V. Helden, M. Kabelac, P. Hobza, and M. S. de Vries. "The Mid-IR Spectra of 9-Ethyl Guanine, Guanosine, and 2-Deoxyguanosine." In: *Journal of Physical Chemistry A* 111 (2007), pp. 7529–7536. DOI: 10.1021/jp072183i.

[97] E. Nir, P. Imhof, K. Kleinermanns, and M. S. De Vries. "REMPI spectroscopy of laser desorbed guanosines." In: *Journal of the American Chemical Society* 122.33 (2000), pp. 8091–8092. DOI: 10.1021/ja000502c.

[98] J. W. Shin and E. R. Bernstein. "Vacuum ultraviolet photoionization of carbohydrates and nucleotides." In: *Journal of Chemical Physics* 140.4 (2014), p. 044330. DOI: 10.1063/1.4862829.

[99] M. Staniforth and V. G. Stavros. "Recent advances in experimental techniques to probe fast excited-state dynamics in biological molecules in the gas phase : dynamics in nucleotides , amino acids and beyond." In: *Proceedings of the Royal Society A* 469 (2013), p. 20130458. DOI: 10.1098/rspa.2013.0458.

[100] B. Lindner and U. Seydel. "Laser Desorption Mass Spectrometry of Nonvolatlles under Shock Wave Conditions." In: *Analitical Chemistry* 57 (1985), pp. 895–899.

[101] C. R. Calvert, L. Belshaw, M. J. Duffy, O. Kelly, R. B. King, A. G. Smyth, T. J. Kelly, J. T. Costello, D. J. Timson, W. A. Bryan, T. Kierspel, P. Rice, I. C. Turcu, C. M. Cacho, E. Springate, I. D. Williams, and J. B. Greenwood. "LIAD-fs scheme for studies of ultrafast laser interactions with gas phase biomolecules." In: *Physical Chemistry Chemical Physics* 14.18 (2012), pp. 6289–6297. DOI: 10.1039/c2cp23840c.

[102] U. Sezer, L. Wörner, J. Horak, L. Felix, J. Tüxen, C. Götz, A. Vaziri, M. Mayor, and M. Arndt. "Laser-induced acoustic desorption of natural and functionalized biochromophores." In: *Analitical Chemistry* 87.11 (2015), pp. 5614–5619. DOI: 10.1021/acs.analchem.5b00601.

[103] W.-P. Peng, Y.-C. Yang, M.-W Kang, T. Y.-K., Z. Nie, H.-C. Chang, W. Chang, and C.-H. Chen. "Laser-Induced Acoustic Desorption Mass Spectrometry of Single Bioparticles." In: *Angewandte Chemie* 45 (2006), pp. 1423–1426. DOI: 10.1002/anie.200503271.

[104] J. Chen, L. Jia, L. Zhao, X. Lu, W. Guo, J. Weng, and F. Qi. "Analysis of Petroleum Aromatics by Laser-Induced Acoustic Desorption/Tunable Synchrotron Vacuum Ultraviolet Photoionization Mass Spectrometry." In: *Energy Fuels* 27 (2013), pp. 2010–2017.

[105] Z. Huang, T. Ossenbrüggen, I. Rubinsky, M. Schust, D. A. Horke, and J. Küpper. "Development and Characterization of a Laser-Induced Acoustic Desorption Source." In: *Analytical Chemistry* 90.6 (2018), pp. 3920–3927. ISSN: 15206882. DOI: 10.1021/acs.analchem.7b04797.

[106] R. Pandey. "UV Induced Processes in Biomolecules , Hydrated Clusters and Stark Deflected Beams." Doctoral dissertation. The Open University, 2017.

[107] P. Allegretti, M. Schiavonni, E. Castro, and J. Furlong. "Tautomeric Equilibria Studies by Mass Spectrometry." In: *Nature Precedings* (2008), pp. 1–76. DOI: 10.1038/npre.2008.1842.1.

[108] E. W. Spisz, A. J. Weigund, R. L. Bowmun, and J. R. Jack. "Solar absorptances and spectral reflectances of 12 metals for temperatures ranging from 300 to 500 K." In: *Nasa, Tn D-5353* (1969).

[109] F. S. Boydağ. "The optical properties of some steel surfaces with different surface preparations for high temperature use." In: *Solar Energy Materials* 13.3 (1986), pp. 185–195. DOI: 10.1016/0165-1633(86)90017-1.

[110] S. B. Boyden and Y. Zhang. "Temperature and wavelength-dependent spectral absorptivities of metallic materials in the infrared." In: *Journal of Thermophysics and Heat Transfer* 20.1 (2006), pp. 9–15. DOI: 10.2514/1.15518.

[111] V. Periquet, A. Moreau, S. Carles, J. P. Schermann, and C. Desfrançois. "Cluster size effects upon anion solvation of N-heterocyclic molecules and nucleic acid bases." In: *Journal of Electron Spectroscopy and Related Phenomena* 106.2-3 (2000), pp. 141–151. DOI: 10.1016/s0368-2048(99)00072-9.

[112] H. Chen and S. Li. "Theoretical study on the excitation energies of six tautomers of guanine: Evidence for the assignment of the rare tautomers." In: *Journal of Physical Chemistry A* 110.45 (2006), pp. 12360–12362. DOI: 10.1021/jp064513p.

[113] X. J. Wang and J. Z. You. "Study on the molecular structure and thermal stability of pyrimidine nucleoside analogs." In: *Journal of Thermal Analysis and Calorimetry* 120.1 (2015), pp. 1009–1025. DOI: 10.1007/s10973-014-4362-6.

[114] J. Lin, S. Peng, I. Aklyama, K. Li, L. K. Lee, and P. R. LeBreton. "Ultraviolet photoelectron studies of the ground state electronic structure and gas phase tautomerism of hypoxanthine and guanine." In: *Journal of Physical Chemistry* 84 (1980), pp. 1006–1012. DOI: 10.1021/j100446a015.

[115] J. M. Rice and G. Dudek. "Mass Spectra of Nucleic Acid Derivatives. II. Guanine, Adenine, and Related Compounds." In: *Journal of the American Chemical Society* 89.11 (1967), pp. 2719–2725. DOI: 10.1021/ja00987a039.

[116] N. S. Hush and A. S. Cheung. "Ionization potentials and donor properties of nucleic acid bases and related compounds." In: *Chemical Physics Letters* 34.1 (1975), pp. 11–13.

[117] D. Dougherty and S. P. McGlynn. "Photoelectron spectroscopy of carbonyls. Biological molecules." In: *Journal of Chemical Physics* 67.3 (1977), pp. 1289–1290. DOI: 10.1063/1.434949.

[118] D. Dougherty, E. S. Younathan, R. Voll, S. Abdulnur, and S. P. McGlynn. "Photoelectron spectroscopy of some biological molecules." In: *Journal of Electron Spectroscopy and Related Phenomena* 13.3 (1978), pp. 379–393. DOI: 10.1016/0368-2048(78)85042-7.

[119] E. Nir, C. Janzen, P. Imhof, K. Kleinermanns, and M. S. De Vries. "Guanine tautomerism revealed by UV-UV and IR-UV hole burning spectroscopy." In: *Journal of Chemical Physics* 115.10 (2001), pp. 4604–4611. DOI: 10.1063/1.1391443.

[120] H. Abdoul-Carime, J. Langer, M. A. Huels, and E. Illenberger. "Decomposition of purine nucleobases by very low energy electrons." In: *European Physical Journal D* 35.2 (2005), pp. 399–404. DOI: 10.1140/epjd/e2005-00194-5.

[121] M. Y. Choi and R. E. Miller. "Four tautomers of isolated guanine from infrared laser spectroscopy in helium nanodroplets." In: *Journal of the American Chemical Society* 128.22 (2006), pp. 7320–7328. DOI: 10.1021/ja0607411.

[122] O. Plekan, V. Feyer, R. Richter, M. Coreno, M. de Simone, and K. C. Prince. "Photofragmentation of guanine, cytosine, leucine and methionine." In: *Chemical Physics* 334 (2007), pp. 53–63. DOI: 10.1016/j.chemphys.2007.02.013.

[123] I. L. Zaytseva, A. B. Trofimov, J. Schirmer, O. Plekan, V. Feyer, R. Richter, M. Coreno, and K. C. Prince. "Theoretical and experimental study of valence-shell ionization spectra of guanine." In: *Journal of Physical Chemistry A* 113.52 (2009), pp. 15142–15149. DOI: 10.1021/jp905299z.

[124] A. N. Zavilopulo. "Electron impact ionization of gas-phase guanine near the threshold." In: *Journal Physical B: Atomic, Molecular and Optical Physics* 42 (2009), p. 025101. DOI: 10.1088/0953-4075/42/2/025101.

[125] J. Zhou, C. Nicolas, X. Tang, L. Belau, M. S. De Vries, and M. Ahmed. "Experimental observation of guanine tautomers with VUV photoionization." In: *Journal of Physical Chemistry A* 113.17 (2009), pp. 4829–4832. DOI: 10.1021/jp811107x.

[126] B. F. Minaev, M. I. Shafranyosh, Y. Svida, M. I. Sukhoviya, I. I. Shafranyosh, G. V. Baryshnikov, and V. A. Minaeva. "Fragmentation of the adenine and guanine molecules induced by electron collisions." In: *Journal of Chemical Physics* 140.17 (2014). DOI: 10.1063/1.4871881.

[127] A. Ostroverkh, A. Zavilopulo, and O. Shpenik. "Ionization of guanine, adenine and thymine molecules by electron impact." In: *European Physical Journal D* 73.38 (2019). DOI: 10.1140/epjd/e2019-90532-3.

[128] *AIST spectral database for organic compounds SDBS-Guanine-EII-MS*. URL: https://sdbs.db.aist.go.jp/sdbs/cgi-bin/direct_frame_top.cgi.

[129] M. Ryszka, R. Pandey, C. Rizk, J. Tabet, B. Barc, M. Dampc, N. J. Mason, and S. Eden. "Dissociative multi-photon ionization of isolated uracil and uracil-adenine complexes." In: *International Journal of Mass Spectrometry* 396 (2016), pp. 48–54. DOI: 10.1016/j.ijms.2015.12.006. URL: http://dx.doi.org/10.1016/j.ijms.2015.12.006.

[130] P. J. M. V. D. Burgt, M. A. Brown, J. Bockova, A. Rebelo, M. Ryszka, J. C. Poully, and S. Eden. "Fragmentation processes of ionized 5-fluorouracil in the gas phase and within clusters." In: *European Physical Journal D* 73 (2019), p. 184. DOI: 10.1140/epjd/e2019-100107-7.

[131] E. Nir, C. Plützer, K. Kleinermanns, and M. De Vries. "Properties of isolated DNA bases, base pairs and nucleosides examined by laser spectroscopy." In: *European Physical Journal D* 20.3 (2002), pp. 317–329. DOI: 10.1140/epjd/e2002-00167-2.

[132] M. Mons, I. Dimicoli, F. Piuzzi, B. Tardivel, and M. Elhanine. "Tautomerism of the DNA base guanine and its methylated derivatives as studied by gas-phase infrared and ultraviolet spectroscopy." In: *Journal of Physical Chemistry A* 106 (2002), pp. 5088–5094. DOI: 10.1021/jp0139742.

[133] L. Serrano-Andrés, M. Merchán, and A. C. Borin. "A Three-State Model for the Photophysics of Guanine." In: *Journal of the American Chemical Society* 130 (2008), pp. 2473–2484. DOI: 10.1021/ja0744450.

[134] M. Barbatti, J. J. Szymczak, A. J. Aquino, D. Nachtigallovà, and H. Lischka. "The decay mechanism of photoexcited guanine - A nonadiabatic dynamics study." In: *Journal of Chemical Physics* 134 (2011), p. 014304. DOI: 10.1063/1.3521498.

[135] M. Mons, F. Piuzzi, I. Dimicoli, L. Gorb, and J. Leszczynski. "Near-UV resonant two-photon ionization spectroscopy of gas phase guanine: Evidence for the observation of three rare tautomers." In: *Journal of Physical Chemistry A* 110.38 (2006), pp. 10921–10924. DOI: 10.1021/jp063738x.

[136] C. M. Marian. "The guanine tautomer puzzle: Quantum chemical investigation of ground and excited states." In: *Journal of Physical Chemistry A* 111.8 (2007), pp. 1545–1553. DOI: 10.1021/jp068620v.

[137] I. I. Shafranyosh, Y. Y. Svida, M. I. Sukhoviya, M. I. Shafranyosh, B. F. Minaev, G. V. Baryshnikov, and V. A. Minaeva. "Absolute effective cross sections of ionization of adenine and guanine molecules by electron impact." In: *Technical Physics* 60.10 (2015), pp. 1430–1436. DOI: 10.1134/S1063784215100278.

[138] R. Pandey, M. Ryszka, T. da Fonseca Cunha, M. Lalande, M. Dampc, P. Limão-Vieira, N. J. Mason, J. C. Poully, and S. Eden. "Threshold behavior in metastable dissociation of multi-photon ionized thymine and uracil." In: *Chemical Physics Letters* 684 (2017), pp. 233–238. DOI: 10.1016/j.cplett.2017.06.051.

[139] T. Shannon and F. McLafferty. "Identification of gaseous organic ions by the use of metastable peaks." In: *Journal of the American Chemistry Society* 88.21 (1966), pp. 5021–5022.

[140] J. M. Rice, G. Dudek, and M. Barber. "Mass Spectra of nucleic acid derivatives-pyrimidines." In: *Journal of the American Chemistry Society* 87.20 (1965), pp. 4569–4576. DOI: 10.1021/ja00948a029.

[141] A. Mauracher, S. Denifl, A. Edtbauer, M. Hager, M. Probst, O. Echt, T. D. Märk, P. Scheier, T. A. Field, and K. Graupner. "Metastable anions of dinitrobenzene: Resonances for electron attachment and kinetic energy release." In: *Journal of Chemical Physics* 133.24 (2010), p. 244302. DOI: 10.1063/1.3514931.

[142] W. F. Haddon and F. W. McLafferty. "Metastable Ion Characteristics. Measurements with a Modified Time-of-Flight Mass Spectrometer." In: *Analytical Chemistry* 41.1 (1969), pp. 31–36. DOI: 10.1021/ac60270a006.

[143] A. G. Shard and I. S. Gilmore. "Analysis of metastable ions in the ToF-SIMS spectra of polymers." In: *International Journal of Mass Spectrometry* 269.1-2 (2008), pp. 85–94. DOI: 10.1016/j.ijms.2007.09.011.

[144] J. M. L'Hermite, F. Rabilloud, P. Labastie, and F. Spiegelman. "Evidence for trimers evaporation in silver bromide clusters." In: *European Physical Journal D* 8.3 (2001), pp. 77–80. DOI: 10.1007/s100530170064.

[145] I. Bald, H. D. Flosadóttir, B. Ómarsson, and O. Ingólfsson. "Metastable fragmentation of a thymidine-nucleotide and its components." In: *International Journal of Mass Spectrometry* 313 (2012), pp. 15–20. DOI: 10.1016/j.ijms.2011.12.007. URL: http://dx.doi.org/10.1016/j.ijms.2011.12.007.

[146] I. S. Gilmore and M. P. Seah. "Static SIMS: Metastable decay and peak intensities." In: *Applied Surface Science* 144-145 (1999), pp. 26–30. DOI: 10.1016/S0169-4332(98)00757-0.

[147] J. M. L'Hermite, L. Marcou, F. Rabilloud, and P. Labastie. "A new method to study metastable fragmentation of clusters using a reflectron time-of-flight mass spectrometer." In: *Review of Scientific Instruments* 71.5 (2000), pp. 2033–2037. DOI: 10.1063/1.1150573.

[148] J.-M. L'Hermite, F. Rabilloud, L. Marcou, and P. Labastie. "Metastable fragmentation of silver bromide clusters." In: *European Physical Journal D* 14.3 (2001), pp. 323–330. DOI: 10.1007/s100530170199.

[149] C. R. Ponciano, F. E. Ávalos, A. Rentería, and E. F. Da Silveira. "Analysis of metastable decay by time-of-flight coincidence and kinetics energy measurements." In: *International Journal of Mass Spectrometry* 209.2-3 (2001), pp. 197–208. DOI: 10.1016/S1387-3806(01)00496-1.

[150] J. Laskin and C. Lifshitz. "Kinetic energy release distributions in mass spectrometry." In: *Journal of Mass Spectrometry* 36.5 (2001), pp. 459–478. DOI: 10.1002/jms.164.

[151] S. Wei, W. B. Tzeng, and A. W. Castleman. "Kinetic energy release measurements of ammonia cluster ions during metastable decomposition and determination of cluster ion binding energies." In: *Journal of Chemical Physics* 92.1 (1990), pp. 332–339. DOI: 10.1063/1.458434.

[152] A. Baldwin, P. Derrick, and R. Morgan. "Correction of metastable peak shapes to allow for instrumental broadening and the translational energy spread of the parent ion." In: *Organic Mass Spectrometry* 11 (1976), pp. 440–442. DOI: 10.1002/oms.1210110418.

[153] P. Colarusso, K. Q. Zhang, B. Guo, and P. F. Bernath. "The infrared spectra of uracil, thymine, and adenine in the gas phase." In: *Chemical Physics Letters* 269.1-2 (1997), pp. 39–48. DOI: 10.1016/S0009-2614(97)00245-5.

[154] P. Cheng, Y. Li, S. Li, M. Zhang, and Z. Zhou. "Collision-induced dissociation (CID) of guanine radical cation in the gas phase: An experimental and computational study." In: *Physical Chemistry Chemical Physics* 12.18 (2010), pp. 4667–4677. DOI: 10.1039/b919513k.

[155] L. Sadr-Arani, P. Mignon, H. Chermette, H. Abdoul-Carime, B. Farizon, and M. Farizon. "Fragmentation mechanisms of cytosine, adenine and guanine ionized bases." In: *Physical Chemistry Chemical Physics* 17.17 (2015), pp. 11813–11826. DOI: 10.1039/C5CP00104H.

[156] URL: http://www.chemspider.com/Chemical-Structure.6544.html.

[157] E. Nir, I. Hünig, K. Kleinermanns, and M. S. De Vries. "Conformers of guanosines and their vibrations in the electronic ground and excited states, as revealed by double-resonance spectroscopy and ab initio calculations." In: *ChemPhysChem* 5 (2004), pp. 131–137. DOI: 10.1002/cphc.200300862.

[158] *NIST-Guanosine-EII-MS*. URL: https://webbook.nist.gov/cgi/cbook.cgi?ID=C118003\&Units=SI\&Mask=200\#Mass-Spec.

[159] *AIST spectral database for organic compounds SDBS-Guanosine-EII-MS*. URL: https://sdbs.db.aist.go.jp/sdbs/cgi-bin/direct_frame_disp.cgi?sdbsno=831.

[160] L. Feketeová, E. Yuriev, J. D. Orbell, G. N. Khairallah, and R. A. O'Hair. "Gas-phase formation and reactions of radical cations of guanosine, deoxyguanosine and their homodimers and heterodimers." In: *International Journal of Mass Spectrometry* 304.2-3 (2011), pp. 74–82. DOI: 10.1016/j.ijms.2010.04.012.

[161] R. J. Levis. "Laser desorption and ejection of the biomolecules from the condensed phase into the gas phase." In: *Annual Reviews in Physical Chemistry* 45.8 (1994), pp. 483–518. DOI: 10.1146/annurev.pc.45.100194.002411.

[162] V. B. Delchev. "Computational (DFT and TD DFT) study of the electron structure of the tautomers/conformers of uridine and deoxyuridine and the processes of intramolecular proton transfers." In: *Journal of Molecular Modeling* 16.4 (2010), pp. 749–757. DOI: 10.1007/s00894-009-0593-z.

[163] R. So and S. Alavi. "Vertical excitation energies for ribose and deoxyribose nucleosides." In: *Journal of Computational Chemistry* 28 (2007), pp. 1776–1782. DOI: 10.1002/jcc.20699.

[164] J. M. L. Pecourt, J. Peon, and B. Kohler. "Ultrafast internal conversion of electronically excited RNA and DNA nucleosides in water." In: *Journal of the American Chemical Society* 122.38 (2000), pp. 9348–9349. DOI: 10.1021/ja0021520.

[165] N. K. Schwalb, T. Michalak, and F. Temps. "Ultrashort fluorescence lifetimes of hydrogen-bonded base pairs of guanosine and cytidine in solution." In: *Journal of Physical Chemistry B* 113.51 (2009), pp. 16365–16376. DOI: 10.1021/jp904883n.

[166] A. Abo-Riziq, L. Grace, E. Nir, M. Kabelac, P. Hobza, and M. S. De Vries. "Photochemical selectivity in guanine-cytosine base-pair structures." In: *Proceedings of the National Academy of Sciences of the United States of America* 102.1 (2005), pp. 20–23. DOI: 10.1073/pnas.0408574102.

[167] A. L. Sobolewski, W. Domcke, and C. Hättig. "Tautomeric selectivity of the excited-state lifetime of guanine/cytosine base pairs: The role of electron-driven proton-transfer processes." In: *Proceedings of the National Academy of Sciences of the United States of America* 102.50 (2005), pp. 17903–17906. DOI: 10.1073/pnas.0504087102.

[168] D. Tuna, A. L. Sobolewski, and W. Domcke. "Mechanisms of ultrafast excited-state deactivation in adenosine." In: *Journal of Physical Chemistry A* 118.1 (2014), pp. 122–127. DOI: 10.1021/jp410121h.

[169] H. Levola, K. Kooser, E. Itälä, and E. Kukk. "Comparison of VUV radiation induced fragmentation of thymidine and uridine nucleosides - The effect of methyl and hydroxyl groups." In: *International Journal of Mass Spectrometry* 370 (2014), pp. 96–100. DOI: 10.1016/j.ijms.2014.07.008.

[170] K. Biemann and J. A. McCloskey. "Application of Mass Spectrometry to Structure Problems.1 VI. Nucleosides." In: *Journal of the American Chemistry Society* 84.10 (1962), pp. 2005–2007. DOI: 10.1021/ja00869a048.

[171] *NIST-Deoxyguanosine-EII-MS*. URL: https://webbook.nist.gov/cgi/cbook.cgi?ID=C961079\&Units=SI\&Mask=200\#Mass-Spec.

[172] *NIST-Adenosine-EII-MS*. URL: https://webbook.nist.gov/cgi/cbook.cgi?ID=C58617\&Units=SI\&Mask=200\#Mass-Spec.

[173] *NIST-Deoxyadenosine-EII-MS*. URL: https://webbook.nist.gov/cgi/cbook.cgi?ID=C958098\&Units=SI\&Mask=200\#Mass-Spec.

[174] *NIST-Cytidine-EII-MS*. URL: https://webbook.nist.gov/cgi/cbook.cgi?ID=C65463\&Units=SI\&Mask=200\#Mass-Spec.

[175] *NIST-Deoxycytidine-EII-MS*. URL: https://webbook.nist.gov/cgi/cbook.cgi?ID=C951779\&Units=SI\&Mask=200\#Mass-Spec.

[176] *NIST-Uridine-EII-MS*. URL: https://webbook.nist.gov/cgi/cbook.cgi?ID=C58968\&Units=SI\&Mask=200\#Mass-Spec.

[177] *NIST-Thymidine-EII-MS*. URL: https://webbook.nist.gov/cgi/cbook.cgi?ID=C50895\&Units=SI\&Mask=200\#Mass-Spec.

[178] Z. Aliakbar Tehrani, A. Fattahi, and A. Pourjavadi. "Influence of metal complexation on acidity of cytosine nucleosides: Part I, Li +, Na + and K + cation." In: *Scientia Iranica C* 19.3 (2012), pp. 535–545. DOI: 10.1016/j.scient.2011.11.042.

[179] A. Y. Ivanov, S. G. Stepanian, V. A. Karachevtsev, and L. Adamowicz. "Nucleoside conformers in lowerature argon matrices: Fourier transform IR spectroscopy of isolated thymidine and deuterothymidine molecules and quantum-mechanical calculations." In: *Low Temperature Physics* 45.9 (2019), pp. 1181–1191. DOI: 10.1063/1.5121271.

[180] D. Touboul, G. Bouchoux, and R. Zenobi. "Gas-phase protonation thermochemistry of adenosine." In: *Journal of Physical Chemistry B* 112.37 (2008), pp. 11716–11725. DOI: 10.1021/jp804786e.

[181] W. Gerlach and O. Stern. "Das magnetische Moment des Silberatoms." In: *Zeitschrift für Physik* 9 (1922), pp. 353–355.

[182] J. M. Rost, J. C. Griffin, B. Friedrich, and D. R. Herschbach. "Pendular states and spectra of oriented linear molecules." In: *Physical Review Letters* 68.9 (1992), pp. 1299–1302. DOI: 10.1103/physrevlett.68.1299.

[183] T. Kierspel, D. A. Horke, Y. P. Chang, and J. Küpper. "Spatially separated polar samples of the cis and trans conformers of 3-fluorophenol." In: *Chemical Physics Letters* 591 (2014), pp. 130–132. DOI: 10.1016/j.cplett.2013.11.010.

[184] S. Trippel, Y. P. Chang, S. Stern, T. Mullins, L. Holmegaard, and J. Küpper. "Spatial separation of state- and size-selected neutral clusters." In: *Physical Review A* 86.3 (2012), pp. 1–6. DOI: 10.1103/PhysRevA.86.033202.

[185] M. Johny, J. Onvlee, T. Kierspel, H. Bieker, S. Trippel, and J. Küpper. "Spatial separation of pyrrole and pyrrole-water clusters." In: *Chemical Physics Letters* (2019), pp. 149–152. DOI: 10.1016/j.cplett.2019.01.052.

[186] S. Heiles, S. Schäfer, and R. Schäfer. "Mass spectrometry and beam deflection studies of tin-lead nanoalloy clusters." In: *Physical Chemistry Chemical Physics* 12.1 (2010), pp. 247–253. DOI: 10.1039/b917206h.

[187] "Electric dipole moment and charge transfer in alkali-C60 molecules." In: *European Physical Journal D* 12.1 (2000), pp. 147–151. DOI: 10.1007/s100530070051.

[188] I. Compagnon, R. Antoine, D. Rayane, M. Broyer, and P. Dugourd. "Vibration Induced Electric Dipole in a Weakly Bound Molecular Complex." In: *Physics Review Letters* 89.25 (2002), pp. 2–5. DOI: 10.1103/PhysRevLett.89.253001.

[189] S. A. Rangwala, T. Junglen, T. Rieger, P. W. Pinkse, and G. Rempe. "Continuous source of translationally cold dipolar molecules." In: *Physics Review A* 67.4 (2003), p. 4. DOI: 10.1103/PhysRevA.67.043406.

[190] M. Motsch, M. Schenk, L. D. Van Buuren, M. Zeppenfeld, P. W. Pinkse, and G. Rempe. "Internal-state thermometry by depletion spectroscopy in a cold guided beam of formaldehyde." In: *Physics Review A* 76.6 (2007), pp. 1–4. DOI: 10.1103/PhysRevA.76.061402.

[191] T. Junglen, T. Rieger, S. A. Rangwala, P. W. Pinkse, and G. Rempe. "Slow ammonia molecules in an electrostatic quadrupole guide." In: *European Physical Journal D* 31.2 (2004), pp. 365–373. DOI: 10.1140/epjd/e2004-00130-3.

[192] M. Motsch, L. D. Van Buuren, C. Sommer, M. Zeppenfeld, G. Rempe, and P. W. Pinkse. "Cold guided beams of water isotopologs." In: *Physical Review A* 79.1 (2009), pp. 1–13. DOI: 10.1103/PhysRevA.79.013405.

[193] N. A. Kuebler, M. B. Robin, J. J. Yang, A. Gedanken, and D. R. Herrick. "Fully resolved zeeman pattern in the stern-gerlach deflection spectrum of O2 (3g-, K=1)." In: *Physical Review A* 38.2 (1988), pp. 737–749. DOI: 10.1103/PhysRevA.38.737.

[194] U. Buck and F. Huisken. "Infrared spectroscopy of size-selected water and methanol clusters." In: *Chemical Reviews* 100.11 (2000), pp. 3863–3890. DOI: 10.1021/cr990054v.

[195] A. Schwettmann, J. Franklin, K. R. Overstreet, and J. P. Shaffer. "Stark slowing asymmetric rotors: Weak-field-seeking states and nonadiabatic transitions." In: *Journal of Chemical Physics* 123.19 (2005), pp. 1–6. DOI: 10.1063/1.2112787.

[196] F. F. Da Silva, S. Ptasińska, S. Denifl, D. Gschliesser, J. Postler, C. Matias, T. D. Märk, P. Limão-Vieira, and P. Scheier. "Electron interaction with nitromethane embedded in helium droplets : Attachment and ionization measurements." In: *Journal of Chemical Physics* 135 (2011), p. 174504. DOI: 10.1063/1.3656680.

[197] W. Gordy and R. L Cook. *Microwave molecular spectra*. Second. Vol. 11. 2. New York: John Wiley & Sons, 1984. DOI: 10.1016/0022-2860(72)80039-5.

[198] Y. P. Chang, F. Filsinger, B. G. Sartakov, and J. Küpper. "CMIstark: Python package for the Stark-effect calculation and symmetry classification of linear, symmetric and asymmetric top wavefunctions in dc electric fields." In: *Computer Physics Communications* 185.1 (2014), pp. 339–349. DOI: 10.1016/j.cpc.2013.09.001.

[199] S. Y. Van De Meerakker, H. L. Bethlem, N. Vanhaecke, and G. Meijer. "Manipulation and control of molecular beams." In: *Chemical Reviews* 112.9 (2012), pp. 4828–4878. DOI: 10.1021/cr200349r.

[200] Havenith, M. "Infrared spectroscopy of molecular clusters." In: 1st ed. Vol. 176. Springer-Verlag Berlin Heidelberg, 2002. Chap. 4, pp. 35–46.

[201] M. D. Morse. "2. Supersonic Beam Sources." In: *Experimental Methods in the Physical Sciences*. Vol. 29. 1996, pp. 21–47. DOI: 10.1016/S0076-695X(08)60784-X.

[202] J. B. Anderson and J. B. Fenn. "Velocity distributions in molecular beams from nozzle sources." In: *Physics of Fluids* 8.5 (1965), pp. 780–787. DOI: 10.1063/1.1761320.

[203] G. M. McClelland, K. L. Saenger, J. J. Valentini, and D. R. Herschbach. "Vibrational and rotational relaxation of iodine in seeded supersonic beams." In: *Journal of Physical Chemistry* 83.8 (1979), pp. 947–959. DOI: 10.1021/j100471a014.

[204] A. Amirav, U. Even, and J. Jortner. "Cooling of larger and heavy molecules in seeded supersonic beams." In: *Chemical Physics* 51 (1980), pp. 31–42. DOI: 10.1016/0301-0104(80)80077-2.

[205] C. Zener. "Interchange of translational, roatational and vibrational energy in molecular collisions." In: *Physical Review* 1930 (1931). DOI: 10.1103/PhysRev.37.556.

[206] D. H Levy. "The Spectroscopy of very cold gases." In: *Science* 214.4518 (1981), pp. 263–269.

[207] S. Yang, L. Philippe, and M. Châtelet. "Formation of (CH4)N van der Waals clusters by seeded supersonic expansion." In: *International Journal of Mass Spectrometry* 263 (2007), pp. 190–194. DOI: 10.1016/j.ijms.2007.01.020.

[208] L. Verlet. "Computer "experiments"on classical fluids I. Thermodynamical properties of Lennard-Jones molecules." In: *Physical Review* 159.1 (1967), pp. 98–103. DOI: 10.1088/0022-3727/9/2/008.

[209] M. Abd El Rahim, R. Antoine, M. Broyer, D. Rayane, and P. Dugourd. "Asymmetric top rotors in electric fields: Influence of chaos and collisions in molecular beam deflection experiments." In: *Journal of Physical Chemistry A* 109.38 (2005), pp. 8507–8514. DOI: 10.1021/jp053127p.

[210] R. Antoine, M. Abd El Rahim, M. Broyer, D. Rayane, and P. Dugourd. "Asymmetric top rotors in electric fields. II. Influence of internal torsions in molecular beam deflection experiments." In: *Journal of Physical Chemistry A* 110.33 (2006), pp. 10006–10011. DOI: 10.1021/jp0614345.

[211] F. Rohart. "Microwave spectrum of nitromethane internal rotation Hamiltonian in the low barrier case." In: *Journal of Molecular Spectroscopy* 57.2 (1975), pp. 301–311. DOI: 10.1016/0022-2852(75)90033-8.

[212] J.-S. Li, H.-M. Xiao, and H.-S. Dong. "A theoretical study on the intermolecular interaction of energetic system-Nitromethane dimer." In: *Chinese Journal of Chemistry* 18.6 (2010), pp. 815–819. DOI: 10.1002/cjoc.20000180604.

[213] E. Bernestein. *Chemical reactions in clusters*. New York, Oxford: Oxford University Press, 1996, p. 238.

[214] S. Putzke, F. Filsinger, J. Küpper, and G. Meijer. "Alternating-gradient focusing of the benzonitrile-argon van der Waals complex." In: *Journal of Chemical Physics* 137.10 (2012). DOI: 10.1063/1.4748814.

[215] G. Vaidyanathan, M. T. Coolbaugh, W. R. Peifer, J. F. Garvey, G. Vaidyanathan, M. T. Coolbaugh, W. R. Peifer, and J. F. Garvey. "Argon mediated electron impact ionization of Arn(CH3OH)m heteroclusters." In: *Journal of Chemical Physics* 94 (1991), pp. 1850–1858.

[216] H. Shinohara, N. Nishi, and N. Washida. "Photoionization of ammonia clusters : Detection and distribution of unprotonated cluster ions (NH3)+ n=2-25." In: *Journal of Chemical Physics* 83 (1985), pp. 1939–1947.

[217] H. Shinohara, N. Nishi, and N. Washida. "Photoionization of water clusters at 11.83 eV: Observation of unprotonated cluster ions (H2O)+ n (2<n<10)." In: *Journal of Chemical Physics* 84 (1986), pp. 5561–5567. DOI: 10.1063/1.449914.

[218] G. Seifert. "Tight-binding density functional theory: An approximate Kohn-Sham DFT scheme." In: *Journal of Physical Chemistry A* 111.26 (2007), pp. 5609–5613. DOI: 10.1021/jp069056r.

[219] T. Frauenheim, G. Seifert, M. Elstner, Z. Hajnal, G. Jungnickel, D. Porezag, S. Suhai, and R. Scholz. "A self-consistent charge density-functional based tight-binding method for predictive materials simulations in physics, chemistry and biology." In: *Physica Status Solidi B* 217.1 (2000), pp. 41–62. DOI: 10.1002/3527603107.ch3.

[220] M. Gaus, Q. Cui, and M. Elstner. "DFTB3: Extension of the self-consistent-charge density-functional tight-binding method (SCC-DFTB)." In: *Journal of Chemical Theory Computation* 7.4 (2011), pp. 931–948. DOI: 10.1021/ct100684s.

[221] B. Aradi, B. Hourahine, and T. Frauenheim. "DFTB+, a sparse matrix-based implementation of the DFTB method." In: *Journal of Physical Chemistry A* 111.26 (2007), pp. 5678–5684. DOI: 10.1021/jp070186p.

[222] M. Gaus, A. Goez, and M. Elstner. "Parametrization and Benchmark of DFTB3 for Organic Molecules." In: *Journal of Chemical Theory and Computation* 9.1 (2013), pp. 338–354. DOI: 10.1021/ct300849w.

[223] Y. Yang, H. Yu, D. York, Q. Cui, and M. Elstner. "Extension of the self-consistent-charge density-functional tight-binding method: Third-order expansion of the density functional theory total energy and introduction of a modified effective coulomb interaction." In: *Journal of Physical Chemistry A* 111.42 (2007), pp. 10861–10873. DOI: 10.1021/jp074167r.

[224] S. Fias, S. V. Damme, and P. Bultinck. "Multidimensionality of delocalization indices and nucleus independent chemical shifts in polycyclic aromatic hydrocarbons." In: *Journal of Computational Chemistry* 29.858 (2008), pp. 358–366. DOI: 10.1002/jcc.

[225] M. Brehm and B. Kirchner. "TRAVIS - A free analyzer and visualizer for monte carlo and molecular dynamics trajectories." In: *Journal of Chemical Information and Modeling* 51.8 (2011), pp. 2007–2023. DOI: 10.1021/ci200217w.

[226] O. Svoboda, D. Hollas, M. Ončák, and P. Slavíček. "Reaction selectivity in an ionized water dimer: Nonadiabatic ab initio dynamics simulations." In: *Physical Chemistry Chemical Physics* 15.27 (2013), pp. 11531–11542. DOI: 10.1039/c3cp51440d.

[227] S. Heinbuch, F. Dong, J. J. Rocca, and E. R. Bernstein. "Single photon ionization of hydrogen bonded clusters with a soft x-ray laser: (HCOOH)x and (HCOOH)y (H2O)z." In: *Journal of Chemical Physics* 126.24 (2007), pp. 1–11. DOI: 10.1063/1.2746036.

[228] S. Y. Lee, D. N. Shin, S. G. Chot, and K.-H. Jungt. "Proton-transfer Reactions Within Ionized Methanol Clusters : Mass Spectrometric and Molecular Orbital Studies." In: *Journal of Mass Spectrometry* 30.7 (1995), pp. 969–976. DOI: 10.1002/jms.1190300706.

[229] A. Golan, K. B. Bravaya, R. Kudirka, O. Kostko, S. R. Leone, A. I. Krylov, and M. Ahmed. "Ionization of dimethyluracil dimers leads to facile proton transfer in the absence of hydrogen bonds." In: *Nature Chemistry* 4.4 (2012), pp. 323–329. DOI: 10.1038/nchem.1298.

[230] S. Nosé. "A unified formulation of the constant temperature molecular dynamics methods." In: *Journal of Chemical Physics* 81.1 (1984), pp. 511–519. DOI: 10.1063/1.447334.

[231] W. G. Hoover. "Canonical dynamics: Equilibrium phase-space distributions." In: *Physical Review A* 31.3 (1985), pp. 1695–1697. DOI: 10.1103/PhysRevA.31.1695.

[232] G. J. Martyna, M. L. Klein, and M. Tuckerman. "Nosé-Hoover chains: The canonical esemble via continuous dynamics." In: *Journal of Chemical Physics* 97.4 (1992), pp. 2635–2644. DOI: 10.1063/1.463940.

[233] W. J. Hehre, K. Ditchfield, and J. A. Pople. "Self-consistent molecular orbital methods. XII. Further extensions of gaussian-type basis sets for use in molecular orbital studies of organic molecules." In: *Journal of Chemical Physics* 56.5 (1972), pp. 2257–2261. DOI: 10.1063/1.1677527.

[234] M. J. Frisch, J. A. Pople, and J. S. Binkley. "Self-consistent molecular orbital methods XXV. Supplementary functions for Gaussian basis sets." In: *Journal of Chemical Physics* 80.7 (1984), pp. 3265–3269. DOI: 10.1063/1.447079.

[235] C. A. Bauer and S. Grimme. "Elucidation of electron ionization induced fragmentations of adenine by semiempirical and density functional molecular dynamics." In: *Journal of Physical Chemistry A* 118.49 (2014), pp. 11479–11484. DOI: 10.1021/jp5096618.

[236] C. A. Bauer and S. Grimme. "How to Compute Electron Ionization Mass Spectra from First Principles." In: *Journal of Physical Chemistry A* 120.21 (2016), pp. 3755–3766. DOI: 10.1021/acs.jpca.6b02907.

[237] V. Ásgeirsson, C. A. Bauer, and S. Grimme. "Quantum chemical calculation of electron ionization mass spectra for general organic and inorganic molecules." In: *Chemical Science* 8.7 (2017), pp. 4879–4895. DOI: 10.1039/c7sc00601b.

[238] E. R. Bernstein. "Dynamics and photochemsitry of neutral van der Waals clusters." In: *Annual Review of Physical Chemistry* 46 (1995), pp. 197–222.

[239] R. S. Mulliken. "Electronic Population Analysis on LCAOMO Molecular Wave Functions. I." In: *Journal of Chemical Physics* 23 (1955), pp. 1833–1840. DOI: 10.1063/1.1740588.

[240] E. Szymańska. "Dissociative electron attachment and dipolar dissociation processes in organic molecules found in the interstellar medium." Doctoral dissertation. The Open University, 2014.

[241] D. Nandi, V. S. Prabhudesai, E. Krishnakumar, and A. Chatterjee. "Velocity slice imaging for dissociative electron attachment." In: *Review of Scientific Instrumentation* 76.5 (2005), p. 053107. DOI: 10.1063/1.1899404.

[242] J. R. Pierce. "Rectilinear Electron Flow in Beams." In: *Journal of Applied Physics* 11 (1940), pp. 548–554. DOI: 10.1063/1.1712815.

[243] P. Hawkes and E. Kasper. "General Features of Electron Guns." In: *Principles of electron optics*. 2nd. Elsevier Ltd., 2018. Chap. 43, pp. 1051–1061. DOI: 10.1016/B978-0-12-813369-9.00043-9.

[244] M. A. Rahman and E. Krishnakumar. "Communication: Electron ionization of DNA bases." In: *Journal of Chemical Physics* 144.16 (2016), p. 161102. DOI: 10.1063/1.4948412.

Appendix A

Unimolecular rate constants for guanine cation tautomers

A.0.1 Simulation of unimolecular rate constants within QET

The following code, written in Mathematica, calculates unimolecular rate constants for HCN and HCNO neutral loss from the five lowest energy tautomers of guanine cations. Eigenfrequency vectors are given for each initial guanine cation tautomer, transition states and intermediate products along the reaction paths. Transition states have a negative eigenfrequency, which is not included in the respective vectors. The relative zero-point energies are also provided. The bsFrequencyUpdate updates the lists of sum and density of states for a given vibrational frequency, while bsDirectCount runs over the frequencies in νList. The bsComputeSumofStates routine compute the sum of states up to the internal energy specified by energy_ for the intermediate product with eigenfrequency list νList and an energy relative to the minimum energy structure relEnergy_. The bsComputeDensityofStates routine calculate the density of states up to the internal energy specified by energy_ for TS structures, with eigenfrequency list νList and an energy relative to the minimum energy structure relEnergy_.

```
energy=100000;
bsFrequencyUpdate[stateList_,ν_]:=Block[{out = stateList,k},
  For[k = ν+1,k ≤ Length[out],k++,out[[k]]+=out[[k−ν]]];
  out
]
bsDirectCount[stateList_,νList_]:=Fold[bsFrequencyUpdate,stateList,νList]
bsComputeSumOfStates[νList_,energy_,relEnergy_:0]:=bsDirectCount[Table[1,
energy − relEnergy+1],νList]
bsComputeDensityOfStates[νList_,energy_,relEnergy_:0]:=bsDirectCount[
PadRight[{1},energy − relEnergy+1],νList]
bsSumOfStates = bsComputeSumOfStates[νList,energy];
bsDensityOfStates = bsComputeDensityOfStates[νList,energy];
```

(**Reaction pathways for HCN loss from keto-N9H-amino guanine+**)

vN9HG = {121, 157, 209, 318, 321, 353, 479, 486, 519, 552, 575, 628, 643, 656, 701, 744, 808, 844, 925, 933, 1054, 1070, 1101, 1130, 1185, 1248, 1377, 1403, 1432, 1452, 1514, 1572, 1608, 1703, 1720, 1886, 3276, 3574, 3586, 3621, 3713};

vN9HTS1 = {95, 151, 158, 244, 300, 309, 358, 433, 455, 504, 420, 535, 603, 630, 644, 649, 650, 740, 763, 784, 839, 1028, 1038, 1103, 1216, 1237, 1307, 1367, 1385, 1549, 1570, 1630, 1724, 1834, 2094, 3354, 3531, 3574, 3614, 3742};

vN9HP1 = {83, 128, 161, 185, 229, 329, 355, 357, 433, 447, 472, 497, 532, 537, 626, 636, 652, 663, 680, 751, 756, 790, 818, 1031, 1053, 1114, 1151, 1231, 1288, 1386, 1417, 1451, 1568, 1613, 1707, 1878, 2319, 3385, 3452, 3578, 3608, 3740};

vN9HTS2 = {72, 83, 128, 150, 163, 199, 340, 350, 411, 498, 513, 543, 554, 575, 602, 650, 667, 670, 734, 782, 845, 849, 856, 917, 1032, 1056, 1076, 1111, 1245, 1340, 1490, 1613, 1752, 1892, 1946, 1987, 3371, 3520, 3574, 3595, 3701};

vN9HTS1II = {63, 81, 163, 238, 340, 369, 458, 510, 528, 549, 562, 574, 599, 628, 660, 668, 740, 783, 814, 859, 932, 983, 1053, 1072, 1165, 1225, 1247, 1339, 1445, 1493, 1621, 1750, 1756, 1890, 1972, 3131, 3568, 3574, 3609, 3694};

vN9HP1II = {69, 84, 143, 163, 196, 227, 343, 388, 455, 519, 523, 567, 581, 597, 623, 659, 664, 678, 743, 793, 825, 887, 920, 999, 1068, 1093, 1170, 1238, 1255, 1342, 1461, 1501, 1622, 1753, 1770, 1884, 1973, 3130, 3554, 3573, 3589, 3696};

vN9HTS2II = {36, 51, 108, 155, 162, 225, 345, 384, 442, 521, 537, 545, 592, 602, 648, 662, 671, 721, 769, 813, 828, 847, 890, 974, 1018, 1060, 1073, 1239, 1243, 1340, 1461, 1619, 1648, 1765, 1931, 1969, 3266, 3562, 3588, 3688};

vN9HP1III = {119, 195, 230, 289, 320, 355, 496, 535, 571, 583, 629, 645, 653, 662, 672, 682 ,758, 814, 844, 931, 945, 1036, 1055, 1118, 1170, 1245, 1273, 1360, 1392, 1450, 1461, 1492, 1532, 1591, 1631, 1681, 1733, 3266, 3557, 3622, 3693, 3801};

vN9HTS1III = {130, 160, 220, 322, 335, 363, 480, 554, 555, 574, 602, 631, 662, 675, 737, 742, 790, 849, 923, 1052, 1095, 1109, 1129, 1180, 1248, 1346, 1386, 1433, 1457, 1495, 1548, 1593, 1689, 1713, 1744, 2113, 3265, 3582, 3625, 3713};

vN9HP2III = {137, 184, 227, 277, 334, 376, 481, 542, 553, 624, 634, 655, 674, 675, 697, 770, 803, 821, 846, 928, 948, 954, 1089, 1130, 1175, 1217, 1263, 1306, 1345, 1385, 1412, 1451, 1462, 1527, 1582, 1683, 1699, 3264, 3516, 3550, 3621, 3767};

vN9HTS2III = {135, 188, 228, 278, 334, 424, 498, 547, 551, 607, 655, 659, 662, 685, 739, 769, 797, 856, 936, 938, 1045, 1072, 1119, 1141, 1179, 1258, 1286, 1329, 1389, 1433, 1453, 1489, 1526, 1584, 1647, 1726, 2092, 3271, 3558, 3624, 3781};

vN9HP3III = {67, 105, 159, 190, 203, 295, 312, 350, 381, 435, 499, 516, 560, 566, 583, 628, 674, 682, 742, 774, 915, 924, 927, 1085, 1119, 1180, 1224, 1247, 1286, 1330, 1392, 1470, 1505, 1568, 1721, 1747, 2364, 3268, 3523, 3612, 3776, 3784};

vN9HTS3III = {93, 123, 196, 266, 302, 302, 460, 473, 487, 527, 569, 574, 599, 630, 659, 699, 748, 781, 870, 910, 929, 1095, 1119, 1177, 1200, 1233, 1273, 1334, 1419, 1462, 1505, 1590, 1690, 1767, 2179, 3265, 3549, 3609, 3702, 3787};

vN9HP4III = {57, 97, 131, 171, 173, 295, 343, 358, 402, 424, 450, 531, 578, 597, 606, 666, 686, 694, 735, 758, 768, 903, 962, 1090, 1120, 1153, 1211, 1231, 1263, 1356, 1444, 1493, 1585, 1604, 1676, 1720, 2342, 3281, 3440, 3566, 3603, 3723};

vN9HTS4III = {60, 102, 140, 163, 181, 220, 307, 367, 398, 459, 518, 562, 583, 617, 637, 681, 693, 695, 765, 766, 928, 1116, 1131, 1189, 1222, 1228, 1266, 1337, 1396, 1469, 1534, 1617, 1629, 1695, 2052, 2372, 3297, 3448, 3617, 3789};

vN9HP5III = {27, 36, 69, 77, 108, 122, 148, 175, 250, 269, 392, 423, 448, 508, 549, 586, 633, 651, 653, 688, 748, 860, 930, 938, 953, 1109, 1134, 1136, 1231, 1252, 1396, 1401, 1483, 1568, 1680, 2393, 2438, 3291, 3592, 3609, 3788, 3791};

vN9HTS5III = {53, 65, 105, 114, 136, 272, 292, 312, 414, 452, 472, 550, 563, 591, 610, 680, 683, 705, 736, 749, 844, 882, 940, 1004, 1138, 1175, 1223, 1227, 1251, 1416, 1444, 1539, 1578, 1684, 2187, 2308, 3300, 3548, 3565, 3604, 3652};

(**Reaction pathways for HCN loss from enol(trans)-N9H-amino guanine+**)

vN9HEnolG = {119, 195, 230, 289, 320, 355, 498, 535, 571, 583, 629, 645, 653, 662, 672, 682, 758, 814, 844, 931, 945, 1036, 1055, 1118, 1170, 1245, 1273, 1360, 1392, 1450, 1461, 1492, 1532, 1592, 1631, 1681, 1733, 3267, 3556, 3622, 3693, 3801};

vN9HEnolGTS1 = {97, 176, 213, 253, 267, 334, 435, 461, 475, 482, 533, 554, 607, 612, 621, 637, 672, 699, 723, 741, 790, 797, 924, 1033, 1101, 1162, 1223, 1265, 1284, 1352, 1499, 1512, 1615, 1691, 2050, 3348, 3501, 3612, 3746, 3873};

vN9HEnolGP1 = {69, 146, 190, 207, 222, 341, 346, 396, 439, 459, 490, 499, 527, 556, 570, 627, 646, 648, 663, 727, 756, 803, 823, 1019, 1042, 1160, 1199, 1236, 1282, 1357, 1377, 1509,

1545, 1548, 1698, 2296, 3385, 3468, 3608, 3744, 3896};

vN9HEnolGTS2 = {46, 61, 117, 141, 146, 195, 204, 236, 341, 359, 478, 538, 559, 573, 591, 598, 656, 666, 716, 765, 781, 830, 845, 956, 1024, 1121, 1178, 1232, 1290, 1367, 1431, 1472, 1561, 1695, 1849, 2259, 3412, 3450, 3593, 3602, 3732};

vN9HEnolGTS1II = {65, 90, 158, 204, 247, 340, 416, 487, 529, 549, 558, 565, 600, 636, 642, 669, 685, 747, 804, 837, 883, 910, 1031, 1083, 1143, 1203, 1228, 1238, 1364, 1453, 1494, 1575, 1629, 1746, 1759, 1872, 3126, 3566, 3584, 3716, 3837};

vN9HEnolGP1II = {67, 89, 135, 189, 203, 237, 340, 422, 463, 504, 554, 562, 581, 635, 651, 657, 684, 703, 751, 809, 866, 870, 902, 1066, 1093, 1146, 1206, 1224, 1251, 1365, 1465, 1500, 1575, 1629, 1747, 1772, 1866, 3130, 3540, 3582, 3709, 3850};

vN9HEnolGTS2II = {74, 121, 155, 180, 194, 226, 343, 418, 491, 527, 560, 601, 617, 632, 655, 674, 694, 718, 773, 816, 840, 860, 897, 957, 1064, 1093, 1138, 1242, 1287, 136 111443, 1570, 1613, 1657, 1760, 1940, 3276, 3542, 3563, 3692, 3694};

(**Reaction pathways for HCNO loss from enol(trans)-N9H-amino guanine+**)

vN9HEnolGTS1III = {135, 188, 228, 278, 334, 424, 498, 547, 551, 607, 655, 659, 662, 685, 739, 769, 797, 856, 936, 938, 1045, 1072, 1119, 1141, 1179, 1258, 1286, 1329, 1389, 1433, 1453, 1489, 1526, 1584, 1647, 1726, 2092, 3271, 3558, 3624, 3781};

vN9HEnolGP1III = {137, 184, 227, 277, 334, 376, 481, 542, 553, 624, 634, 655, 674, 675, 697, 770, 803, 821, 846, 928, 948, 954, 1089, 1130, 1175, 1217, 1263, 1306, 1345, 1385, 1412, 1451, 1462, 1527, 1582, 1683, 1699, 3264, 3516, 3550, 3621, 3767};

vN9HEnolGTS2III = {93, 123, 196, 266, 302, 302, 460, 473, 487, 527, 569, 574, 599, 630, 659, 699, 748, 781, 870, 910, 929, 1095, 1119, 1177, 1200, 1233, 1273, 1334, 1419, 1462, 1505, 1590, 1690, 1767, 2179, 3265, 3549, 3609, 3702, 3787};

vN9HEnolGP2III = {67, 105, 159, 190, 203, 295, 312, 350, 381, 435, 499, 516, 560, 566, 583, 628, 674, 682, 742, 774, 915, 924, 927, 1085, 1119, 1180, 1224, 1247, 1286, 1330, 1392, 1470, 1505, 1568, 1721, 1747, 2364, 3268, 3523, 3612, 3776, 3784};

vN9HEnolGTS3III = {60, 102, 140, 163, 181, 220, 307, 367, 398, 459, 518, 562, 583, 617, 637, 681, 693, 695, 765, 766, 928, 1116, 1131, 1189, 1222, 1228, 1266, 1337, 1396, 1469, 1534, 1617, 1629, 1695, 2052, 2372, 3297, 3448, 3617, 3789};

vN9HEnolGP3III = {57, 97, 131, 171, 173, 295, 343, 358, 402, 424, 450, 531, 578,

597, 606, 666, 686, 694, 735, 758, 768, 903, 962, 1090, 1120, 1153, 1211, 1231, 1263, 1356,
1444, 1493, 1585, 1604, 1676, 1720, 2342, 3281, 3440, 3566, 3603, 3723};

vN9HEnolGTS4III = {53, 65, 105, 114, 136, 272, 292, 312, 414, 452, 472, 550, 563, 591,
610, 680, 683, 705, 736, 749, 844, 882, 940, 1004, 1138, 1175, 1223, 1227, 1251, 1416,
1444, 1539, 1578, 1684, 2187, 2308, 3300, 3548, 3565, 3604, 3652};

vN9HEnolGP4III = {27, 36, 69, 77, 108, 122, 148, 175, 250, 269, 392, 423, 448, 508,
549, 586, 633, 651, 653, 688, 748, 860, 930, 938, 953, 1109, 1134, 1136, 1231, 1252, 1396,
1401, 1483, 1568, 1680, 2393, 2438, 3291, 3592, 3609, 3788, 3791};

(**Reaction pathways for HCN loss from keto-N7H-amino guanine+**)

vN7HG = {123, 162, 198, 305, 313, 354, 479, 487, 531, 565, 635, 650, 670, 677, 711,
742, 788, 843, 930, 945, 1028, 1047, 1076, 1140, 1181, 1292, 1379, 1395, 1423, 1486, 1546,
1578, 1615, 1689, 1716, 1849, 3261, 3566, 3577, 3608, 3708};

vN7HTS1 = {109, 151, 157, 329, 334, 354, 385, 412, 473, 492, 519, 520, 577, 600, 626,
663, 671, 728, 782, 800, 824, 882, 982, 1057, 1091, 1121, 1229, 1370, 1395, 1527, 1558,
1613, 1659, 1719, 1904, 2112, 3379, 3477, 3580, 3601, 3729};

vN7HP1 = {85, 118, 148, 152, 326, 339, 354, 374, 403, 439, 453, 501, 532, 554, 577, 608,
679, 680, 729, 790, 818, 824, 938, 1061, 1089, 1160, 1243, 1384, 1400, 1514, 1570, 1619,
1655, 1716, 1901, 2234, 3395, 3464, 3581, 3604, 3732};

vN7HTS2 = {55, 69, 106, 143, 157, 206, 340, 345, 364, 445, 487, 534, 549, 619, 624, 693,
713, 741, 798, 811, 819, 828, 984, 1001, 1045, 1082, 1201, 1338, 1401, 1506, 1601, 1685,
1725, 1749, 1924, 2257, 3422, 3429, 3557, 3570, 3697};

vN7HP2 = {46, 61, 81, 118, 129, 160, 185, 280, 331, 366, 446, 456, 540, 577, 612, 640,
706, 715, 722, 799, 804, 833, 846, 962, 1010, 1041, 1086, 1195, 1346, 1404, 1496,
1614, 1739, 1749, 1804, 1937, 2261, 3429, 3432, 3547, 3560, 3681};

(**Reaction pathways for HCNO loss from keto-N7H-amino guanine+**)

vN7HGTS1III = {111, 120, 162, 256, 294, 337, 345, 384, 446, 456, 477, 557, 588, 624,
677, 684, 713, 720, 751, 929, 959, 1030, 1111, 1128, 1163, 1210, 1248, 1323, 1407, 1421,
1474, 1538, 1591, 1610, 1771, 2146, 3282, 3433, 3540, 3622, 3665};

vN7HGP1III = {27, 71, 130, 169, 181, 214, 320, 359, 388, 396, 491, 505, 512, 519, 604, 609,
688, 696, 736, 758, 904, 963, 1069, 1112, 1125, 1154, 1238, 1263, 1347, 1417, 1431,

1458, 1561, 1607, 1622, 1686, 2513, 3263, 3441, 3536, 3594, 3648};

vN7HGTS2III = {36, 58, 100, 109, 122, 245, 296, 314, 327, 340, 447, 464, 500, 506, 563, 569,
624, 688, 701, 873, 880, 941, 956, 1113, 1128, 1207, 1222, 1251, 1375, 1419, 1434,
1564, 1584, 1629, 2202, 2491, 3286, 3542, 3584, 3615, 3661};

vN7HGP2III = {25, 28, 54, 64, 75, 128, 131, 145, 300, 314, 434, 444, 488, 494, 502, 566, 609,
650, 658, 688, 753, 887, 932, 977, 1112, 1129, 1206, 1241, 1359, 1397, 1405, 1429,
1547, 1581, 1624, 2434, 2477, 3264, 3532, 3545, 3644, 3776};

(**Reaction pathways for HCN loss from enol(cis)-N7H-amino guanine+**)

vN7HEnolG = {120, 189, 230, 295, 315, 352, 492, 543, 545, 606, 633, 643, 647, 661, 664,
694, 754, 803, 840, 929, 943, 1021, 1034, 1058, 1146, 1254, 1280, 1364, 1380, 1412,
1464, 1517, 1597, 1660, 1680, 1718, 3258, 3557, 3611, 3692, 3775};

vN7HEnolGTS1 = {106, 153, 220, 327, 337, 347, 398, 492, 500, 508, 509, 564, 615, 630,
631, 647, 653, 735, 789, 800, 827, 836, 970, 1056, 1087, 1121, 1248, 1351, 1400, 1494,
1542, 1606, 1712, 2167, 3384, 3517, 3601, 3735, 3794};

vN7HEnolGP1 = {86, 115, 149, 218, 331, 336, 351, 389, 434, 465, 511, 516, 561, 604,
618, 627, 638, 663, 741, 796, 815, 824, 876, 955, 1057, 1085, 1147, 1249, 1364, 1437,
1490, 1536, 1558, 1595, 1691, 1712, 2267, 3381, 3490, 3601, 3737, 3796};

vN7HEnolGTS2 = {57, 64, 100, 150, 198, 204, 332, 345, 369, 452, 490, 550, 597, 645,
668, 700, 725, 761, 800, 816, 828, 966, 990, 1037, 1086, 1251, 1319, 1438, 1485, 1547,
1645, 1715, 1723, 1763, 2254, 3422, 3462, 3565, 3698, 3779};

vN7HEnolGP2 = {30, 60, 78, 110, 120, 147, 215, 269, 340, 371, 460, 469, 559, 591, 654,
698, 720, 742, 747, 793, 814, 826, 834, 949, 985, 1046, 1088, 1258, 1326, 1438, 1502,
1559, 1660, 1735, 1752, 1832, 2259, 3424, 3450, 3551, 3681, 3750};

(**Reaction pathways for HCNO loss from enol(cis)-N7H-amino guanine+**)

vN7HEnolGTS1III = {103, 125, 174, 241, 268, 322, 343, 403, 444, 488, 494, 531, 571, 626,
654, 677, 699, 727, 755, 920, 961, 1087, 1112, 1135, 1196, 1242, 1272, 1372, 1421,
1455, 1477, 1526, 1601, 1621, 1654, 2176, 3279, 3533, 3626, 3654, 3807};

vN7HEnolGP1III = {46, 72, 111, 181, 189, 224, 314, 336, 402, 434, 452, 492, 506, 520,
614, 626, 672, 693, 702, 745, 911, 963, 1075, 1124, 1126, 1196, 1241, 1267, 1370, 1420,
1440, 1455, 1556, 1613, 1643, 1730, 2447, 3284, 3523, 3625, 3634, 3831};

vN7HEnolGTS2III = {58, 58, 70, 121, 140, 209, 222, 286, 305, 308, 410, 449, 495, 498, 544, 563, 598, 660, 698, 891, 939, 951, 1095, 1114, 1128, 1204, 1225, 1244, 1372, 1407, 1428, 1541, 1571, 1619, 2260, 2470, 3284, 3540, 3645, 3651, 3778};

vN7HEnolGP2III = {23, 40, 55, 81, 99, 116, 178, 208, 345, 400, 425, 498, 503, 512, 550, 597, 602, 650, 697, 853, 879, 936, 976, 1106, 1164, 1187, 1210, 1225, 1235, 1359, 1412, 1428, 1567, 1573, 1639, 2439, 2490, 2890, 3268, 3597, 3634, 3802};

(**Reaction pathways for HCN loss from keto-N7H-imino guanine+**)

vN7HIminoG = {116, 147, 188, 291, 315, 376, 475, 500, 561, 604, 625, 675, 677, 690, 698, 763, 774, 841, 855, 933, 941, 969, 1053, 1067, 1156, 1229, 1298, 1324, 1370, 1404, 1445, 1483, 1506, 1602, 1639, 1710, 1891, 3262, 3530, 3557, 3580, 3583};

vN7HIminoTS1 = {96, 130, 136, 278, 334, 379, 392, 402, 454, 477, 510, 522, 561, 622, 649, 672, 698, 776, 818, 825, 836, 921, 991, 1010, 1087, 1179, 1283, 1346, 1392, 1438, 1456, 1629, 1710, 1780, 1900, 2047, 3368, 3474, 3562, 3566, 3578};

vN7HIminoP1 = {80, 115, 116, 129, 264, 318, 346, 379, 381, 435, 440, 485, 507, 564, 602, 657, 683, 697, 780, 819, 828, 846, 964, 980, 1001, 1092, 1192, 1286, 1353, 1399, 1444, 1455, 1605, 1705, 1780, 1893, 2162, 3368, 3439, 3573, 3579, 3593};

vN7HIminoTS2 = {44, 62, 83, 105, 133, 149, 152, 296, 340, 392, 446, 468, 521, 616, 628, 671, 701, 779, 812, 830, 846, 889, 915, 1019, 1040, 1066, 1262, 1315, 1371, 1418, 1454, 1718, 1746, 1831, 1911, 2268, 3421, 3428, 3483, 3562, 3588};

vN7HIminoP2 = {44, 62, 83, 105, 133, 149, 152, 296, 340, 392, 446, 468, 521, 616, 628, 671, 701, 779, 812, 830, 838, 846, 889, 915, 1019, 1040, 1066, 1262, 1315, 1371, 1418, 1454, 1718, 1746, 1831, 1911, 2268, 3421, 3428, 3562, 3588};

(**Reaction pathways for HCNO loss from keto-N7H-imino guanine+**)

vN7HIminoP2III = {27, 71, 130, 169, 181, 214, 320, 359, 388, 396, 491, 505, 512, 519, 604, 609, 688, 696, 736, 758, 904, 963, 1069, 1112, 1125, 1154, 1238, 1263, 1347, 1417, 1431, 1458, 1561, 1607, 1622, 1686, 2513, 3263, 3441, 3536, 3594, 3648};

vN7HIminoTS3III = {36, 58, 100, 109, 122, 245, 296, 314, 327, 340, 447, 464, 500, 506, 563, 569, 624, 688, 701, 873, 880, 941, 956, 1113, 1128, 1207, 1222, 1251, 1375, 1419, 1434, 1564, 1584, 1629, 2202, 2491, 3286, 3542, 3584, 3615, 3661};

(**Relative energies (in cm^{-1}, ZPE corrected) of TS and intermediate products involved in HCN loss from keto-N9H-amino guanine+**)

reN9HG = 0;
reN9HTS1 = 21454;
reN9HP1 = 18308;
reN9HTS2 = 37585;
reN9HTS1II = 23632;
reN9HP1II = 20970;
reN9HTS2II = 43473;

(**Relative energies (in cm^{-1}, ZPE corrected) of TS and intermediate products involved in HCNO loss from keto-N9H-amino guanine+**)

reN9HP4III = 16453;
reN9HTS5III = 27745;

(**Relative energies (in cm^{-1}, ZPE corrected) of TS and intermediate products involved in HCN loss from enol(trans)-N9H-amino guanine+**)

reN9HEnolG = 0;
reN9HEnolGTS1 = 23632;
reN9HEnolGP1 = 20370;
reN9HEnolGTS2 = 43473;
reN9HEnolGTS1II = 42102;
reN9HEnolGP1II = 41053;
reN9HEnolGTS2II = 46941;

(**Relative energies (in cm^{-1}, ZPE corrected) of TS and intermediate products involved in HCNO loss from enol(trans)-N9H-amino guanine+**)

reN9HEnolGTS1III = 14679;
reN9HEnolGP1III = 3790;
reN9HEnolGTS2III = 13469;
reN9HEnolGP2III = 11453;
reN9HEnolGTS3III = 21454;
reN9HEnolGP3III = 15324;
reN9HEnolGTS4III = 26616;
reN9HEnolGP4III = 22180;

(**Relative energies (in cm^{-1}, ZPE corrected) of TS and intermediate products involved in

HCN loss from keto-N7H-amino guanine+)*

reN7HG = 0;
reN7HTS1 = 15243;
reN7HP1 = 14598;
reN7HTS2 = 26535;
reN7HP2 = 24115;

(**Relative energies (in cm^{-1}, ZPE corrected) of TS and intermediate products involved in HCNO loss from keto-N7H-amino guanine+*)*

reN7HTS1III = 24115;
reN7HP1III = 20244;
reN7HTS2III = 61620;
reN7HP2III = 25648;

(**Relative energies (in cm^{-1}, ZPE corrected) of TS and intermediate products involved in HCN loss from enol(cis)-N7H-amino guanine+*)*

reN7HEnolG = 0;
reN7HEnolGTS1 = 15243;
reN7HEnolGP1 = 14598;
reN7HEnolGTS2 = 27100;
reN7HEnolGP2 = 24599;

(**Relative energies (in cm^{-1}, ZPE corrected) of TS and intermediate products involved in HCNO loss from enol(cis)-N7H-amino guanine+*)*

reN7HEnolGTS1III = 18308;
reN7HEnolGP1III = 15727;
reN7HEnolGTS2III = 31616;
reN7HEnolGP2III = 26616;

(**Relative energies (in cm^{-1}, ZPE corrected) of TS and intermediate products involved in HCN loss from keto-N7H-imino guanine+*)*

reN7HIminoG = 0;
reN7HIminoTS1 = 17905;
reN7HIminoP1 = 17340;
reN7HIminoTS2 = 27342;
reN7HIminoP2 = 27180;

(*Relative energies (in cm^{-1}, ZPE corrected) of TS and intermediate products involved in HCNO loss from keto-N7H-imino guanine+*)

reN7HIminoP2III = 16050;
reN7HIminoTS3III = 57346;

sumsOfStates = Parallelize@MapThread[bsComputeSumOfStates[#1, energy, #2]&, {
{vN9HTS1, vN9HTS2, vN9HTS1II, vN9HTS2II, vN9HEnolGTS1, vN9HEnolGTS2,
vN9HEnolGTS1II, vN9HEnolGTS2II, vN9HTS5III, vN9HEnolGTS4III, vN7HGTS2III,
vN7HEnolGTS2III, vN7HIminoTS3III, vN7HTS2, vN7HEnolGTS2, vN7HIminoTS2},
{reN9HTS1, reN9HTS2, reN9HTS1II, reN9HTS2II, reN9HEnolGTS1, reN9HEnolGTS2,
reN9HEnolGTS1II, reN9HEnolGTS2II, reN9HTS5III, reN9HEnolGTS4III, reN7HTS2III,
reN7HEnolGTS2III, reN7HIminoTS3III, reN7HTS2, reN7HEnolGTS2, reN7HIminoTS2}}];
densitiesOfStates = Parallelize@MapThread[bsComputeDensityOfStates[#1, energy, #2]&, {
{vN9HG, vN9HP1, vN9HP1II, vN9HEnolG, vN9HEnolGP1, vN9HEnolGP1II,
vN9HP4III, vN9HEnolGP3III, vN7HGP1III, vN7HEnolGP1III, vN7HIminoP2III, vN7HP1,
vN7HEnolGP1, vN7HIminoP1}, {reN9HG, reN9HP1, reN9HP1II, reN9HEnolG,
reN9HEnolGP1, reN9HEnolGP1II, reN9HP4III, reN9HEnolGP3III, reN7HP1III,
reN7HEnolGP1III, reN7HIminoP2III, reN7HP1, reN7HEnolGP1, reN7HIminoP1}}];

h = QuantityMagnitude@UnitConvert[Quantity[1, PlanckConstant], SIBase] * 5.034 * 10^{22};
ple[vec_]:=PadLeft[vec, energy+1];
paddedDivide[x_, y_]:=Quiet[ple[x] / ple[y]]/.{ComplexInfinity →0}
{k1, k2, k3, k4, k5, k6, k7, k8, k9, k10, k11, k12, k13, k14, k15, k16} =
MapThread[paddedDivide, {sumsOfStates[[{1, 2, 3, 4, 5, 6, 7, 8, 9, 10, 11, 12, 13, 14, 15, 16}]],
h * densitiesOfStates[[{1, 2, 1, 3, 4, 5, 4, 6, 7, 8, 9, 10, 11, 12, 13, 14}]]}];

Show[
ListLinePlot@Log10[takeEvery[10000]/@{k2, k6, k14, k15, k16}],
ImageSize → 400, Frame → True, FrameLabel → {Internal energy (cm^{-1}), k(E) (s^{-1})},
FrameTicks → {Automatic, {#, HoldForm[$10^{\#}$]}&/@Range[0, 40, 2]}
]

The unimolecular rate constants obtained are shown in the following graphs

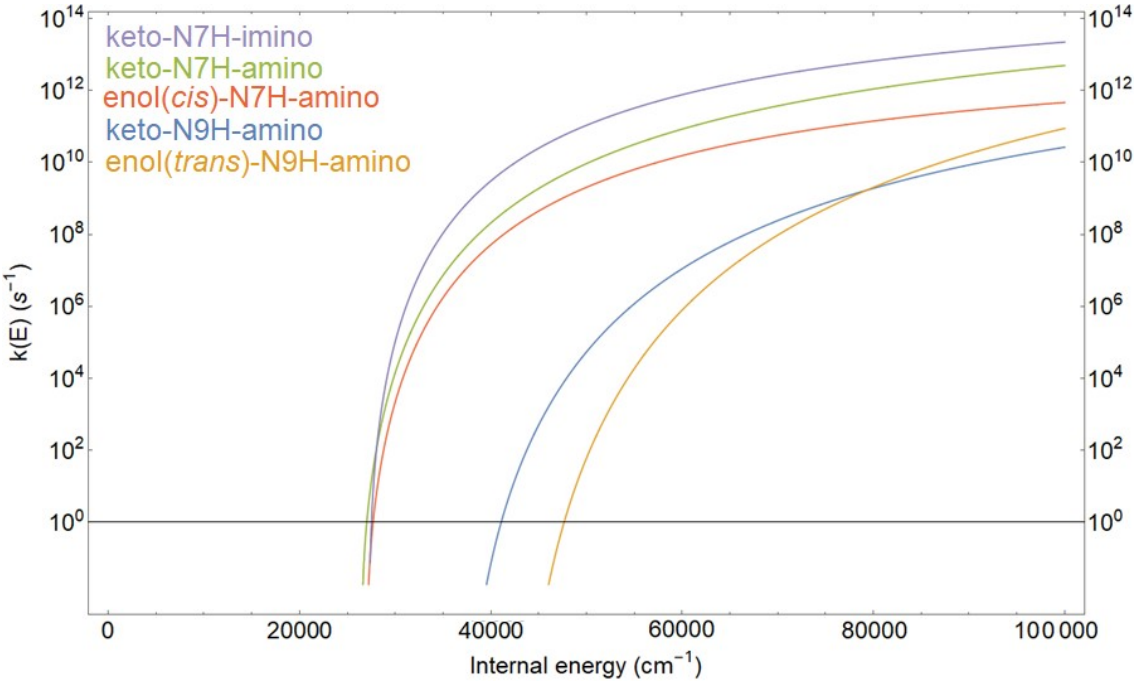

Figure A.1: Unimolecular rate constants calculated with the quasi-equilibrium theory for the five lowest guanine tautomers concerning the $G^+ \rightarrow [G\text{-}HCN]^+ + HCN$ reaction.

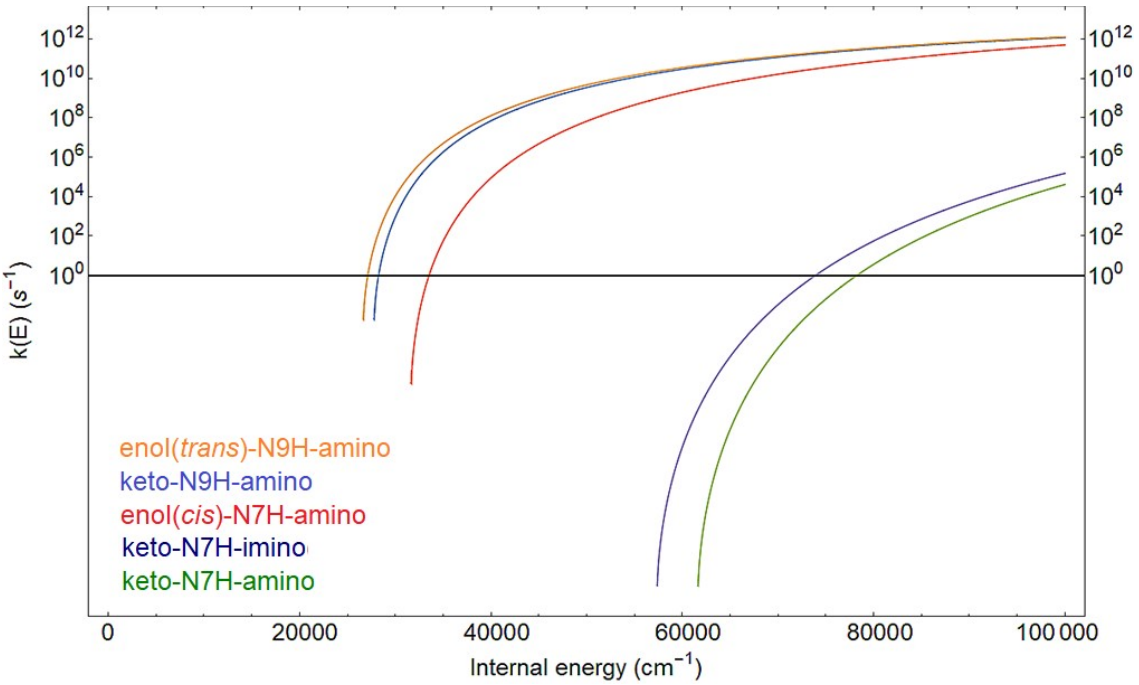

Figure A.2: Unimolecular rate constants calculated with the quasi-equilibrium theory for the five lowest guanine tautomers concerning the $G^+ \rightarrow [G\text{-}HCNO]^+ + HCNO$ reaction.

A.0.2 Calculation of mean kinetic energy release and unimolecular rate constants from mass spectra information

The mean kinetic energy release in a delayed fragmentation and respective unimolecular rate constant can be calculated from experimental mass spectra. According to Castleman *et al.* [151] it is possible to adjust the reflection voltage so that the parent and the metastable fragment ion present the same time-of-flight in two mass spectra. In that case, the mean kinetic energy released of the fragment ion is given by the equation 3.1 where $\langle L^2 \rangle$ has the form

$$\langle L^2 \rangle = a + b \times \left(\frac{Y}{X}\right) + c \times \left(\frac{Z}{X}\right) \tag{A.1}$$

and

$$a = l^2 - 2 \times \left(\frac{l v_0}{k}\right) + 2 \times \left(\frac{v_0^2}{k^2}\right)$$

$$b = 2 \times \left(\frac{v_0^2}{k}\right) - 2 \times (l v_0)$$

$$c = v_0^2$$

$$X = e^{-kt_1} - e^{-kt_2}$$

$$Y = t_1 \times e^{-kt_1} - t_2 \times e^{-kt_2}$$

$$Z = t_1^2 \times e^{-kt_1} - t_2^2 \times e^{-kt_2}$$

$l = l_1 + l_2$ is the total FFR flight path length, subdivided in the first FFR with length l_1 and second FFR with length l_2 , v_0 is the velocity of the ion in the FFR, k the unimolecular rate constant and t_1 and t_2 the times that the ion spent from the ionization region to the first FFR and from the first FFR until the reflection region respectively. t_1 can be calculated using the time of flight equations for ions in a Wiley-Maclaren ToF mass spectrometer, and t_2 by dividing the length of the first FFR by the velocity of the ion in that same region. The unimolecular rate constant can be calculated from the parent and daughter ion intensities (P and D, respectively) in the two mass spectra, k=-$\left(\frac{1}{t}\right)\left(\frac{l_1+l_2}{l_1}\right) ln\left(\frac{P}{P+D}\right)$. The following two tables contain the geometrical parameters of our reflectron time-of-flight mass spectrometer as well as the the parameters discussed above for the calculation of $\langle KER \rangle$, $\langle L^2 \rangle$ and k. Information about the guanine parent ion was obtained from four mass spectra with a reflection voltage V_r=−100 V. Information reagrding the metastable fragment ion originated from HCN and HCNO neutral loss was extracted from mass spectra where the reflection voltage conditions were −400 V and −580 V, respectively. Due to the weak signal for the former case, its analysis was based on the sum of four mass spectra.

Parameter	**Spec.**1	**Spec.**2	**Spec.**3	**Spec.**4
l (m)		1.193		
l_1 (m)		0.749		
l_2 (m)		0.444		
U_0 (V)		2040		
v_0 (m/s)		51032		
P	5898	8223	2143	2959
D	407	1471	215	330
t_1 (μs)		1.63		
t_2 (μs)		14.7		
t (μs)		16.3		
k (s^{-1})	6516	16071	9336	10325
a (m^2)	105	14	48	38
b (m^2/s)	6.77×10^{5}	2.02×10^{5}	4.36×10^{5}	3.82×10^{5}
c (m^2/s^2)		2.60×10^{9}		
X	8.06×10^{-2}	1.84×10^{-1}	1.13×10^{-1}	1.24×10^{-1}
Y (s)	-1.17×10^{-5}	-1.00×10^{-5}	-1.12×10^{-5}	-1.10×10^{-5}
Z (s^2)	-1.93×10^{-10}	-1.68×10^{-10}	-1.85×10^{-10}	-1.82×10^{-10}
$\langle L^2\rangle$ (m^2)	6.48×10^{-1}	6.58×10^{-1}	6.51×10^{-1}	6.52×10^{-1}
$\langle KER\rangle$ (meV)	8.64	6.26	10.3	3.36

Table A.1: Reflectron time of flight parameters and deduced parameters for the estimation of metastable kinetics for a reflection voltage of V_r=−580 V. Under these conditions, the fragment ion originated from HCNO loss from guanine cation has the same ToF as the parent ion at V_r=−100 V.

Parameter	**Spec.**1 **+ Spec.**2 **+ Spec.**3 **+ Spec.**4
P	27655
D	478
k (s^{-1})	1673
a (m^2)	1788
b (m^2/s)	2.99×10^{6}
c (m^2/s^2)	2.60×10^{9}
X	2.15×10^{-2}
Y (s)	-1.27×10^{-5}
Z (s^2)	-2.02×10^{-10}
$\langle L^2\rangle$ (m^2)	6.43×10^{-1}
$\langle KER\rangle$ (meV)	15.6

Table A.2: Reflectron time of flight parameters and deduced parameters for the estimation of metastable kinetics for a reflection voltage of V_r=−400 V. Under these conditions, the fragment ion originated from HCN loss from guanine cation has the same ToF as the parent ion at V_r=−100 V.

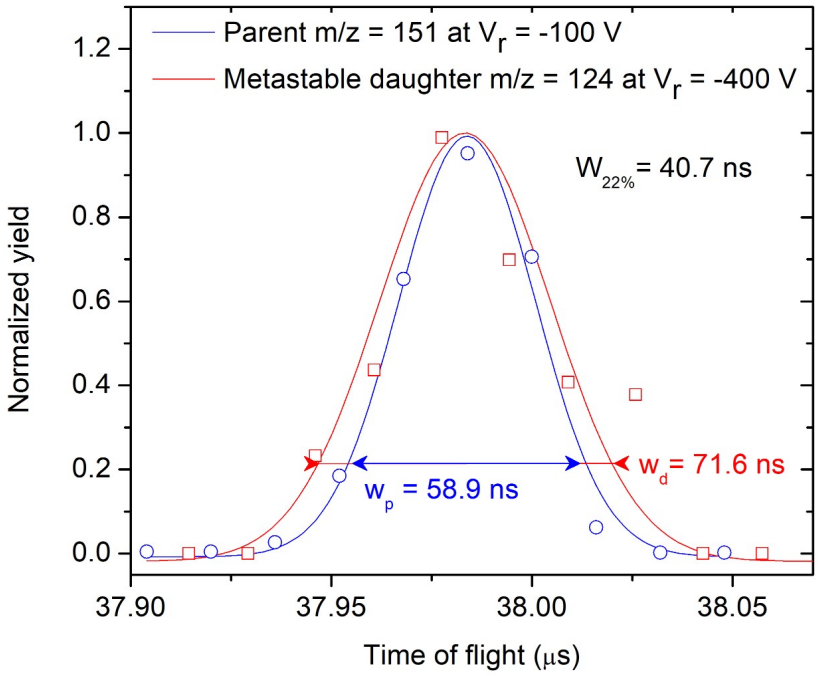

Figure A.3: Time of flight broadening of the $[G–HCN]^+$ fragment ion signal due to kinetic energy released in the dissociation. Owing to the low intensity of the fragment ion signal, four different mass spectra were summed.

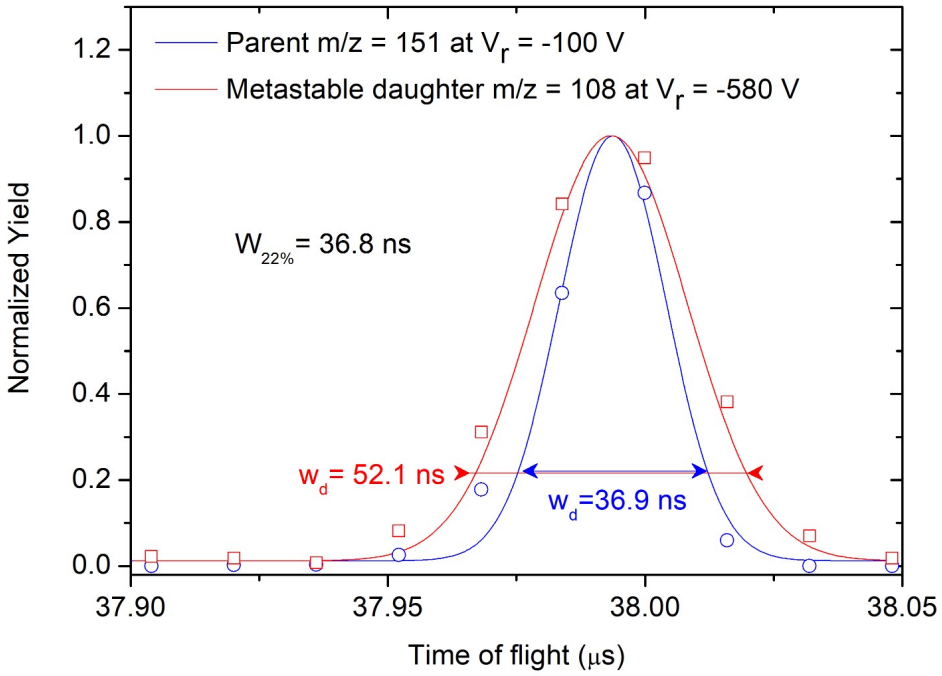

Figure A.4: Time of flight broadening of the $[G-HCNO]^+$ fragment ion signal due to kinetic energy released in the dissociation. This is one of the four ion signals used to calculate the mean KER.

Appendix B

Vertical and adiabatic excitations of guanosine tautomers

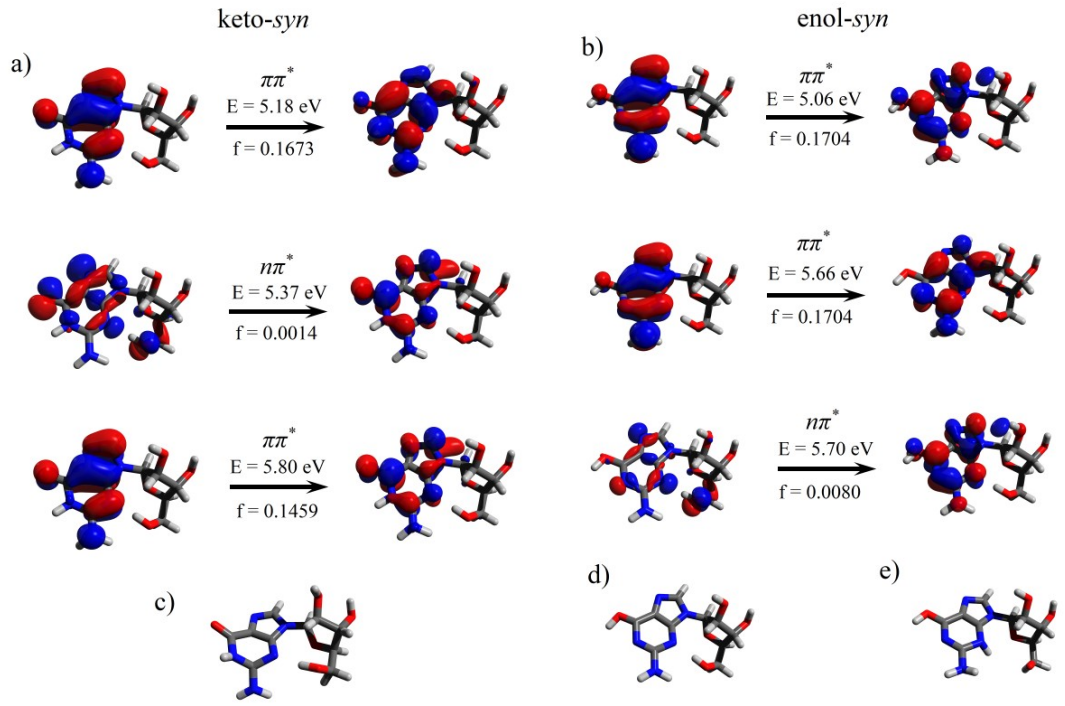

Figure B.1: Vertical excited states of a) guanosine-keto-*syn* and b) guanosine-enol-*syn*. Optimised S_1 geometry of c) guanosine-keto-*syn* for 5'O-H bond distance of 0.98 Å , d) guanosine-enol-*syn* for 5'O-H bond distance of 0.98 Å and e) guanosine-enol-*syn* after hydrogen transfer from the 5'O position to the N3 site. The optimised geometry of guanosine-keto-*syn* after hydrogen transfer could not be found due to a degenerancy of S_1 and S_2 electronic states. The calculations were performed at TDDFT level with the M06-2X functional and 6-31+G(d) basis set.

Appendix C

C++ code for simulation of Stark deflection profiles

```
#pragma hdrstop
#pragma argsused

#ifdef _MSC_VER
#define _CRT_SECURE_NO_WARNINGS
#endif


#ifdef _WIN32
#include <tchar.h>
#else
typedef char _TCHAR;
#define _tmain main
#endif

#include <stdio.h>
#include <iostream>
#include <fstream>
#include <iomanip>
#include <string>
#include <ctype.h>
#include <math.h>
#include <cstdio>
#include <algorithm>
#include <sstream>
#include <stdlib.h>

using namespace std;
const int STR_LEN = 75;
const int WRD_LEN = 12;
const double DER_STEP = 0.0000336, Boltzmann_const = 1.38E-23, Mass_unit = 1.67E-27,
    ↪ charge_unit=1.6E-19; //0.000028m (12kV case) step for the calculation of the
    ↪ electric field, using solely that file for all the voltages
```

```
32 const float nitromethane_rad = 2.19E-10;
33 const float helium_rad = 1.28E-10;
34 const float argon_rad = 1.73E-10;
35 const float B_const = 1.38E-23;
36
37
38 void calculate_beam_velocity(int car_gas_type, float car_gas_p, int car_gas_temp, int &
       ↪ mean_vel, int &max_vel)
39 {
40   int p_Pa = car_gas_p * 101300;
41   float flow, nozzle_radius = 1.0E-5, throughput, gamma = 1.67, exp_chb_pressure,
         ↪ Mach_Disk, Ter_Mach = 0, density = 0;
42   float beam_temp, car_gas_mass;
43   int R = 208, pumping_speed = 4000;
44   char car_gas_name[10];
45   flow = sqrt((gamma / R)*pow(2. / (gamma + 1), 1.0*((gamma + 1) / (gamma - 1))))*(p_Pa /
         ↪ sqrt(1.0*car_gas_temp))*3.14*pow(1.0*nozzle_radius, 2.0);
46   throughput = flow * 1.685E-2 / 2.8E-8;
47   exp_chb_pressure = throughput / pumping_speed;
48   Mach_Disk = 0.67*(200 * nozzle_radius)*pow(car_gas_p*1000.0 / exp_chb_pressure, 0.5);
49   density = car_gas_p * 100000 / (B_const*car_gas_temp);
50
51   switch (car_gas_type)
52   {
53   case 1: {
54     car_gas_mass = 4 * Mass_unit;
55     strcpy(car_gas_name, "Helium");
56     Ter_Mach = 2.05*pow(1 / ((2 * nozzle_radius)*(1.414*3.14*pow(2 * helium_rad, 2) *
           ↪ density*0.02)), -0.4);
57     break;
58     }
59   case 2: {
60     car_gas_mass = 40 * Mass_unit;
61     strcpy(car_gas_name, "Argon");
62     Ter_Mach = 2.05*pow(1 / ((1.414*3.14*pow(2 * argon_rad, 2) * density*(2 *
           ↪ nozzle_radius)*0.25)), -0.4);
63     break;
64     }
65   case 3: {
66     car_gas_mass = 36 * Mass_unit;
67     strcpy(car_gas_name, "Krypton");
68     break;
69     }
70   }
71   beam_temp = (car_gas_temp) / (1 + (0.5*(gamma - 1))*pow(Ter_Mach, 2));
72   max_vel = sqrt((2 * Boltzmann_const / car_gas_mass)*(gamma / (gamma - 1))*car_gas_temp);
73   mean_vel = Ter_Mach * sqrt(gamma*Boltzmann_const*car_gas_temp / car_gas_mass) / sqrt(1 +
         ↪  (0.5*(gamma - 1)*pow(Ter_Mach, 2)));
74   {
75     std::ofstream obeam("C:\\Users\\ASUS\\Desktop\\Beam_Properties.txt");
```

```
76    obeam << "For " << car_gas_name << " as carrier gas, with a pressure of " << car_gas_p
          ↪  * 1000 << " mbar and temperature of " << car_gas_temp << " Kelvin, the
          ↪ molecular beam has the following properties:" << std::endl;
77    obeam << '\n' << "Terminal Mach number: " << Ter_Mach << std::endl;
78    obeam << "Beam temperature (K): " << beam_temp << std::endl;
79    obeam << "Mean and Maximum velocity: " << mean_vel << "," << max_vel << ",
          ↪ respectively." << std::endl;
80    obeam.close();
81  }
82 }
83
84 float calculate_acel(int Max_E, int Min_E, int mass)
85 {
86   float grad = 0, a_def = 0, t_def = 0, y_def = 0, vy_chb = 0, t_chb = 0, y_chb = 0,
         ↪ tot_def = 0;
87   grad = ((Min_E*6.6E-28) - (Max_E*6.6E-28)) / DER_STEP; //Calculate gradient
88   a_def = grad / (mass*Mass_unit); //Aceleration in the deflector
89   return a_def;
90 }
91
92 float calculate_mu_eff(int Max_E, int Min_E, int voltage)
93 {
94   float grad = 0, mu_eff = 0;
95   grad = ((Min_E*6.6E-28) - (Max_E*6.6E-28)) / DER_STEP; //Calculate gradient
96   mu_eff = (grad / ((voltage + 1)*4.61E8)) / 3.33E-30;
97   return mu_eff;
98
99 }
100 float return_values(char *string,int flag)
101 {
102   int order = 0,a=0, i = 0,k=1,sig=0;
103   float value = 0;
104   if (flag == 0)
105   {
106     if (string[0]=='-')
107     {
108       sig = -1;
109       i++;
110     }
111     else
112       sig = 1;
113
114     while (!ispunct(string[i])) //Search for decimal place in the field value
115       i++;
116     order = i;
117
118     if (sig == -1)
119     {
120       for (int p = (order - 1); p > 0; p--)
121         value = value + ((string[p] - '0')*pow(10., (order - p - 1)));
122       i++;
```

```
123     }
124     else if (sig == 1)
125     {
126       for (int p = (order - 1); p >= 0; p--)
127         value = value + ((string[p] - '0')*pow(10., (order - p - 1)));
128       i++;
129     }
130
131
132     while (string[i] != '\t')
133     {
134       value = value + ((string[i] - '0')*0.1);
135       i++;
136       k++;
137     }
138     value = value * sig;
139
140
141   }
142
143   else if (flag == 1)
144   {
145     int k = -1;
146     while ((string[i]) != '\t') //Search for delimiter
147       i++;
148     a = i + 1;
149     for (i = a; !ispunct(string[i]); i++)
150       order++; //Finds how big is the energy
151     for (i = (a + order - 1); i >= a; i--)
152       value = value + ((string[i] - '0')*pow(10., (a + order - i - 1)));
153     i = a + order + 1;
154     while (string[i] != '\0')
155     {
156       value = value + (string[i] - '0')*pow(10., k);
157       i++;
158       k--;
159     }
160   }
161   cout << value << endl;
162   return value;
163
164 }
165
166 float return_Field_value(char *string)
167 {
168   int Field_order = 0, i = 0;
169   float Field = 0;
170
171   while (!ispunct(string[i])) //Search for decimal place in the field value
172     i++;
173   Field_order = i;
```

```
174   i = 0;
175   for (i = (Field_order - 1); i >= 0; i--)
176     Field = Field + ((string[i] - '0')*pow(10., (Field_order - i - 1)));
177   i = Field_order + 1;
178   Field = Field + (string[i] - '0')*pow(10.,-1);
179 
180   return Field;
181 }
182 
183 int return_Energy_value(char *string)
184 {
185   int Energy = 0, sig = 0, a = 0, i = 0, Energy_order = 0;
186   while (string[i] != '␣')
187     i++;
188   a = i + 1;
189   if (!isdigit(string[a]))
190     sig = -1; //Reads the Min_Energy signal; -1 if is negative, 1 if it is positive
191   else
192     sig = 1;
193   if (sig == -1)
194   {
195     for (i = a + 1; !ispunct(string[i]); i++)
196       Energy_order++; //Finds how big is the energy
197     for (i = (a + Energy_order); i >= a + 1; i--)
198       Energy = Energy + ((string[i] - '0')*pow(10., (a + Energy_order - i)));
199     Energy = -1 * Energy;
200   }
201   if (sig == 1)
202   {
203     for (i = a; !ispunct(string[i]); i++)
204       Energy_order++; //Finds how big is the energy
205     for (i = (a + Energy_order - 1); i >= a; i--)
206       Energy = Energy + ((string[i] - '0')*pow(10., (a + Energy_order - i - 1)));
207   }
208   return Energy;
209 }
210 
211 void read_FFE(unsigned long int &FFE, char *string)
212 {
213   int FF_Order = 0, a = 0, i = 0;
214   while (string[i] != '␣')
215     i++;
216   a = i + 1;
217   for (i = a; !ispunct(string[i]); i++)
218     FF_Order++; //Finds how big is the energy
219   for (i = (a + FF_Order - 1); i >= a; i--)
220     FFE = FFE + ((string[i] - '0')*pow(10., (a + FF_Order - i - 1)));
221 }
222 
223 float set_Boltzmann(long int FFE, float T)
224 {
```

```
225   return (exp(-(FFE*6.62E-28) / (Boltzmann_const*T)));
226 }
227
228 float determine_local_field(int voltage, float vertical_position) //Determine the local
        ↪ field according to the vertical position (in kV/cm)
229 {
230   switch (voltage)
231   {
232   case 1:
233     return (2.03455*vertical_position + 7.0438);
234   case 2:
235     return (4.0691*vertical_position + 14.0876);
236   case 4:
237     return (8.1650*vertical_position + 28.1825);
238   case 6:
239     return (12.2618* vertical_position + 42.2754);
240   case 8:
241     return (16.3491* vertical_position + 56.3673);
242   case 10:
243     return (20.3822* vertical_position + 70.4463);
244   case 12:
245     return(24.459*vertical_position + 84.535);
246   default:
247   {
248     cout << "Not␣possible␣to␣calculate␣local␣field␣for␣this␣voltage" << endl;
249     return 0;
250   }
251   }
252
253 }
254
255 void quickSort_float(float arr[], int left, int right)
256 {
257   int i = left, j = right;
258   float tmp = 0;
259   float pivot = arr[(int)((left + right) / 2)];
260   if (left >= right)
261     return;
262
263   /* partition */
264   while (i <= j) {
265     while (arr[i] > pivot)
266       i++;
267     while (arr[j] < pivot)
268       j--;
269     if (i <= j) {
270       tmp = arr[i];
271       arr[i] = arr[j];
272       arr[j] = tmp;
273       i++;
274       j--;
```

```
    }
  };
  if (left < j)
    quickSort_float(arr, left, j);
  if (i < right)
    quickSort_float(arr, i, right);
}

void quickSort_int(int arr[], int left, int right)
{
  int i = left, j = right;
  int tmp = 0;
  int pivot = arr[(int)((left + right) / 2)];
  if (left >= right)
    return;

  /* partition */
  while (i <= j) {
    while (arr[i] > pivot)
      i++;
    while (arr[j] < pivot)
      j--;
    if (i <= j) {
      tmp = arr[i];
      arr[i] = arr[j];
      arr[j] = tmp;
      i++;
      j--;
    }
  };
  if (left < j)
    quickSort_int(arr, left, j);
  if (i < right)
    quickSort_int(arr, i, right);
}


int main(int argc, _TCHAR* argv[])
{
  int t_step = 0, gas = 0, voltage = 0, NTraj = 0, NStates = 0, state_range = 2, Energy =
      ↪ 0, dyn_flag=0, prog=0;
  int i = 0, vx = 0, mass, mean_vel = 0, &beam_mean_velocity = mean_vel, max_vel = 0, &
      ↪ beam_max_velocity = max_vel;
  int &Energy_ref = Energy;
  char word[WRD_LEN], line[STR_LEN], ch;
  float pressure, mu_eff = 0, temp_analysis = 0, cumulation = 0, num = 0, pos_it=0,
      ↪ temperature=0;
    unsigned long int j = 0, Free_Field_Energy = 0, &FFE_ref = Free_Field_Energy ;
  string name;

```

```
322 float undef_beam2[][2] = { {-3.0,0}, {-2.9,0},{-2.8,0 }, { -2.7,0 }, { -2.6,0 }, {
        ↪ -2.5,0 }, { -2.4,0 }, { -2.3,0 }, { -2.2,0.05194 }, { -2.1,0.19443 }, {
        ↪ -2.0,0.38948 }, { -1.9,0.66 }, { -1.8,1.04043 }, { -1.7,1.58319 },
323 { -1.6,2.3689 },{ -1.5,3.52253 },{ -1.4,5.23785 },{ -1.3,7.81153 },{ -1.2,11.68111 },{
        ↪ -1.1,17.43871 },{ -1.0,25.74156 },{ -0.9,36.98574 },{ -0.8,50.70919 },{
        ↪ -0.7,65.1788 },{ -0.6,78.00044 },{ -0.5,87.56252 },{ -0.4,93.75939 },
324 { -0.3,97.43079 },{ -0.2,99.51503 },{ -0.1,100.64848 },{ 0.0,101.15192 },{ 0.1,101.14313
        ↪  },{ 0.2,100.62024 },{ 0.3,99.46013 },{ 0.4,97.33262 },{ 0.5,93.58894 },{
        ↪ 0.6,87.28435 },{ 0.7,77.59656 },{ 0.8,64.68049 },{ 0.9,50.19631 },
325 { 1.0,36.53844 },{ 1.1,25.39761 },{ 1.2,17.19479 },{ 1.3,11.51555 },{ 1.4,7.70118 },{
        ↪ 1.5,5.16449 },{ 1.6,3.47343 },{ 1.7,2.33566 },{ 1.8,1.56038 },{ 1.9,1.02455 },{
        ↪ 2.0,0.64878 },{ 2.1,0.38143 },{ 2.2,0.18859 },{ 2.3,0.04764 },
326 { 2.4,0 },{ 2.5,0 },{ 2.6,0 },{ 2.7,0 },{ 2.8,0 },{ 2.9,0},{ 3.0,0 } }; //Obtained
        ↪ during 3-aminophenol measurements in Argon
327 float undef_beam1[][2] = { {-3.0,0}, { -2.9,0 },{ -2.8,0 },{ -2.7,0 },{ -2.6,0 },{
        ↪ -2.5,0 },{ -2.4,0 },{ -2.3,0 },{ -2.2,0 },{ -2.1,0 },{ -2.0,5.95304 },
328 { -1.9,8.22359 },{ -1.8,11.09184 },{ -1.7,14.6075 },{ -1.6,18.78551 },{ -1.5,23.59583
        ↪ },{ -1.4,28.9577 },{ -1.3,36.73403 },{ -1.2,42.81173 },{ -1.1,48.88858 },{
        ↪ -1.0,54.78854 },{ -0.9,60.37814 },{ -0.8,65.58819 },{ -0.7,70.4232 },
329 { -0.6,74.95346 },{ -0.5,79.28873 },{ -0.4,83.5366 },{ -0.3,87.75349 },{ -0.2,91.89941
        ↪ },{ -0.1,95.80852 },{ 0.0,99.18546 },{ 0.1,102.1636 },{ 0.2,102.67784 },{
        ↪ 0.3,101.27564 },{ 0.4,97.69395 },{ 0.5,91.86014 },{ 0.6,83.92253 },
330 { 0.7,74.24451 },{ 0.8,63.36312 },{ 0.9,51.92051 },{ 1.0,40.58178 },{ 1.1,29.95447 },{
        ↪ 1.2,20.5233 },{ 1.3,12.60951 },{ 1.4,6.35824 },{ 1.5,0.55912 },{ 1.6,0 },{ 1.7,0
        ↪ },{ 1.8,0 },{ 1.9,0 },{ 2.0,0 },
331 { 2.1,0 },{ 2.2,0 },{ 2.3,0 },{ 2.4,0 },{ 2.5,0 },{ 2.6,0 },{ 2.7,0 },{ 2.8,0 },{ 2.9,0
        ↪ }, {3.0,0} }; //GCAS fit obtained during nitromethane measurements in Helium
332 float undef_beam3[][2] = { { -2.9,0 },{ -2.8,0 },{ -2.7,0 },{ -2.6,0 },{ -2.5,0 },{
        ↪ -2.4,0 },{ -2.3,0 },{ -2.2,0 },{ -2.1,0 },{ -2.0 },
333 { -1.9,1.88206 },{ -1.8,4.65934 },{ -1.7,8.22044 },{ -1.6,12.63167 },{ -1.5,17.92688 },{
        ↪  -1.4,24.09573 },{ -1.3,31.07293 },{ -1.2,38.73018 },{ -1.1,46.87298 },{
        ↪ -1.0,55.24439 },{ -0.9,63.53799 },{ -0.8,71.42146 },{ -0.7,78.57093 },
334 { -0.6,84.71294 },{ -0.5,89.66675 },{ -0.4,93.37373 },{ -0.3,95.89812 },{ -0.2,97.38782
        ↪ },{ -0.1,98.00085 },{ 0.0,97.82563 },{ 0.1,96.83519 },{ 0.2,94.90121 },{
        ↪ 0.3,91.85982 },{ 0.4,87.59329 },{ 0.5,82.0903 },{ 0.6,75.46652 },
335 { 0.7,67.94918 },{ 0.8,59.83982 },{ 0.9,51.47099 },{ 1.0,43.16699 },{ 1.1,35.21425 },{
        ↪ 1.2,27.84264 },{ 1.3,21.21691 },{ 1.4,15.43628 },{ 1.5,10.54014 },{ 1.6,6.51753
        ↪ },{ 1.7,3.31854 },{ 1.8,0.8661 },{ 1.9,0 },{ 2.0,0 },
336 { 2.1,0 },{ 2.2,0 },{ 2.3,0 },{ 2.4,0 },{ 2.5,0 },{ 2.6,0 },{ 2.7,0 },{ 2.8,0 },{ 2.9,0
        ↪ } }; //Pseudo voigt fit obtained during nitromethane measurements in Helium
337 float Broadened_Profile_mid[201] = { 0 }, Broadened_Profile_Plus[67] = { 0 },
        ↪ Broadened_Profile_Minus[51] = { 0 }, deflections[141][2] = { 0,0 };
338 //Some inputs
339 cout << "Program?:␣0-␣Stark␣deflection␣profiles;␣1-␣Profile␣broadener" << endl;
340 cin >> prog;
341 if (prog == 0)
342 {
343   cout << "What␣is␣the␣carrier␣gas?" << '\n';
344   cout << "Press:" << '\n';
345   cout << '\n';
```

```
346     cout << "1␣for␣Helium" << '\n' << "2␣for␣Argon" << '\n' << "3␣for␣Krypton" << '\n' <<
            ↪ endl;
347     cin >> gas;
348     cout << "Carrier␣gas␣pressure␣(in␣bar)?" << endl;
349     cin >> pressure;
350     cout << "Carrier␣gas␣temperature␣(in␣Kelvin)?" << endl;
351     cin >> temperature;
352     cout << "Mass␣of␣the␣seeded␣molecule" << endl;
353     cin >> mass;
354     cout << "Time␣step␣for␣the␣dynamics␣(in␣microseconds)?" << endl;
355     cin >> t_step;
356     cout << "Generate␣dynamic␣files␣for␣each␣state?␣(0:␣No␣or␣1:␣Yes)" << endl;
357     cin >> dyn_flag;
358   }
359
360   cout << "Name␣of␣the␣seeded␣molecule" << endl;
361   cin >> name;
362   cout << "Deflector␣voltage␣in␣kV?" << endl;
363   cin >> voltage;
364   cout << "Temperature␣to␣use␣in␣Boltzmann␣distribution?" << endl;
365   cin >> temp_analysis;
366   cout << "Initial␣position?" << endl;
367   cin >> pos_it;
368   cout << "..." << endl << endl;
369
370   string str_name = static_cast<ostringstream*>(&(ostringstream() << name))->str();
371   string str_volt = static_cast<ostringstream*>(&(ostringstream() << voltage))->str();
372   string str_pos = static_cast<ostringstream*>(&(ostringstream() << pos_it))->str();
373   string str_temp = static_cast<ostringstream*>(&(ostringstream() << temp_analysis))->str
            ↪ ();
374
375   if (prog == 0)
376   {
377     calculate_beam_velocity(gas, pressure, temperature, beam_mean_velocity,
            ↪ beam_max_velocity);
378     vx = beam_mean_velocity;
379
380     ifstream ifile("C:\\Users\\ASUS\\Desktop\\" + str_name + "_" + "12kV.txt", ios::binary
            ↪ );
381     if (!ifile)
382     {
383       cout << "Error␣in␣opening␣the␣input␣file" << endl;
384       std::getchar();
385       return 0;
386     }
387     ifile >> resetiosflags(ios::skipws);
388
389     while (ifile >> ch) // count the number of states in the file.
390     {
391       int i = 0;
392       ifile.putback(ch);
```

```
393       ifile.getline(line, STR_LEN);
394       if (line[0] == '0' && line[2] == '0')
395         NStates++;
396     }
397     ifile.close();
398
399     int* FFE_vector = new int[NStates]; //Allocates memory for all FFE's
400     float* Boltzmann_vector = new float[NStates]; //Allocates memory for Boltzmann
            ↪ distributions
401     float state_field[174] = { 0. }; //Vector to store the fields
402     int state_energy[174] = { 0. }, total_steps = (int)(0.15 / (vx*t_step*0.000001)); //
            ↪ Vector to store the energies of different states
403
404     ifstream ifile2("C:\\Users\\ASUS\\Desktop\\" + str_name + "_" + "12kV.txt", ios::
            ↪ binary);
405     ofstream ofile("C:\\Users\\ASUS\\Desktop\\" + str_name + "_" + str_pos + "mm_" +
            ↪ str_temp + "K_" + str_volt + "_kV_Dynamics.csv");
406     ofile << "NState" << ',' << "Y␣Vel.␣at␣def.␣exit␣(m/s)" << ',' << "X␣Vel.␣at␣def.␣exit
            ↪ ␣(m/s)" << ',' << "Deflection␣at␣def.␣end␣(mm)" << ',' << "Tot.␣def.␣(mm)" << ',
            ↪ ' << "Boltzmann␣distribution" << endl;
407
408
409     while (ifile2 >> ch) //Fill FFE_vector with the FFE values
410     {
411       int step_it = 0, m = 0, f_it = 0;
412       float Y1 = pos_it * 1E-3, Y2 = 0, at = 0, field = 0, mu_eff = 0, vy = 0,
            ↪ Free_Field_energy = 0;
413       float Y_vector[10000] = { 0. };
414       Y_vector[0] = pos_it * 1E-3;
415
416       ifile2.putback(ch);
417       ifile2.getline(line, STR_LEN);
418
419       if (line[0] == '0' && line[2] == '0') //Reads FFE's, stores them and the respective
            ↪ Boltzmann distributions
420       {
421         read_FFE(FFE_ref, line);
422         FFE_vector[j] = Free_Field_Energy;
423         Boltzmann_vector[j] = set_Boltzmann(FFE_vector[j], temp_analysis);
424
425         while (true) //Read each field and energies for a given state and stores them in
              ↪ the arrays
426         {
427           ifile2.getline(line, STR_LEN);
428           if (abs(return_Field_value(line) - (voltage * 10)) <= 1)
429             break;
430           state_field[m] = return_Field_value(line);
431           state_energy[m] = return_Energy_value(line);
432           m++;
433         }
434         m = 0;
```

```
435
436         string State = static_cast<ostringstream*>(&(ostringstream() << j + 1))->str();
437
438         switch (dyn_flag)
439         {
440         case 0: //Do not produce dynamic files for each state
441         {
442           for (; step_it < total_steps; step_it++)    //Iterate through a single trajectory
443           {
444             field = determine_local_field(voltage, Y1 * 1000); //Determine the local field
                  ↪ at Y position
445             for (; state_field[f_it] < field;)
446               f_it++;
447             at = calculate_acel(state_energy[f_it], state_energy[f_it - 1], mass); //
                  ↪ Calculate the aceleration from potential energy variation and mass
448             f_it = 0;
449
450             //Verlet algorithm
451             if (step_it == 0) //Initial step
452             {
453               Y1 = Y1 + 0 * (t_step * 0.000001) + 0.5 * at * pow((t_step * 0.000001), 2);
                    ↪ //Vertical position Y in meters (written in trajectory file in meters)
454               Y_vector[step_it + 1] = Y1;
455             }
456             if (step_it >= 1) //Steps others than the first
457             {
458               Y1 = 2 * Y1 - Y_vector[step_it - 1] + at * pow((t_step * 0.000001), 2);
459               Y_vector[step_it + 1] = Y1;
460             }
461             if ((Y1 * 1000 <= -0.7 || Y1 * 1000 >= 0.7))//Collision restritions
462             {
463               ofile << State << ',' << "-" << ',' << "-" << ',' << "Collision" << ',' << "
                    ↪ Collision" << ',' << Boltzmann_vector[j] << endl;
464               j++;
465               step_it = 0;
466               Free_Field_Energy = 0;
467               goto here; //use goto
468             }
469           }
470           vy = (Y_vector[step_it] - Y_vector[step_it - 1]) / (t_step * 0.000001);//
                ↪ transverse velocity
471           Y2 = (Y1 + (vy * (0.477 / vx))) * 1000;//Total deflection
472           ofile << State << ',' << vy << ',' << vx << ',' << Y1 * 1000 << ',' << Y2 << ','
                ↪ << Boltzmann_vector[j] << endl;
473           j++;
474           Free_Field_Energy = 0;
475         here:
476           continue;
477           break;
478         }
479         case 1: //Produce dynamic files for each state
```

```
480         {
481           ofstream ofile2("C:\\Users\\ASUS\\Desktop\\Trajectories\\" + str_name + "_" +
                  ↪ str_volt + "␣kV_State_" + State + "_" + str_pos + "mm.csv");//File
                  ↪ containing the trajectory
482           ofile2 << "Time␣(us)" << ',' << "Longitudinal␣position␣(mm)" << ',' << "Vertical␣
                  ↪ position␣(mm)" << ',' << "Aceleration␣(m/s^2)" << endl;
483           for (; step_it < total_steps; step_it++) //Iterate through a single trajectory
484           {
485             field = determine_local_field(voltage, Y1 * 1000); //Determine the local field
                    ↪ at Y position
486             for (; state_field[f_it] <= field;)
487               f_it++;
488             at = calculate_acel(state_energy[f_it], state_energy[f_it - 1], mass); //
                    ↪ Calculate the aceleration from potential energy variation and mass
489             f_it = 0;
490
491             //Verlet algorithm
492             if (step_it == 0)
493             {
494               ofile2 << step_it * t_step << ',' << vx * (step_it * t_step * 1E-6) * 1000 <<
                      ↪ ',' << Y1 * 1000 << ',' << at << endl;
495               Y1 = Y1 + 0 * (t_step * 0.000001) + 0.5 * at * pow((t_step * 0.000001), 2); //
                      ↪ Vertical position Y in meters (written in trajectory file in mm)
496               Y_vector[step_it + 1] = Y1;
497             }
498             if (step_it >= 1)
499             {
500               ofile2 << step_it * t_step << ',' << vx * (step_it * t_step * 1E-6) * 1000 <<
                      ↪ ',' << Y1 * 1000 << ',' << at << endl;
501               Y1 = 2 * Y1 - Y_vector[step_it - 1] + at * pow((t_step * 0.000001), 2);
502               Y_vector[step_it + 1] = Y1;
503             }
504             if ((Y1 * 1000 <= -0.7 || Y1 * 1000 >= 0.7))//Collision restritions, rod-trough
                    ↪ gap
505             {
506               ofile2 << step_it * t_step << ',' << vx * (step_it * t_step * 1E-6) * 1000 <<
                      ↪ ',' << "Collision" << ',' << at << endl;
507               ofile2.close();
508               ofile << State << ',' << "-" << ',' << "-" << ',' << "Collision" << ',' << "
                      ↪ Collision" << ',' << Boltzmann_vector[j] << endl;
509               j++;
510               step_it = 0;
511               Free_Field_Energy = 0;
512               goto there;
513             }
514           }
515           vy = (Y_vector[step_it] - Y_vector[step_it - 1]) / (t_step * 0.000001);
516           Y2 = (Y1 + (vy * (0.477 / vx))) * 1000;
517           ofile << State << ',' << vy << ',' << vx << ',' << Y1 * 1000 << ',' << Y2 << ','
                  ↪ << Boltzmann_vector[j] << endl;
518           j++;
```

```
519           Free_Field_Energy = 0;
520           ofile2.close();
521         there:
522           continue;
523           break;
524         }
525         default:
526           break;
527         }
528       }
529     }
530     ifile2.close();
531     ofile.close();
532   }
533
534   if(prog==1)
535   {
536     ifstream ifile3("C:\\Users\\ASUS\\Desktop\\" + str_name + "_" + str_volt + "kV_"+
          ↪ str_pos+"mm.txt"); //Open file with undeflected profile
537     ofstream ofile2("C:\\Users\\ASUS\\Desktop\\" + str_name + "_" + str_temp + "K_" +
          ↪ str_volt + "_kV_Final_Profile.txt");
538     int it = 0;
539     while (ifile3 >> ch) //Read values from file and write on an array
540     {
541       ifile3.putback(ch);
542       ifile3.getline(line, STR_LEN);
543       deflections[it][0]=return_values(line,0);
544       deflections[it][1]= return_values(line,1);
545       it++;
546     }
547
548     int g = 0, h=0;
549     for (int k = 0; k <= 60; k++)
550       for (int l = 0; l <= 140; l++)
551         Broadened_Profile_mid[k+l] = Broadened_Profile_mid[k+l] + (deflections[l][1] *
              ↪ undef_beam1[k][1]);
552
553
554     for (int p=0; p<=200; p++)
555       ofile2 << Broadened_Profile_mid[p] << endl;
556     ofile2.close();
557     ifile3.close();
558
559   }
560
561   return 0;
562
563 }
```

Appendix D

Extended tests on Stark deflection profiles and Stark removal curves

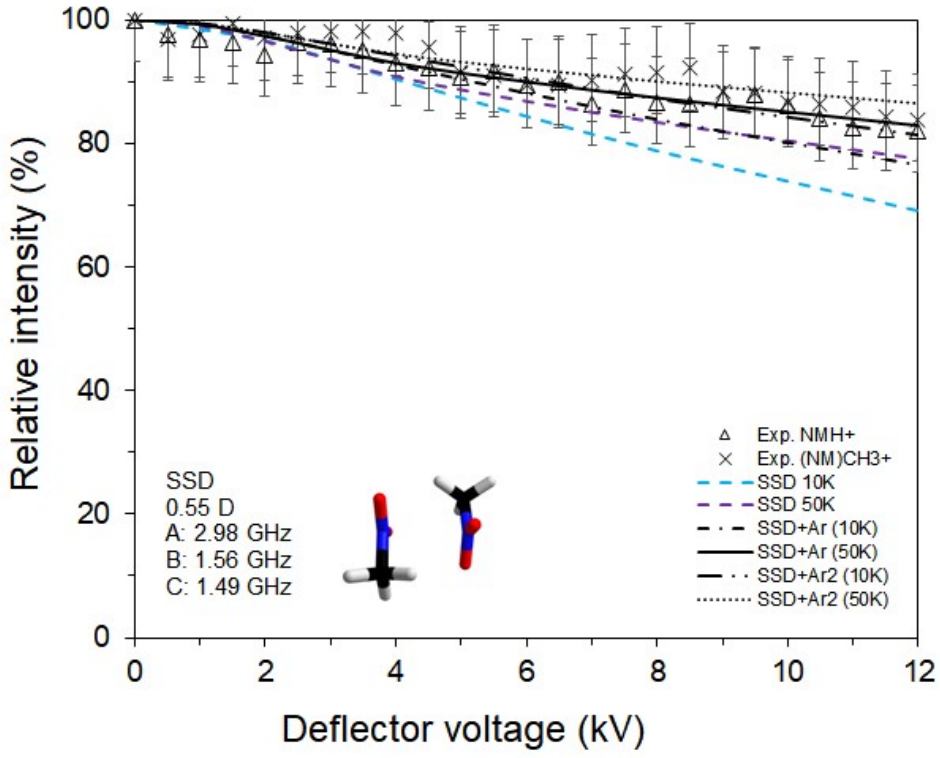

Figure D.1: Simulated removal curves of side-by-side monomers with a rotational temperature of 10 K (dashed blue) and 50 K (dashed purple). Removal curves for SSD-argon complexes are represented by dashed-dotted, dashed-dotted-dotted, solid and dotted lines. These curves were obtained by scaling the pure SSD curves. The experimental protonated nitromethane and methylated nitromethane ion signals are represented by open black triangles and black crosses, respectively.

Appendix E

CAD of the new DEA / EII / MPI experiment

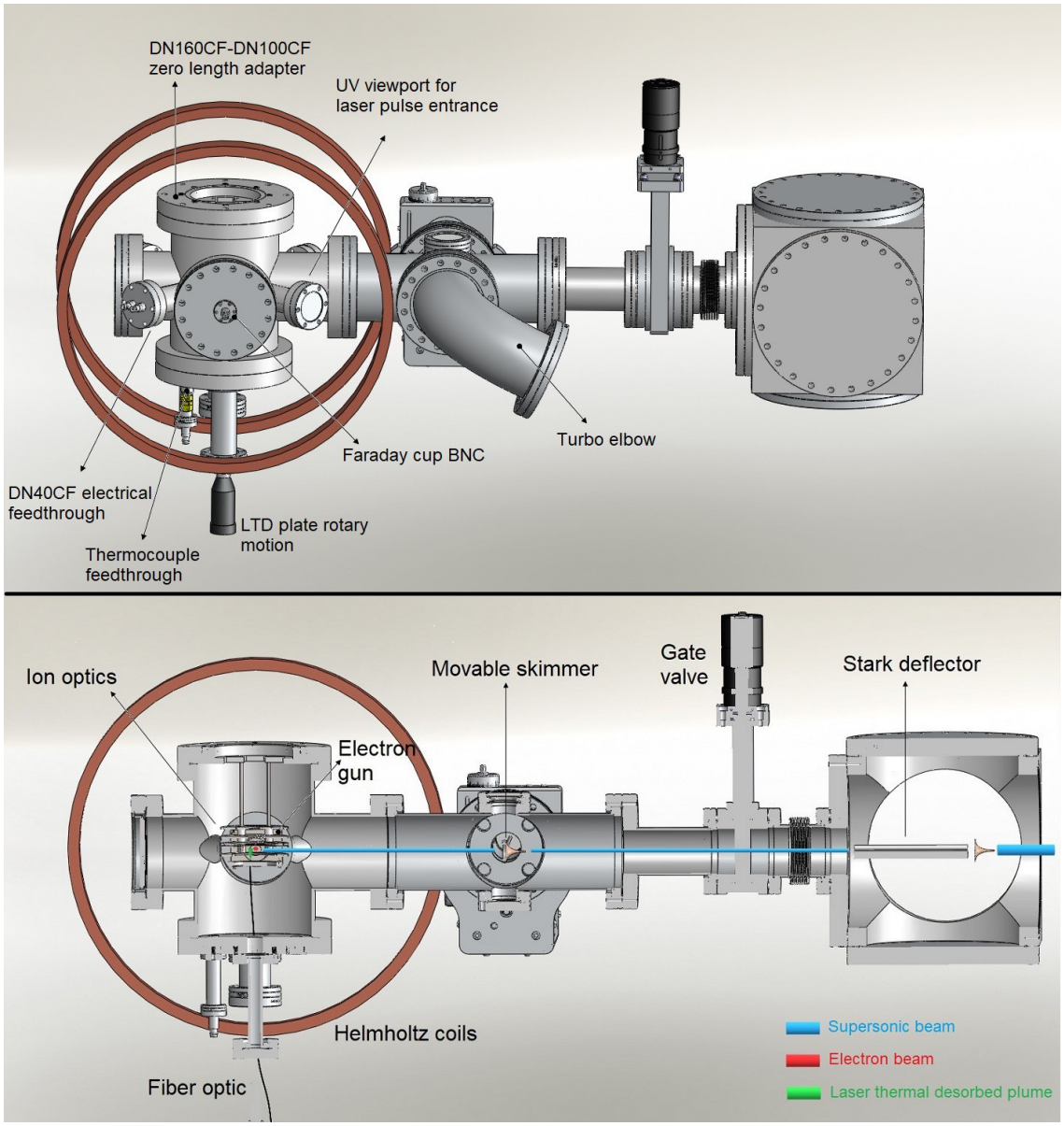

Figure E.1: CAD of the new DEA / EII / MPI apparatus. The expansion chamber is not depicted. The bottom figure shows a cut plane of the experiment where components in the vacuum side are visible. The supersonic beam, the electron beam and the ILT-desorbed plume are represented by blue, red and green colours, respectively.

Appendix F

Publications

Published

- O. Ghafur, S.W. Crane, M. Ryszka, J. Bockova, A. Rebelo, L. Saalbach, S. De Camillis, J.B. Greenwood, S. Eden and D. Townsend, "Ultraviolet relaxation dynamics in uracil: Time-resolved photoion yield studies using a laser-based thermal desorption source", *Journal of Chemical Physics* 149 (2018), p. 034301.

- J. Bocková, A. Rebelo, M. Ryszka, R. Pandey, T. da Fonseca Cunha, P. Limão-Vieira, N. J. Mason, J. C. Poully and S. Eden, "Mapping the complex metastable fragmentation pathways of excited 3-aminophenol", *International Journal of Mass Spectrometry* 442 (2019), pp. 95−101.

- P.J.M. van der Burgt, M.A. Brown, J. Bockova, A. Rebelo, M. Ryszka, J.C. Poully and S. Eden, "Fragmentation processes of ionized 5-fluoruracil in the gas phase and within clusters", *European Physical Journal D* 73:184 (2019).

- M. Abdelmouleh, M. Lalande, J. El Feghaly, V. Vizcaino, A. Rebelo, S. Eden, T. Schlathölter and J. C. Poully, "Mass spectral signatures of complex post-translational modifications in proteins: a proof-of-principle based on X-ray irradiated Vancomycin", *Journal of the American Society for Mass Spectrometry* 31:8 (2020) pp. 1738−1743.

Accepted

- F. da Silva, T. Cunha, A. Rebelo, A. Gil, M. Calhorda, G. Garcia, O. Ingolfsson and P. Limão-Vieira, "Electron transfer induced side-chain cleavage in tryptophan facilitated through potassium induced transition-state stabilization in the gas-phase", *Journal of Physical Chemistry A*

In preparation / Under review

- J. Bockova, A. Rebelo, M. Ryszka, R. Pandey, D. Mészáros, P. Limão-Vieira, P. Papp, N. J. Mason, D. Townsend, K.L. Nixon, V. Vizcaino, J.C. Poully and S. Eden, "Thermal desorption effects on fragment ion production from multi-photon ionized uridine and selected analogues"

- A. Rebelo, J. Bockova, P. Limão-Vieira, J.C. Poully, K.L. Nixon, and S. Eden,"Investigating the fragmentation pathways of excited guanine ions: metastable dissociation experiments and DFT calculations of tautomer-dependent fragmentation"
- A. Rebelo, M. Ryszka, J. Bockova, R. Pandey, K.L. Nixon, P. Limão-Vieira, J.C. Poully, J. Küpper, and S. Eden, "Tracing reaction products to distinct neutral cluster precursors in Stark deflected CW beams: a proof of principle based on dissociative ionisation experiments on nitromethane clusters"